Department of Electrical Engineering and Automation

Earth Fault Distance Computation Methods Based on Transients in Power Distribution Systems

---

Mohd Rafi Adzman

Aalto University

DOCTORAL
DISSERTATIONS

Aalto University publication series
DOCTORAL DISSERTATIONS 189/2014

Earth Fault Distance Computation Methods Based on Transients in Power Distribution Systems

Mohd Rafi Adzman

A doctoral dissertation completed for the degree of Doctor of Science (Technology) to be defended, with the permission of the Aalto University, School of Electrical Engineering, at a public examination held at the Lecture hall S3 of the school on 8 December 2014 at 12 noon.

Aalto University
School of Electrical Engineering
Department of Electrical Engineering and Automation
Power System and High Voltage Engineering

Supervising professor
Professor Matti Lehtonen

Preliminary examiners
Professor Mansour H. Abdel-Rahman
University of Mansoura
Egypt

Ass. Prof. Dr. Ing. Peter Braciník
University of Žilina
Slovakia

Opponents
Ass. Prof. Dr. Ing. Peter Braciník
University of Žilina
Slovakia

Dr. Seppo Hänninen
VTT Technical Research Centre of Finland
Finland

Aalto University publication series
DOCTORAL DISSERTATIONS 189/2014

ISBN 978-952-60-5973-0 (printed)
ISBN 978-952-60-5974-7 (pdf)
ISSN-L 1799-4934
ISSN 1799-4934 (printed)
ISSN 1799-4942 (pdf)
http://urn.fi/URN:ISBN:978-952-60-5974-7

Unigrafia Oy
Helsinki 2014

Finland

NORDIC ECOLABEL
441 697
Printed matter

Aalto University

Abstract

Aalto University, P.O. Box 11000, FI-00076 Aalto www.aalto.fi

Author
Mohd Rafi Adzman

Name of the doctoral dissertation
Earth Fault Distance Computation Methods Based on Transients in Power Distribution Systems

Publisher School of Electrical Engineering

Unit Department of Electrical Engineering

Series Aalto University publication series DOCTORAL DISSERTATIONS 189/2014

Field of research Power System and High Voltage Engineering

Manuscript submitted 25 August 2014 **Date of the defence** 8 December 2014

Permission to publish granted (date) 4 November 2014 **Language** English

☒ **Monograph** ☐ **Article dissertation (summary + original articles)**

Abstract

The most common fault type in MV distribution network is single line to earth fault. The initial transients of earth faults are important especially for unearthed and compensated neutral networks. The earth fault transient signals consist of many different frequency components, which result from charging and discharging of the network capacitances. The transient components provide valuable information for fault location purposes. The charging component has higher amplitude and lower frequency than the discharge component and hence is more suitable to be used for fault location purposes.

In this thesis, we discuss algorithms to locate an earth fault in unearthed or a compensated neutral MV networks using the information of the measured transient signal. The networks considered are assumed to be radially operated and they are modeled using Electromagnetic Transient Program-Alternative Transient Program (EMTP-ATP). Five types of fault location algorithms have been developed which are called general model (GM) algorithm, exact model (EM) algorithm, continuous wavelet transform (CWT) based method, multiple regression analysis (MRA) based method and artificial neural network (ANN). GM algorithm is developed based on a simplified model of symmetrical components while EM algorithm is developed with exact ″pi″-model of symmetrical components. Both algorithms utilize the frequency of charging transient to estimate the fault distance. CWT based algorithm requires both voltage and current of transient signals to estimate the fault path inductance. MRA and NN algorithms were developed using the transient signal measured from the secondary side of the MV/LV distribution transformer. In addition, an algorithm to find a correct path towards the position of fault in network which has many branches is presented.

The results from intensive simulations and experiments in actual distribution networks are also presented in this thesis. The results are analyzed using signal processing techniques. The algorithms apply continuous wavelet transform (CWT) to locate the dominant charge transient frequency and extract the specific coefficient corresponding to the charge transient frequency. In this thesis, the properties of Hilbert transformation (HT) are used to estimate the damping attenuation of the transient signal.

Finally the performance of the proposed fault location algorithms is evaluated and the results are compared. Based on the simulation results, it is found that the proposed algorithms work at a reasonable level of accuracy. The results from real experiment data show that both CWT and GM algorithms have a comparable result.

Keywords Earth fault, fault location, distribution network, continuous wavelet transform, charge transient, neural network, multiple regression analysis, ATP-EMTP

ISBN (printed) 978-952-60-5973-0 **ISBN (pdf)** 978-952-60-5974-7

ISSN-L 1799-4934 **ISSN (printed)** 1799-4934 **ISSN (pdf)** 1799-4942

Location of publisher Helsinki **Location of printing** Helsinki **Year** 2014

Pages 234 **urn** http://urn.fi/URN:ISBN:978-952-60-5974-7

Preface

First of all, thanks and praise is due to almighty Allah, The Most Gracious, The Most Merciful, who guide me in every step I take.

This work would have been impossible without the help and guidance of several people, whose contribution I would like to acknowledge. First of all, I would like to express my deepest gratitude to my supervisor Professor Matti Lehtonen, for accepting and giving me this wonderful research project. His supervision and his guidance both helped me to channel and specify the discussed ideas and at the same time provided much appreciated freedom and support to explore new ways and concepts. I am also thankful to the pre-examiners Professor Dr. Mansour H. Abdel-Rahman and Assoc. Professor Dr. Ing. Peter Braciník for reading the thesis manuscript and I appreciate their valuable comments.

I owe special thanks to Dr. David Topolanek for a useful discussions and providing me a data used in this research and Mr. Tatu Nieminen for front cover picture of my dissertation. Many thanks go to a research colleague at room I344, Muzamir, M. Shafiq, Zoko, Michael, Ilhan, Ali, Rizk, Gang Liu and to all the wonderful people at Department of Electrical Engineering who have offered me a pleasant and encouraging working environment.

I would like to express my appreciation for the financial support I received from Universiti Malaysia Perlis (UniMAP), Ministry of Education Malaysia (MOE), as well as research support from Aalto University, Graduate School of Electrical Energy and Engineering, Ella and Georg Ehrnrooth Foundation and FORTUM Foundation.

I am personally want to thank all of my Malaysian friends and their families for their outstanding support, encouragement and concerns during my stay in Finland.

Last but not least, I want to express my heartfelt thanks to my beloved family, wife Normiza Mohd Noor and children Nurin Yasmin, Mohammad Haziq Fiqri and Mohammad Wafiq Ziqri for their love, patience and endless support. My sincere appreciations to my parents, Sumyati Sauji and Adzman Ibrahim, parents-in-law, Endon Ibrahim and Mohd Noor Che Chik, and my families in Malaysia for their love and prayers.

Vantaa, November 10, 2014,

Mohd Rafi Adzman

Contribution of the author

The author has developed the methodology presented and used in the analyses and made all the analyses himself. The results and conclusions are the sole work of the author.

Contents

Preface **5**

Contribution of the author **7**

Contents **9**

List of Tables **13**

List of Figures **17**

List of Symbols **25**

List of Abbreviations **31**

1. Introduction **33**
- 1.1 Background and Problem Statement 33
- 1.2 Research Objective 35
- 1.3 Research Contribution 36
- 1.4 Organization of Thesis 37

2. Transients of Single Phase to Earth Fault **39**
- 2.1 The Discharge Transient 39
- 2.2 The Charge Transient 41
- 2.3 Transient of Suppression Coil Current 44

3. Fault Location Methods Based on Earth Fault Transient Signals **47**
- 3.1 Method based on Frequency of Charging Transient 47
- 3.2 Wavelet Method 49
- 3.3 Differential Equation Method 50
- 3.4 Least Square Fitting Method 50
- 3.5 Fourier Transform Method 51

3.6 Traveling Wave method 52
3.7 Artificial Intelligence Method 53

4. Determination of Transient Components with Signal Processing Methods 55
4.1 Filtering of 50 Hz Component 55
4.2 Spectrum Analysis using Discrete Fourier Transform 56
4.3 Time-Frequency Analysis 57
4.4 Identification of Charge Transient Component 58
4.5 Analytic Representation and Damping Estimation Using Hilbert Transform (HT) 60

5. Fault Distance Estimation Using Transient Signals 65
5.1 General Model (GM) of Symmetrical Components 66
  5.1.1 General Model 1 (GM1) 68
  5.1.2 General Model 2 (GM2) 71
  5.1.3 General Model 3 (GM3) 72
  5.1.4 General Model 4 (GM4) 74
5.2 Exact Model (EM) of Symmetrical Components 77
  5.2.1 Exact Model 1 (EM1) 78
  5.2.2 Exact Model 2 (EM2) 80
  5.2.3 Exact Model 3 (EM3) 81
5.3 Continuous Wavelet Transform (CWT) 83
5.4 Transient Signal Recorded from the Secondary side of the MV\LV Distribution Transformer 85
  5.4.1 Pre-processing stage 87
  5.4.2 Multiple Regression Analysis (MRA) 89
  5.4.3 Artificial Neural Network (ANN) 90
  5.4.4 Correct path location in branches of feeders 92

6. Performance Evaluation of Proposed Fault Location Algorithms Using EMTP/ATP Simulation Model 95
6.1 Simulated Network Model 1 96
  6.1.1 Description of the simulation and the network model 96
  6.1.2 Result Analysis and Discussion 97
6.2 Simulated Network Model 2 126
  6.2.1 Description of the simulation and the network model 126
  6.2.2 Result Analysis and Discussion 128
6.3 Simulated Network Model 3 135

6.3.1 Description of the simulation and the network model 135
6.3.2 Result Analysis and Discussion 137
6.4 Simulated Network Model 4 148
6.4.1 Description of the simulation and the network model 148
6.4.2 Result Analysis and Discussion 151

7. Performance Evaluation of Proposed Fault Location Algorithms Using Transients Recorded in Real Networks 163
7.1 Case study 1 163
7.1.1 Description of Real Network Case 1 163
7.1.2 Result Analysis and Discussion 167
7.2 Case study 2 174
7.2.1 Description of Real Network Case 2 174
7.2.2 Result Analysis and Discussion 174
7.3 Case study 3 183
7.3.1 Description of Real Network Case 3 183
7.3.2 Result Analysis and Discussion 185

8. Conclusions and Future Work 191

References 195

Appendix A. Mathematical Derivations and MATLAB Scripts 209
A.1 Derivation of Equation for General Model 1 Damped Natural Frequencies 209
A.2 Derivation of Equation for General Model 2 Undamped Natural Frequencies 210
A.3 Derivation of Equation for General Model 3 Damped Natural Frequencies 211
A.4 Derivation of Equation for General Model 4 Undamped Natural Frequencies 213
A.5 Example of Matlab Script for MRA model 214

Appendix B. ATPDraw OH Line Configurations and Load Variation 215
B.1 ATPDraw OH Line Geometrical and Electrical Configurations 215
B.2 Load Variation for Simulation Model 4 216

Appendix C. Tables of Simulation Results 217
C.1 Tabulated Results of Simulated Network Model 1 217
C.2 Tabulated Results of Simulated Network Model 2 224

C.3 Tabulated Results of Simulated Network Model 4 229

List of Tables

5.1 Description of the composite components. 67

6.1 Test results of single line to earth fault for 90° fault inception angle using the WT algorithm. 138
6.2 Test results of single line to earth fault for 45° fault inception angle 139
6.3 Data generation for MRA and NN formulation. 150
6.4 Data generation for testing the MRA and NN algorithm. . . 150

7.1 Case 1 network parameters. 167
7.2 Calculation results using CWT and GM2 algorithm. 167
7.3 Case 2 network parameters. 175
7.4 Calculation results using CWT and GM2 algorithm. 182
7.5 Description of actual single line to earth fault experiment. . 185
7.6 Test result of single line to earth fault using recorded signal. 189

B1 Simulation model 4 data. 216

C1 Comparison of simulation test result to the theory of earth fault transient using GM1 equations. 217
C2 Comparison of the distance estimates obtained using GM algorithms. 218
C3 Comparison of simulation test result to the theory of earth fault transient with the effect of fault resistance using GM1 equations. 219
C4 Comparison of the distance estimates obtained of the GM algorithm methods with effect of fault resistance. 220
C5 Comparison of simulation test result to the theory of ground fault transient with effect of fault inception angle using GM1 equations. 221

C6 Comparison of the distance estimates obtained of the GM algorithm methods with the effect of fault inception angle. . 221
C7 Comparison of simulation test result to the theory of ground fault transient with the effect of composite loads using GM3 equations. 222
C8 Comparison of the distance estimates obtained of the GM algorithm methods with effect of composite loads. 223
C9 Comparison of the distance estimates obtained between EX1 and GM2 algorithm. 224
C10 Comparison of the distance estimates obtained between EM1 and GM2 algorithm with the effect of fault resistance. 225
C11 Comparison of the distance estimates obtained between EM1 and GM2 algorithm with the effect of fault inception angle. . 225
C12 Comparison of the distance estimates obtained between EM1 and GM2 algorithm with the effect of resistive loads. 226
C13 Comparison of the distance estimates obtained between EM1 and GM2 algorithm with the effect of inductive loads. 227
C14 Comparison of the distance estimates obtained between EM1 and GM2 algorithm with the effect of loads of 0.9 power factor. The loads are located at the end of each feeders. 228
C15 Comparison of the distance estimates obtained between EM1 and GM2 algorithm with the effect of loads of 0.5 power factor. The loads are located at the end of each feeders. 228
C16 Comparison of the distance estimates obtained from multiple regression (MRA) and neural network (NN) algorithm with the effect of fault resistance. Fault inception angle is 90°. 229
C17 Comparison of the distance estimates obtained from multiple regression (MRA) and neural network (NN) algorithm with the effect of fault resistance. Fault inception angle is 45°. 230
C18 Comparison of the distance estimates obtained from GM algorithms with the effect of fault resistance. Signal measured from MV/LV side and fault inception angle is 90°. . . . 231
C19 Comparison of the distance estimates obtained from GM algorithms with the effect of fault resistance. Signal measured from MV/LV side and fault inception angle is 45°. . . . 232

C20 Comparison of the distance estimates obtained from EM algorithms with the effect of fault resistance. Signal measured from MV/LV side and fault inception angle is 90°. . . . 233
C21 Comparison of the distance estimates obtained from EM algorithms with the effect of fault resistance. Signal measured from MV/LV side and fault inception angle is 45°. . . . 234

List of Figures

2.1 An example of the earth fault transient signal in MV overhead line network. 40
2.2 Discharge of faulty lines in isolated neutral network. 40
2.3 Charge of healthy lines in isolated neutral network. 42
2.4 Equivalent circuit for charge transient calculation. 42
2.5 An example of composite earth fault transient signal and its CWT analsyis. 43
2.6 Charge of healthy lines in a suppression coil network. 45
2.7 Equivalent circuit model of transient of the suppression coil 46

3.1 Propagation of traveling wave in power network due to earth fault. 52

4.1 Example of the ouput of pre-processing of transient signal using CWT. 60
4.2 Example of the output from pre-processing of current transient signals using CWT 62
4.3 Example of instantaneous current amplitude, envelope and the linear decaying of the extracted CWT coefficient of charge component. 63

5.1 The general model for earth fault transients. 67
5.2 The basic idea of fault location algorithm using general model of symmetrical components. 68
5.3 The equivalent circuit for earth fault transient of general model 1 (GM1) algorithm. 69
5.4 The equivalent circuit for earth fault transient of general model 2 (GM2) algorithm. 71

5.5 The equivalent circuit for earth fault transient of general model 3 (GM3) algorithm. 72
5.6 The equivalent circuit for earth fault transient of general model 4 (GM4) algorithm. 74
5.7 Flowchart for fault location algorithm using general model of symmetrical components. 75
5.8 Exact π-model equivalent circuit with damping included. . . 77
5.9 The equivalent circuit for earth fault transient of exact model 1 (EM1) algorithm. 79
5.10 The equivalent circuit for earth fault transient of exact model 2 (EM2) algorithm. 80
5.11 The equivalent circuit for earth fault transient of exact model 3 (EM3) algorithm. 81
5.12 Flowchart for fault location algorithm using exact π-model of symmetrical component. 82
5.13 Flowchart for fault location algorithm based on CWT. 84
5.14 Flowchart for MRA and NN fault location algorithms based on recorded transient signal of single MV/LV distribution transformer. 86
5.15 An example of simulated transient signal recorded at MV and MV/LV distribution transformer. 87
5.16 Characteristics of extracted CWT coefficient of transient signal recorded from MV/LV distribution transformer. 88
5.17 Architecture of neural network for estimate the fault distance. 91
5.18 Flowchart for correct path location algorithm based on recorded transients of MV/LV distribution transformers. 92

6.1 A schematic diagram and ATPdraw simulated network model for earth fault simulation analysis in 20 kV unearthed medium votage network. 97
6.2 Simulated transient voltage signal in the faulty phase when a single phase to earth fault happens at a feeder in an example of a network with overhead line. 98
6.3 Simulated transient current signal in the faulty phase when a single phase to earth fault happens at a feeder in an example of a network with overhead line. 99
6.4 Example of the output from pre-processing of voltage transient signals using CWT and Hilbert transformation. 101

6.5 Example of the output from pre-processing of current transient signals using CWT and Hilbert transformation. 102

6.6 Example of the output from pre-processing of current transient signals using CWT with the effect of fault resistance (R_f=25 Ω, R_f=50 Ω and R_f=100 Ω). 103

6.7 Example of the output from pre-processing of current transient signals using CWT with the effect of fault resistance (R_f=200 Ω, R_f=300 Ω and R_f=400 Ω). 104

6.8 Example of scale-dependent energy percentage distribution with R_f=25 Ω, R_f=50 Ω and R_f=100 Ω. 106

6.9 Example of scale-dependent energy percentage distribution with R_f=200 Ω, R_f=300 Ω and R_f=400 Ω. 107

6.10 Comparison of simulation test result to the theory of earth fault transient. 108

6.11 Comparison of the distance estimates obtained using general model (GM) algorithms for the simulated single line to earth faults with varies fault distance. 109

6.12 Results of calculated and estimated damped (f_{dc}, f_{dm}) and undamped (f_{nc}, f_{nm}) frequencies with the effect of fault resistance (R_f). 110

6.13 Comparison of results of calculated (f_{dc}) and estimated (f_{dm}) damped frequencies with the effect of fault resistance (R_f). . 111

6.14 Comparison of results of calculated (f_{nc}) and estimated (f_{nm}) undamped frequencies with the effect of fault resistance (R_f).112

6.15 Result of calculated (ζ_c) and estimated (ζ_m) damping factors with the effect of fault resistance (R_f). 113

6.16 Comparison of results of calculated (ζ_c) and estimated (ζ_m) damping factors with the effect of fault resistance (R_f). . . . 114

6.17 Distance estimates with the effect of fault resistance 115

6.18 Comparison of simulated transient signal and its scalogram with the effect of inception angle. The fault distance is 4 km and without fault resistance. 117

6.19 Distance estimates with fault inception angle 117

6.20 Comparison of calculated damped frequencies with the effect of load and fault resistance 118

6.21 Comparison of estimated damped frequencies with the effect of load and fault resistance 119

6.22 Comparison of calculated undamped frequencies with the effect of load and fault resistance 121
6.23 Comparison of estimated undamped frequencies with the effect of load and fault resistance 122
6.24 Calculated and estimated damping factor (ζ) with the effect of load and fault resistance. 123
6.25 Distance estimates with the effect of 5 MVA load and fault resistances for general model networks. 124
6.26 Distance estimates with the effect of 12 MVA load and fault resistances for general model networks. 125
6.27 A schematic network diagram and its simulation model for a single phase to earth fault in a distribution network. . . . 127
6.28 The effect of fault distance, fault resistance and fault inception angle on fault distance calulation 129
6.29 Fault location performance with the effect of resistive load located at the end of each feeder 131
6.30 Fault location performance with the effect of inductive load located at the end of each feeder 132
6.31 Fault location performance with the effect of load with 0.9 PF and 0.5 PF located at the end of each feeder 134
6.32 A schematic diagram of 20 kV, 227.6 km, unearthed neutral MV network. 136
6.33 ATPdraw circuit for the simulated network model 3. 136
6.34 CWT FFT amplitude of MV/LV substation for fault test number 1 with fault inception angle of 90° and 45°. The arrow indicates the substation with the highest amplitude. 140
6.35 CWT FFT amplitude of MV/LV substation for fault test number 7, 2, 8, 10 and 4 with fault inception angle of 90°. The arrow indicates the substation with the highest amplitude. . 141
6.36 CWT FFT amplitude of MV/LV substation for fault test number 9, 11, 3, 6 and 5 with fault inception angle of 90°. The arrow indicates the substation with the highest amplitude. . 142
6.37 CWT FFT amplitude of MV/LV substation for fault test number 7, 2, 8, 10 and 4 with fault inception angle of 45°. The arrow indicates the substation with the highest amplitude. . 143
6.38 CWT FFT amplitude of MV/LV substation for fault test number 9, 11, 3, 6 and 5 with fault inception angle of 45°. The arrow indicates the substation with the highest amplitude. . 144

6.39 Test number 2 (11.70 km) correct path identification. 145
6.40 Test number 3 (22.80 km) correct path identification. 145
6.41 Test number 4 (17.50 km) correct path identification. 146
6.42 Test number 6 (25.83 km) correct path identification. 146
6.43 Test number 8 (12.53 km) correct path identification. 147
6.44 Schematic diagram of the simulated 20 kV ungrounded neutral MV network. 148
6.45 ATPdraw circuit for the simulated network model 4. 149
6.46 A comparison of estimated FFT amplitudes of extracted CWT coefficient at 4 different MV/LV distribution transformers (DT) with inception angle of 90 °. 152
6.47 A comparison of estimated FFT amplitudes of extracted CWT coefficient at 4 different MV/LV distribution transformers (DT) with inception angle of 60°. 153
6.48 A comparison of estimated FFT amplitudes of extracted CWT coefficient at 4 different MV/LV distribution transformers (DT) with inception angle of 30°. 154
6.49 Comparison of the distance estimate errors obtained from multiple regression (MRA) and neural network (NN) algorithm with the effect of fault resistance (R_f). Fault inception angle is 90°. 156
6.50 Comparison of the distance estimate errors obtained from multiple regression (MRA) and neural network (NN) algorithm with the effect of fault resistance (R_f). Fault inception angle is 45°. 157
6.51 Comparison of the distance estimate errors obtained from general model (GM1,GM2,GM4) algorithms with the effect of fault resistance (R_f). Signal measured from MV/LV substation and fault inception angle is 90°. 158
6.52 Comparison of the distance estimate errors obtained from general model (GM1,GM2,GM4) algorithms with the effect of fault resistance (R_f). Signal measured from MV/LV substation and fault inception angle is 45°. 159
6.53 Comparison of the distance estimate errors obtained from exact model (EM1-EM3) algorithms with the effect of fault resistance (R_f). Signal measured from MV/LV substation and fault inception angle is 90°. 160

6.54 Comparison of the distance estimate errors obtained from exact model (EM1-EM3) algorithms with the effect of fault resistance (R_f). Signal measured from MV/LV substation and fault inception angle is 45°. 161

7.1 Compensated neutral network test diagram for test 1-2 . . . 164
7.2 Compensated neutral network test diagram for test 3-4 . . . 165
7.3 Isolated neutral network test diagram for test 5-8 166
7.4 Recorded signals of single line to earth fault at 0.46 km. . . 168
7.5 Recorded signals of single line to earth at 10.40 km. 169
7.6 Recorded signals of single line to earth fault at 14.20 km. Test number 5 and 6. 170
7.7 Recorded signals of single line to earth fault at 14.20 km. Test number 7 and 8. 171
7.8 Example of output from pre-processing of test number 1 (0.76 km) transient signal using CWT analysis. 172
7.9 Example of output from fault distances algorithm based on CWT for test number 1. 173
7.10 Results of fault distance estimation (l_f) using CWT algorithm.173
7.11 Lounais-Suomen Sahko OY network test diagram. 175
7.12 Recorded signals of single line to earth fault at 25.40 km. Test number 1 and 2. 176
7.13 Recorded signals of single line to earth fault at 25.40 km. Test number 3 and 4. 177
7.14 Recorded signals of single line to earth fault at 25.40 km (test number 5) and 36.0 km (test number 6). 178
7.15 Recorded signals of single line to earth fault at 36.0 km. . . 179
7.16 Example of CWT scalogram and energy percentage distribution of test number 4 (25.4 km) transient signal. 180
7.17 Example of CWT extracted coefficients, FFT frequency spectrum of ectracted coefficent and, voltage and current linear decaying of extracted CWT coefficient of test number 4 (25.4 km) transient signal. 181
7.18 Fault distances calculated using CWT algorithm. 182
7.19 Schematic diagram of Czech distribution network. 183
7.20 Photo taken during the experiment. 184
7.21 Recorded signals of experiments 1. 186
7.22 Recorded signals of experiments 2. 186
7.23 Recorded signals of experiments 3. 187

7.24 Recorded signals of experiments 4. 187
7.25 Recorded signals of experiments 5. 188
7.26 Fault distances calculated using CWT algorithm. 188

A1 The equivalent circuit for ground fault transient model 1 . . 209
A2 The equivalent circuit for ground fault transient model 2 . . 210
A3 The equivalent circuit for ground fault transient model 3 . . 211
A4 The equivalent circuit for ground fault transient model 4 . . 213

B1 Simulation network model 3 ATPDraw OH configurations . 215
B2 Simulation network model 4 ATPDraw OH configurations . 215

List of Symbols

a	Positive scale
a_0^m	Scaling (dilation) parameters
A	Ampere
	FFT amplitude of extracted CWT coefficient
	Amplitude
b	Time shifting factor
	Time position
C	Capacitance
	Coefficient
	Phase to phase capacitance
$C(a, b)$	Wavelet coefficient
C_e	Phase to earth capacitance
C_{eq}	Equivalent capacitance
$C_{j,0}$	Zero sequence capacitance of sound line
$C_{j,p}$	Positive sequence capacitance of sound line
$C_{l,n}$	Capacitance per unit length of negative sequence system
$C_{l,0}$	Capacitance per unit length of zero sequence system
$C_{l,0'}$	Zero sequence capacitance of faulty line located behind of the fault point (F)
$C_{l,p}$	Capacitance per unit length of positive sequence system
$C_{l,p'}$	Positive sequence capacitance of faulty line located behind of the fault point (F)
C_p	Positive sequence capacitances of the network
C_0	Zero sequence capacitances of the network
$C_V(a, b)$	Wavelet coefficient of voltage transient signals
$C_I(a, b)$	Wavelet coefficient of current transient signals
C_E	Phase to earth capacitance
E_{SC}	Sum of percentage energy coefficient associated to same scale

f	Frequency
f_c	Charge transient frequency(Hz)
	Calculated transient frequency(HZ)
	Natural frequency(Hz)
f_d	Discharge transient frequency (Hz)
f_{dc}	Calculated damped transient frequency(Hz)
f_{dm}	Estimated damped transient frequency (HZ)
f_m	Estimated transient frequency(Hz)
f_{nc}	Calculated undamped transient frequency(Hz)
f_{nm}	Estimated undamped transient frequency (Hz)
f_s	Sampling frequency(Hz)
$f(t)$	Original signal
F	Fault point
F_c	Pseudo-frequency
F_0	Center frequency
g	Output of filter
i	Phase current
$\hat{i}_c$	Initial amplitude of charge transient
$\hat{i}_e$	Uncompensated steady state earth fault current
I	Current amplitude coefficient
I_c	Charging current
I_ω	Complex wavelet coefficient of current
k	Integer variable parameters
	Sample number
	Node
ka_0^m	Translation (time shift) parameters
l	Fault distance
l_{cl}	Length of connected line
l_f	Fault distance
L	Inductance
	Total loads
	Line
L_c	Inductance of suppression coil
L_{dt}	Inductance of distribution transformer
L_{eq}	Equivalent inductance
$L_{j,0}$	Zero sequence inductance of sound line
$L_{j,p}$	Positive sequence inductance of sound line
L_l	Fault path inductance

$L_{l,n}$	Inductance per unit length of negative sequence system
$L_{l,0}$	Inductance per unit length of zero sequence system
$L_{l,0'}$	Zero sequence inductance of faulty line located behind of the fault point (F)
$L_{l,p}$	Inductance per unit length of positive sequence system
$L_{l,p'}$	Positive sequence inductance of faulty line located behind of the fault point (F)
L_p	Sum of the inductances of coupling transformer, suppression coil, faulty line and fault
L_L	Inductance of the line Inductance of composite loads
L_T	Substation transformer phase inductance
n	Integer variable parameters
N	Samples
r	Neural network correlation coefficient
R	Resistance
R_{dt}	Resistance of distribution transformer
R_f	Fault resistance
$R_{l,n}$	Resistance per unit length of negative sequence system
$R_{l,0}$	Resistance per unit length of zero sequence system
$R_{l,p}$	Resistance per unit length of positive sequence system
R_p	Sum of the resistances of coupling transformer, suppression coil, faulty line and fault
R_L	Resistance of composite loads
R_T	Resistance of substation transform
s	Complex frequency
S	Scale of extracted CWT coefficient Root of the transient characteristic equation Complex frequency
SC	Percentage of the energy for each CWT coefficient Scalogram
t	Time
t_d	Time difference between two consecutive peaks
T	Period of fundamental frequency
$\tilde{u}(t)$	Hilbert transform of signal $u(t)$
U	Voltage amplitude coefficient
U_ω	Complex wavelet coefficient of voltage
$U(t)$	Analytic signal

U_v	Analytic form of the extracted wavelet coefficient of the voltage transient
U_i	Analytic form of the extracted wavelet coefficient of the current transient
v	Phase voltage
	Velocity of the travelling wave
	Wave propagation velocity
$\hat{v}$	Phase voltage peak value
v_e	Instantaneous phase to earth voltage
x	Estimated fault distance
Y	Admittance
$Y_{012}(s)$	Line sequence admittance matrix in the complex frequency domain
Z	Impedance
$\underline{Z}(\omega)$	Frequency component of impedance
Z_{kk}^1	Positive sequence diagonal element in the k node
Z_{kk}^0	Zero sequence diagonal element in the k node
$Z_{012}(s)$	Line sequence impedance matrix in the complex frequency domain
Z_T	Substation transformer impedance
α_c	Damping attenuation corresponding to charge transient
α_d	Damping attenuation corresponding to discharge transient
α_m	Estimated damping attenuation
β	Slope
	Coefficient
δ	Damping attenuation
Δ	Sampling period
	Increment
ζ	Damping factor
ζ_c	Damping factor corresponding to charge transient
	Calculated damping factor
ζ_d	Damping factor corresponding to discharge transient
ζ_m	Estimated damping factor
λ	Local coefficient
ϕ	Phase angle
φ	Phase
	Phase shift
Ψ	Mother wavelet
ψ	Mother wavelet
ω	Frequency (rad/s)
ω_c	Damped charge transient frequency (rad/s)
ω_d	Damped discharge transient frequency (rad/s)

ω_{dm}	Estimated damped transient frequency (rad/s)
ω_f	Fundamental angular frequency (rad/s)
ω_{nc}	Estimated undamped transient frequency for charge transient(rad/s)
ω_{nd}	Estimated undamped transient frequency for discharge transient(rad/s)
ω_{nm}	Estimated undamped transient frequency (rad/s)
ω_0	Undamped natural frequency (rad/s)
1	Primary
	Index of transient root
2	Secondary
	Index of transient root

List of Abbreviations

AC	Alternating current
AMR	Automatic meter reading
ANN	Artificial neural network
ATP	Alternative transient program
CWD	Choi-Williams distribution
CWT	Continuous wavelet transform
DC	Direct current
DFT	Discrete Fourier transform
DOM	'Domanin' distribution substation
DT	Distribution transformer
DWT	Discrete wavelet transform
DWF	Discrete wavelet filter
EM	Exact model
$EMTP$	Electromagnetic transient program
FD	Frequency-dependent
FL	Fault location
FT	Fourier transform
GM	General model
HT	Hilbert transform
HV	High voltage
Im	Imaginary part of a complex number
$IEDS$	Intelligent electronic devices
ln	Natural logarithm
LV	Low voltage
MLP	Multilayer perceptron
MRA	Multiple regression analysis
MV	Medium voltage
$NOVE$	'Nove Mesto' distribution substation

OLE	'Olesna' distribution substation
POH	'Pohledec' distribution substation
RMS	Root mean square
STFT	Short time Fourier transform
WVT	Wigner-Ville transform

1. Introduction

1.1 Background and Problem Statement

This thesis focuses on single phase to earth faults in medium voltage (MV) distribution feeders. Single phase to earth fault is the most common fault type in power distribution networks. In Nordic countries, about 50% to 80% of the faults are of this type [1, 2]. In Finland, about 70% of the permanent faults that occur in rural MV networks are caused by animals and weather conditions, like thunder, snow, icing, storm, hard wind and fallen trees [3]. One of the solution to reduce an earth fault in overhead line feeders is by replacing the bare conductor to covered conductor type of overhead line. However, the solution requires a huge amount of investment. Based on the statistics survey done by [4], a typical feeder construction in MV distribution network was a mixture of both covered conductors and bare overhead lines on the same feeders. The share of covered conductors per feeder varies between 10% to 50% and all the permanent faults at covered conductor feeders were earth faults [4].

In 2010, a fault statistic studied by utility company in Dresden Germany shows that 75% of all faults are earth faults [5]. In Finland, over 80% of the annual outage costs of customers are due to to faults in medium voltage distribution networks [6]. In rural overhead networks, earth fault currents are typically 10 - 40 A [7]. The small earth fault current is an advantage to system operation and is unlikely to cause damage to the power system components. However, the detection and localization of the fault is difficult due to the small current that reduces the sensitivity of the conventional relay which is normally based on currents and voltages at power frequency.

Basically, electricity supply system differs from one country to another.

In Finland and in most of countries in Europe the medium voltage (MV) networks are operated with neutral isolated or resonant earthed systems (i.e earthed via an arc-suppression coil also known as Peterson coil) [8]. The way the neutral is connected is important since it will affect the type of protection system needed and power system component selection. In isolated neutral networks earth fault currents are relatively small compared with earthed systems. With unearthed or resonant earthed system, the earth fault current is small and usually lower than the normal load current. When earth fault happens, the outage cost are accumulated during the time taken to locate and isolate the fault. In addition, a high fault resistance might also contribute to the losses. It is not possible to detect the high fault resistance using conventional feeder protection methods [9]. Therefore, it is very important to developed efficient methods for locating the faults. In recent years, several earth fault location algorithms in unearthed and compensated neutral networks has been developed and proposed [10–15]. However, there is no single method that can be used for locating a fault in all types of earth fault. Since the topology of distribution network usually has many branches compared to the transmission line, the task is even more tough since bare fault distance calculation gives several possible places.

In general, fault location algorithms can be categorized to three types [16], based on using fault generated signals, utilizing external signal sources and knowledge-based approaches. The fault generated signals can further be divided into three groups which are conventional [17–19], transients [20–23] and travelling waves [24–26]. Fault location algorithms based on injecting an external signal e.g. with a pulse generator are still being used by some of electric utilities nowadays. These algorithms use the concept of analyzing the relationship between the transmitted and reflected pulse of the injected signal [27, 28]. In another development the injected signal is use of a different frequency than are present in the network [29]. Several papers have proposed the use of knowledge based approach such as artificial neural networks, fuzzy set theory, expert systems and genetic algorithms for locating a fault in distribution system [30, 31]. The successfulness of these methods is highly depending on the amount and quality of the supplied data.

The initial transients of earth faults are important for fault location especially in unearthed and compensated neutral networks. The electromagnetic transient during a few milliseconds after the fault inception will provide the available information for estimating fault location. Even though the transient may cause problems to the conventional protective schemes it may work properly under transient protective scheme. The transient disturbance recorder can be installed at the monitored network to support the conventional signal measurement that is only based on the root mean square (RMS) voltage and current of the power frequency component. Nowadays, fault localization and detection based on fault transient signals in transmission and distribution network has been a subject of keen interest to utility and researchers [32–35].

With the upgrading of the distribution network towards the concept of "SmartGrids", more measuring and recording equipment such as smart meter, microprocessor digital relay, digital fault recorder and multi utility controller will be installed in low and medium voltage distribution substations. In order to adapt and apply the concept of distribution automation system in the network, those equipments are monitored and time synchronized. Thus, the realization of this kind of system will open more opportunity to control, optimize and enhance the reliability of current system. This will also affect the development and enhancement of current protection system and fault location algorithms in power networks.

The term fault location can be represented as the determination of the faulty feeder, branch or line section. It also can be used as a general term when we discuss about fault distance computation or estimation. This dissertation proposes fault location algorithms based on earth fault transient signals measured at secondary side of MV and LV distribution transformers in order to locate a single line to earth fault in unearthed and compensated neutral MV distribution networks.

1.2 Research Objective

In order to reduce the outage costs and to satisfy the quality of supply requirements, fault location algorithms have to locate fault as soon as possible and with an efficient way. This can be achieved by utilizing the information of initial transients of earthed faults. The idea of using transient signal as a basis of developing fault location algorithm is not a new thing. However, the formulation used to calculate the exact fault distance may be different. In addition, the implementation and the execution of algorithm might also be dissimilar. The main objective of this research is to developed accurate and efficient fault location algorithms for locating a single line to earth fault in unearthed and compensated neutral MV distribution networks. The developed fault location algorithms mainly utilize the information extracted from measured earth fault transient signal in MV substation and also from secondary side of MV/LV transformer. The work is intended to develop a variety of fault location algorithms. The developed fault location algorithms can be used as a tools to locate and estimate the fault distance of an earth fault in a faulty feeder.

1.3 Research Contribution

The contribution of the research can be divided into three main categories. In the first category, there are fault location algorithms based on measured transient signals using general model(GM) of symmetrical components, exact model (EM) of symmetrical components and continuous wavelet transform (CWT) based algorithm. The proposed algorithms mainly use measured transient signal from MV side of the faulty feeder, for example from MV main substation. In GM and EM algorithm, 4 general models (GM) and 3 exact models (EM) of symmetrical components has been presented and tested using simulated earth fault. Due to the limitation of information of line parameters in real networks, only GM2 and CWT algorithm were tested using real recorded data. Based on the results, GM2 and CWT algorithms managed to produce an acceptable accuracy in estimating the fault distance in a real network.

In the second category, were the algorithms based on earth fault transient signals measured from the secondary side of the MV/LV distribution transformer (DT). Fault location algorithm based on multiple regression analysis (MRA) and artificial neural network (ANN) was developed in this category. In addition, an algorithm which can be used as indication to select the correct path to the fault position when earth fault happens in a network that have several branches was developed.

In the third category, a technique to measure the damping factor of charge transient signal was proposed, based on continuous wavelet transform (CWT) analysis and Hilbert transformation. CWT analysis is a powerful tool to visualize the non-stationary signal such as earth fault transient. In this case, the calculated damping factor is used to estimate the undamped charge transient frequency which in turn will be used to estimate the fault distance in the GM algorithm.

1.4 Organization of Thesis

The thesis is organized into the following chapters:

Chapter 2 presents general knowledge of earth fault transient signals. The creation of charge and discharge transient signals when earth fault is established is also presented. In this chapter, transient of suppression coil current is also discussed.

Chapter 3 presents some known fault location methods based on earth fault transient signals. Methods based on frequency of charge transient, wavelet transform, differential equation, least square fitting, Fourier transform, traveling wave and artificial intelligence are presented.

Chapter 4 presents the determination of transient components with a signal processing method. In this chapter, filtering of 50 Hz components, spectrum analysis using discrete Fourier Transform (DFT) and Time frequency analysis are presented. Furthermore, identification of charge transient component is discussed. Then, analytic representation and damping estimation using Hilbert transformation (HT) is presented.

Chapter 5 presents the proposed fault distance estimation algorithms in this thesis. The proposed general model (GM), exact model (EM) and continuous wavelet transform (CWT) fault distance based algorithm are presented in this chapter. In addition, the proposed fault location algorithms based on transient signals recorded from secondary side of MV/LV distribution transformer, which are MRA and NN fault location algorithm are discussed. Furthermore, a fault path indication algorithm will also presented.

Chapter 6 presents performance evaluation of the proposed fault location algorithms using EMTP/ATP simulation model. In this chapter, the performance of proposed algorithms is evaluated with four simulated network models.

Chapter 7 presents performance evaluation of proposed fault location algorithms using transients recorded in real networks. In this chapter, three real case studies are presented.

2. Transients of Single Phase to Earth Fault

This chapter studies the transient signals which are generated from single line to earth fault. In [36], a technical analysis of transient phenomena associated with earth fault in a three phase system is given. According to [36], the transients are caused by redistribution of conductor voltage throughout the whole system, with the fault location as the origin of the change. When single line to earth fault occurs, two different processes are superposed [37–39]. Both charge and discharge transient processes start at the same time but with different duration. Figure 2.1 shows a typical single line to earth fault transient in the voltage and current of the faulted phase. The depicted signals were recorded in a 20 kV overhead line network.

In this chapter, we provide general knowledge about the transients which arise during the single phase to earth fault. In the following section, the process of charge and discharge transient will be explained using lumped model of two feeders and the earth fault at phase 3 of faulty feeder as shown in Figure 2.2 and Figure 2.3.

2.1 The Discharge Transient

In Figure 2.2, when earth fault is established at phase 3, the electric charge stored in the earth capacitance of faulty phase of faulty and healthy feeder has to be drained off starting at the fault location. The discharge transient will propagate in both directions to the end of line with the speed of traveling wave at certain characteristic impedance of the line. Then, the traveling waves are reflected at the end of the line respectively. The impedance of the faulty and healthy line, fault impedance at the fault location and the grounding resistance are the important parameters which affect the behavior of the discharge transient [37].

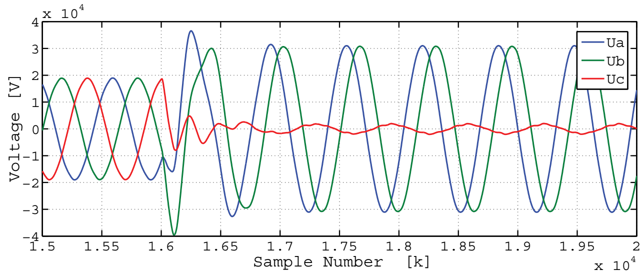

(a) Phase voltage

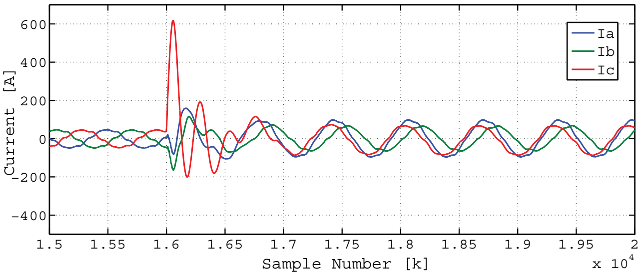

(b) Phase current

Figure 2.1. An example of the earth fault transient signal in MV overhead line network.

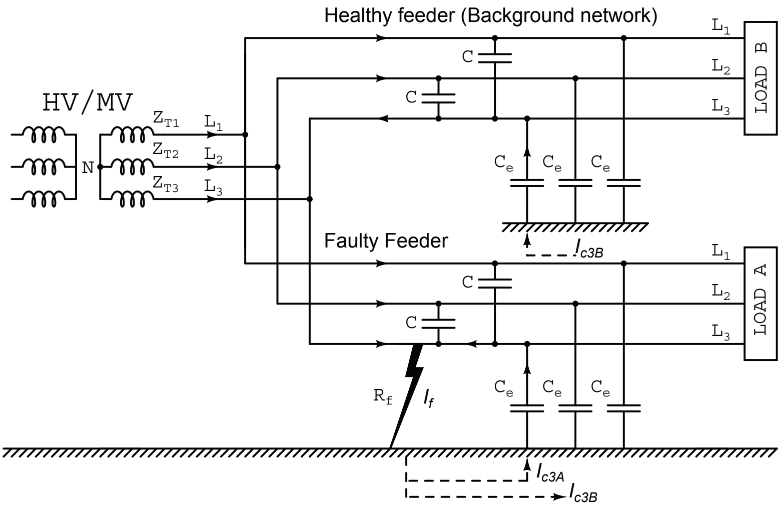

Figure 2.2. Discharge of faulty lines in isolated neutral network.

According to [38], the frequency of the discharge transient can be calculated as:

$$f_d = \frac{v}{4l_f} \tag{2.1}$$

where, v is the velocity of the traveling wave and l_f is the fault distance. According to [16], due to the influence of the connected line at the healthy feeder which contribute to the discharging of the capacitance, Equation (2.1) has to be modified and the discharge transient can be calculated as:

$$f_d = \frac{v}{4(l_f + l_{cl})} \tag{2.2}$$

where, v is the velocity of the traveling wave, l_f is the fault distance and l_{cl} represent the length of the connected line. Generally, the discharge transient components are short duration high frequency components. The discharge transient components are highly damped and disappear much quicker than the charge transient component. Based on the real tests conducted in [40], the amplitude of discharge component was typically 5 to 10% of the amplitude of charge component and their frequencies varied through the range of 500 to 2500 Hz for distribution network. Based on the Equation (2.1) and Equation (2.2), the fault distance significantly affects the frequency of the discharge transient. In HV transmission networks, the discharge transient frequency is about 300 to 5000 Hz [16].

2.2 The Charge Transient

Due to the ground fault, the voltage of the sound phases rapidly increases and subsequently increase the charge stored in their capacitances. In Figure 2.1, rapid increase of two sound phases right after the inception of the earth fault can be seen clearly. Figure 2.3 show the illustration of charging process of healthy phases in isolated neutral network. In the process, all the capacitive charging currents (I_c) of the healthy and faulty feeder have to flow over the fault location back to the transformer in phase 3. Assuming an earth fault is located at high voltage or medium voltage substation, according to [37, 38], based on the simplified lump circuit as shown in Figure 2.4, the frequency of charge component in undamped condition can be calculated as:

$$L_{eq} = 1.5L_T \tag{2.3}$$

$$C_{eq} = 2(C + C_e) \tag{2.4}$$

$$\omega_c = \frac{1}{\sqrt{L_{eq}C_{eq}}} = \frac{1}{\sqrt{3L_T(C + C_e)}} \tag{2.5}$$

where, L_T is the substation transformer phase inductance, C is the phase to phase capacitance and C_e is phase to earth capacitance of the network. Equation (2.5) is used when the fault happens at the busbar or when the inductance of the transformer is much higher compared to the line inductance. The faulty line inductance (L_f) can be added to transformer inductance (L_T) in Equation (2.5) for more exact solution.

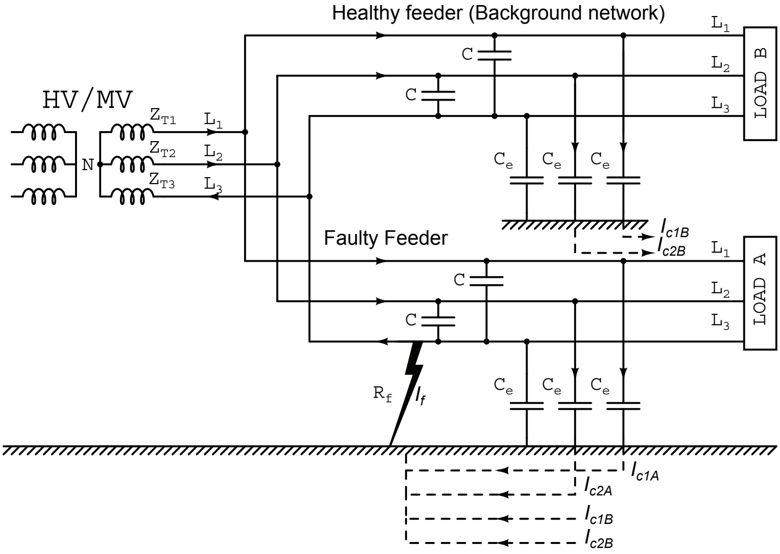

Figure 2.3. Charge of healthy lines in isolated neutral network.

The initial amplitude of the charge transient in an undamped case can be calculated as:

$$\hat{i}_c = \frac{v_e}{\omega_c L_{eq}} = v_e \omega_c C_{eq} \tag{2.6}$$

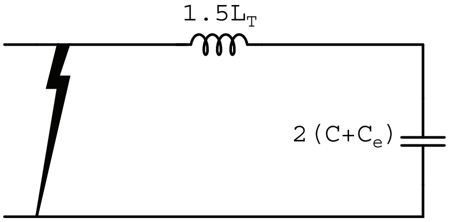

Figure 2.4. Equivalent circuit for charge transient calculation.

Assuming that the fault happens at the instantaneous phase voltage maximum, then the transient amplitude is calculated as in Equation (2.7):

$$\hat{i}_c = \frac{C_{eq}\omega_c}{3C_e\omega_f}\hat{i}_e \tag{2.7}$$

where ω_f is the fundamental angular frequency, v_e is the instantaneous phase to earth voltage at the fault moment and $\hat{i}_e$ is the uncompensated steady state earth fault current [40].

Figure 2.5 shows an example of spectral information of earth fault transient voltage and current signals recorded from general model of three sequence component networks. The general model will be discussed in detail in Chapter 5. The spectral information is obtained using continuous wavelet transform (CWT) analysis.

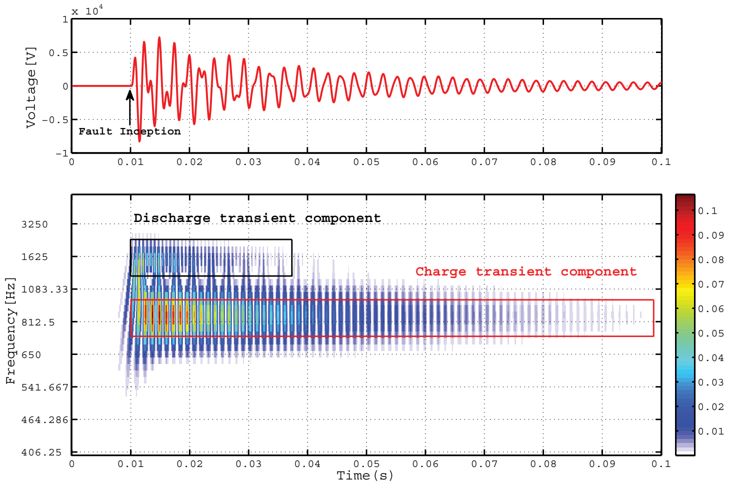

(a) Composite earth fault transient voltage (above) and its CWT Scalogram(below)

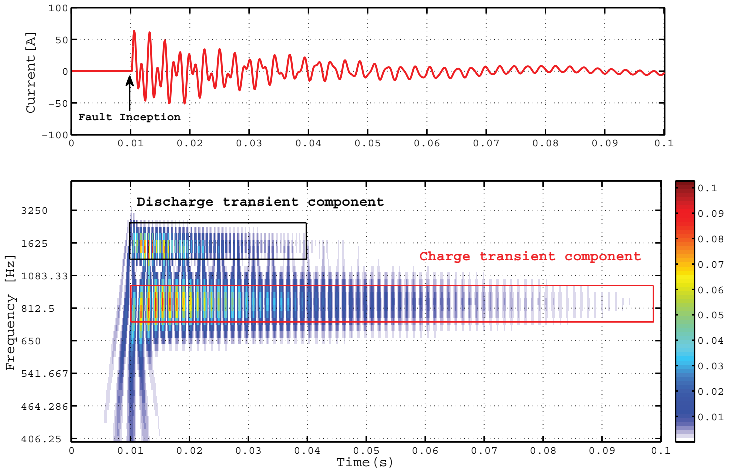

(b) Composite earth fault transient current (above) and its CWT Scalogram (below)

Figure 2.5. An example of composite earth fault transient signal and its CWT analysis. The red box referred most energy of charge transient component while the black box is for discharge transient component.

In Figure 2.5, it shows that the charge transient component has lower frequency and longer duration than the discharged transient component.

The time-frequency localization of the earth fault transient signals shows clearly the difference in terms of frequency and duration between these two transient components. The scalogram in Figure 2.5 represents the percentage of energy for each coefficient of the CWT analysis. The color bar in the figure represents the level of percentage of energy calculated. From the color bar the white color has the lowest energy while the red color shows the highest. It is found that the charge transient components carry much more energy than the discharge transient components. The energy is at its highest level at the beginning of the fault inception and then decreases towards the end of the signal. From the CWT analysis, both analyzed signals gave almost similar information with regard to the charge and discharge component. CWT analysis of simulated and recorded real earth fault transient signals will be discussed further in detail in Chapter 6 and Chapter 7.

Since charge transient components have lower band of transient frequency and longer compared to discharge transient components they are more suitable for the purpose of fault location and fault detection. Based on real measurements recorded in distribution and transmission systems, the typical value of charge transient is in the range of 100 - 800 Hz and 80 to 600 Hz, respectively [7, 16].

2.3 Transient of Suppression Coil Current

In resonant earthed network, also known as compensated neutral network, a Petersen coil is connected between the neutral point of the power system and the earth. In this case, in addition to the discharge and charge transients, we also have to consider the current of the suppression coil circuit as shown in Figure 2.6. According to [7], based on the fault loop impedance of the suppression coil, coupling transformer winding, faulty line length and the fault, the equation for the voltage becomes:

$$L_p \frac{di}{dt} + R_p i = \hat{v} sin(\omega_f t + \phi_v) \tag{2.8}$$

where i is the current that is composed of transient and permanent current, $\hat{v}$ is the phase voltage peak value, ω_f is the fundamental angular frequency, ϕ_v is initial phase angle, and L_p and R_p represents sums of the inductances and resistances of the suppression coil, coupling transformer winding, faulty line length and fault.

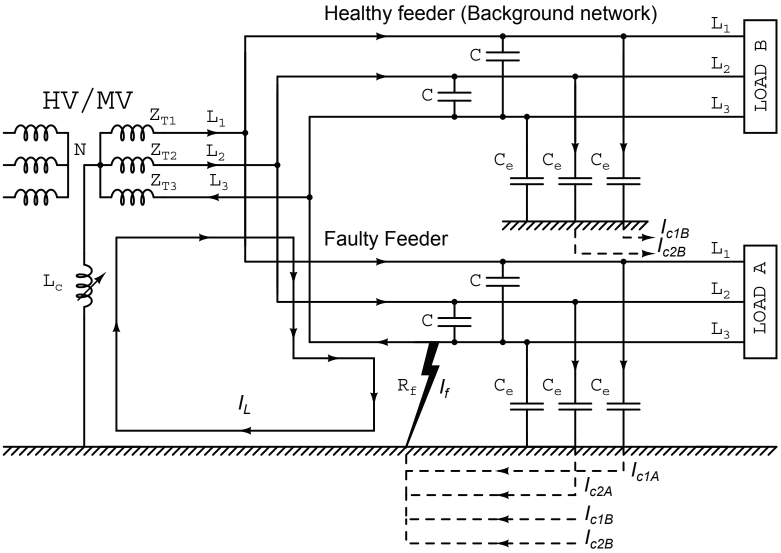

Figure 2.6. Charge of healthy lines in a suppression coil network.

The current i in Equation (2.8), can be expressed as [7]:

$$i = \frac{\hat{v}}{Z}[sin(\omega_f t + \phi_v - \phi) - e^{(-\frac{t}{\tau})} sin(\phi_v - \phi)] \tag{2.9}$$

where:

$$Z = \sqrt{(R_p)^2 + (\omega_f L_p)^2}$$
$$\phi = arctan\frac{\omega_f L_p}{R_p}$$
$$\tau = \frac{L_p}{R_p}$$

In Equation (2.9), the transient signal includes fundamental frequency component and exponential decaying DC component. The DC component will be zero if the fault happens at the moment of zero of the permanent current and in the maximum level at the moment of the permanent current maximum. Using Thevenin's theorem, the transient of suppression coil is investigated using simplified equivalent circuit as shown in Figure 2.7 [7].

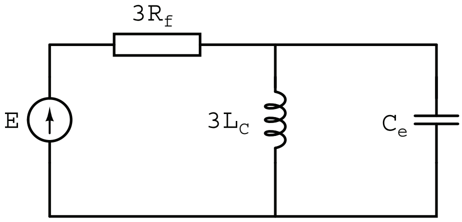

Figure 2.7. Equivalent circuit model of transient of the suppression coil [7].

The characteristic equation of the circuit in Figure 2.7 is given in complex frequency domain as follow [7]:

$$S^2 + S\delta + \omega_0^2 \tag{2.10}$$

The roots of the characteristic Equation (2.10) is given as:

$$S_{1,2} = -\delta \pm \sqrt{\delta^2 - \omega_0^2} \tag{2.11}$$

where:

$$\delta = \frac{1}{6R_f C_e}$$
$$\omega_0 = \sqrt{3L_c C_e}$$

where L_c is the inductance of the suppression coil, C_e is the total earth capacitance per phase of the system and R_f is the fault resistance.

3. Fault Location Methods Based on Earth Fault Transient Signals

Transient signals have been used and utilized for many purposed in power systems. Protection system for example is one of the areas in power systems where researchers and engineers have studied the characteristics of the transient signal for the purpose of fault location and detection. The main idea is to improve the efficiency and reliability that can bring a higher performance of the system itself. Actually, using earth fault transients for the purpose of fault location is not a new idea. However, the idea and the technique proposed by the researchers for their algorithms might be different by one and another. With new technologies which offer better, faster, cheaper and more robust services than their outdated technologies, studies on fault location becomes more challenging and interesting. In this chapter, an overview of several existing ideas related to single line to earth fault location algorithms using earth fault initial transient signals is presented.

3.1 Method based on Frequency of Charging Transient

Based on studies done by [38], when earth fault happens in a network, the fault line inductance L_f can be added to the transformer inductance (L_T) as given in Equation (2.5) for more exact solution. The frequency of the charging transient can be calculated using following equation:

$$f_c = \frac{1}{2\pi}\sqrt{\frac{1}{3(L_T + L_f)(C + C_e)}} \tag{3.1}$$

where L_T is inductance of the substation transformer, L_f is inductance of the line from transformer to the earth fault location, C is phase to phase capacitance of the the whole network and C_e is phase to earth capacitance of the whole network. The inductance of the line corresponding to the location of the fault can be calculated by rearranged Equation (3.1) as follow:

$$L_f = \frac{1}{3(2\pi f_c)^2(C + C_e)} - L_T \tag{3.2}$$

The method is simple since only one measurement is needed per substation transformer. Another advantage is that the fault distance at different feeders can be estimated only by knowing their line inductance [41].

A research done by [42], studied fault location in an unearthed neutral network with various types of RLC-circuit with and without damping as a basis of fault location algorithm. In this work, the algorithm used a measured damped transient frequency and a frequency shifting factor a for estimating undamped transient frequency. The proposed algorithm estimates the fault distance with the information of the damped and undamped transient frequency, estimated frequency shifted factor, network parameters and its configuration. The algorithm required a small number of iterations for estimating the inductance of the faulty line.

In [7], the author proposed a correlation of transient frequency to the fault distance as the basis of fault location. The method requires only one measurement per substation transformer for measuring the transient frequency. Furthermore, a data base on network components, real time data on network connections and a computer model are needed. In this work, the single line to earth fault circuit was modelled completely. The accuracy of the method was tested with simulated and real data. A similar work has been done by a previous researcher with a simple RLC-circuit. However, the simplifications and and approximations reduce the accuracy of the methods. A parametric on-line fault location method for distribution MV networks is proposed by [15]. The method uses the upper frequency of free oscillations caused by the faulted phase capacitance discharge in the transient process of earth fault as the basis of fault location. In order to produce a distance to frequency response, five single phase arcing ground faults at difference distances were initiated using horn electrodes. The method used discrete Fourier transform (DFT) to calculate the frequencies of the generated transient signals. According to [15], the fault distance to frequency response curve has to be corrected when there is a significant change of load or network structure.

3.2 Wavelet Method

In case of a single phase to earth fault, the fault path inductance of the faulty line is a composed of a series connection of zero, positive and negative sequence inductance as follows [40]:

$$L_f = \frac{1}{3}(L_{l,p} + L_{l,n} + L_{l,0}) \cdot l \tag{3.3}$$

where, l is the fault distance and $L_{l,0}$, $L_{l,p}$, $L_{l,n}$ are the inductance per unit length of zero-, positive- and negative-sequence systems.

A fault location algorithm based on wavelet transform was presented by [43] to estimate the fault path inductance of the faulty line length using transient signal. According to [43], the fault path inductance can be estimated with the following equation:

$$L_f = \frac{1}{\omega} imag \left[\frac{U_\omega(k\Delta t, f)}{I_\omega(k\Delta t, f)} \right] \tag{3.4}$$

where U_ω and I_ω are the complex wavelet coefficients of voltage and current and ω is the angular frequency. According to [44], the algorithm first determines the maximum wavelet coefficient of the current including the amplitude, frequency and location of the wavelet. Using this frequency with different time translations, the equivalent fault inductance can be calculated. The 2 ms inductance interval, corresponding to 10 subestimates, is then determined with the smallest standard deviation. The mean value of the inductance, calculated in this interval, is finally used to determine the fault distance.

Researcher in [16] deals with an earth fault in subtransmission networks. His work related to transient based ground fault location using charge transient. He proposed of to use discrete wavelet filter (DWF), the FIR filter with the Gaussian wavelet and amplitude correction in filtering specific coefficient of transient component. Instead of using DWT in many frequency scales, DWF only uses a single scale where the transient is of interest. However, the method still required a pre-processing technique to locate the specific transient frequency. This is done by using discrete Fourier Transform (DFT). The equation of DWF is given as follows:

$$DWF\left[n\right] = \frac{2}{a\sqrt{2\pi}\delta} \sum_{n} x\left[n\right] \cdot e^{-(\frac{(n-b)/a)^2}{2\delta^2}) + j\omega_0 (n-b)/a} \tag{3.5}$$

where, $x[n]$ is a discrete function of the samples, a is scaling factor, b is the translation, $\delta = \sqrt{3/2}$, $\omega_0 = 5.336\ rads^{-1}$ and n is an integer variable parameter which represents discrete time. In Equation (3.5), the scaling factor is calculated from sampling frequency (f_s) and the filtered frequency of the charge transient (f_c) as $a = f_s/f_c$ [16].

3.3 Differential Equation Method

Considering an earth fault in electrical power network, the network can be modelled with a simple first order model of a RL-circuit. The voltage and current signals of the faulty phase have the following relation [45]:

$$u(t) = Ri(t) + L\frac{di}{dt} \tag{3.6}$$

where u, i, R and L are the voltage, current, resistance and the inductance of the faulty phase, respectively. According to [45], since the differentiation is sensitive to higher frequency noise, the solution of above equation is done by using the integration technique. With samples of voltage and current signal, inductance L is calculated by using three equally spaced pairs of voltage and current using trapezoidal rule as follows:

$$L = \frac{\Delta t}{2}\frac{((i_{k+1}+i_k)(u_{k+2}+u_{k+1}) - (i_{k+2}+i_{k+1})(u_{k+1}+u_k))}{((i_{k+1}+i_k)(i_{k+2}-i_{k+1}) - (i_{k+2}+i_{k+1})(i_{k+1}-i_k))} \tag{3.7}$$

An earth fault transient signal has been applied to differential equation method by Schegner [46]. The total length of the time window was 16 to 24 samples, with sampling frequency of 10 kHz. Differential-equation algorithms work in theory for all the voltage and current components which satisfy Equation (3.6). The best result is, however, obtained if all the other frequencies are first filtered out, except the charge transient [40].

3.4 Least Square Fitting Method

According to [47], considering the first-order line modelled with capacitances neglected, the parameters of voltage and current transient waveform can be model directly using least square fitting method in time domain as follows:

$$i(t) = I_1 e^{s_1 t} + I_2 e^{s_2 t} \tag{3.8}$$

$$u(t) = U_1 e^{s_1 t} + U_2 e^{s_2 t} \tag{3.9}$$

where, $s_{1,2} = \delta \pm j\omega_c$ is the complex frequency of the charging transient. For oscillating transients, the amplitude coefficients U_1, U_2, and I_1, I_2, are also pairs of complex conjugates. The voltages and currents of a line written in complex frequency domain have the following relation:

$$U_s = RI(s) + sLI(s) \tag{3.10}$$

By separating the sub-components s_1 and s_2, we obtain the following equation:

$$U_1 = RI_1 + s_1 LI_1 \tag{3.11}$$

$$U_2 = RI_2 + s_2 LI_2 \tag{3.12}$$

Then, the fault distance is solved as reactance of the faulty line length:

$$L = \frac{U_2 I_1 - U_1 I_2}{I_1 I_2 (s_2 - s_1)} \tag{3.13}$$

For proper computation, least square fitting methods require signal filtering and pre processing. Equation (3.13) is the basic equation based on first order line model. For better result, the model can be replaced with a higher order model which includes capacitances at the close end of the line [47].

3.5 Fourier Transform Method

An algorithm based on Fourier transform method was suggested by [48]. The basic idea is to solve the line impedance in the frequency domain. In case of first order line model, the reactance of the faulty line length is obtained directly as the imaginary part of the impedance calculated from the corresponding frequency spectrum components of currents and voltages of the faulty phase [48]. The distance to earth fault location is obtained as follows:

$$\underline{Z} = \frac{\underline{U}(\omega)}{\underline{I}(\omega)} \tag{3.14}$$

$$l = \frac{3Im(\underline{Z}(\omega))}{(L_{l,0}(\omega) + 2L_{l,p}(\omega))\omega} \tag{3.15}$$

where, $\underline{Z}(\omega)$, $\underline{U}(\omega)$ and $\underline{I}(\omega)$ are the frequency (ω) component of impedance, measured voltage and current, $L_{l,0}$ and $L_{l,p}$ are the inductance per unit length of zero- and positive-sequence per length of the faulty line. As explained in [48], the fault distance is calculated as a weighted average of the estimates made for the n dominating frequencies in the spectrum. Also a higher order model, which allows for the phase to earth capacitances, is presented in [48].

3.6 Traveling Wave method

Researchers have long been studying traveling wave transients for fault location and fault detection purposes [49–53]. A fundamental concept of using traveling waves when earth fault happens in the network is described in Figure 3.1.

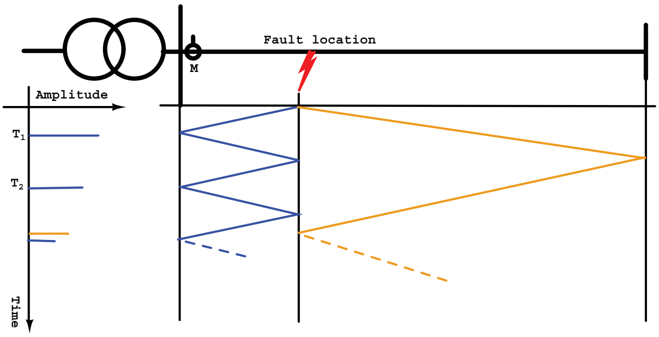

Figure 3.1. Propagation of traveling wave in power network due to earth fault.

When earth fault happens in a power network, it will create a transient signal which propagates along the line as waves [54]. The waves will travel across the line towards line ends and then a reflection will occur. The process will continue until it diminished. The fault distance can be estimated precisely by measuring the time difference between two consecutive peaks of waves and the knowledge of the wave velocity as given in following equation [55]:

$$x = \frac{\nu t_d}{2} \tag{3.16}$$

where, x is estimated fault distance, $t_d = (t_2 - t_1)$ is the time difference between two consecutive peaks and ν is wave propagation velocity. The wave propagation velocity depends on the overhead line parameters and the traveling waves' propagation path [55–58].

A research done by [57] shows that there is a correlation between the typical frequencies of generated earth fault transient and the specific path of the network covered by the traveling waves originated by the fault. Continuous wavelet transform (CWT) is used to identify the typical frequencies. Fault location methods based on traveling waves have better performance compared to the conventional and other transient fault location methods [16]. However the method usually requires a high sampling frequency in the range of MHz and the actual data need to be time-synchronized [16, 59–62].

3.7 Artificial Intelligence Method

Over the past few decades, a number of fault location algorithms based on artificial neural networks (ANN) have been developed, including event signal characteristics neural network approach [63–65], wavelet analysis and neural network approach [66–68], radial basis function neural network approach [69–71], support vector machine and neural network approach [72–74] and fuzzy and neural network approach [75–77].

A transient based ANN algorithm for locating single line to earth fault has been developed in [78]. In this work, Multilayer Perceptron (MLP) with one hidden layer was used as ANN-structure and was trained with Backpropagation method. The ANN-structure has only one hidden layer which is sufficient for representing any given input-output transformation [78, 79].

Two algorithms has been developed and presented in [14, 78]. The first algorithm uses either the phase voltage or the phase voltage and current samples as input data and the second algorithm uses harmonic components of the neutral voltage transient as input data. The transient required filtering and pre processing technique before it can be used as an input data. Both algorithms use fault distance as an output value. The first algorithm was compared with conventional algorithms which are differential and wavelet algorithm. According to the author [78], the performance of ANN was comparable to the conventional algorithms.

4. Determination of Transient Components with Signal Processing Methods

Earth fault transient signal is non-stationary signal and it consists of many frequency components. Therefore, determination of interesting part of transient signal is very important and crucial since the fault location algorithm is mainly based on the information of the specific transient component. The error of the fault location algorithm could be high if the wrong selection of transient component is used. In a real network, the transient signal is recorded using a disturbance recording system that is installed in substation. Nowadays, most of disturbance recording systems are embedded in intelligent electronic devices (IEDS) that are aligned to the protection, control, measurement and supervision of utility and industrial power distribution systems. A proper design of filters such as low pass and anti aliasing filter that are used in IEDS is important in order to maintain a correct information gathered from recorded transient signal to be used in fault location algorithm. The transient frequency of interest should fall inside the interested frequency band region. In order to determine the information of the recorded transient signal, several signal processing techniques have to be implemented. This chapter examines a number of signal processing methods used to allocate and extract the important part of the transient components.

4.1 Filtering of 50 Hz Component

Basically, the 50 Hz frequency component can be removed using comb filters [80]. According to [40], the steady state of fundamental component can be filtered using Equation (4.1) as follows:

$$g(t) = f(t) - f(t+T) \tag{4.1}$$

where $g(t)$ is the output of the filter, $f(t)$ the original signal and T is the period of fundamental frequency. In case of the fundamental frequency is 50 Hz, T is 20 ms.

4.2 Spectrum Analysis using Discrete Fourier Transform

Discrete Fourier transform (DFT) is probably one of the best known methods to transform the signal from time domain into frequency domain. It has been used for a decade to estimate the amplitude and phase of the fundamental frequency and associated harmonics of current and voltage [81]. The Fourier transform (FT) and discrete Fourier transform (DFT) is defined as [82]:

$$FT(f) = \int_{-\infty}^{\infty} x(t) \cdot e^{-j2\pi ft} dt \tag{4.2}$$

$$DFT[k] = \sum_{n=0}^{N-1} x[n] \cdot e^{-j\dfrac{2\pi kn}{N}} \tag{4.3}$$

$$x[n] = x(nT_s), n = 0, 1, 2, ..., N-1$$

where t is time, f is frequency, n and k are integer variable parameters, and $x[n]$ is a sequence obtained by sampling the continuous time signal $x(t)$ every T_s seconds for N samples.

The fast Fourier Transform (FFT) is an algorithm used for computing DFT with less computational effort and in an efficient way [83]. Both forms have performed successfully for harmonic measurement and analysis in many applications of power systems [84–93]. Even though, FFT provide an efficient way to compute the transform digitally, the result of the analysis is time averaged. The transformation contains only the averaged information and does not provide any time-domain information about the signal. It becomes inadequate when one is interested in the local frequency contents of a signal or location specific features such as charge and discharge transient component within the earth fault transient signal. In other words, it will not detect efficiently signals that have sharp changes and it has the tendency to obscure transient [81,82,94–96]. Therefore, the analyzed signal of FFT must be stationary. In order to overcome this problem a time frequency analysis is required.

4.3 Time-Frequency Analysis

A time frequency signal analysis is very important for interpretation of transient signal components in both time and frequency. There are number of time-frequency methods available for decomposition of transient signal into time-frequency plane such as short time Fourier Transform (STFT) [97–100], Wigner-Ville transform (WVT) [101–104], Choi-Williams distribution (CWD) [101, 105–107] and Wavelet transform (WT) [97, 98, 102, 108–111].

Among all of these methods, wavelet transform has emerged in recent years as one of the most favoured tool used by researchers and engineers for analyzing transient signals in the areas of protection systems, fault location, power quality, power system transients, partial discharges, condition monitoring, load forecasting and power system measurements [112–120]. Wavelet transform can be divided into two categories which are discrete wavelet transform (DWT) and continuous wavelet transform (CWT). A DWT can be calculated as follows [121]:

$$DWT(f,m,n) = \frac{1}{\sqrt{a_0^m}} \sum_k f(k) \cdot \psi^*(\frac{n - ka_0^m}{a_0^m}) \tag{4.4}$$

where ψ is the mother wavelet, the asterisk in Equation (4.4) denotes a complex conjugate, a_0^m , ka_0^m are the scaling (dilation) and translation (time shift) parameters respectively, and k and m are integer variables.

In mutiresolution analysis, DWT usually works within a frequency of band. In DWT, the analyzed signal will be decomposed into a discrete number of logarithmic frequency bands [82]. Using DWT to locate and measure the transient component frequency may be prone to errors when the transient component is located at the boundary of the frequency band [122]. Hence, the error from that measurement will affect the fault location algorithm as well. Compared to DWT, instead of using a decomposition of frequency band to locate the charge frequency components, we prefer determining specific frequencies that will be used in fault location algorithm. In next section, an identification of charge transient component using CWT will be discussed.

4.4 Identification of Charge Transient Component

In this section, the identification of charge transient component is performed using continuous wavelet transformation (CWT). The CWT possesses the capability of illustrating the frequency contents of the transient signal with respect to the time function. The main purpose that we used CWT is first to identify the dominant transient frequency that corresponds to the charge transient component generated by the earth fault. Second, after we identified the dominant frequency of the transient signal, the wavelet coefficients belonging to that dominant frequency will be extracted which later will be used as the input of the fault location algorithm.

Let us briefly explain the main features of this transform. According to [43], the CWT is the inner multiplication of a wavelet family $\Psi_{a,b}(t)$ with the signal $s(t)$ and it could be expressed as:

$$C(a,b) = \int_{-\infty}^{+\infty} s(t) \cdot \overline{\Psi}_{a,b}(t)dt \tag{4.5}$$

In Equation (4.5), $\Psi_{a,b}(t)$ are derived from a chosen function $\Psi(t)$ called "mother wavelet" given as [43]:

$$\Psi_{a,b}(t) = \frac{1}{\sqrt{|a|}}\Psi(\frac{t-b}{a})dt \tag{4.6}$$

The mother wavelet $\Psi(t)$ must be short and oscillatory, and it must have zero average and decay quickly at both ends [43]. In Equation (4.6), a and b are the parameters for positive scale and time position (time shifting factor). The $\overline{\Psi}$ in Equation (4.5) is known as the complex conjugate of Ψ and the output of CWT would be the wavelet coefficient denoted as $C(a,b)$. In literature, several mother wavelets have been used to analyze transient signals [8, 20, 22, 23, 43, 57, 123]. In [16, 43, 122, 124, 125], Morlet wavelet has been applied to earth fault transient signal for the purpose of fault detection and fault location. Therefore, on the basis of their investigation results the Morlet wavelet has been chosen in this study.

The expression of Morlet wavelet is given in Equation (4.7) as follows:

$$\Psi(t) = e^{(-t^2/2)}e^{j2\pi F_0 t} \tag{4.7}$$

In Equation (4.8), F_0 is the center frequency of mother wavelet $\Psi(t)$ and Δ is a sampling period. According to [126], the pseudo-frequency F_c associating to scale a, can be expressed as follows:

$$F_c = \frac{F_0}{a\Delta} \tag{4.8}$$

Based on the output of the CWT, in Equation (4.9) SC represents the percentage of the energy for each coefficient which is illustrated as so-called ”scalogram” and can be computed as [126]:

$$SC(a,b) = \frac{abs(C(a,b)^{*}C(a,b))}{sum(abs(C(a,b)^{*}C(a,b)))}100 \tag{4.9}$$

From the obtained scalogram, the sum of percentage energy coefficient associated to the same scale E_{SC} can be calculated as:

$$E_{SC}(a) = \sum_{n=1}^{N} SC(a,b) \tag{4.10}$$

Then, the detection of charge transient frequency is performed by inspecting the peak amplitude of the obtained E_{SC}. Figure 4.1 shows an example of CWT scalogram of measured transient signal and its peak energy percentage detection. In Figure 4.1, it shows that the dominant transient frequency is located at scale number 24. Then, with this information the specific wavelet coefficient will be extracted and the damped charge transient frequency (ω_{dm}) will be estimated with FFT algorithm. Since the identification of charge transient component using CWT requires a step-by-step process, which is heavy computational and time consuming, in practical case the application is much more suitable for offline calculation and analysis application.

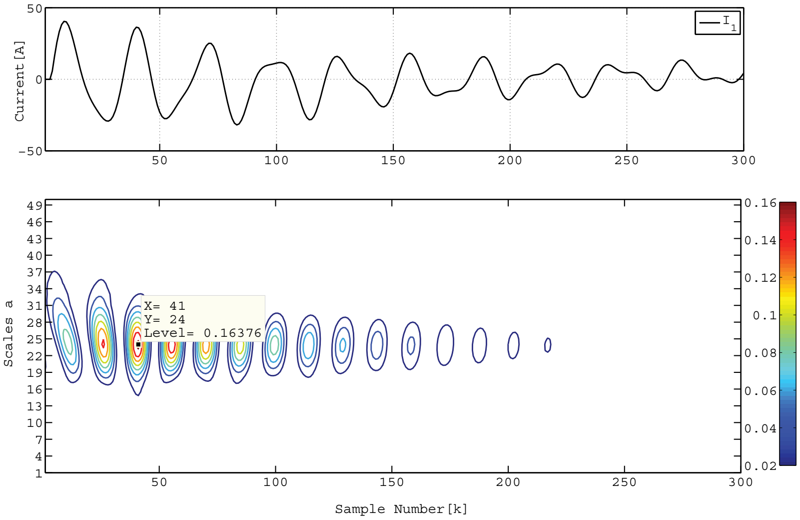

(a) Simulated transient current (above) and its CWT scalogram (below)

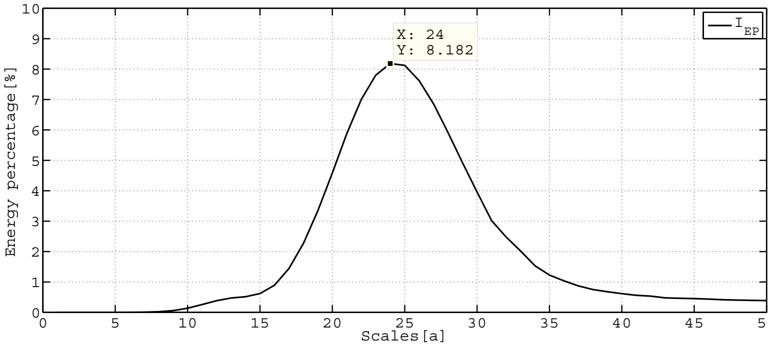

(b) Scale-dependent energy percentage distribution

Figure 4.1. Example of the ouput of pre-processing of transient signal using CWT.

4.5 Analytic Representation and Damping Estimation Using Hilbert Transform (HT)

In this section we discuss the application of Hilbert transformation to estimate the damping (α_m) of the transient signal. Assuming that the transient signal has been identified and the specific transient component has been extracted, as explained in previous section, then the extracted wavelet coefficient will be transformed into the analytic signal using the Hilbert transformation (HT). According to [127], the Hilbert Transform

$\tilde{u}(t)$ of a signal $u(t)$ can be expressed as shown in Equation (4.11):

$$\tilde{u}(t) = (\pi t)^{-1*} u(t) \tag{4.11}$$

The significance of the Hilbert transform is that it is used to form so called ”analytic signal” or ”pre-envelope” from a real data sequence. The analytic signal $U(t)$, the real signal $u(t)$ and its Hilbert Transform $\tilde{u}(t)$ defines a complex function as:

$$U(t) = u(t) + j\tilde{u}(t) \tag{4.12}$$

Since the analytic signal is complex, it can be expressed in time domain as [23, 128]:

$$U(t) = A(t)e^{j\varphi(t)} \tag{4.13}$$

where:

$$A(t) = \sqrt{u^2(t) + \tilde{u}^2(t)} \tag{4.14}$$

$$\varphi(t) = \tan^{-1}\left(\frac{\tilde{u}(t)}{u(t)}\right) \tag{4.15}$$

$$\omega(t) = \frac{d\varphi(t)}{dt} \tag{4.16}$$

where $A(t)$ is instantaneous amplitude, $\varphi(t)$ is instantaneous phase and $\omega(t)$ is instantaneous frequency. In this work, the analytic signal of extracted wavelet coefficient of voltage and current signal can be represented in Equation (4.17) and Equation (4.18) respectively as follows:

$$U_v(t) = u_v(t) + j\tilde{u}_v(t) \tag{4.17}$$

$$U_i(t) = u_i(t) + j\tilde{u}_i(t) \tag{4.18}$$

where, $u_v(t)$ and $u_i(t)$ are the extracted wavelet coefficients of voltage and current signal respectively, while $\tilde{u}_v$ and $\tilde{u}_i$ are their Hilbert transformations.

The main steps needed to obtain an estimation of the attenuation (α_m) through Hilbert transformation can be summarized as follows [129],

(i) Assume that we have obtained the interesting part of the transient signal which is extracted CWT coefficient of charge transient component as shown in Figure 4.2(c)

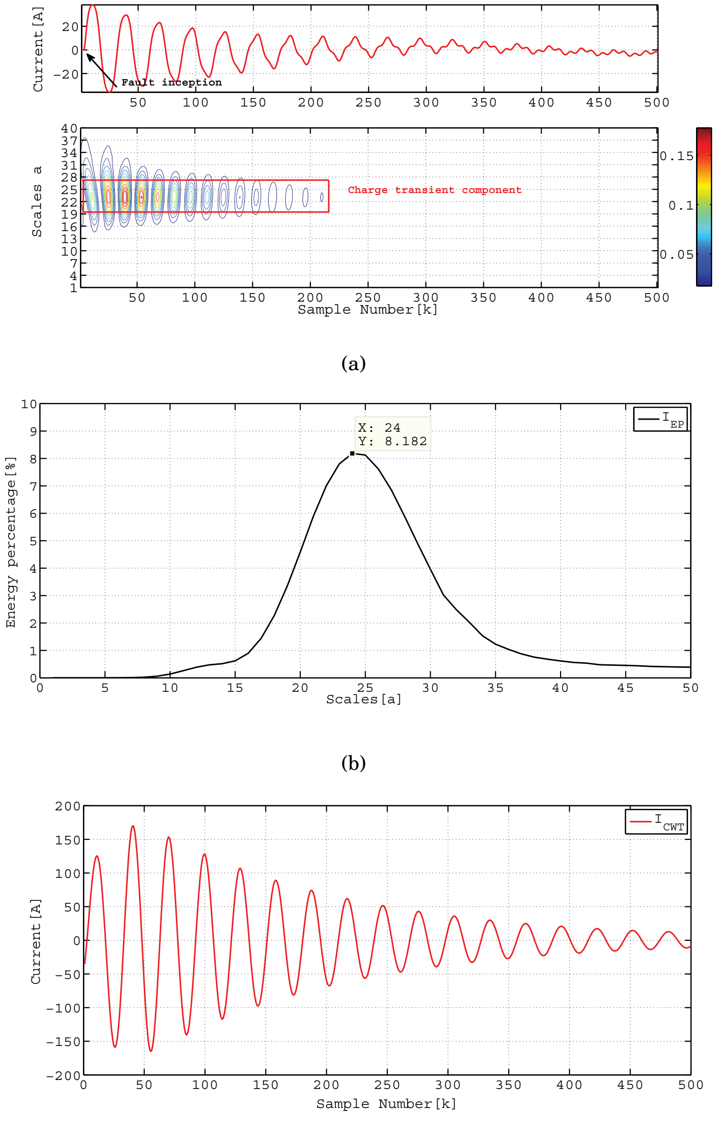

(a)

(b)

(c)

Figure 4.2. Example of the output from pre-processing of current transient signals using CWT. (a) Simulated transient current (above) and its CWT scalogram (below), (b) scale-dependent energy percentage distribution and (c) extracted CWT coefficient

(ii) Then, the Hilbert transformation is used to obtain the envelope of the interesting part as a function of time as shown in Figure 4.3(a)

(iii) The damping attenuation (α_m) is estimated from the plot of instantaneous amplitude of the signal ($Ax(t)$) versus time as given in Figure 4.3 (a). In Figure 4.3 (b), the attenuation (α_m) is the approximated slope of the logarithm of the amplitude peaks ($InAx(t)$). A straight line can be fitted through a plot of the log of the peaks. Basically, the damping can be estimated slightly after the time of the earth fault inception. For example, in Figure 4.3 (b), the damping factor is estimated from the time of 0.03 seconds to 0.06 seconds. If the damping is linear, a first order least square polynomial curve fitting method will be sufficient to fit the curve. Otherwise, the damping can be estimated by calculating the slope of the amplitudes of two successive peaks and then averaging it.

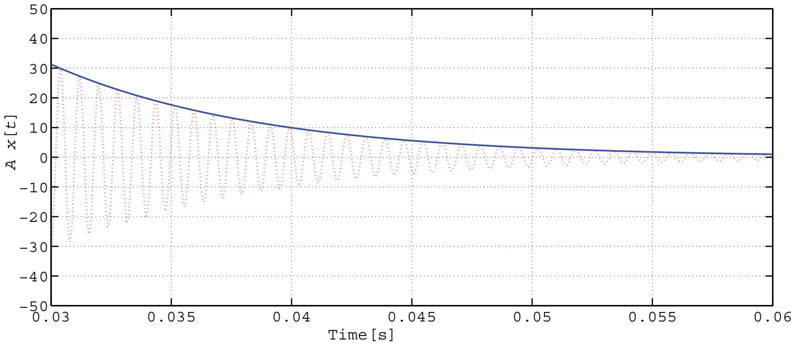

(a) Instantaneous current amplitude signal decaying characteristic (red) and its envelope (blue)

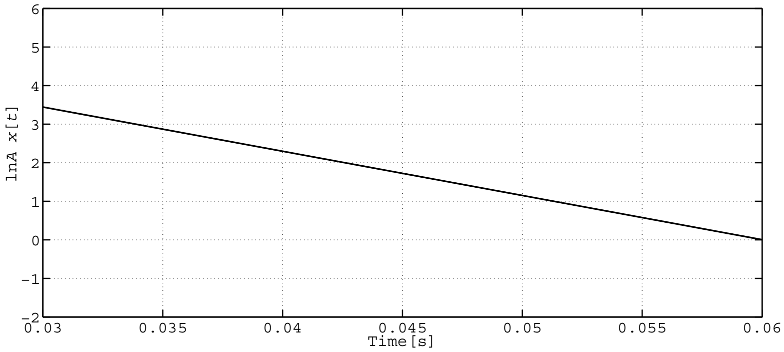

(b) Linear decaying

Figure 4.3. Example of instantaneous current amplitude, envelope and the linear decaying of the extracted CWT coefficient of charge component.

The undamped charge transient frequency (f_{nm}) can be estimated using the following equation:

$$\omega_{nm} = \sqrt{\alpha_m^2 + \omega_{dm}^2} \tag{4.19}$$

$$f_{nm} = \frac{\omega_{nm}}{2\pi} \tag{4.20}$$

where ω_{dm} , f_{nm} and α_m are estimated damped charge transient frequency (rad/s) , estimated undamped charged transient frequency (Hz) and attenuation of the extracted wavelet coefficients, respectively.

5. Fault Distance Estimation Using Transient Signals

In this chapter, we discuss and propose fault distance algorithms based on measured transient signals. In first and second section of this chapter, algorithms based on the correlation of fault distance and the charge transient frequency are first presented using general network model (GM) and then an exact model (EM) of symmetrical components. Both algorithms require only a single measurement of the transient signal to estimate the transient frequency. This can be obtained, for example from the main substation of the network. The third algorithm is based on continuous wavelet transform (CWT) of both voltage and current, and it is essentially an impedance measurement algorithm. The function of using CWT to extract the charge transient signal has been explained in Chapter 4. The proposed CWT algorithm has some similarity to an algorithm developed in [43]. Their similarity and differences will be discussed in Section 5.3. In this work, we also developed two earth fault location algorithms based on the amplitudes and frequencies of the transient signals recorded from the secondary side of the distribution transformers. The idea of using transient signals measured from secondary side of MV/LV for the purpose of fault location and fault detection is still new for most of the researchers, in the area of power systems. We have developed two algorithms that use multiple regression analysis (MRA) and artificial neural network (ANN) to estimate the correlation of fault distance and the measured quantities using this kind of transient signal. In addition, with the recorded transient signal from MV/LV side of secondary transformer, we propose an algorithm that can be used to identify the correct path of fault location towards the position of the fault in the network with tree structure. The performance of proposed fault location algorithms in this chapter will be discussed in the next chapter.

5.1 General Model (GM) of Symmetrical Components

The main principle of the general model (GM) algorithm is based on estimating the fault distance using its correlation with the single frequency of the charging process during the earth fault. As explained in Chapter 2, the charging transient is usually of higher amplitude and lower frequency than discharge transient. In the algorithm, in order to estimate the earth fault distance, we use the estimated earth fault charge transient frequency and compare it with the calculated earth fault charge transient frequency. The earth fault charge transient frequency is estimated using CWT and FFT analysis as explained in previous chapter, while the calculated charge transient frequency is formulated using developed simplified lumped parameter model.

The idea of using simplified model for locating an earth fault in power system have been proposed by several researcher [40,42,129,130]. According to [40], in case of single phase to earth fault, an interconnection of its phase sequence networks can be simplified into a composite forms of sequence networks as shown in Figure 5.1 and its description is given in Table 5.1. In case of a compensated neutral network, the compensation coil can usually be omitted since at the transient frequencies its impedance is high compared to that of the network earth capacitances.

The general models developed by [40] as given in Figure 5.1 were used to formulate the equation of charge and discharge transient frequency. In order to examine the best choice of model to be used for estimating the earth fault distance, four general models have been examined. The models are called as general model 1 (GM1), general model 2 (GM2), general model 3 (GM3) and general model 4 (GM4). The details of the models is explained in the following section. The advantages of the algorithm is that only one measurement is needed per primary substation transformer. The developed algorithm is used in simple iteration to compare the estimated and calculated earth fault charge transient frequencies. Figure 5.2 shows the basic idea of estimating earth fault distance based on general model of symmetrical component algorithm, the details flowchart of the algorithms is given in Figure 5.7 at the end of this section. The next is subsection concerned with a formulated equation that was developed from the general model of symmetrical components of earth fault transient.

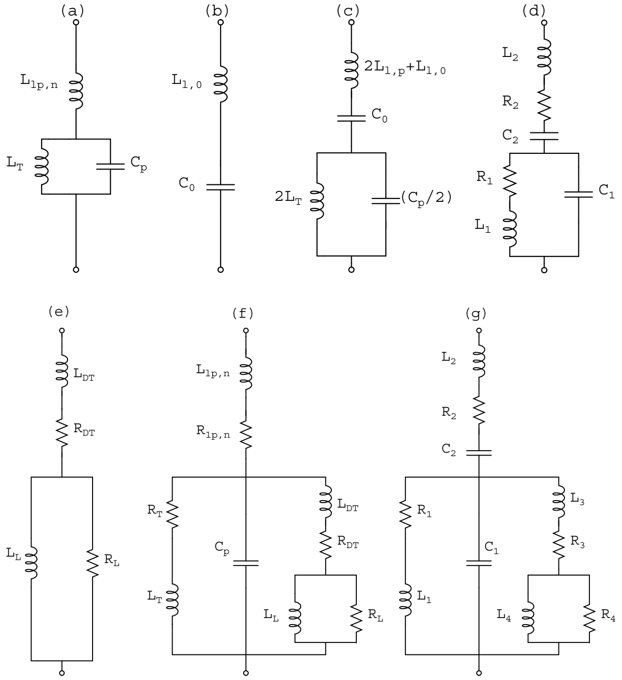

Figure 5.1. The general model for ground fault transients. Positive and negative sequence networks (a), zero sequence network for isolated networks (b), the composite connection for isolated networks without (c) and with damping included (d), model for load impedances (e), the equivalent circuit with loads included for positive and negative sequence (f) and the combinations of all sequence networks (g) [40].

Table 5.1. Description of the composite components.

Composite components	Remarks
C_1	$0.5C_p$
C_2	C_o
L_1	$2L_T$
L_2	$2L_{l,p} + L_{l,0}$
L_3	$2L_{DT}$
L_4	$2L_L$
R_1	$2R_T$
R_2	$2R_{l,p} + R_{l,0} + 3R_f$
R_3	$2R_{DT}$
R_4	$2R_L$

Notes:

R_T and L_T = resistance and inductance of substation transformer, $R_{l,p}$, $R_{l,0}$ and $L_{l,p}$, $L_{l,0}$ = sequence resistances and inductances of faulty line length, R_{DT} and L_{DT} = resistance and inductance of distribution transformer, C_p and C_0= sequences capacitances of the network, R_L and L_L= resistance and inductance of composite loads and R_f = fault resistance.

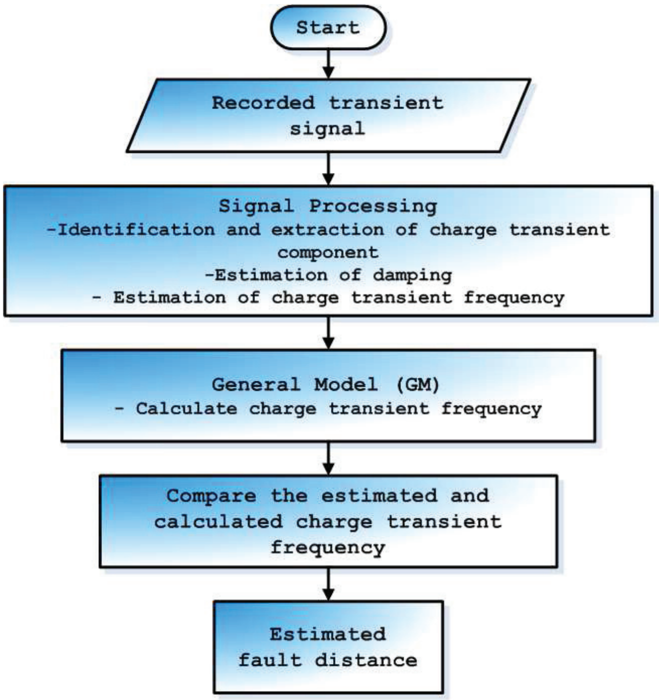

Figure 5.2. The basic idea of fault location algorithm using general model of symmetrical components.

5.1.1 General Model 1 (GM1)

Let us consider an equivalent circuit model for ground fault transients as shown in Figure 5.3. The equivalent circuit is a composite form of sequence networks. In the equivalent circuit, we neglected the influence of sound lines, distribution transformers, low voltage loads and network, compensation capacitors and the transmission network. From the circuit, the characteristic equation of the circuit can be obtained by solving the equations for voltages around the loops of the circuit. The derivation of the characteristic equation for circuit in Figure 5.3 is given in Appendix A Section A.1. A simplified characteristic equation of circuit in Figure 5.3 is given as follows:

$$\begin{aligned} S^4 L_1 L_2 C_1 C_2 + S^3 (L_1 R_2 C_1 C_2 + L_2 R_1 C_1 C_2) + \\ S^2 (L_1 C_1 + L_2 C_2 + L_1 C_2 + R_1 R_2 C_1 C_2) + \\ S(R_1 C_1 + R_2 C_2 + R_1 C_2) + 1 = 0 \end{aligned} \tag{5.1}$$

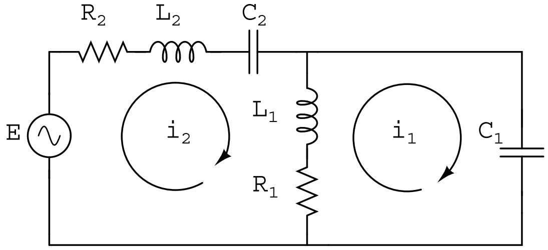

Figure 5.3. The equivalent circuit for earth fault transient of general model 1 (GM1) algorithm. [40].

In Equation (5.1), the estimated fault distance (l_f) is included in parameter L_2, where $L_2 = l_f(L_{l,p}+L_{l,n}+L_{l,0})$. By substituting all the required parameters as given in Table 5.1 into Equation (5.1) and then solving the roots of the equation, we obtain two pairs of complex frequencies with negative real parts as follows:

$$S_{1,2} = -\alpha_c \pm j\omega_c \tag{5.2}$$

$$S_{3,4} = -\alpha_d \pm j\omega_d \tag{5.3}$$

where, ω_d, ω_c, α_d and α_c are damped natural frequency of the discharge transient, damped natural frequency of charge transient, damping attenuation corresponding to discharge transient and damping attenuation corresponding to charge transient respectively.

In the presence of damping the charge and discharge transient signals will oscillate with damped natural frequencies. Due to the damping, the damped natural frequency is lower than undamped natural frequency. In case of decaying oscillation at frequency ω_d and ω_c , the undamped natural frequency is related to the damped natural frequency as follows [131]:

$$\omega_{nd} = \sqrt{\omega_d^2 + (\alpha_d)^2} \tag{5.4}$$

$$\omega_{nc} = \sqrt{\omega_c^2 + (\alpha_c)^2} \tag{5.5}$$

By substituting the above Equations into Equation (5.2) and Equation (5.3), $S_{1,2}$ and $S_{3,4}$ now can be written as:

$$S_{1,2} = -\alpha_c \pm j\sqrt{\omega_{nc}^2 - (\alpha_c)^2} \tag{5.6}$$

$$S_{3,4} = -\alpha_d \pm j\sqrt{\omega_{nd}^2 - (\alpha_d)^2} \tag{5.7}$$

where ω_{nc} and ω_{nd} are undamped natural frequency of charge and discharge transient. For damping factor $\zeta < 1$, Equation (5.6) and Equation (5.7), can now be written as:

$$S_{1,2} = -\zeta_c \omega_{nc} \pm j\sqrt{\omega_{nc}^2 - (\alpha_c)^2} \tag{5.8}$$

$$S_{3,4} = -\zeta_d \omega_{nd} \pm j\sqrt{\omega_{nd}^2 - (\alpha_d)^2} \tag{5.9}$$

where $\alpha_c = \zeta_c \omega_{nc}$ and $\alpha_d = \zeta_d \omega_{nd}$. And, the damping factors for charge and discharge transient are given as:

$$\zeta_d = \sqrt{\frac{1}{1 + \left(\frac{\omega_d}{\alpha_d}\right)}} \tag{5.10}$$

$$\zeta_c = \sqrt{\frac{1}{1 + \left(\frac{\omega_c}{\alpha_c}\right)}} \tag{5.11}$$

Subsequently, the undamped natural frequency is related to the damping factor as follows:

$$\omega_{nd} = \frac{-\alpha_d}{\zeta_d} \tag{5.12}$$

$$\omega_{nc} = \frac{-\alpha_c}{\zeta_c} \tag{5.13}$$

Equation (5.12) and Equation (5.13) can further be expressed as:

$$f_{nd} = \frac{\omega_{nd}}{2\pi} \tag{5.14}$$

$$f_{nc} = \frac{\omega_{nc}}{2\pi} \tag{5.15}$$

5.1.2 General Model 2 (GM2)

Let us consider the LC circuit as shown in Figure 5.4. The equivalent circuit is similar as in Figure 5.3 but without the effect of damping. From the circuit, the characteristic equation can be obtained by solving the equations for voltages around the loops of the circuit. The derivation of the characteristic equation is given in Appendix A Section A.2. The characteristic equation of circuit in Figure 5.4 is given as follows:

$$S^4 L_1 C_1 L_2 C_2 + S^2(L_1 C_1 + L_2 C_2 + L_1 C_2) + 1 = 0 \tag{5.16}$$

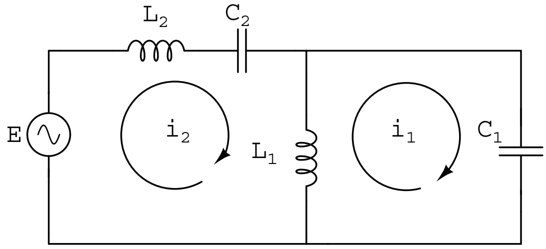

Figure 5.4. The equivalent circuit for earth fault transient of general model 2 (GM2) algorithm. [40].

By substituting all the required parameters as given in Table 5.1 into Equation (5.16) and then solving the roots of the equation, we obtain the roots as two pairs of complex frequencies as follows:

$$S_{1,2} = \pm j\omega_{nc} \tag{5.17}$$

$$S_{3,4} = \pm j\omega_{nd} \tag{5.18}$$

where ω_{nc} and ω_{nd} are undamped natural frequency of charge and discharge transient. Equation (5.17) and Equation (5.18) can further be expressed as in Equation (5.15) and Equation (5.14), respectively.

5.1.3 General Model 3 (GM3)

In this section, we consider the equivalent circuit with the effect of load impedances on the earth fault transients as shown in Figure 5.5. The composite load impedance is the combination of impedances of the low voltage network and impedances of the loads. The combination is connected as a series connection. In a low voltage network, the most significant component is the reactance of the distribution transformer [40]. However, in this model we consider the resistances of the distribution transformer as well. We may also consider the impedances of the low voltage lines which can be connected in series to the impedance of the distribution transformer. In transient analysis, a single load, with reasonable accuracy, can be modeled as resistance and inductance [40]. The load is modeled as a connection of these components. In isolated and compensated neutral networks, there is no path for zero sequence current through the transformer, therefore the load impedance only affects the positive and negative sequence networks. In Figure 5.1 (g), the impedance of the composite load is coupled in parallel to the network positive sequence capacitances.

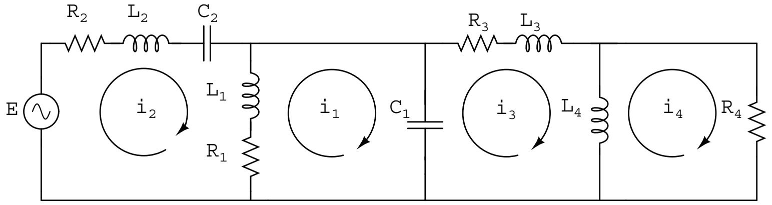

Figure 5.5. The equivalent circuit for earth fault transient of general model 3 (GM3) algorithm.

From the circuit, the characteristic equation can be obtained by solving the equations for voltages around the loops of the circuit. The derivation of the characteristic equation for circuit in Figure 5.5 is given in Appendix A, Section A.3. A simplified characteristic equation of circuit in Figure 5.5 is given as follows:

$$
\begin{aligned}
S^6(L_3L_1L_2C_2L_4C_1)+ \\
S^5(C_1L_4L_3L_1R_2C_2 + C_1L_3R_4L_1L_2C_2 + C_1L_4L_3R_1L_2C_2 \\
+R_4L_4L_1C_1L_2C_2 + C_1L_4R_3L_1L_2C_2)+ \\
S^4(C_1L_4R_3R_1L_2C_2 + L_4L_1L_2C_2 + C_1L_4R_3L_1R_2C_2 \\
+C_1L_4L_3R_1R_2C_2 + R_4L_4R_1C_1L_2C_2 + R_4L_4L_1C_1R_2C_2 \\
+C_1L_3R_4L_1R_2C_2 + L_4L_3L_2C_2 + C_1R_3R_4L_1L_2C_2 \\
+C_1L_3R_4R_1L_2C_2 + L_3L_4L_1C_2 + L_1L_3C_1L_4)+ \\
S^3(R_4L_4R_1C_1R_2C_2 + C_1L_3R_4R_1R_2C_2 + C_1R_3R_4R_1L_2C_2 \\
+C_1L_4R_3R_1R_2C_2 + C_1R_3R_4L_1R_2C_2 + L_4R_3L_2C_2 \\
+L_4R_4L_2C_2 + L_4L_1R_2C_2 + L_4L_3R_2C_2 + R_4L_1L_2C_2 \\
+L_3R_4L_2C_2 + L_4R_1L_2C_2 + L_1L_3C_1R_4 + L_1L_4C_1R_4 \\
+L_1R_3C_1L_4 + L_3R_4L_1C_2 + L_4R_4L_1C_2 + R_3L_4L_1C_2 \\
+R_1L_3C_1L_4 + L_3L_4R_1C_2)+ \\
S^2(L_4R_4R_2C_2 + L_4R_3R_2C_2 + L_4R_1R_2C_2 \\
+R_4L_1R_2C_2 + R_3R_4L_2C_2 + L_3R_4R_2C_2 \\
+L_1L_4 + R_4R_1L_2C_2 + C_1R_3R_4R_1R_2C_2+ \\
L_3R_4R_1C_2 + R_3L_4R_1C_2 + R_3R_4L_1C_2 + L_1R_3C_1R_4 \\
+L_4R_4R_1C_2 + R_1L_3C_1R_4 + R_1L_4C_1R_4 + L_3L_4 \\
+R_1R_3C_1L_4) + S(R_3R_4R_2C_2 + R_4R_1R_2C_2 \\
+L_4R_4 + L_3R_4 + R_3L_4 + L_1R_4 + R_3R_4R_1C_2 + R_1R_3C_1R_4 \\
+L_4R_1) + R_1R_4 + R_3R_4 = 0
\end{aligned}
\tag{5.19}
$$

By substituting all the required parameters as given in Table 5.1 into Equation (5.19) and simplifying the equation, the roots of the equation have the following expression:

$$S_{1,2} = -\alpha_c \pm j\omega_c \tag{5.20}$$

$$S_{3,4} = -\alpha_d \pm j\omega_d \tag{5.21}$$

$$\lambda_1 = -a_1 \tag{5.22}$$

$$\lambda_2 = -a_2 \tag{5.23}$$

where, ω_d, ω_c, α_d, α_c, a_1 and a_2 are damped natural frequency of the discharge transient, damped natural frequency of charge transient, damping attenuation corresponding to discharge transient, damping attenuation corresponding to charge transient and two local coefficients, respectively. The undamped natural frequencies and damping factors of charge and discharge transient can be added into Equation (5.20) and Equation (5.21) as we explained in Section 5.1.1.

5.1.4 General Model 4 (GM4)

An equivalent circuit for undamped earth fault transient as shown in Figure 5.6 is similar as in Figure 5.4 except with additional reactance L_5 connected in parallel to C_1. L_5 represents the imaginary part of total network load impedances. In real network, the loads are scattered all over the network. Hence, their reactance can be modeled as lumped and connected parallel to the positive sequence network.

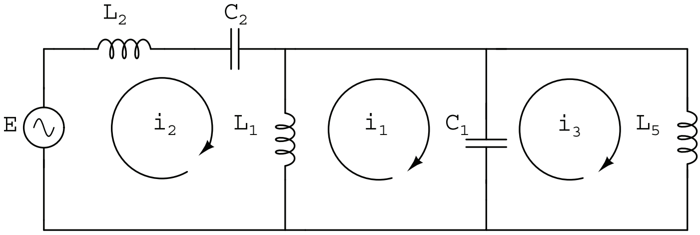

Figure 5.6. The equivalent circuit for earth fault transient of general model 4 (GM4) algorithm.

From the circuit, the characteristic equation can be obtained by solving the equations for voltages around the loops of the circuit. The derivation of the characteristic equation for circuit in Figure 5.6 is given in Appendix A Section A.3. A simplified characteristic equation is given as follows:

$$S^4C_1C_2L_1L_2L_5 + S^2(C_1L_1L_5 + C_2L_1L_2 + C_2L_1L_5 + C_2L_2L_5) + L_1 + L_5 = 0 \quad (5.24)$$

By substituting all the required parameters as given in Table 5.1 and including L_5 into Equation (5.24) and simplifying the equation, the roots of the equation have the expression similar as in Equation (5.17) and Equation (5.18).

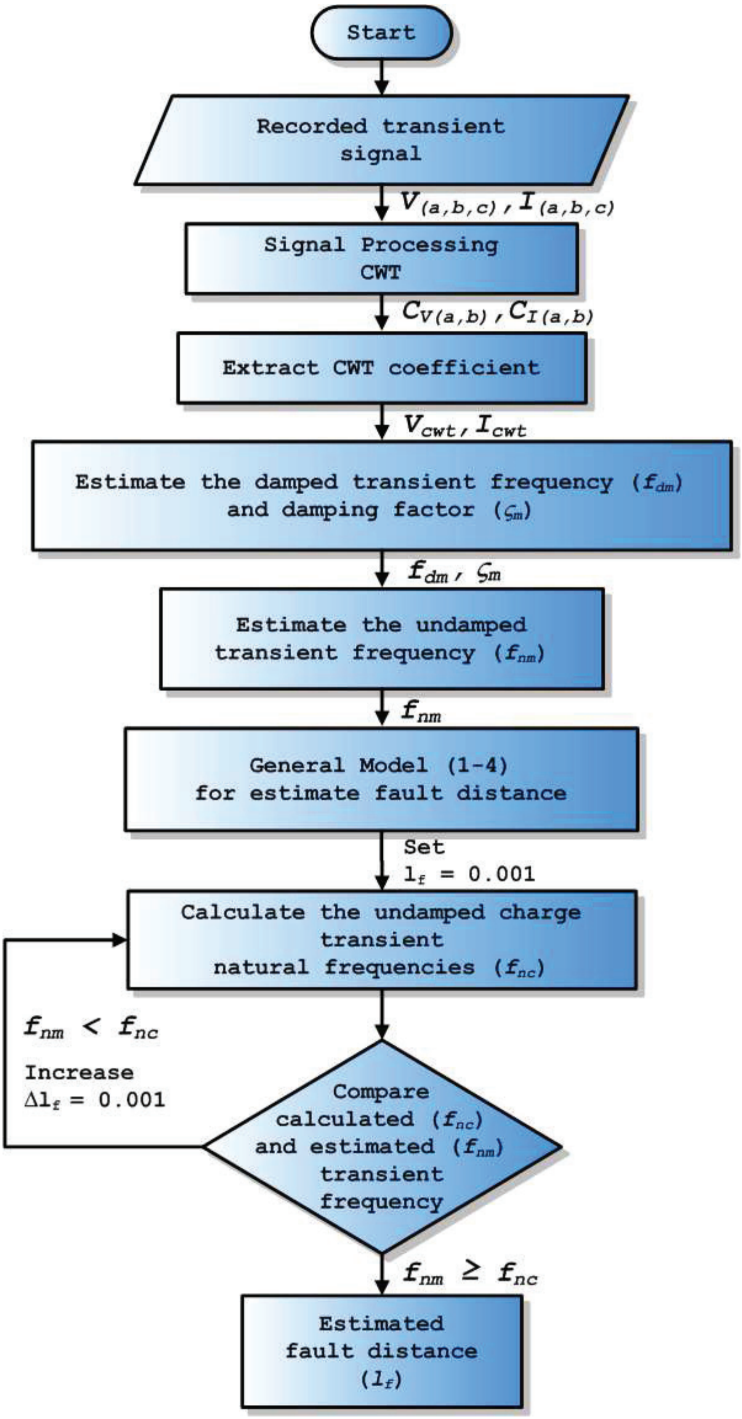

Figure 5.7. Flowchart for fault location algorithm using general model of symmetrical components.

In Figure 5.7, let us assume that an earth fault at one of the feeders has been detected. First, the transient signal is recorded and sampled. Then, signal processing is made to the recorded transient signal by using CWT analysis as described in Chapter 4. From CWT, the wavelet coefficient belonging to identified charge transient component is extracted. In the next step, the extracted CWT coefficient is used to estimate the damping factor (ζ_m) and damped transient frequency (f_{dm}). Both estimated parameters are used to estimate the undamped transient frequency (f_{nm}). Basically, the damped transient frequency (f_{dm}) can be used by general model 1 (GM1) and general model 3 (GM3) algorithm provided that the earth fault that happens has zero fault resistance. However, in a real case, there is always some damping due to the fault resistance. Therefore, in order to cancel the effect of fault resistance, we used the estimated undamped transient frequency (f_{nm}) to be compared with the calculated frequency (f_{nc}).

Assume that, general model 1 (GM1) algorithm is selected to estimate the fault distance. The algorithm use simple iterative process to estimate the fault distance. A low value of calculated fault distance (l_f) is used as an initial condition of the iteration process. From the formulated equation of general model 1 (GM1), we calculate the undamped natural frequencies (f_{nc}) and compare them with the estimated undamped charge transient frequency (f_{nm}) that was recorded in the previous step. If the estimated frequency is lower than the calculated frequency the iteration process will be repeated by calculating the next calculated frequency (f_{nc}) with the increased fault distance by increment value (Δl_f). Finally, the estimated fault distance (l_f) is successfully achieved if the estimated frequency (f_{nm}) is same or higher than the calculated frequency (f_{nc}). In order to reduce the number of iterations required to reach the final solution, the fault distance increment value (Δl_f) can be increased to accelerate the iteration process.

5.2 Exact Model (EM) of Symmetrical Components

Early investigation done by [130, 132, 133] shows that the transient frequency can be correlated to the fault distance by using the simple RLC-circuit. However due to the reduction and simplification of the circuit the accuracy of the methods is reduced. The accuracy can be improved if the network can be modeled completely. Similar to the GM algorithm, the main principle of exact model (EM) algorithm that we propose in this section is based on estimating the fault distance using the single frequency of the charging process during an earth fault. However, in exact model (EM) algorithm, we take into account the effect of inductances of sound lines. In addition, instead of lumped the line capacitances at the substation, we model them as an exact π-model solution. In this solution, the lines are modeled using exact π-model equivalent circuits as shown in Figure 5.8. In Figure 5.8, the exact π-model based on sequence component equivalent circuits represents the positive and zero sequence components of earth fault transients where the distribution transformers, low voltage loads and LV network have been neglected. In the model, we assume that the negative sequence network and positive sequence network is identical.

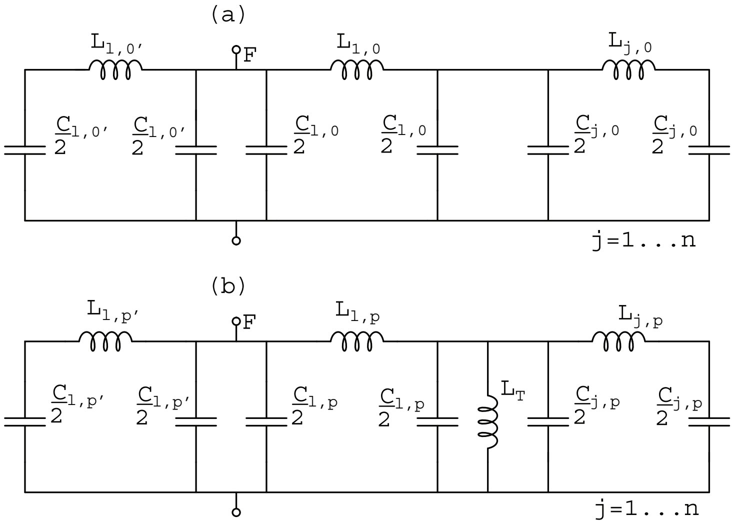

Figure 5.8. Exact π-model equivalent circuit with damping included. $L_{l,0}$, $L_{l,p}$ are zero sequence and positive sequence inductance of faulty line located in front of the fault point (F). $L_{l,0'}$, $L_{l,p'}$ are zero sequence and positive sequence inductance of faulty line located behind of the fault point (F). $L_{j,0}$, $L_{j,p}$ are zero sequence and positive sequence inductance of sound line. L_T is the inductance of the transformer. n is the number of lines. Capacitances correspondingly.

In the exact model (EM) algorithm, the undamped complex frequency is defined from the single phase to earth fault bus impedance matrix of the network in complex frequency domain. For single phase to earth fault, the diagonal elements of the nodal transform impedance matrix in complex frequency (s) is given as:

$$Z_{kk}(s) = \frac{1}{3}Z^{0}_{kk}(s) + \frac{2}{3}Z^{1}_{kk}(s) \tag{5.25}$$

where Z^{0}_{kk} and Z^{1}_{kk}, are the zero and positive sequence diagonal elements in the k node of the corresponding bus impedance matrix. In Equation (5.25), positive and negative sequence impedance is assumed identical.

$$Z^{1}_{kk}(s) = Z^{2}_{kk}(s) \tag{5.26}$$

The fault resistance (R_f) was not required to be added to the equation. This is because, in this work we purposely formed the impedance matrix for undamped case of ground fault transient. Then, in order to estimate the fault distance, we substitute the estimated undamped complex frequency (f_{nm}) of the charge transient for complex frequency (s) in Equation (5.25). Then, we solve the roots of a polynomial equation of $Z_{kk}(s) = 0$. In the computer model, the lowest positive value of the roots from the simulation results gives the estimated fault distance. The explanation of exact the π-model equivalent circuit that was used in exact model (EM) algorithm is the main subject of the next subsection. The flowchart for estimating the earth fault distance based on exact model (EM) algorithm is given at the end of this section.

5.2.1 Exact Model 1 (EM1)

An equivalent circuit of exact π-model for undamped case of earth fault transient is presented in Figure 5.9. In this model, we have neglected the effect of low voltage loads and LV network, compensation capacitors and transmission network. The effect of the neglected components on fault location performance is discussed in next chapter. As seen in Figure 5.9, we purposely modeled the equivalent circuit for undamped case of earth fault transient. This is because we want to avoid the effect of damping due to fault resistance in fault location calculation process. The idea is to calculate the undamped charge transient frequency from estimated damped transient frequency and its damping factor of the earth fault transient signal. The undamped charge transient frequency is then calculated, by using the technique explained in Section 4.4 through Section 4.5. With the information of network components and real time data of their connections, the equivalent circuit exact π-model can be used in computer simulation model using nodal analysis. As an example, Equation (5.27) shows the sequence admittance matrix in complex frequency (s) of Figure 5.9 that has k number of buses.

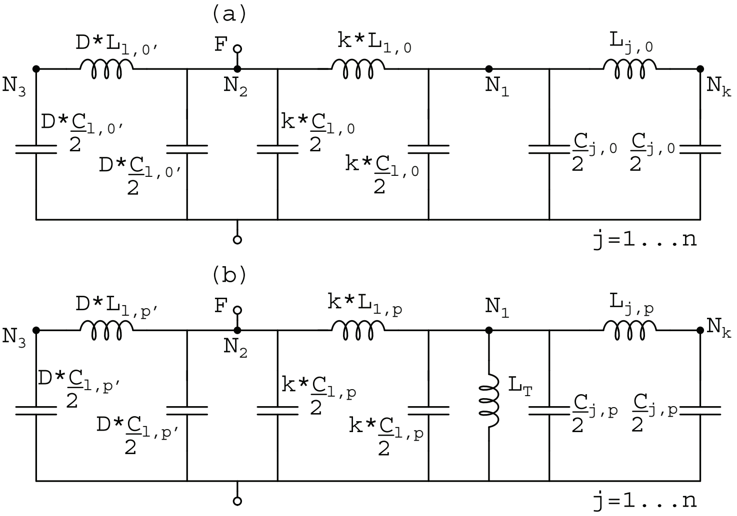

Figure 5.9. The equivalent circuit for earth fault transient of exact model 1 (EM1) algorithm. $L_{l,0}$, $L_{l,p}$ are zero sequence and positive sequence inductance of faulty line located in front of fault point (F). $L_{l,0'}$, $L_{l,p'}$ are zero sequence and positive sequence inductance of faulty line located behind of the fault point (F). $L_{j,0}$, $L_{j,p}$ are zero sequence and positive sequence inductance of sound line. L_T is the inductance of the transformer, k is a fault distance, T is the total lenght of faulty feeder, $D = T - k$ is the total length of faulty feeder (T) minus fault distance (k), N_1 to N_k is the number of the buses and n is the number of lines. Capacitances correspondingly.

$$Y_{012}(s) = \begin{bmatrix} Y_{11}(s) & Y_{12}(s) & Y_{13}(s) & \cdots & Y_{1k}(s) \\ Y_{21}(s) & Y_{22}(s) & Y_{23}(s) & \cdots & Y_{2k}(s) \\ Y_{31}(s) & Y_{32}(s) & Y_{33}(s) & \cdots & Y_{3k}(s) \\ \vdots & \vdots & \vdots & \ddots & \vdots \\ Y_{k1}(s) & Y_{k2}(s) & Y_{k3}(s) & \cdots & Y_{kk}(s) \end{bmatrix} \tag{5.27}$$

By inverting Equation (5.27), the sequence impedance matrix is expressed as follows:

$$Z_{012}(s) = [Y_{012}(s)]^{-1} \tag{5.28}$$

Finally, in computer simulation model, the nodal transform impedance matrix in complex frequency (s) is given as in Equation (5.25).

5.2.2 Exact Model 2 (EM2)

In Exact Model 2 (EM2) algorithm we model a slightly different construction of exact π-model of undamped earth fault transient equivalent circuit compared to the EM1 model. Both models have similar construction except that in EM2 model, the line positive and zero sequence inductances ($L_{l,0'}$, $L_{l,p'}$) located behind the fault point (F) of a faulty feeder section is neglected . In addition, the capacitance in the faulty line feeder are located depending on the location of the earth fault. For example, if the fault happens in the middle of the faulty feeder, capacitance at fault point (F) and bus N1 is shared for each half of the faulty line feeder capacitances. However, if the fault happens at the end of the line, the capacitance is higher at the fault point (F), and vice verse.

We purposely invent the model as it is in order to observe the effect of fault location with different exact π-model constructions. Similarly as in EM1, in order to model it in computer simulation model, the information of network components and real time data of their connections is required. From the computer simulation model, we solved the impedance matrix in complex frequency (s) as given in Equation (5.25).

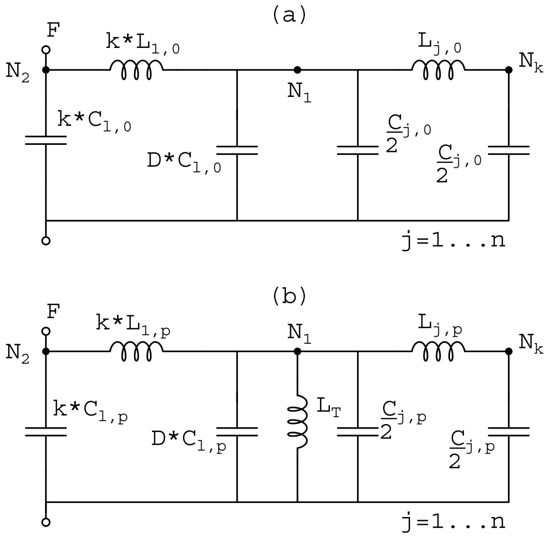

Figure 5.10. The equivalent circuit for earth fault transient of exact model 2 (EM2) algorithm. $L_{l,0}$, $L_{l,p}$ are zero sequence and positive sequence inductance of faulty line located in front of the fault point (F). $L_{j,0}$, $L_{j,p}$ are zero sequence and positive sequence inductance of sound line. L_T is the inductance of the transformer, k is a fault distance, T is the total lenght of faulty feeder, $D = T - k$ is the total length of faulty feeder (T) minus fault distance (k), N_1 to N_k is the number of the buses and n is the number of lines. Capacitances correspondingly.

5.2.3 Exact Model 3 (EM3)

We propose the exact model 3 (EM3) algorithm with the use of exact π-model as shown in Figure 5.11. The model is constructed similar to exact π-model in EM2 algorithm, except that the sequence capacitance ($C_{l,0}$,$C_{l,p}$) of its faulty feeder section is located at bus N_1 as depicted in Figure 5.11. Through the developed computer model, we simulate and solve the impedance matrix in complex frequency (s) as given in Equation (5.25).

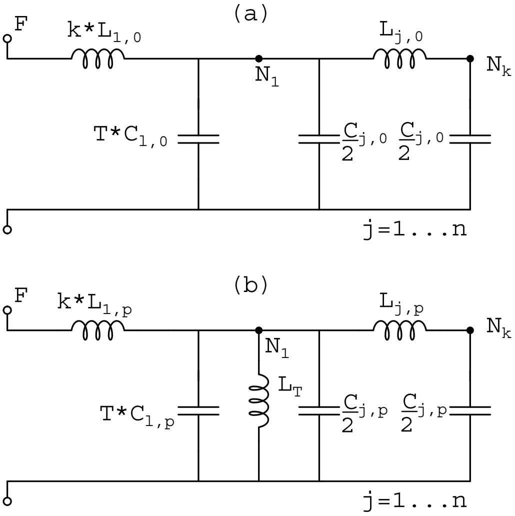

Figure 5.11. The equivalent circuit for earth fault transient of exact model 3 (EM3) algorithm. $L_{l,0}$, $L_{l,p}$ are zero sequence and positive sequence inductance of faulty line located in front of the fault point (F). $L_{j,0}$, $L_{j,p}$ are zero sequence and positive sequence inductance of sound line. L_T is the inductance of the transformer, k is a fault distance, T is the total lenght of faulty feeder, $D = T - k$ is the total length of faulty feeder (T) minus fault distance (k), N_1 to N_k is the number of the buses and n is the number of lines. Capacitances correspondingly.

In Figure 5.12, the flowchart shows the steps used by exact model algorithm for computing the undamped transient frequency (f_{nm}) is similar as explained in previous section. Let us assume that Exact model 1 (EM1) algorithm is selected to estimate the fault distance. Then, using a estimated damped transient frequency (f_{dm}), we calculate the inductance per unit length of line network using Frequency-Dependent(FD) Line Model or known as JMarti FD model in EMTP environment. In EMTP environment, we can calculate the sequence impedance of the line at specific estimated charge transient frequency using line check calculation tools provided that we have the details of line geometrical and electrical values. Next, the estimated undamped frequency (f_{nm}) and calculated line inductance is applied to computer simulation program that was built in MATLAB environment to calculate Equation (5.25) and to solve the roots of the polynomial equation. Finally, the lowest positive value of the roots gives the estimated fault distance.

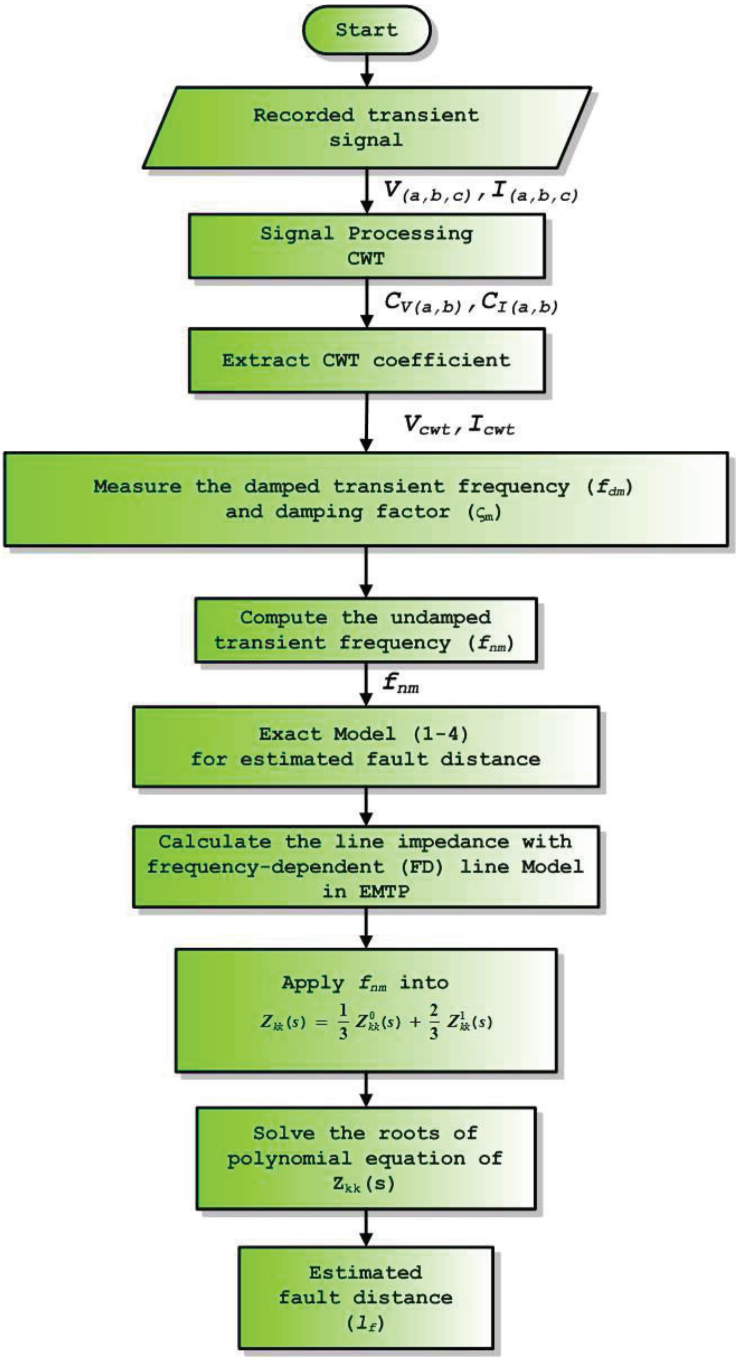

Figure 5.12. Flowchart for fault location algorithm using exact π-model of symmetrical component.

5.3 Continuous Wavelet Transform (CWT)

In this section, we propose a fault location algorithm based on continuous wavelet transform (CWT). The developed CWT algorithm is similar to the algorithm developed by [43] but slightly different process is used to estimate the fault path inductance. [43], applied discrete wavelet transform (DWT) to transient signal for fault distance estimation algorithm. The algorithm first determines the maximum wavelet coefficient of current including the amplitude, frequency and location of the wavelet. Later, the fault path inductance is calculated using the maximum wavelet coefficients of current and voltage and its frequency. Finally, the fault distance is calculated from estimated inductance using the same equation as is expressed in Equation (5.30). A similar method can also be found in [16].

Assuming that the process of identification of charge transient component and transforming it into analytical signal ($U_v(t)$, $U_i(t)$) as described in Section 4.4 and Section 4.5 is accomplished, the fault distance can be estimated by first evaluating the inductance as follows:

$$L_f(t) = \frac{1}{2\pi f_c} Im\left[\frac{U_v(t)}{U_i(t)}\right] \tag{5.29}$$

where, $L_f(t)$ is instantaneous value of inductance, f_c is a estimated charge transient frequency of the extracted wavelet coefficient, and $U_v(t)$ and $U_i(t)$ are the analytic forms of the extracted coefficient of voltage and current transient respectively. Then, the fault distance (l_f), can be calculated by using Equation (5.30) as follows [43]:

$$l_f = \frac{L_f}{\frac{1}{3}(L_0^{'} + L_1^{'} + L_2^{'})} \tag{5.30}$$

where, $L_0^{'}, L_1^{'}, L_2^{'}$ are the inductances per unit length of the zero, positive and negative-sequence systems respectively. The final value of the fault distance (l_f) was selected based on the smallest standard deviation of the mean value of the fault distance calculated in Equation (5.30) for a set of subsequent samples. The flow chart representing the CWT algorithm developed in this work is shown in Figure 5.13.

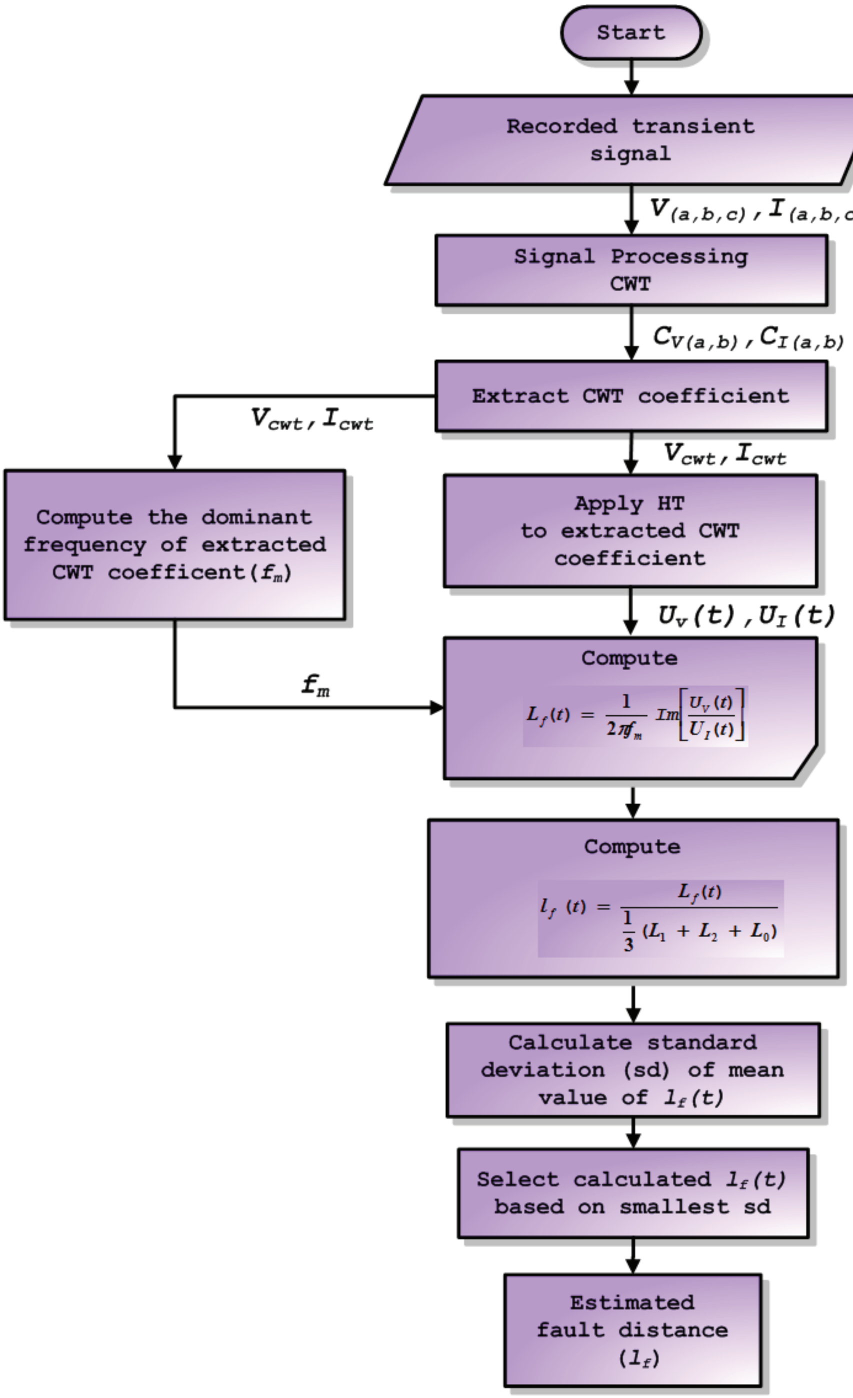

Figure 5.13. Flowchart for fault location algorithm based on CWT.

5.4 Transient Signal Recorded from the Secondary side of the MV\LV Distribution Transformer

The concept of "SmartGrids" which has the characteristics of integrated, merging monitoring, control, protection, maintenance of all the resources for more efficient network management system [134], opens a great opportunity for installation of more measuring and recording devices in the low voltage network. A study done by [135], proved that an advanced AMR meter is able to work as an intelligent monitoring device for locating low voltage network faults and for monitoring voltage level. The information gathered from advanced AMR meter is transmitted using communication infrastructure to the control center. In case that a transient or disturbance recorder is installed at the MV/LV substation, a similar concept as introduced by [135] could be applied for monitoring of transient signal. In recent studies, the transient signal of earth fault in MV network is captured using transient recorder located at low voltage side of a MV/LV distribution transformer [136, 137]. When a fault happens in medium voltage (MV) distribution feeder, the transient features can be distinguished from the secondary side of the MV/LV distribution transformer. In this section, we propose an alternative approach for earth fault location, based on the transient signal measured from the MV/LV distribution transformer. Based on the typical transformer connections and earthing practices in Finland, the MV/LV distribution transformer is modeled as delta connected HV winding, star connected LV winding with neutral brought out (DyN11) [138].

The algorithms are based on the observation, that when measuring from primary substation towards the fault, the amplitude of the charge transient voltage is increased towards the fault location. Behind the fault, the voltage is equal to the voltage in the fault point. In the parallel branches, the voltage is the same as in the point of common coupling, as seen from fault point. Hence, the fault location can be found by analyzing the amplitudes of transient voltages in different network locations.

The algorithms utilize the information gathered from the measured transient voltage signal recorded from the secondary side of the MV/LV distribution transformer and tries to find the correlation between fault distance and measured quantities using either Multiple Regression Analysis or Artificial Neural network. Using the similar technique as we describe in Chapter 4 Section 4.4, we used CWT to identify the dominant transient frequency and extract its coefficients. Besides of the characteristics of the extracted coefficients, the information of the total loads of the distribution network is also required in this algorithm. In the next subsection, we explain the pre-processing stage of the measured transient signal gathered from the MV/LV distribution transformers. The proposed algorithms are depicted in Figure 5.14.

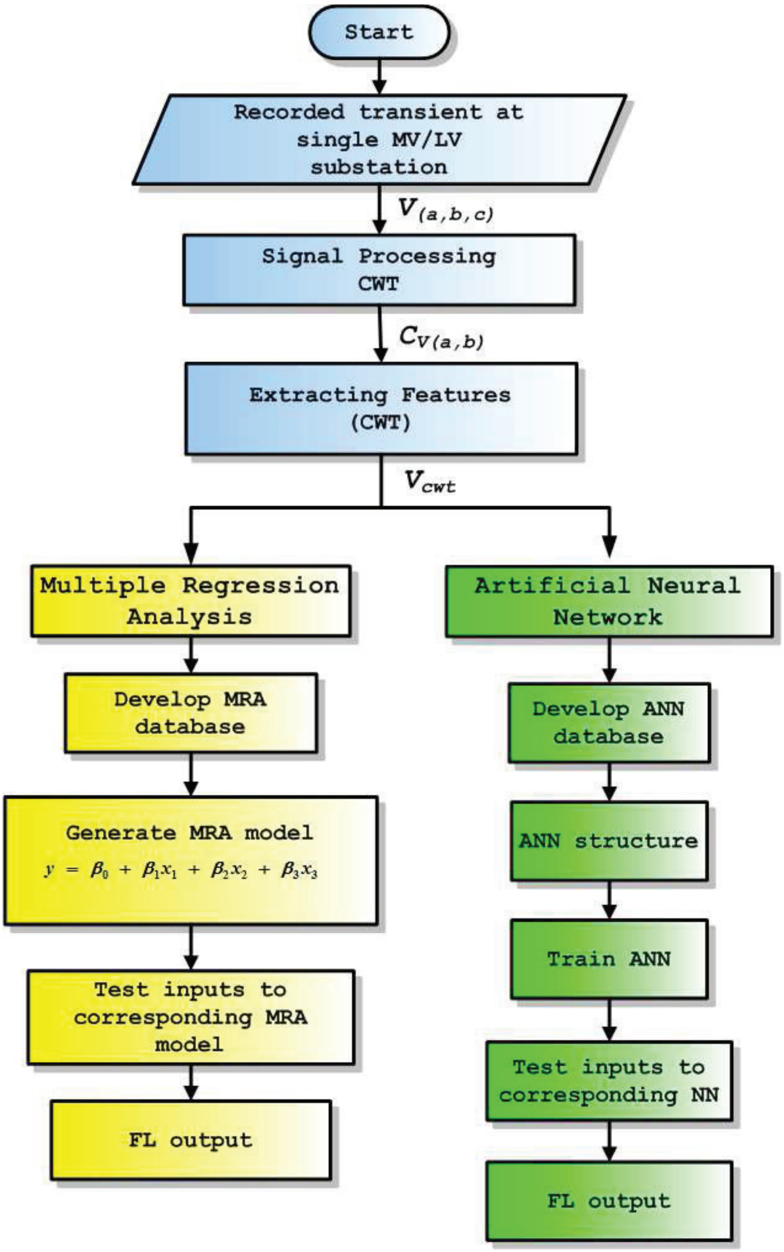

Figure 5.14. Flowchart for MRA and NN fault location algorithms based on recorded transient signal of single MV/LV distribution transformer.

5.4.1 Pre-processing stage

When an earth fault happens in MV feeder, the transient signal can also be detected from the secondary side of the MV/LV distribution transformer. The transient component can easily be distinguished from the fundamental frequency component. Figure 5.15 shows an example of simulated transient signal recorded at the MV and LV side of the network. In Figure 5.14, let us assume that an earth fault has been detected in MV network. From the assumption that an earth fault has been detected, the transient signal measured from MV/LV distribution transformers is recorded and sampled. Then, the recorded signal will be converted from phase to line voltage. Later, the signal is analyzed with CWT and the CWT extraction features process is applied to the transient signal as has been explained in Chapter 4, Section 4.4. Figure 5.16 shows an example of extracted CWT coefficient of transient signal recorded from MV/LV distribution transformer.

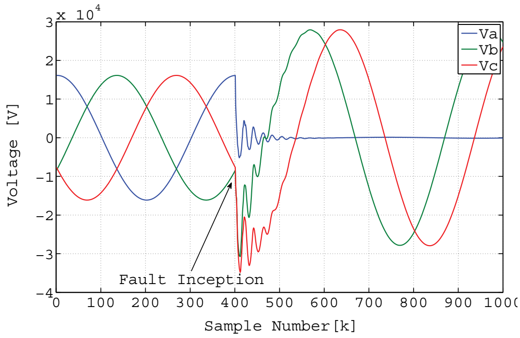

(a) Phase voltage

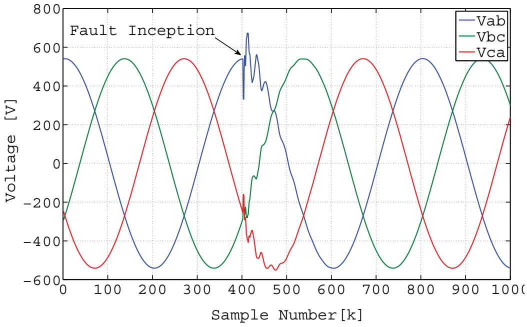

(b) Line voltage

Figure 5.15. An example of simulated transient signal recorded at (a) the MV and (b) LV side of the MV\LV distribution transformer

It has been reported that the loads have a significant effect to the transient signal [40,139]. Therefore, due to this reason, the total load (MVA) of the network prior an earth fault happens in MV network is also recorded. Based on the extracted CWT coefficient characteristics, the peak value of its FFT amplitude and its coefficient scale is recorded. Actually, the scale of CWT coefficient is correlative to its frequency. Therefore, either one of the parameters can be used. After computing and recording the two characteristics of extracted CWT coefficients, with these two parameters including the total load (MVA) of the network prior a to the earth fault they are used as the inputs database of the MRA and ANN algorithms. Multiple regression analysis (MRA), artificial neural network (ANN) and correct path algorithms are the main subject of the following subsection.

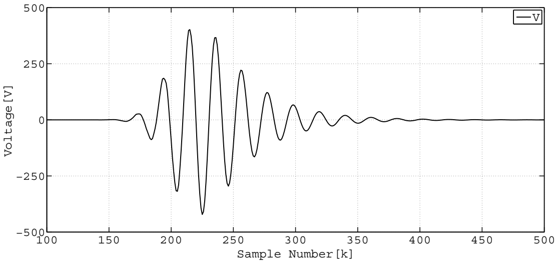

(a) Extracted CWT coefficient

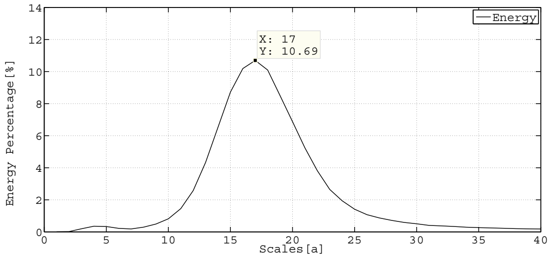

(b) Calculated Energy Percentage of CWT coefficients

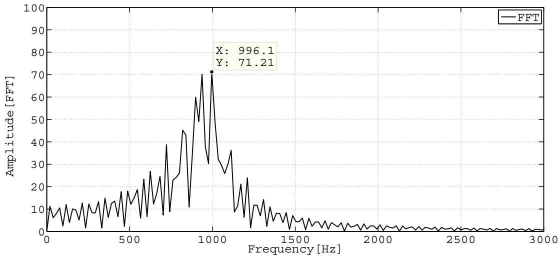

(c) FFT amplitude of Extracted CWT coefficient

Figure 5.16. Characteristics of extracted CWT coefficient of transient signal recorded from MV/LV distribution transformer.

5.4.2 Multiple Regression Analysis (MRA)

A simple linear regression illustrates the relation between the dependent variable y and the independent variable x based on the regression equation below:

$$y_i = \beta_0 + \beta_1 x_1 + e_i \tag{5.31}$$

where, $i = 1, 2, 3, ..., n$, β_0 is intercept or constant, β_1 is called slope or coefficient and e_i refers to error term. Using the least squares method, the best fitting line can be found by minimizing the sum of the squares vertical distance from each data point on the line [140]. In this work we developed the formula in Equation (5.31) using MATLAB matrix commands and the example of the MATLAB matrix commad is given in Appendix A Section A.5. As shown in Figure 5.14, the database developed for MRA algorithm is based on information gathered from measured transient signals of single MV/LV distribution substations. Since there are several MV/LV substations in the MV network, based on our studies using simulation model given in Chapter 6, Section 6.4 of this dissertation, we chose the farthest MV/LV substation in simulation network model for developing the database. The reason why we chose that particular substation is that, when the simulated single line to earth fault happens at the farthest distance from the main MV substation, the estimated FFT amplitude of extracted CWT coefficient of the chosen substation is the highest compared to other substations. Also, we found that when the fault resistance is increased and fault inception angle is decreased, the estimated FFT amplitude of extracted CWT coefficient of MV/LV substations will subsequently be decreased. However, the question that which is the most suitable MV/LV substation could be used for the purpose of designing MRA algorithm based on measured transient signal from MV/LV side of distribution transformer is not being studied in this dissertation but perhaps in future.

According to the multiple linear regression model the dependent variable is related to two or more independent variables. The general model for k variables is of the form:

$$y_i = \beta_0 + \beta_1 x_i + \beta_2 x_{i2} + ... + \beta_k x_{ik} + e_i \tag{5.32}$$

where, $i = 1, 2, 3, ..., n$ and $k = 2, 3, ..., n$, β_0 is intercept or constant, β_k is called slope or coefficient and e_i refer to error term. The multiple regression model developed for fault location in this dissertation is defined in Equation (5.33) as:

$$l = \beta_0 + \beta_1 A + \beta_2 S + \beta_3 L \tag{5.33}$$

where, l is fault distance, A is FFT amplitude of extracted CWT coefficient, S is scale of extracted CWT coefficient and L is total loads (MVA) of the network prior to a single line to earth fault.

The developed multiple regression model used for fault location is specific for the network during the observation. The model needs to be redeveloped if there is a change in network configuration. The reason is, those changes will affect the variables used in the developed multiple regression model. Therefore it is necessary to redeveloped the regression model according to the condition of the network.

Using typical 20 kV isolated neutral distribution network simulated using EMTP-ATP program, the proposed multiple regression model was tested and the result and the performance will be discussed in detail in Chapter 6, Section 6.4.

5.4.3 Artificial Neural Network (ANN)

An algorithm based on artificial neural network (ANN) has been discussed in Chapter 3. In case of fault location in MV network, several researchers mainly used the data measured from MV substation or faulty feeder in order to design a ANN algorithm. In this research we propose a new approach for fault location in unearthed or compensated neutral distribution system using combination of wavelet analysis and artificial neural network (ANN) and based on measured transient voltage signals recorded from secondary side of MV/LV distribution transformers. According to [141], using the relationship of dependent and independent number of n samples, the formula created using artificial neural network (ANN) analysis is in the following expression:

$$y = ANN(x_1, x_2, ..., x_n) \tag{5.34}$$

where ANN is an implicit non mathematical function that can only can be designated as 'knowledge base'. Basically, using the same dependent and independent variables as developed for MRA formula can also be used for artificial neural network analysis. A proposed designed neural network is constructed with a two layers, feed forward network with tangent sigmoid hidden neurons and linear output neuron. The developed neural network training function updates weight and bias values according to Levenberg-Marquardt optimization algorithm. ANN architecture of the proposed ANN algorithm is depicted in Figure 5.17.

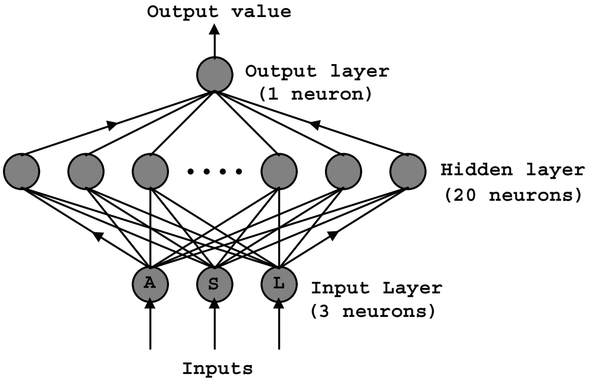

Figure 5.17. Architecture of neural network for estimate the fault distance.

The designed neural network has 3 inputs variables which contain valuable and relevant information for estimating fault distance. Each input unit of neural network has a symbol associated with it where A is represented as the peak value of FFT amplitude of extracted CWT coefficient, S is associated its coefficient scale and L is referred to total loads (MVA) of the network prior to an earth fault. For fault distance estimation algorithm in this work the ANN consists only one hidden layer. For this kind of input-output task, one single hidden layer is assumed to be good enough [79]. The outputs of hidden layer has sigmoid activation function and are transferred to the output layer which is composed of only one neuron which gives the estimated fault distance. It is important to train and test the neural network with a large data set. The training process is done in several times and each time the performance after each iteration is saved where the performance is defined as the correlation coefficient (r). Finally the saved trained network that has the highest value of correlation coefficient (r) is used to for fault location algorithm. Since this method is based on the 'knowledge base' of the specific network, therefore the NN have to retrain if there are any changes in terms of the network topology.

The proposed algorithm have has tested using simulation model based on a practical 20 kV unearthed network distribution network as shown in Chapter 6 Section 6.4. The data set used in training and testing the neural network is given in Chapter 6, Table 6.3 and Table 6.4, respectively. The result and performance of the algorithm will be discussed in that chapter.

5.4.4 Correct path location in branches of feeders

In networks with several branches, indicating the correct fault path is a separate issue. In fault location algorithm it is a difficult task if only one measurement is used to identify the correct branch of a complex tree structure kind of network. Therefore, we propose an algorithm that use the transient signal recorded from secondary side of MV/LV substations as the basis for identifying and selecting a correct path to the fault position. The work flow of the algorithm is shows in Figure 5.18.

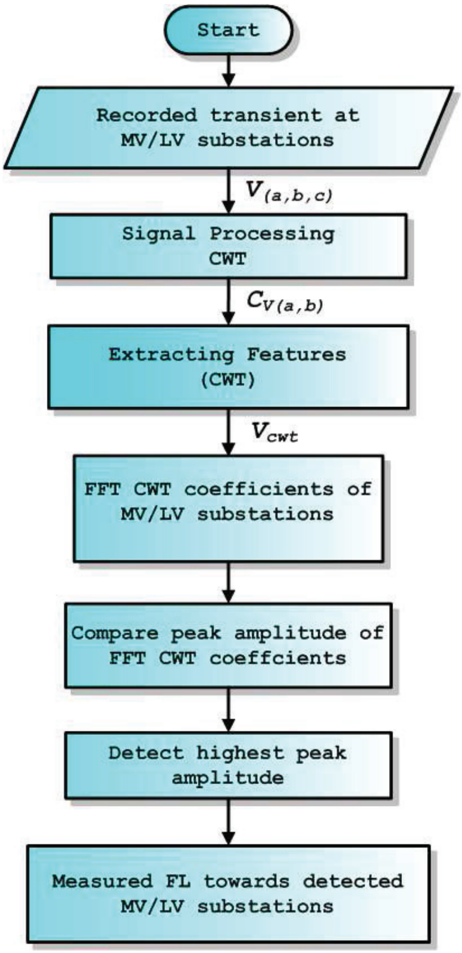

Figure 5.18. Flowchart for correct path location algorithm based on recorded transients of MV/LV distribution transformers.

The line to line fault voltage transient signal measured from the secondary side of MV/LV substation transformer is processed with CWT similarly as in Chapter 4 Section 4.4. Then the peak amplitude of the FFT frequency spectrum of the extracted CWT coefficients for each substation is identified and recorded. For correct path location, a fault distance should be taken from the measured point at main HV/MV substation towards the MV/LV substation which has highest recorded FFT amplitude of the extracted wavelet coefficient. In other words, the highest recorded FFT amplitude will indicate which MV/LV substation should we locate in order to determine the correct fault location if there are several branches. The proposed algorithm has been tested using a simulation model in Chapter 6, Section 6.3. The result and performance of the algorithm will be discussed in that chapter.

6. Performance Evaluation of Proposed Fault Location Algorithms Using EMTP/ATP Simulation Model

In this chapter, the proposed algorithms are tested using transient signal generated by a simulation model. The simulation of the voltage and current transient is required and important in order to validate the proposed fault location algorithms. In this research, we used Alternative Transient Program (ATP/EMTP) as transient simulator. The program was chosen because it is one of the most common simulation tools used by power engineers and researcher for simulating transients [142]. The program software contains extensive modeling capabilities for transmission lines, cables, breakers, loads, converters, protection devices, non-linear elements, electromagnetic coupling, and major power electronics devices and equipment. It also has an enhanced graphical user interface called ATPDraw as a pre processor, which allows an easy entry of system topology and data [143] . The program software will in future be referred to only as EMTP.

In this chapter, four simulation models are presented. The first model is according to general model of symmetrical component as we have discussed in Chapter 5, Section 5.1. In simulation model 2, we modeled the unearthed neutral network with exact π-model as described in Chapter 5, Section 5.2. Then in the following section, we investigate the earth fault network using the line constants EMTP program and taking into account their real geometrical and electrical values. In the last section of this chapter, we tested the fault location algorithms with the modified system from [144] and modeled the network using line constant EMTP program. The earth faults are simulated with different scenarios such as fault distance, fault resistance, fault inception angle and also the effect of load. Some results of this studies can be found in [137].

6.1 Simulated Network Model 1

In the beginning of this work, we studied the correlation of fault distance and the transient frequency using the general model algorithm as explained in Chapter 5 Section 5.1. The simulated network model was based on the model as shown in Figure 5.1 (d) and (g). The model neglected the inductance and resistance of sound lines, distribution transformer and approximated the network capacitances as lumped components located at the substations. According to the Thevenin theorem, the ground fault transient can be produced by injecting a voltage of equal magnitude but opposite sign compared to the phase voltage at the fault point [40]. The description of the network model is given in the following section.

6.1.1 Description of the simulation and the network model

A schematic diagram of the simulated 20 kV unearthed medium voltage network and its EMTP simulation model is shown in Figure 6.1(a) and (b) [129]. The network is radially operated. It consists of 5 feeders with a total of 100 km of overhead lines.

In EMTP simulation, a single line to ground fault was simulated in a 20 km long line and fault distances varied from 2 km to 20 km with 2 km steps. The fault resistances varied from 0 Ω to 100 Ω. The fault distance was maintained at 2 km, 4 km, 10 km and 16 km when the varied fault resistance was applied to the model. In addition, different fault voltage inception angles were applied to investigate the sensitivity of transient frequency and the performance of the fault location algorithm. Fault distance was fixed to 4 km and 16 km with zero fault resistance when fault inception angle variation was applied to the model. A sampling frequency of 20 kHz was used.

The specification of the various elements in the simulation model are as follows: L_T= 5.6 mH, R_T= 0.04 Ω, $L_{l,p}$= 1.0 mH/km, $L_{l,0}$= 5.0 mH/km, $C_{l,p}$= 38.25 nF/km, $C_{l,0}$= 6.12 nF/km, $R_{l,p}$= 0.60 Ω/km, $R_{l,0}$= 1.30 Ω/km, L_{DT}= 19.09 mH, R_{DT}= 0.18 Ω, $L_{L\text{-}5MVA}$= 584.20 mH, $L_{L\text{-}12MVA}$= 233.68 mH, $R_{L\text{-}5MVA}$= 88.89 Ω and $R_{L\text{-}12MVA}$= 35.56 Ω. The details of the various element abbreviations can be found in Table 5.1. The simulation results are discussed in the next section.

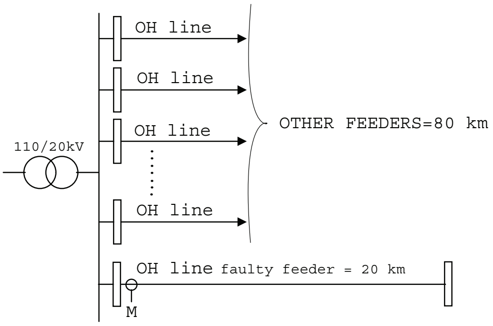

(a) 20kV 100km unearthed neutral MV network

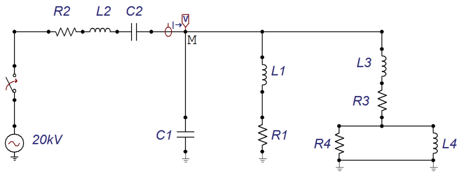

(b) ATPdraw simulation model

Figure 6.1. A Schematic(a) and ATPdraw simulated network model(b) for earth fault simulation analysis in 20 kV unearthed medium votage network. The details of the abbreviations in ATPdraw simulation model can be found in Table 5.1

6.1.2 Result Analysis and Discussion

The performance accuracy of the GM algorithm has been investigated under varied fault distances, several fault resistances, different fault inception angles and load conditions. In these studies, the performance accuracy used to evaluate GM algorithm is defined by mean absolute error ($\mathrm{MAE_{GM}}$) index as expressed in equation below:

$$MAE_{GM} = \frac{1}{n}\sum_{i=1}^{n}|GM_i - l_i| = \frac{1}{n}\sum_{i=1}^{n}|\Delta GM_i| \tag{6.1}$$

where ΔGM_i is the absolute error fault distance using GM algorithm, GM_i is estimated fault distance using GM algorithm, l_i is exact fault distance and n is numbers of observation of fault distance error. Similarly, to evaluate the error between estimated and calculated frequency and damping factor in the simulation result, the mean absolute error ($\mathrm{MAE}_{\{f,\zeta\}}$) is calculated with the following equation:

$$MAE_{\{f,\zeta\}} = \frac{1}{n}\sum_{i=1}^{n}|\Delta\{f_m - f_c, \zeta_m - \zeta_c\}| = \frac{1}{n}\sum_{i=1}^{n}|\Delta\{f_i, \zeta_i\}| \tag{6.2}$$

where $\Delta|\{f_i, \zeta_i\}|$ is the absolute error of the parameters (f, ζ), f_m is estimated transient frequency, f_c is calculated transient frequency, ζ_m is estimated damping factor and ζ_c is calculated damping factor and n is numbers of observation of parameter error.

Figures 6.2 and 6.3 shows the example of earth fault transient voltage and current for earth fault located at 2 km, 10 km and 18 km at faulty line feeder with overhead line as shown in Figure 6.1. The transient signals were captured at location "M" as shown in Figure 6.1. The earth fault was simulated at time t=0 and the signal was captured before the time switch is "on" at t=0.005 second.

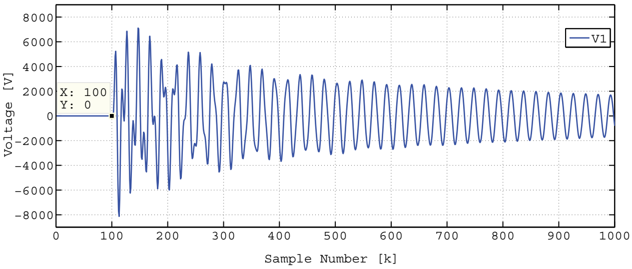

(a) Transient voltage, l_f=2 km

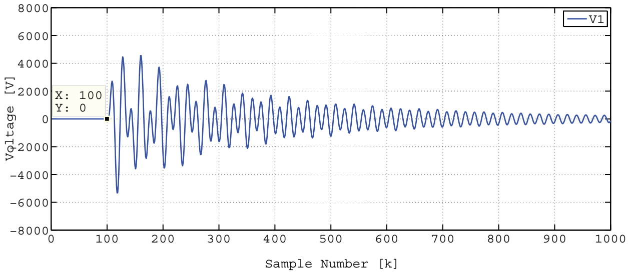

(b) Transient voltage, l_f=10 km

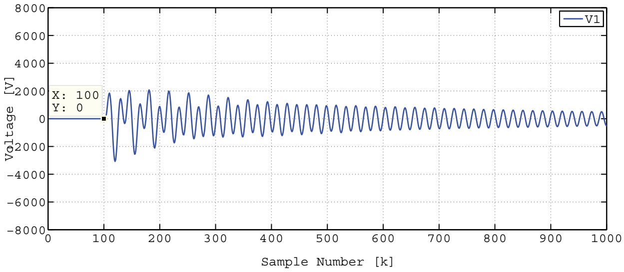

(c) Transient voltage, l_f=18 km

Figure 6.2. Simulated transient voltage signal in the faulty phase when a single phase to earth fault happens at a feeder in an example network with overhead lines. The fault distances (l_f) are 2, 10 and 18 km from the substation. The fault resistance is zero ohm.

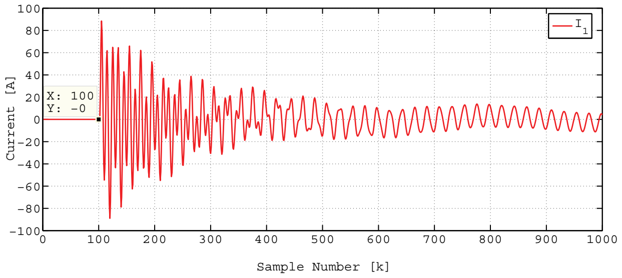

(a) Transient current, l_f=2 km

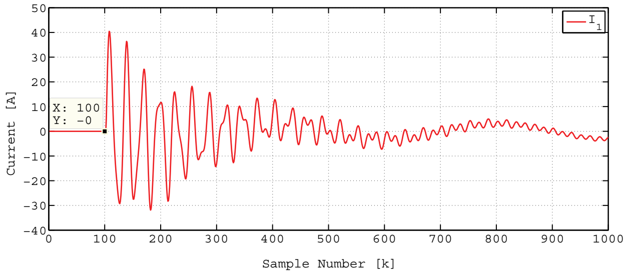

(b) Transient current, l_f=10 km

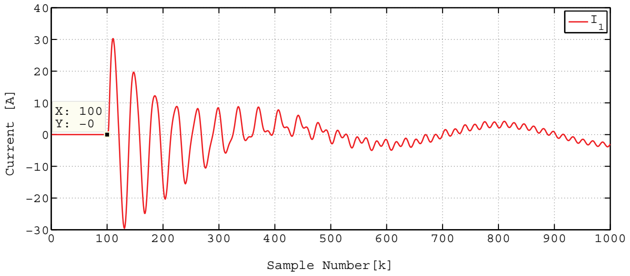

(c) Transient current, l_f=18 km

Figure 6.3. Simulated transient current signal in the faulty phase when a single phase to earth fault happens at a feeder in an example network with overhead lines. The fault distances (l_f) are 2, 10 and 18 km from the substation. The fault resistance is zero ohm.

The earth fault is simulated at the instantaneous voltage maximum and the transient signal is measured at the substation. Figures 6.2 and 6.3 shows that when lower fault distance, the peak amplitude of the transient signal (voltage and current) is higher. Correspondingly, when the fault distance is increased the peak amplitude of the transient signals is decreased.

As an example, a signal pre-processing output for a single phase to earth fault with fault distance 10 km from substation is presented. The fault is simulated with zero fault resistance and fault inception angle 90° (instantaneous voltage maximum). Figure 6.4 shows an example of the output from pre-processing by CWT, Hilbert transformation (HT) and fast Fourier transform (FFT) as described in Chapter 4.

In Figures 6.4 and 6.5, simulated voltage and current transient signals from 10 km earth fault simulated case was analyzed and sampled starting from the beginning of the fault inception. In Figure 6.4(a), a high density of energy spectrum corresponding to the charge and discharge component can be seen clearly from the instant of fault occurrence. Both charge and discharge components can be seen from CWT scalogram of voltage transient. However, in case of CWT scalogram of current transient signal as shown in Figure 6.5(a), only charge component is distinguished. Both signals have higher density of energy level (red color bar) appeared at the beginning of the fault inception which then decreased towards the end of the signal.

In Figures 6.4(b) and 6.5(b), based on the result of scale-dependent energy distribution, we recognize the peak amplitude of the energy percentage (%) that corresponds to the dominant energetic scales within the signal. Hence, the scales obtained from the highlighted peak are 23 and 24 for voltage and current signals, respectively. From the scale-energy distribution spectrum, we can conclude that, for this case of earth fault simulated transient signal, the charge transient component is more dominant than the discharge transient component in both signals. Extracted CWT coefficient of voltage and current signal is depicted in Figures 6.4(c) and 6.5(c), respectively, while its FFT frequency spectrum is presented in Figures 6.4(d) and 6.5(d). The peak amplitude in FFT frequency spectrum is corresponding to the dominant damped transient frequency of the signal. In this case the value is 703.1 Hz. Figures 6.4(e) and 6.5(e), show an envelope of extracted CWT coefficient fitted using polynomial curve fitting technique in MATLAB environment. Hence, from these points, with the estimated value of damped transient frequency and the damping factor, the undamped transient frequency can be estimated.

In order to show the effect of high fault resistance on transient signal as well as to the algorithm, the earth fault was simulated for fault resistance up to 400 Ω. Figures 6.6 and 6.7, shows the simulated current transient signal and its CWT scalogram for fault distance of 10 km from the substation. The fault resistance was varied between 25 Ω and 400 Ω. From the result, it can be seen that the transient signal becomes short and more damped when the fault resistance is increased.

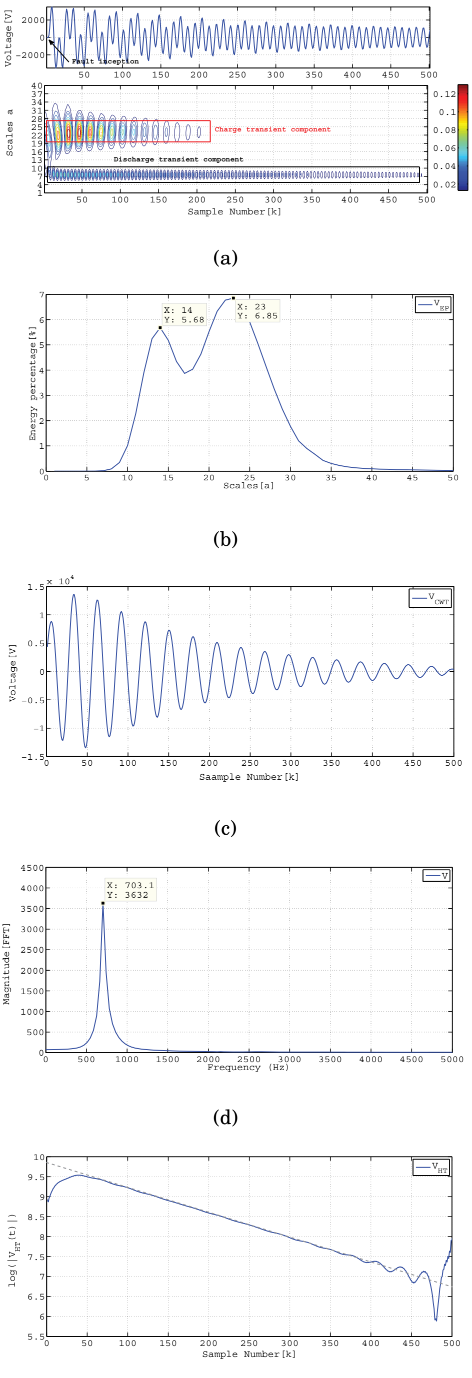

(a)

(b)

(c)

(d)

(e)

Figure 6.4. Example of the output from pre-processing of voltage transient signals using CWT and Hilbert transformation. The fault distance is 10 km from the substation. (a) Simulated transient voltage (above) and its CWT scalogram (below), (b) scale-dependent energy percentage distribution, (c) extracted CWT coefficient, (d) FFT frequency spectrum of extracted CWT coefficient, (e) linear decaying of extracted CWT coefficient.

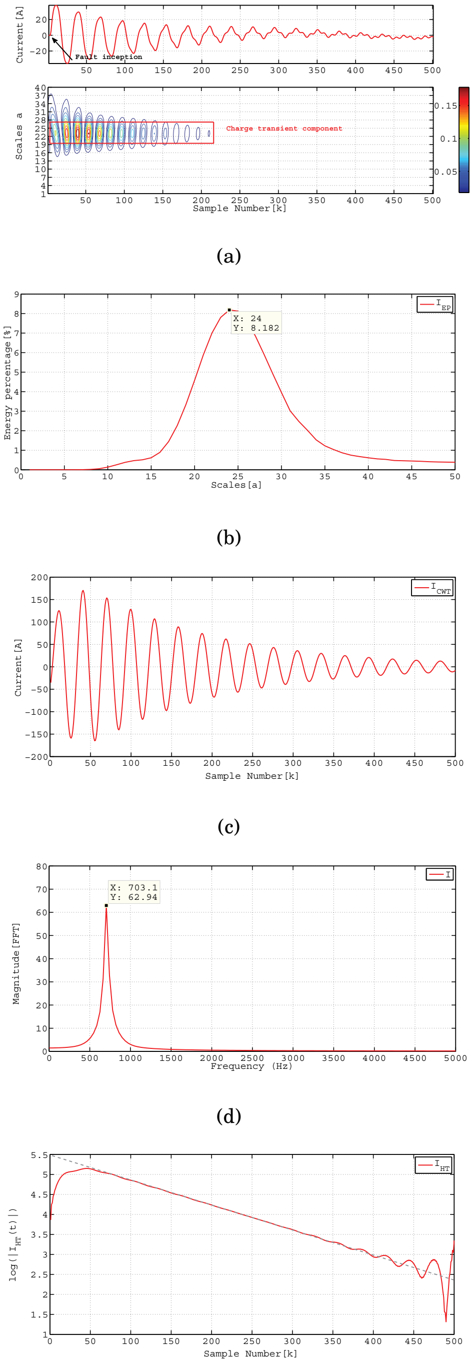

(a)

(b)

(c)

(d)

(e)

Figure 6.5. Example of the output from pre-processing of current transient signals using CWT and Hilbert transformation. The fault distance is 10 km from the substation. (a) Simulated transient current (above) and its CWT scalogram (below), (b) scale-dependent energy percentage distribution, (c) extracted CWT coefficient, (d) FFT frequency spectrum of extracted CWT coefficient, (e) linear decaying of extracted CWT coefficient.

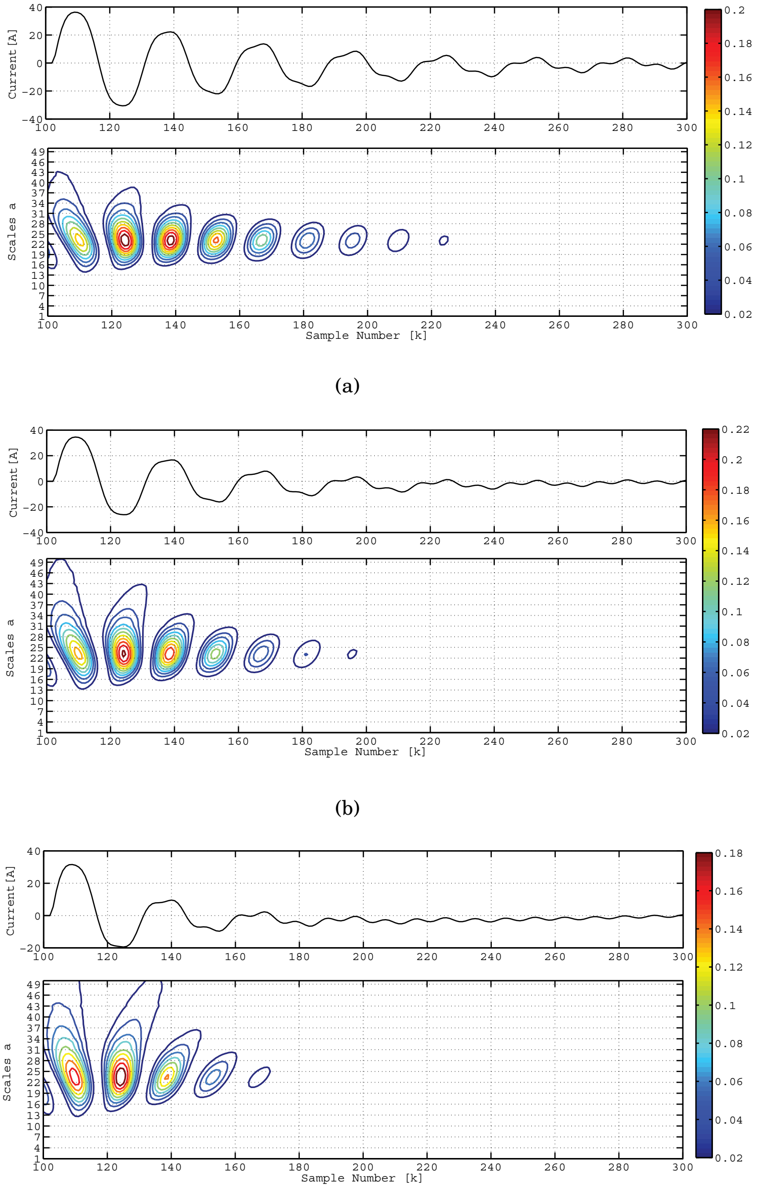

(a)

(b)

(c)

Figure 6.6. Example of the output from pre-processing of current transient signals using CWT with the effect of fault resistance. The fault distance is 10 km from the substation. (a) Simulated transient current (above) and its CWT scalogram (below) with R_f=25 Ω, (b) R_f=50 Ω and (c) R_f=100 Ω.

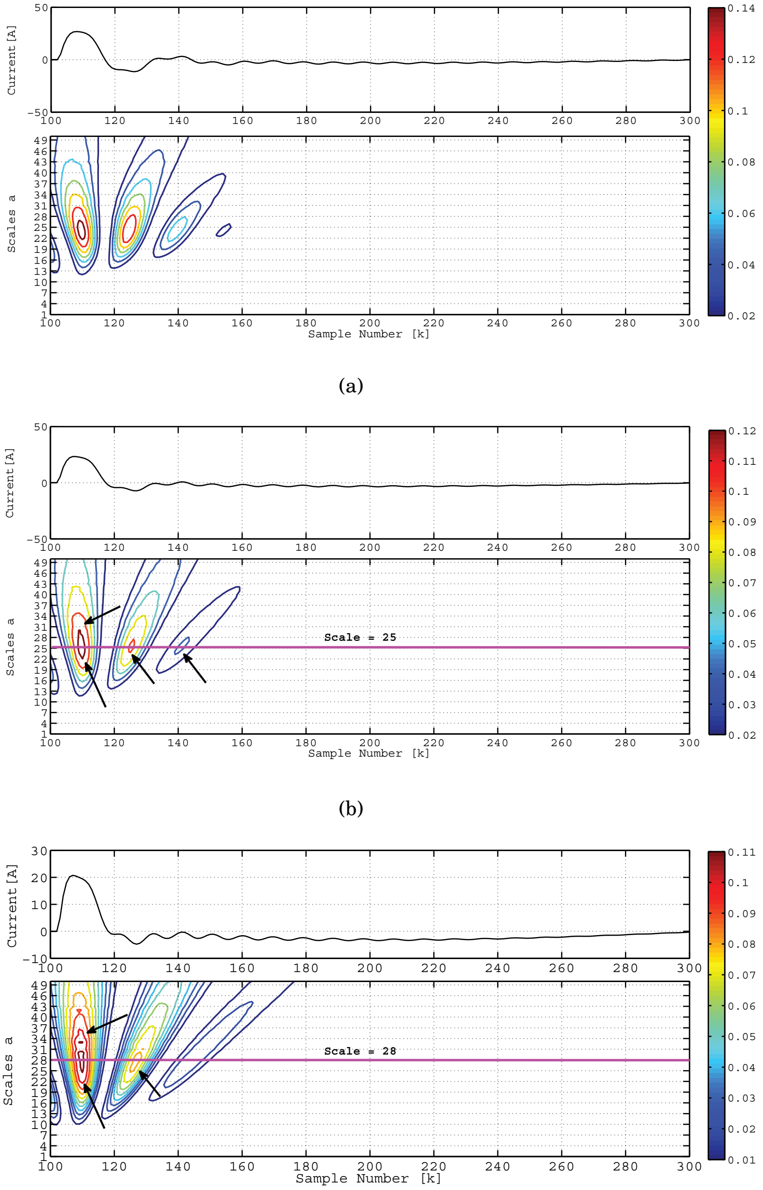

(a)

(b)

(c)

Figure 6.7. Example of the output from pre-processing of current transient signals using CWT with the effect of fault resistance. The fault distance is 10 km from the substation. (a) Simulated transient current (above) and its CWT scalogram (below) with R_f=200 Ω, (b) R_f=300 Ω and (c) R_f=400 Ω.

Figures 6.8 and 6.9 shows the scale-energy percentage distribution for the simulated transient signal. Using the method for identification of charge transient signal as explained in Chapter 4 Section 4.4, in this particular case the charge transient component can only be detected for earth fault with fault resistance up to 200 Ω. However, if we observed the result of CWT scalogram in Figure 6.7(b) and (c), we can make a guess estimation what is the scale corresponding to the charge transient frequency by inspecting the maxima of the energy. The maxima of the energy in Figure 6.7(b) is located between scale 22 and 28, while in Figure 6.7(c), it is located between scale 22 and 37. The arrows in Figure 6.7(b) and (c) show the area of the maxima of the energy. The purple line in Figure 6.7(b) and (c), shows the guess estimation of the scales that correspond to the charge transient frequency of the measured transient signal.

The calculated and estimated frequencies and damping factor of the charge transient signal as a function of fault distance are shown in Figure 6.10, and the tabulated results are found in Appendix C Table C1. Based on the result shown in Figure 6.10, the calculated and the estimated values have a good agreement. The range of estimated damped frequency is between 1132 Hz to 507 Hz. In Figure 6.10(a) and (b), the graph shows that the damped and undamped charge transient frequency is decreasing when the fault distance is increasing. The damping factor is increased when the fault distance is increasing. The mean absolute error (MAE) index of damped and undamped transient frequency is about 10 Hz, and 0.0006 for damping factor, as shown in Appendix C Table C1.

The results of fault distance estimation error using GM1 and GM2 algorithms for simulated earth fault with different fault distances is given in Figure 6.11, and the tabulated results are found in Appendix C Table C2. As shown in Figure 6.11, basically the results from tested algorithms are almost identical. In overall the distance calculation error is less than 1.5 km. The MAE index calculated for all algorithms is 0.36 km, as given in Appendix C Table C2. The fault distance error is slightly higher when the fault happens at the middle and at the end of the faulty feeder. From the results, we found that the lowest fault distance estimation error is when fault is simulated at 18 km from the substation. The reason why it has the lowest fault distance estimation error is because based on the comparison between the estimated (f_{dm}) and the calculated (f_{nm}) undamped charge transient frequency, it has the lowest error (Δf_n) as given in Appendix C Table C1.

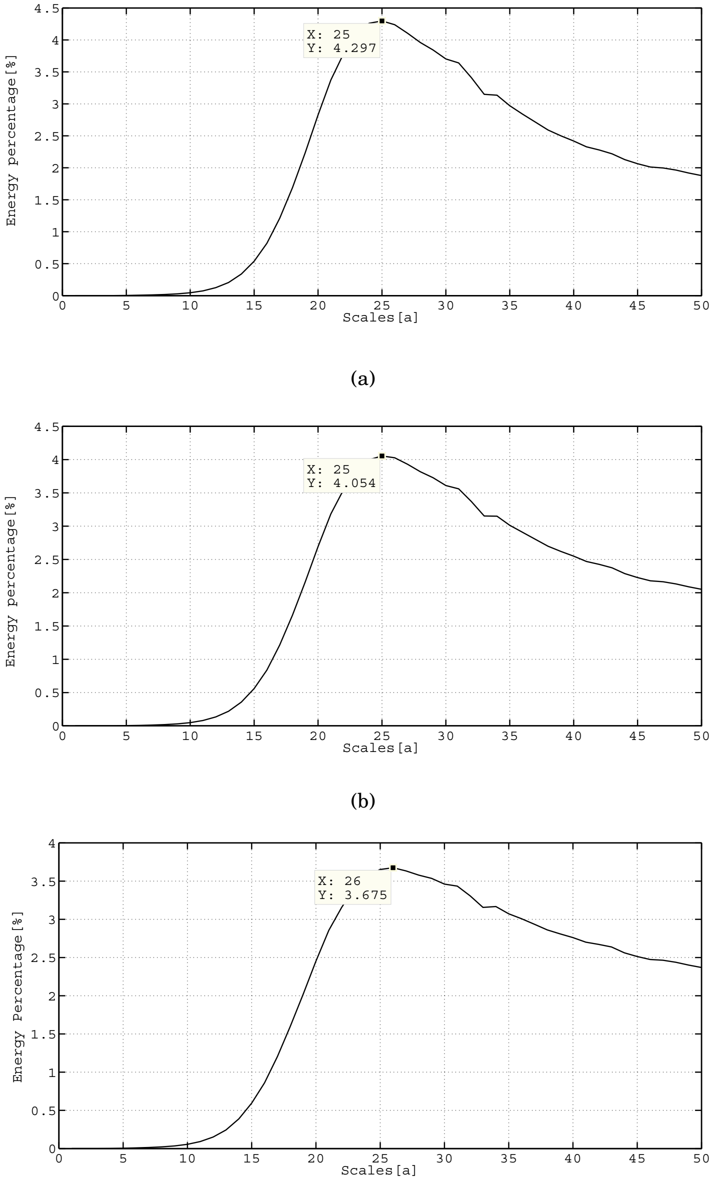

(a)

(b)

(c)

Figure 6.8. Example of scale-dependent energy percentage distribution. The fault distance is 10 km from the substation. (a) Scale-dependent energy percentage distribution with R_f=25 Ω, (b) R_f=50 Ω and (c) R_f=100 Ω.

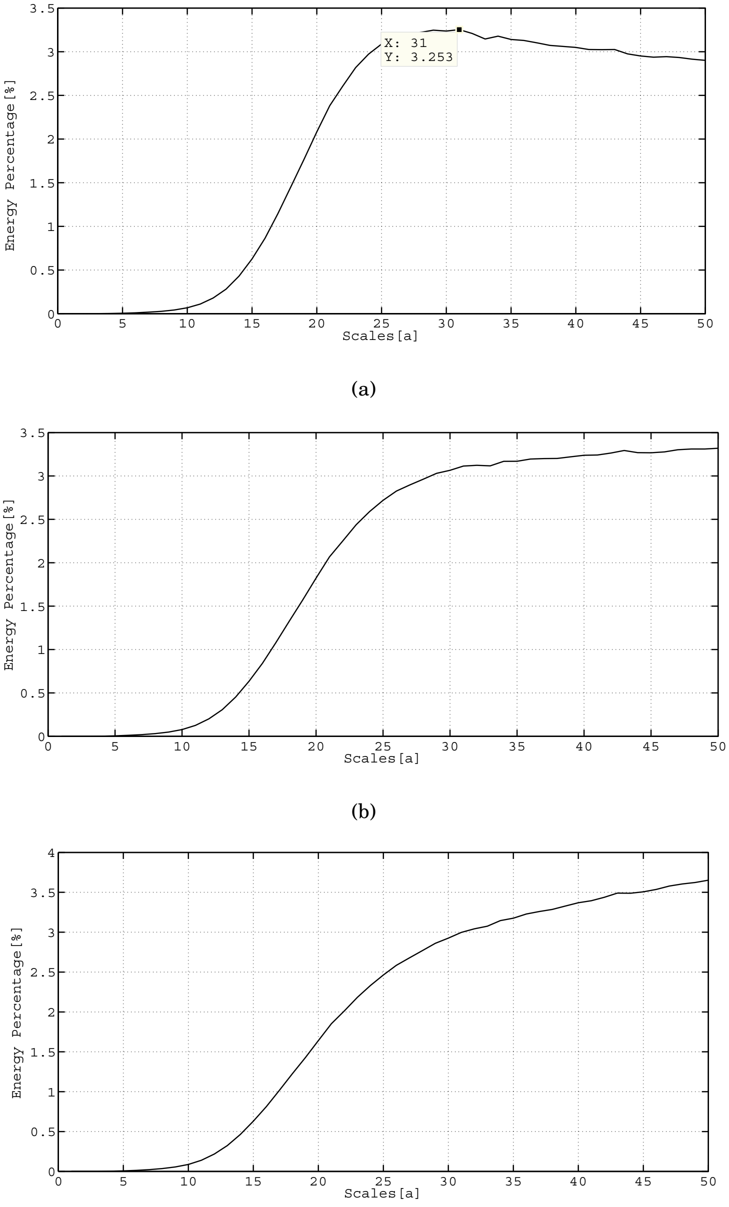

(a)

(b)

(c)

Figure 6.9. Example of scale-dependent energy percentage distribution. The fault distance is 10 km from the substation. (a) Scale-dependent energy percentage distribution with R_f=200 Ω, (b) R_f=300 Ω and (c) R_f=400 Ω.

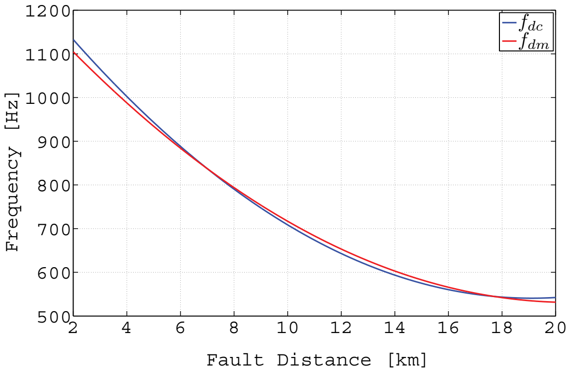

(a) Damped transient frequencies as a function of fault distance

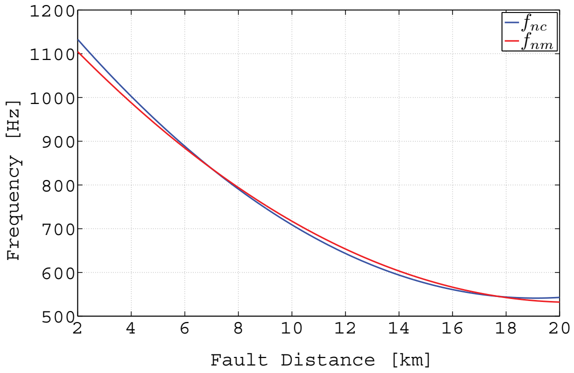

(b) Undamped transient frequencies as a function of fault distance

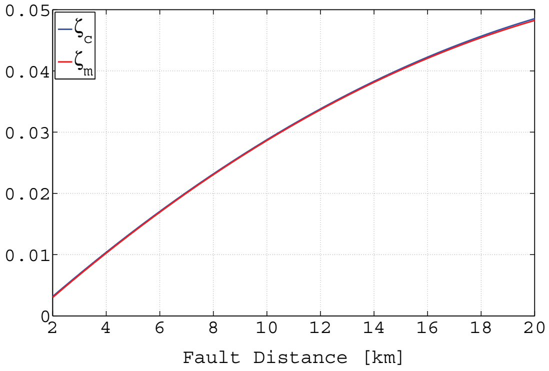

(c) Damping factor as a function of fault distance

Figure 6.10. The comparison of simulation test result to the theory of earth fault transient. f_{dc} , f_{nc} and ζ_c are calculated using the GM1 equations. f_{dm} , f_{nm} and ζ_m are estimated transient parameters from the simulated earth fault transient waveforms. f_{dm} = estimated damped transient frequency (Hz), f_{dc} = calculated damped transient frequency (Hz), ζ_m = estimated damping factor, ζ_c = calculated damping factor, f_n = undamped transient frequency (Hz), f_{nm} = estimated undamped transient frequency (Hz) and f_{nc} = calculated undamped transient frequency (Hz)

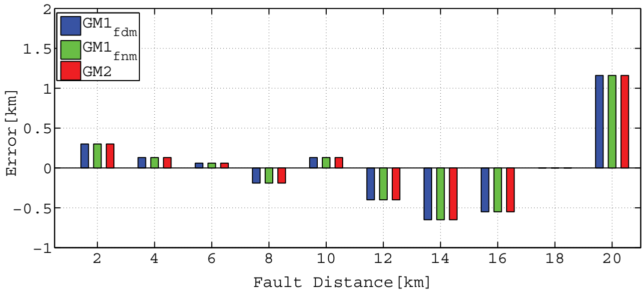

Figure 6.11. Comparison of the distance estimates obtained using general model (GM) algorithms for the simulated single line to earth faults with varies fault distance. GM1$_{fdm}$ denotes a distance calculation error using general model 1 (GM1) with damped transient frequency (f_{dm}), GM1$_{fnm}$ denotes a distance calculation error using general model 1 (GM1) with undamped transient frequency (f_{nm}) and GM2 denotes a distance calculation error using general model 2 (GM2) algorithm.

Figures 6.12, 6.13, 6.14, 6.15 and 6.16 show the results of simulated single line to earth fault transients with the effect of fault resistance, and the tabulated results are found in Appendix C Table C3. In general, referring to general model (GM) equivalent circuit, the transient frequencies become lower when the resistance (R_2) is increased. In Figure 6.12, the graphs show that the calculated and estimated frequencies have small reduction when fault resistance is increased. The reduction can be seen more clearly in estimated frequency when high fault resistance ($R_f = 100\Omega$) is used. In Figure 6.13, the estimated and calculated frequency is almost identical except when fault resistance is 100 Ω.

Based on the results in Figure 6.13 (a), (b) and (c), for fault close to the substation and for the certain range of the fault resistances, the gap between estimated and calculated frequencies can be seen more clearly. Based on the MAE index shown in Appendix C Table C3, the mean absolute error (MAE) index of damped and undamped transient frequency is about 22 Hz. The value is slightly higher compared to the results without the effect of fault resistance. The reason is due to the effect of fault resistance to the transient signal. The fault resistance increases the damping of the estimated signal. The MAE of damping factor is 0.01, this is about 17 times higher than MAE of the damping factor without the effect of fault resistance. When damping is higher the transient almost disappears and subsequently the identification of the charge transient component will be difficult.

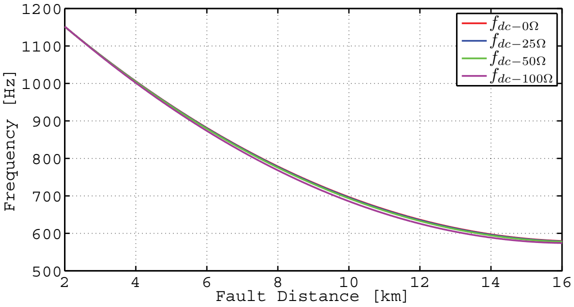

(a) f_{dc} for R_f = 0 - 100 Ω

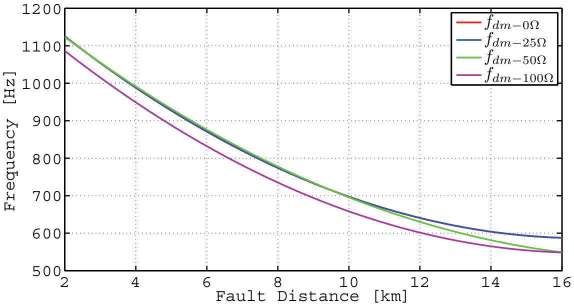

(b) f_{dm} for R_f = 0 - 100 Ω

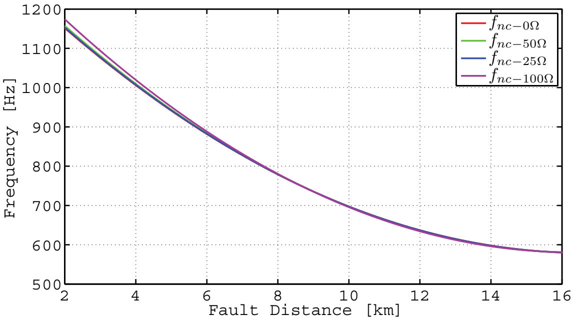

(c) f_{nc} for R_f = 0 - 100 Ω

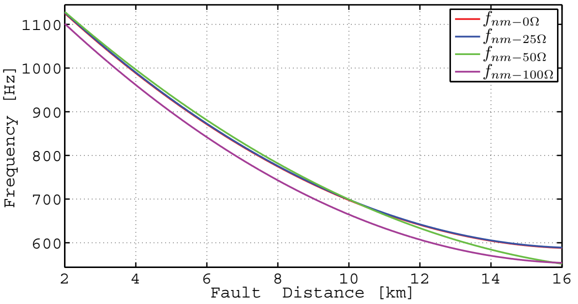

(d) f_{nm} for R_f = 0 - 100 Ω

Figure 6.12. Result of calculated and estimated damped (f_{dc}, f_{dm}) and undamped (f_{nc}, f_{nm}) frequencies with the effect of fault resistance (R_f). Fault resistance (R_f)= 0, 25, 50, 100 Ω. For details of frequencies abbreviations see Figure 6.10.

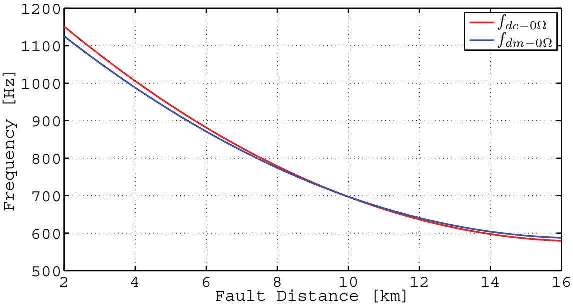

(a) f_{dc} and f_{dm} for R_f = 0 Ω

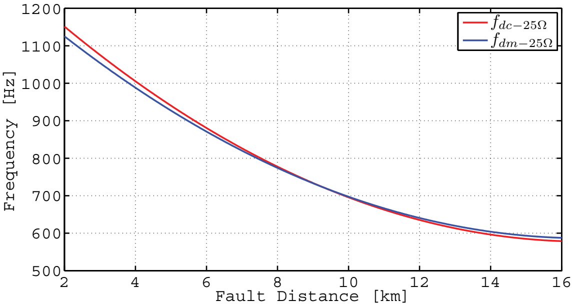

(b) f_{dc} and f_{dm} for R_f = 25 Ω

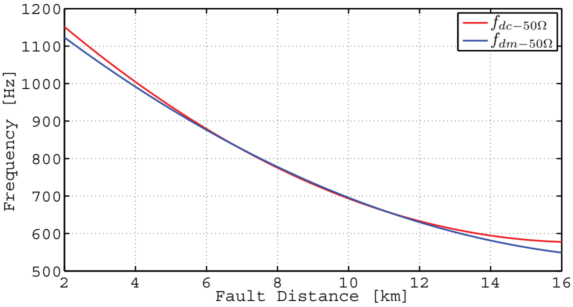

(c) f_{dc} and f_{dm} for R_f = 50 Ω

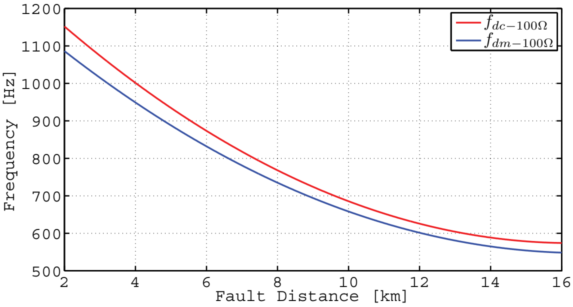

(d) f_{dc} and f_{dm} for R_f = 100 Ω

Figure 6.13. Comparison of result of calculated (f_{dc}) and estimated (f_{dm}) damped frequencies with the effect of fault resistance (R_f). Fault resistance (R_f)= 0, 25, 50, 100 Ω. For details of frequencies abbreviations see Figure 6.10.

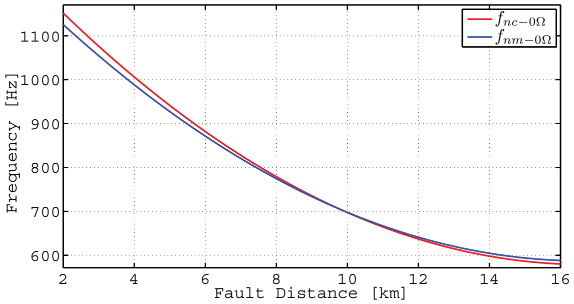

(a) f_{nc} and f_{nm} for R_f = 0 Ω

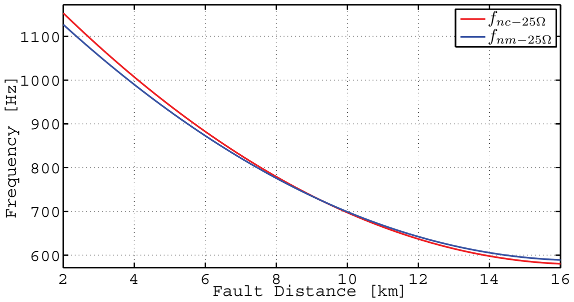

(b) f_{nc} and f_{nm} for R_f = 25 Ω

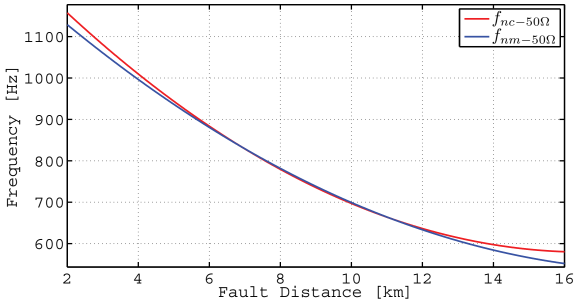

(c) f_{nc} and f_{nm} for R_f = 50 Ω

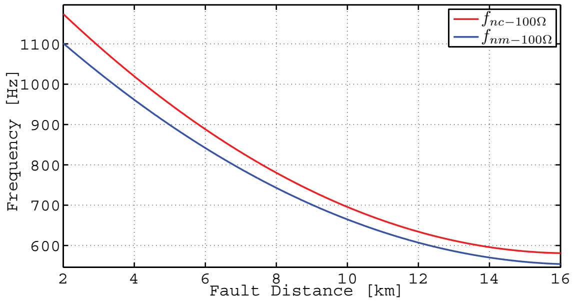

(d) f_{nc} and f_{nm} for R_f = 100 Ω

Figure 6.14. Comparison of result of calculated (f_{nc}) and estimated (f_{nm}) undamped frequencies with the effect of fault resistance (R_f). Fault resistance (R_f)= 0, 25, 50, 100 Ω. For details of frequencies abbreviations see Figure 6.10.

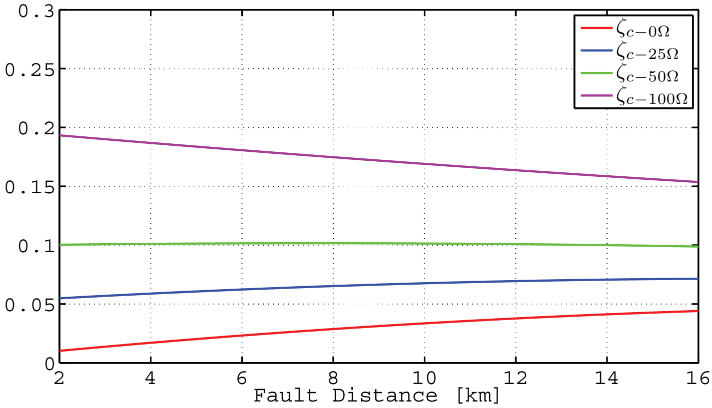

(a) ζc for R_f = 0 - 100 Ω

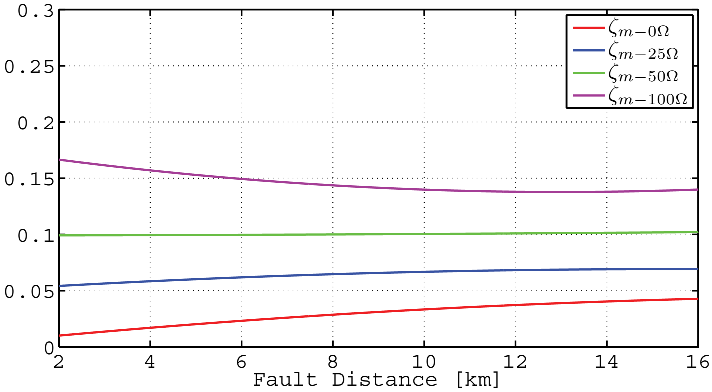

(b) ζ_m for R_f = 0 - 100 Ω

Figure 6.15. Result of calculated (ζ_c) and estimated (ζ_m) damping factor with the effect of fault resistance (R_f). Fault resistance (R_f)= 0, 25, 50, 100 Ω. For details of frequencies abbreviations see Figure 6.10.

As shown in Figure 6.15, the increment of damping factor is significant when an increased fault resistance. In comparison between estimated and calculated damping factor as shown in Figure 6.16, the difference is small for the fault resistance less than 25 Ω, however the gap can be noticed clearly when fault resistance is higher than 25 Ω. In overall, with the effect of fault resistance, the result of MAE of estimated and calculated damped and undamped frequency, is two times higher than MAE of the simulated earth fault without the effect of the fault resistance.

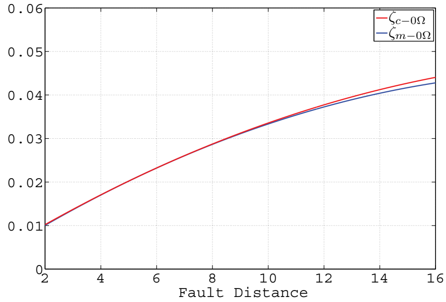

(a) ζ_c and ζ_m for R_f = 0 Ω

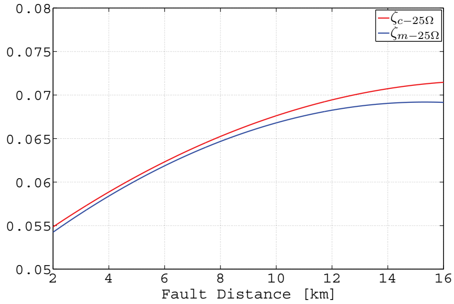

(b) ζ_c and ζ_m for R_f = 25 Ω

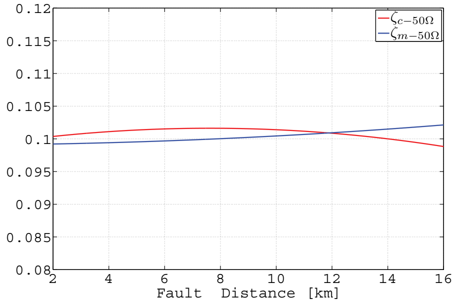

(c) ζ_c and ζ_m for R_f = 50 Ω

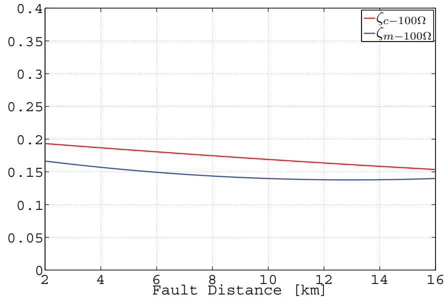

(d) ζ_c and ζ_m for R_f = 100 Ω

Figure 6.16. Comparison of result of calculated (ζ_c) and estimated (ζ_m) damping factor with the effect of fault resistance (R_f). Fault resistance (R_f)= 0, 25, 50, 100 Ω. For details of frequencies abbreviations see Figure 6.10.

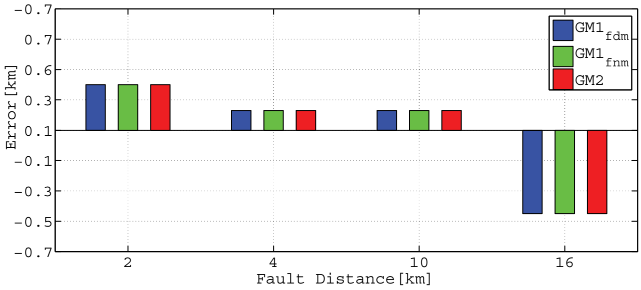

(a) Fault location for $R_f = 0\ \Omega$

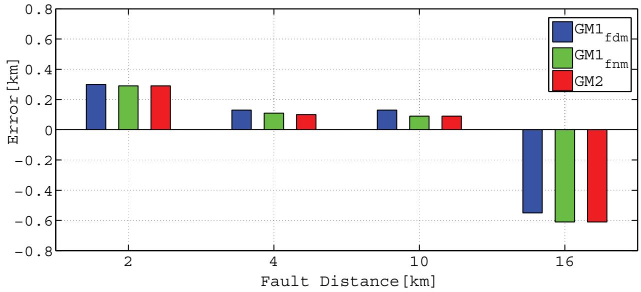

(b) Fault location for $R_f = 25\ \Omega$

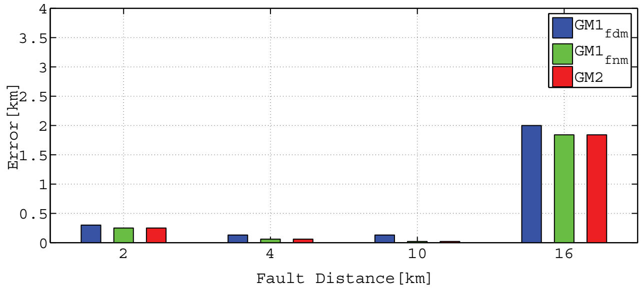

(c) Fault location for $R_f = 50\ \Omega$

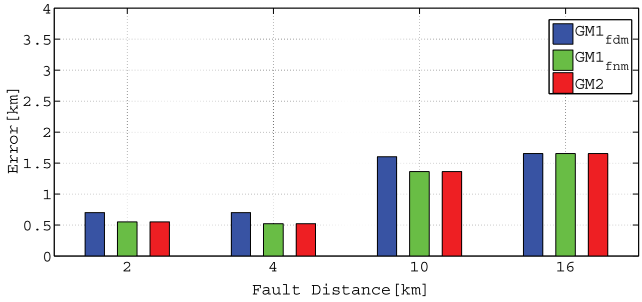

(d) Fault location for $R_f = 100\ \Omega$

Figure 6.17. Distance estimates with effect of fault resistance for general model networks.

Figure 6.17, shows the results of the estimated of fault location using GM1 and GM2 algorithms with the effect of fault resistance, Appendix C Table C4 shows the tabulated simulation results. Referring to Figure 6.17, we can see that result of the distance estimation error is almost identical for the tested algorithms. In overall, the calculated MAE index of all algorithms is less than 0.6 km, as given in Appendix C Table C4. The fault distance error is lower when the fault is simulated at the middle of the faulty feeder with the fault resistance between 0 to 50 Ω. As expected, the fault estimation error is higher when the fault is located at the end of the line. In overall, the fault distance error is less than 2 km.

Appendix C, Table C5 shows the results of simulated single line to earth fault with the effect of fault inception angle. The fault inception angles used are 0, 45 and 90 °. In overall, we found that the fault inception angle does not affect the transient frequencies. Unfortunately, we found that the process to locate the transient component becomes much challenging since the lower fault inception angle will reduce the peak amplitude of the transient, subsequently effecting the process of identification of the charge transient component as shown in Figure 6.18.

In Figure 6.19, the results show estimates of fault location using GM1 algorithm. The fault distance estimation is calculated using a estimated damped and undamped transient frequency. A single line to earth fault was simulated with zero fault resistance. The MAE index of the simulation result was 0.34 km.

Figure 6.20 shows results of calculated damped transient frequencies with the effect of load and fault resistance. The frequency slightly increases when the load is increased and slightly decreases when the fault resistance is increased. The effect of load on damped transient frequency is higher when the fault located close to the substation. Figure 6.21, shows the estimated damped transient frequencies with the effect of load and fault resistance. The estimated damped frequency shows significant decrease when the fault resistance is increased.

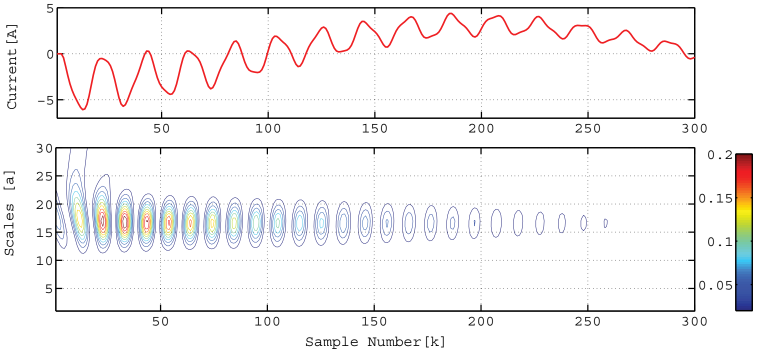

(a) Transient current (above) and its scalogram, fault inception angle 0°

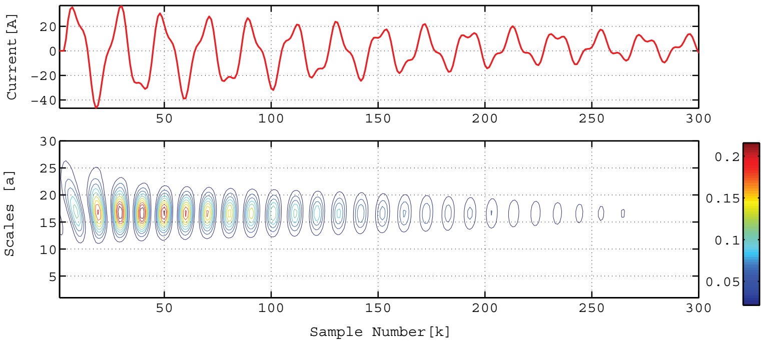

(b) Transient current (above) and its scalogram, fault inception angle 45 °

Figure 6.18. Comparison of simulated transient signal and its scalogram with the effect of inception angle. The fault distance is 4 km and without fault resistance.

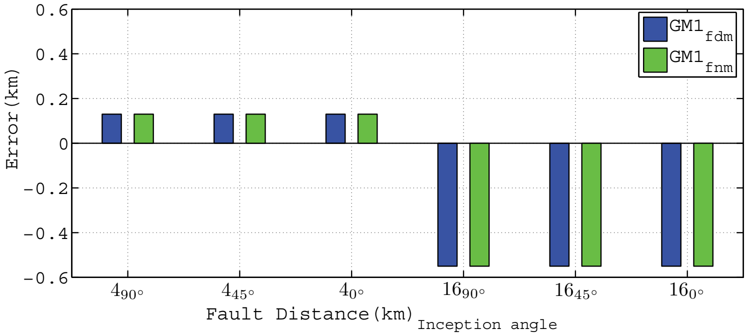

Figure 6.19. Effect of fault inception angle on fault distance estimation. $\mathrm{GM1}_{fdm}$ denotes a distance estimation error using GM1 with damped transient frequency and $\mathrm{GM1}_{fnm}$ denotes a distance estimation error using GM1 with undamped transient frequency.

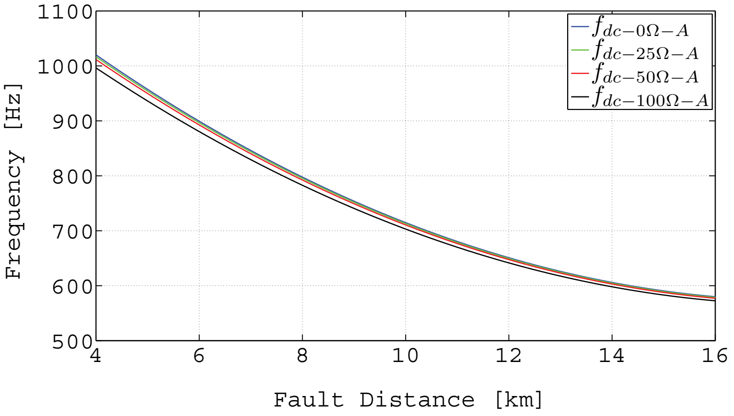

(a) f_{dc} for load A = 5 MVA R_f = 0 - 100 Ω

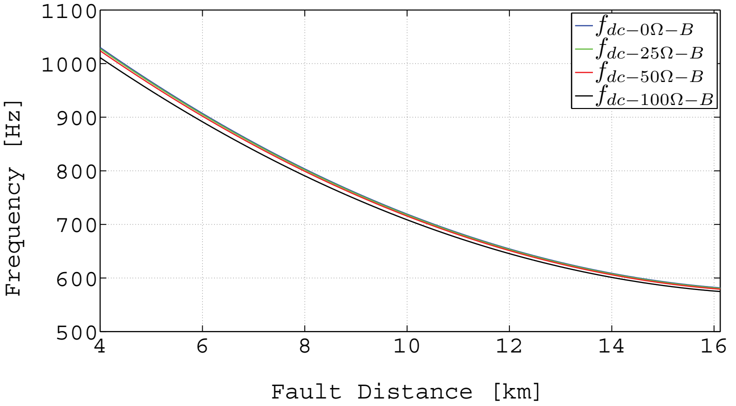

(b) f_{dc} for load B = 12 MVA R_f = 0 - 100 Ω

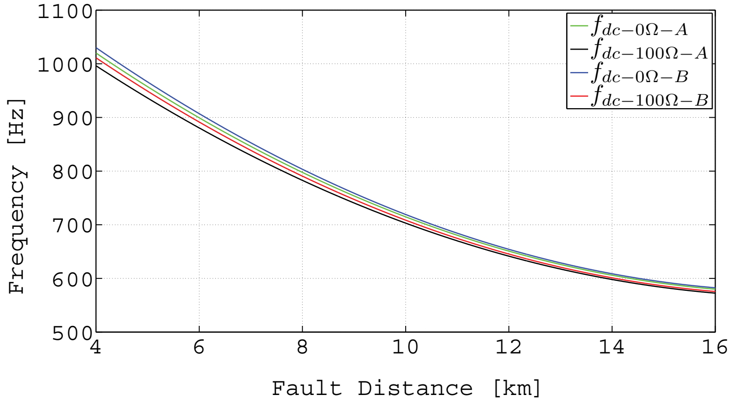

(c) f_{dc} for load A and B , R_f = 0 and 100 Ω

Figure 6.20. Comparison of calculated damped frequencies with the effect of load and fault resistance

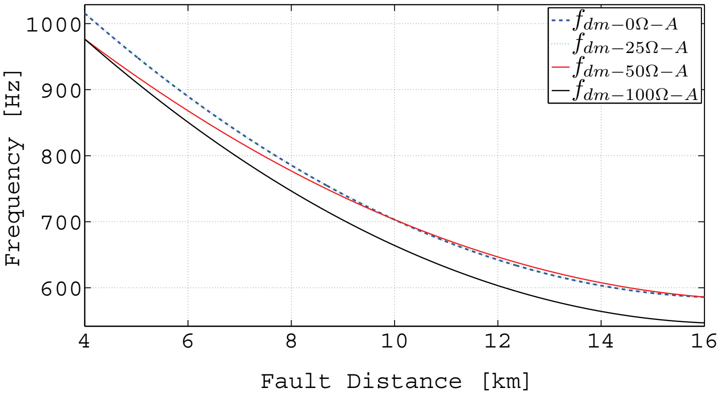

(a) f_{dm} for load A = 5 MVA R_f = 0 - 100 Ω

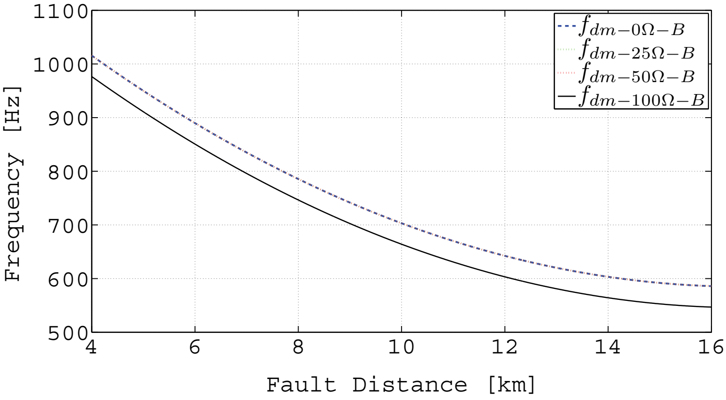

(b) f_{dm} for load B = 12 MVA R_f = 0 - 100 Ω

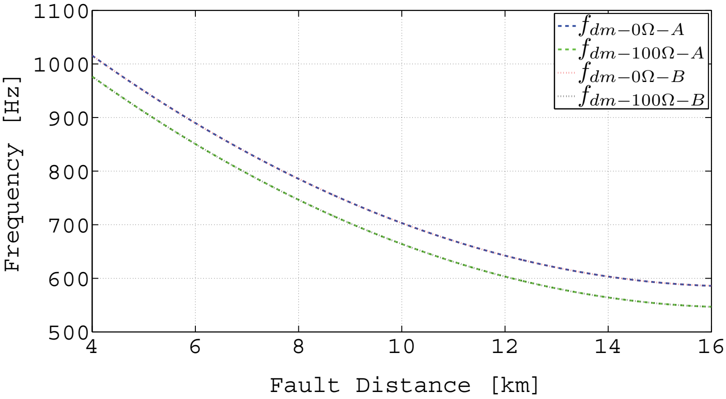

(c) f_{dm} for load A and B , R_f = 0 and 100 Ω

Figure 6.21. Comparison of estimated damped frequencies with the effect of load and fault resistance

Figure 6.22, shows the effect of load and fault resistance on calculated undamped transient frequency. It can be seen that, with the effect of 5 MVA and 12.5 MVA loads, the calculated undamped transient frequency is almost not affected by fault resistance. Based on the result, it is found that the undamped frequency with a higher load (12.5 MVA) has higher frequency than the undamped frequency with a lower load (5 MVA). The results shown in Figure 6.23, tell us that the estimated undamped frequency with high load and lower fault resistance is greater than the estimated undamped frequency having low load and high fault resistance.

In Figure 6.24(d), it can be seen that, the estimated and calculated damping factor proved to be identical with small error. When the fault resistance in increased the damping factor is increased as well. The result shows that, the damping factor with load B is lower than the damping factor with load A.

The bar charts shown in Figures 6.25 and 6.26, present a comparison of earth fault distance estimation error by GM algorithms when calculating earth fault distance in the simulated network. Appendix C, Table C8 shows tabulated overall distance estimation results. A single line to earth fault was simulated at 4 km, 10 km and 16 km from substation for loads 5 MVA and 12.5 MVA. Earth faults were simulated with fault resistance values of 0 Ω , 25 Ω, 50 Ω and 100 Ω.

In overall, based on the results, we found that the fault distance estimation error is less than 1 km when the fault resistance is below 50 Ω. However, when fault resistance is 100 Ω, the estimation error is increased.

In Figures 6.25 and 6.26, when fault happens at 4 km and with the fault resistance less than 25 Ω, GM3 algorithm calculates the fault distance with the lower error compared with the other algorithms. Unfortunately, when the fault distance is simulated at 10 km, GM3 algorithm gives the highest fault estimation error among all algorithms. It can be seen as well that GM3 algorithm has the highest estimation error when the earth fault happens at fault distance 16 km and with fault resistance 100 Ω. The results from GM1, GM2 and GM4 algorithm are almost identical for all cases of simulated earth faults. In overall, the MAE error of estimated fault distance using proposed GM algorithms is less than 0.6 km, when fault resistance is 50 Ω or less.

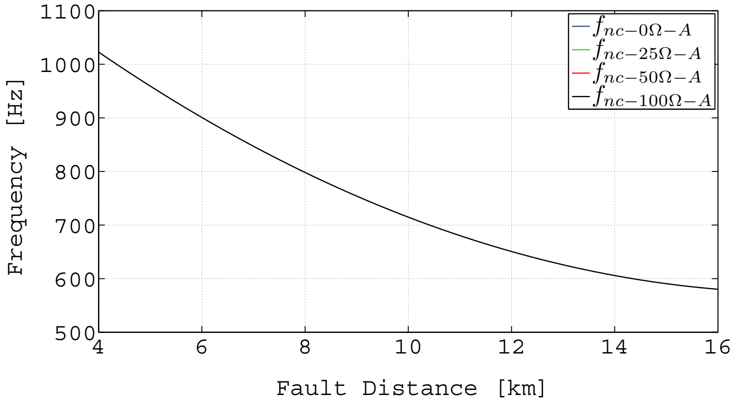

(a) f_{nc} for load A = 5 MVA R_f = 0 - 100 Ω

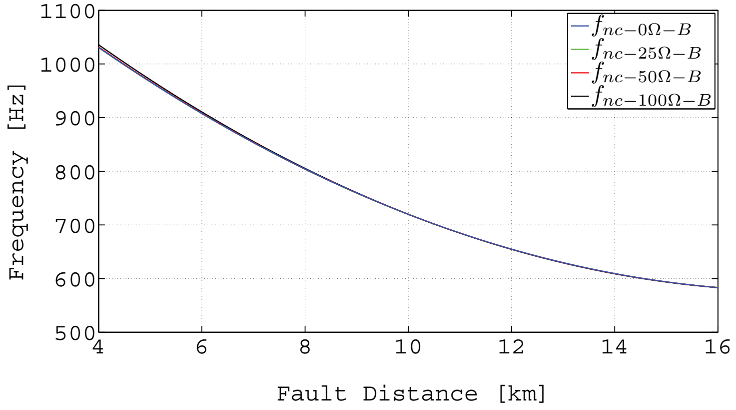

(b) f_{nc} for load B = 12 MVA R_f = 0 - 100 Ω

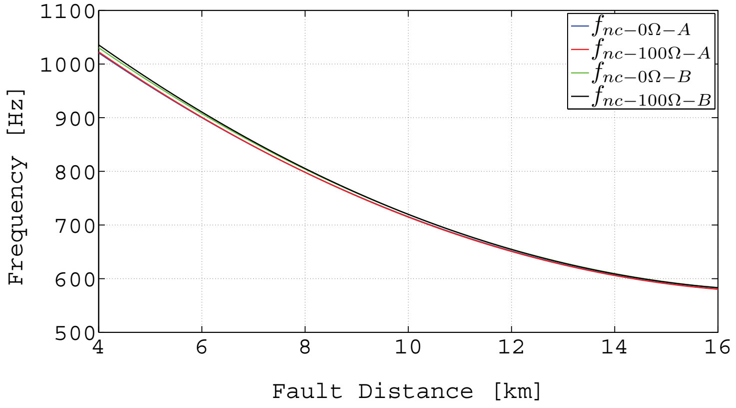

(c) f_{nc} for load A and B , R_f = 0 and 100 Ω

Figure 6.22. Comparison of calculated undamped frequencies with the effect of load and fault resistance

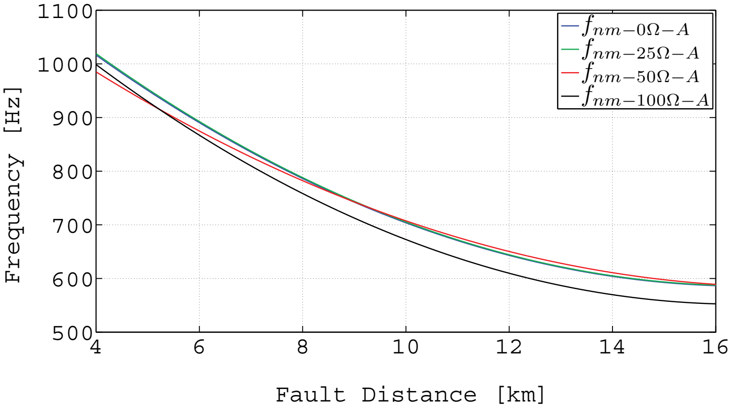

(a) f_{nm} for load A = 5 MVA R_f = 0 - 100 Ω

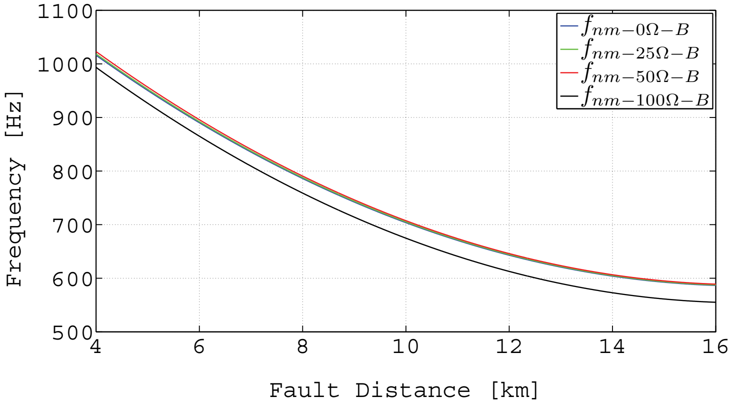

(b) f_{nm} for load B = 12 MVA R_f = 0 - 100 Ω

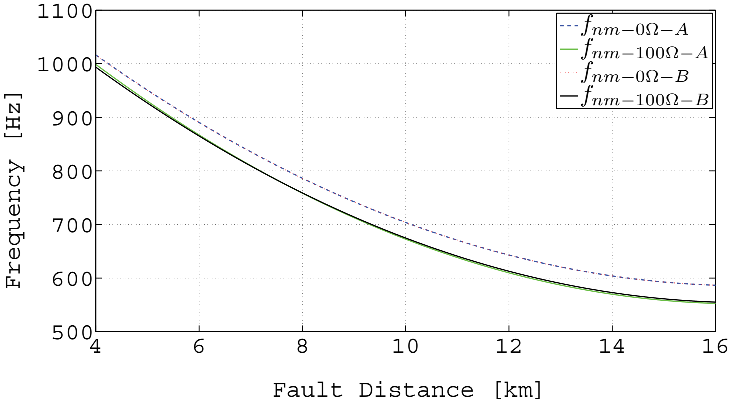

(c) f_{nm} for load A and B , R_f = 0 and 100 Ω

Figure 6.23. Comparison of estimated undamped frequencies with the effect of load and fault resistance

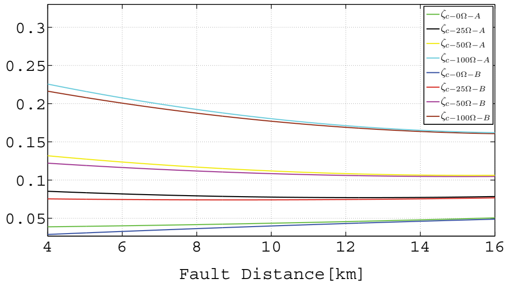

(a) ζ_c for load A and B, R_f = 0 - 100 Ω

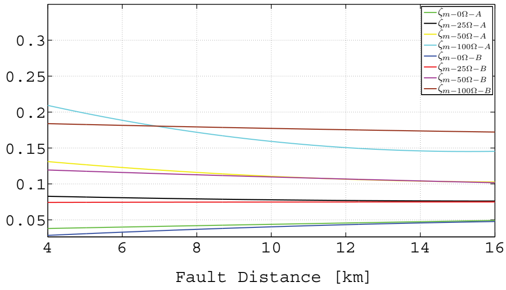

(b) ζ_m for load A and B, R_f = 0 - 100 Ω

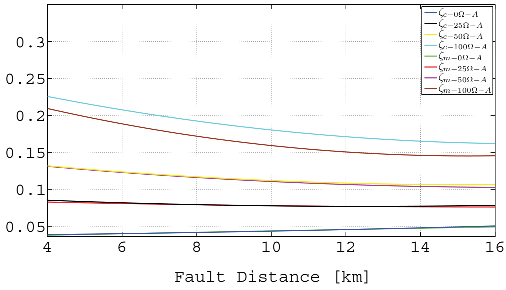

(c) ζ_c and ζ_m for load A , R_f = 0 - 100 Ω

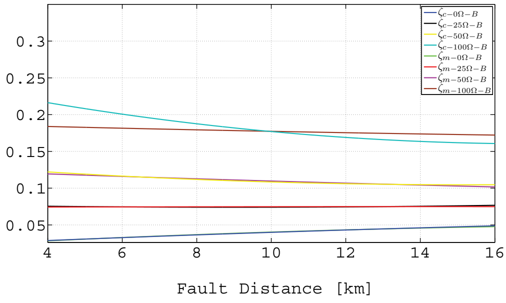

(d) ζ_c and ζ_m for load B , R_f = 0 - 100 Ω

Figure 6.24. Calculated and estimated damping factor (ζ) with the effect of load and fault resistance.

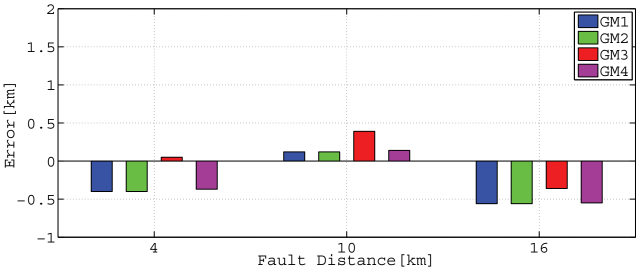

(a) Fault location for R_f = 0 Ω

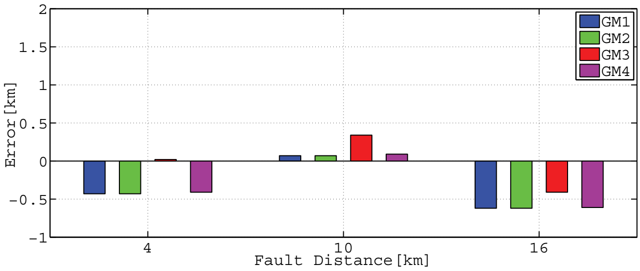

(b) Fault location for R_f = 25 Ω

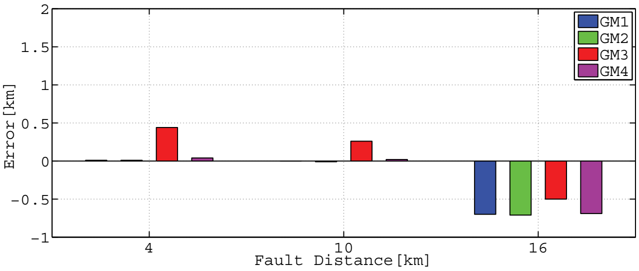

(c) Fault location for R_f = 50 Ω

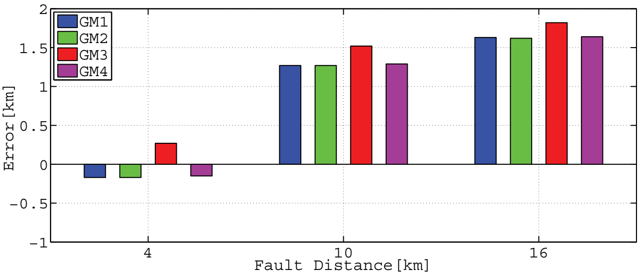

(d) Fault location for R_f = 100 Ω

Figure 6.25. Distance estimates with the effect of 5 MVA load and fault resistances for general model networks.

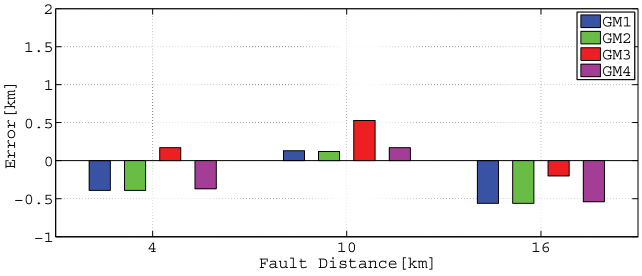

(a) Fault location for R_f = 0 Ω

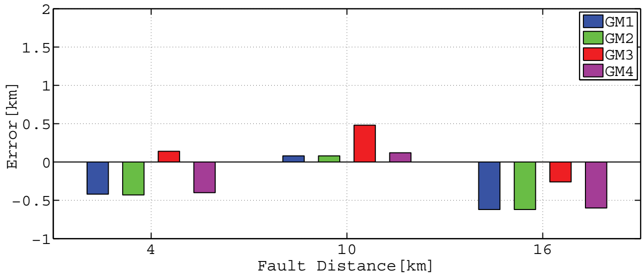

(b) Fault location for R_f = 25 Ω

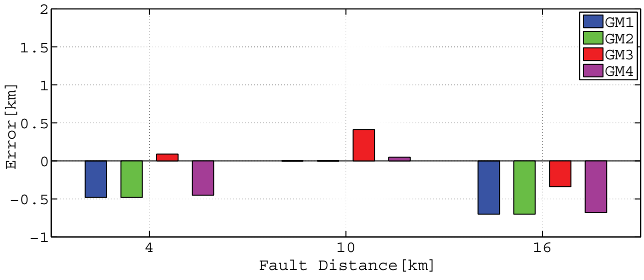

(c) Fault location for R_f = 50 Ω

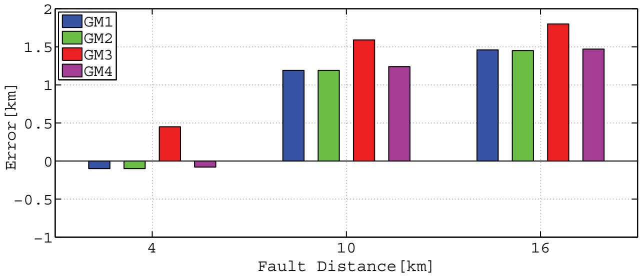

(d) Fault location for R_f = 100 Ω

Figure 6.26. Distance estimates with the effect of 12 MVA load and fault resistances for general model networks.

6.2 Simulated Network Model 2

In this section, we discuss the accuracy of the single line to earth fault location algorithms that has been explained in Chapter 5, Section 5.2. The fault location algorithms used in this section are the accurate model EM1 and for the comparison, the simple model GM2. The accuracy of the methods was tested using the simulation model and the network example with overhead lines. The performance accuracy of EM1 and GM2 algorithm was investigated in various fault conditions. For EM algorithm, the performance accuracy was defined by the mean absolute error ($\mathrm{MAE_{EM}}$) as expressed as in Equation (6.3) below, while for GM algorithm, the performance accuracy was defined as given in Equation (6.1).

$$MAE_{EM} = \frac{1}{n}\sum_{i=1}^{n}|EM_i - l_i| = \frac{1}{n}\sum_{i=1}^{n}|\Delta EM_i| \tag{6.3}$$

In 6.3, ΔEM_i is the absolute error fault distance using EM algorithm, EM_i is estimated fault distance using EM algorithm, l_i is exact fault distance and n is numbers of observation of fault distance error.

6.2.1 Description of the simulation and the network model

The single line diagram of the simulated unearthed medium voltage (MV) network and its simulation model is shown in Figure 6.27. The simulation model is based on the sequence component networks for the exact-π solution for the earth fault transients. The system is 21 kV overhead lines unearthed MV radial network and the line parameters are as follows: $R_{l,p}$=0.6 Ω/km, $R_{l,0}$=1.3 Ω/km, $L_{l,p}$=1.0 mH/km, $L_{l,0}$= 5.0 mH/km, $C_{l,p}$=10.71 nF/km, $C_{l,0}$=6.12 nF/km, R_T=0.0216 Ω, L_T=2.8 mH. We assume the negative sequence parameters to be equal to the positive sequence ones.

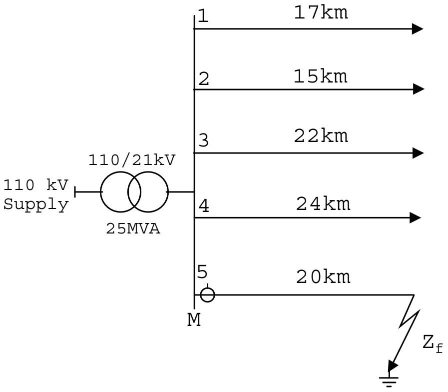

(a) A schematic diagram of 21 kV, 98 km, unearthed neutral MV network

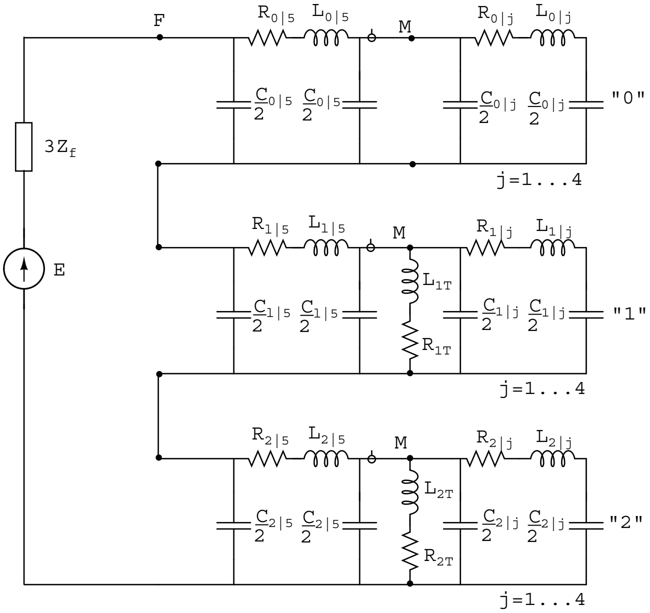

(b) Simulation model based on symmetrical component equivalent circuit for an earth fault located at the end of the faulty feeder

Figure 6.27. A schematic network diagram and its simulation model for a single phase to earth fault in a distribution network. M denotes measurement point, F refers to the fault location and Z_f is the fault impedance. $L_{0|5}$, $L_{1|5}$, $L_{2|5}$ are zero sequence, positive sequence and negative sequence inductance of faulty line located in front of fault point (F). $L_{0|j}$, $L_{1|j}$ are zero sequence and positive sequence inductance of sound line. L_T and R_T is the inductance and resistance of the transformer, capacitances and resistances correspondingly.

The lines were modelled as a chain of exact π-model cells (1 cell per 10 km of the line). The network was 5 feeders and the earth fault was simulated at feeder 5. The total length of the network is 98 km. All faults with several different fault conditions were simulated with the software package ATP (Alternative Transients Program), version of EMTP program where the circuit was realized using ATPDraw. The sampling frequency was 20 kHz. In the simulation analysis, the load was either 0.4 MW, 0.8 MW, 2 MW or zero.

6.2.2 Result Analysis and Discussion

Figure 6.28 shows the results of the simulation without the effect of load and with the effect of fault distance, fault resistance and fault inception angle. The tabulated results can be found in Appendix C Table C9, C10 and C11, respectively. In order to study the performance of the tested algorithms, in Figure 6.28(a), an earth fault was simulated at 10 points starting from 2 km from measuring point (M) with 2 kilometer steps. In case of the effect of fault resistances as shown in Figure 6.28(b), 3 different locations of earth fault was simulated which are 4 km, 10 km and 16 km from the measuring point. Only two fault distances were simulated for the case of fault inception angle variation, which are 4 km and 16 km, as presented in Figure 6.28(c). Based on the MAE results given in Appendix C Table C9, C10 and C11, it can be seen, that the EM1 algorithm provides better results than the GM2 algorithm.

As shown in Figure 6.28(a), the estimation error is increased with the increase of fault distance for both algorithms. GM2 algorithm recorded the highest error, when earth fault was located at 20 km from the substation. For the earth fault distance of 4km, 10km and 16km, the estimation error is further increased when fault distance is increased with the increased of fault resistance, as we seen in Figure 6.28(b).

In Figure 6.28(c), it seems that fault inception angle does not affect both algorithms when fault happens at fault distance 4 km, however, when fault is located at 16 km the error is increasing for EM1 algorithm but decreasing for GM2 algorithm.

If we carefully observe the results in Figure 6.28, Table C10 and Table C11 in Appendix C, in case of fault distance located at 16 km from fault distance, for GM2 algorithm estimation result, indirectly the effect of increased of fault resistance and fault inception angle at 0 degree is decreasing the estimated undamped charge transient frequency (f_{nm}) and at the same time improving the algorithm accuracy.

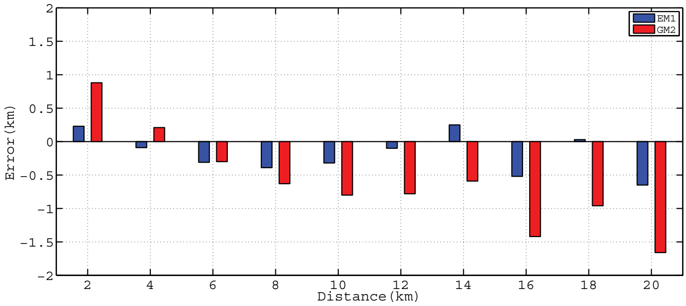

(a) Calculation error as a function of fault distance

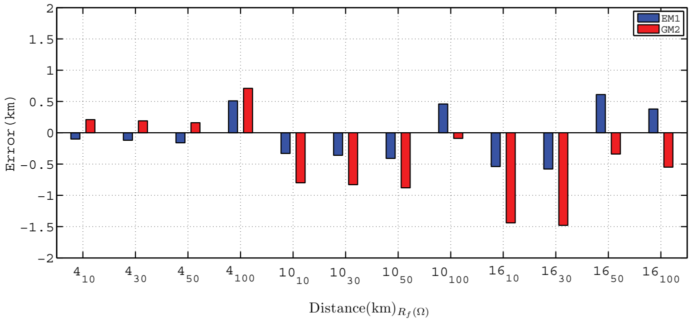

(b) Calculation error as a function of fault distance and fault resistance

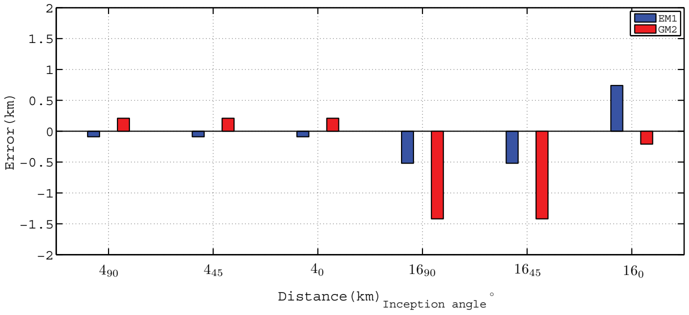

(c) Calculation error as a function of fault inception angle

Figure 6.28. The effect of fault distance, fault resistance and inception angle on fault distance calulation. EM1 denotes the distance calculation error using exact model 1 and GM2 denotes the distance calculation error using general model 2.

Figure 6.29 shows the results of fault location performance with the effect of resistive load located at the end of each feeder. The tabulated results can be found in Appendix C Table C12. In this part of simulation, each feeder has same amount of load with three different cases which were 400 kW, 800 kW and 2 MW.

Based on the MAE results given in Appendix C Table C12, it can be seen, that the EM1 algorithm again provides better results than the GM2 algorithm. In overall, both algorithms have an increase of total MAE when resistive load is added to the simulated network.

As shown in Figure 6.29, the fault distance error seems to be increased when the load is increased. The more far the fault happens from the substation the higher is the fault distance error. In Figure 6.29, in some cases corresponding to GM2, we can see that the fault distance error is slightly decreased when fault resistance is increased. In overall, the fault distance estimation error is less than 1.5 km.

Figure 6.30 shows the results of fault fault location performance with the effect of inductive load located at the end of each feeder. The tabulated results can be found in Appendix C Table C13. In this part of simulation, each feeder has same amount of load with three difference cases which were 400 kVAr, 800 kVAr and 2 MVAr. Corresponding to the overall MAE result shown in Appendix C Table C13, EM1 algorithm provides better results than the GM2 algorithm.

It is found that the performance accuracy for EM1 algorithm is increased with the effect of inductive load compared to than when it is been affected by resistive load. However, in case of GM2 algorithm, the performance accuracy is decreased with the effect of inductive load. In Figure 6.30, in overall, the results show that the fault distance estimation error is less than 1.5 km.

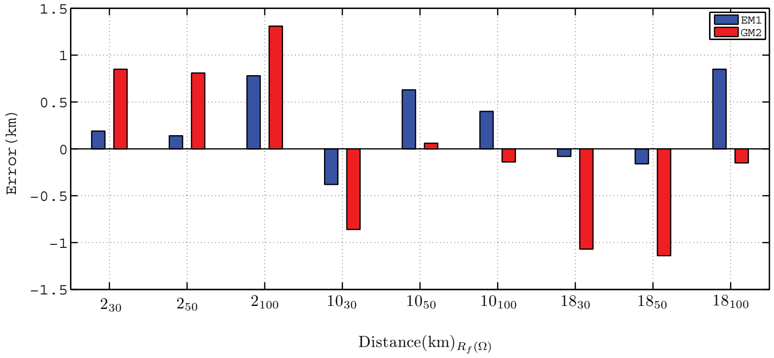

(a) 400 kW

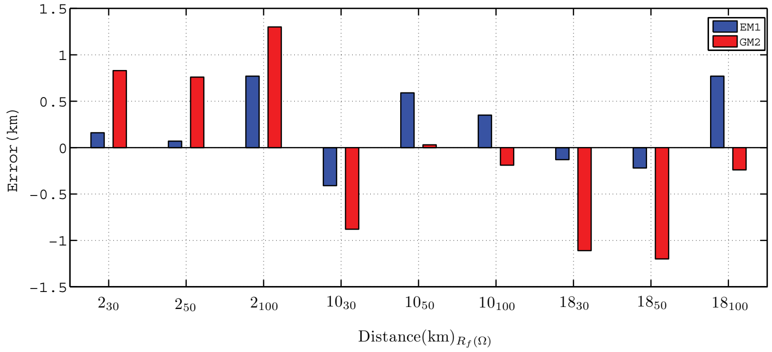

(b) 800 kW

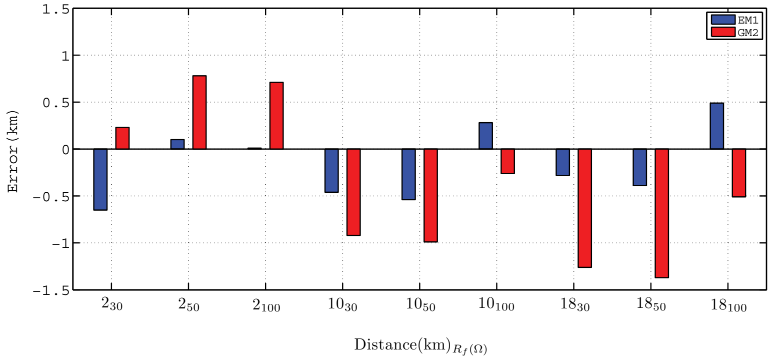

(c) 2 MW

Figure 6.29. Fault location performance with the effect of resistive load located at the end of each feeder. EM1 denotes a distance calculation error using exact model 1 and GM2 denotes a distance calculation error using general model 2.

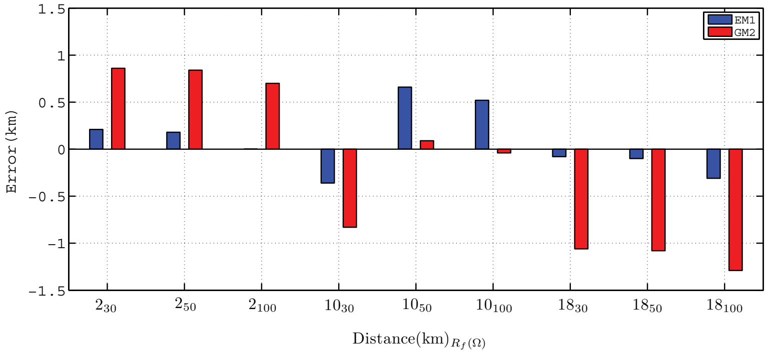

(a) 400 kVAr

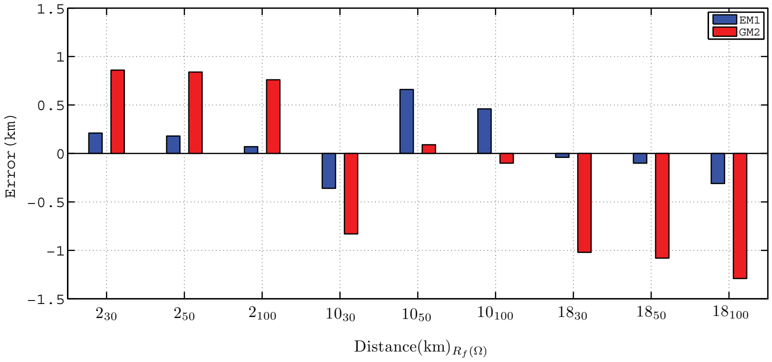

(b) 800 kVAr

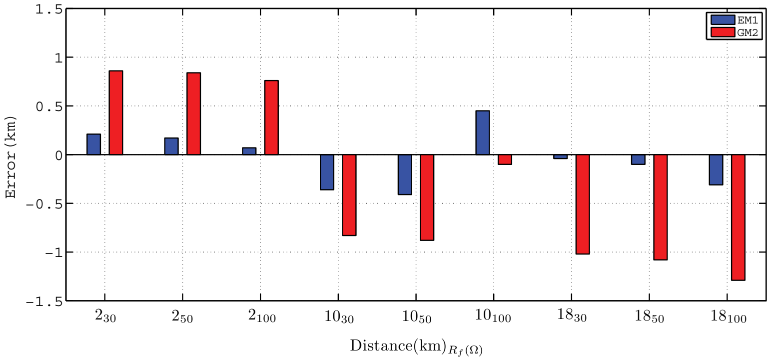

(c) 2 MVAr

Figure 6.30. Fault location performance with the effect of inductive load located at the end of each feeder. EM1 denotes a distance calculation error using 1 and GM2 denotes a distance calculation error using general model 2.

Figure 6.31 shows the results of fault fault location performance with the effect of load for 0.9 and 0.5 power factor. The tabulated results can be found in Appendix C Table C14 and Table C15, respectively. In this part of simulation, each feeder has same amount of load with two difference cases which were 400 KVA and 800 KVA.

Based on the MAE result given in Appendix C Table C14 and Table C14, it can be seen, that the EM1 algorithm provides again better results than the GM2 algorithm. By comparison of MAE results in Appendix C Table C14 and Table C14, we found that both algorithms have a decrease of MAE when low power factor is used.

In this work, the most influential source of error was resistive load. Theoretically, the load can be compensated by adding the corresponding impedance to the algorithm models. However, the data of load devices and their transient impedances is difficult to get. Another way is to use the curve fitting technique to compensate the error with known load conditions.

Another source of error is inaccuracy in estimating the undamped complex frequency. This error is caused by the inaccuracy in estimation of the damping attenuation through Hilbert transformation method and also by an inaccurate detection of charge transient component using CWT. When the magnitude of fault resistance or resistive loads is increased, the transients become more damped, with the result that the estimation of the charge transient frequency becomes more difficult which affects the overall computation of fault distance. In following section, the investigation of performance accuracy of proposed algorithms is performed using JMarti (frequency-dependent) line model which is more practical compared to the exact-π solution that we presented in this section.

Considering which one of the algorithms is easy to be implement in real operation, the general model algorithm should be much easier to be implement compare to the exact model algorithm. It is because its required a simple iteration process to estimate the fault distance. While exact model algorithm required a heavy computation to solve a higher order equation, which generally may not be easy.

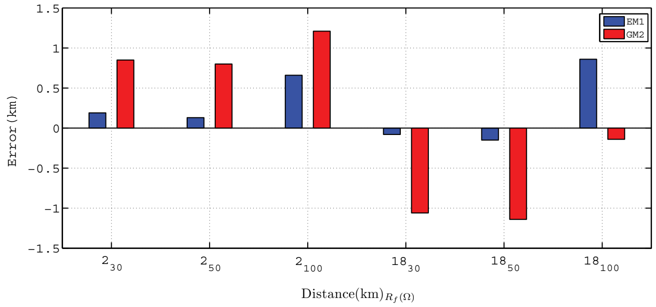

(a) 400 kVA, 0.9 PF

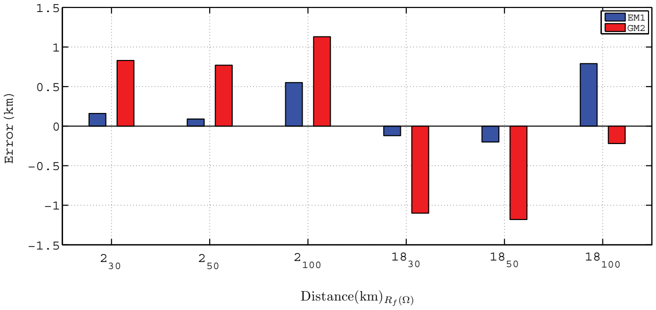

(b) 800 kVA, 0.9 PF

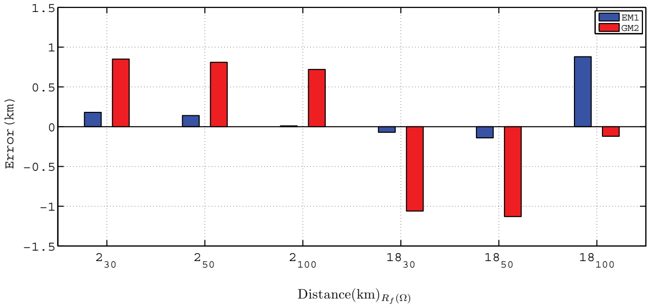

(c) 400 kVA, 0.5 PF

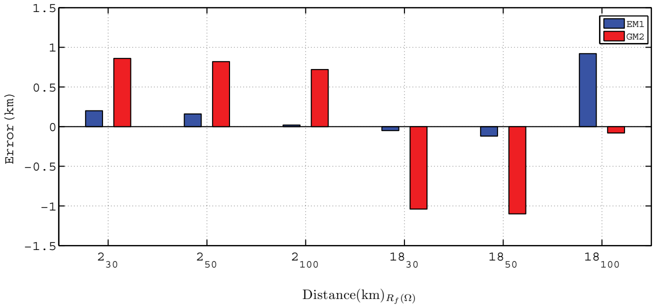

(d) 800 kVA, 0.5 PF

Figure 6.31. Fault location performance with the effect of load with 0.9 and 0.5 PF located at the end of each feeder. EM1 denotes the distance calculation error using exact model 1 and GM2 denotes the distance calculation error using general model 2.

6.3 Simulated Network Model 3

In this section, we investigate the proposed fault location algorithms as described in Chapter 5, which use the earth fault transient signals measured at the secondary sides of MV and LV distribution transformers to locate the single line to earth fault. The performance accuracy of the wavelet transform (WT) version of the algorithms, is defined by mean absolute error ($\mathrm{MAE_{WT}}$) as expressed as in Equation (6.4) below:

$$MAE_{WT} = \frac{1}{n}\sum_{i=1}^{n}|WT_i - l_i| = \frac{1}{n}\sum_{i=1}^{n}|\Delta WT_i| \qquad (6.4)$$

In 6.4, ΔWT_i is the absolute error fault distance using WT algorithm, WT_i is estimated fault distance using WT algorithm, l_i is exact fault distance and n is numbers of observation of fault distance error.

6.3.1 Description of the simulation and the network model

A 20 kV, 227.6 km overhead lines, unearthed neutral MV network was modelled using the JMarti line constants of ATP/EMTP program taking into account the real geometrical and electrical values. A schematic diagram of the simulated unearthed neutral medium voltage (MV) network and its ATPdraw circuit are shown in Figures 6.32 and 6.33, respectively. The configuration of the feeders and the ATPDraw circuit are given in Appendix B, Figure B1. The overhead lines were energized by AC sinusoidal waveform via 110/20 kV, delta/star unearthed neutral transformer. An earth fault was simulated at 11 difference places as indicated in Figure 6.32. Each of the simulated earth faults were performed for fault resistances of 0 Ω, 25 Ω and 50 Ω. For each case the fault inception angle used were 45° and 90°. The sampling frequency used was 20 kHz.

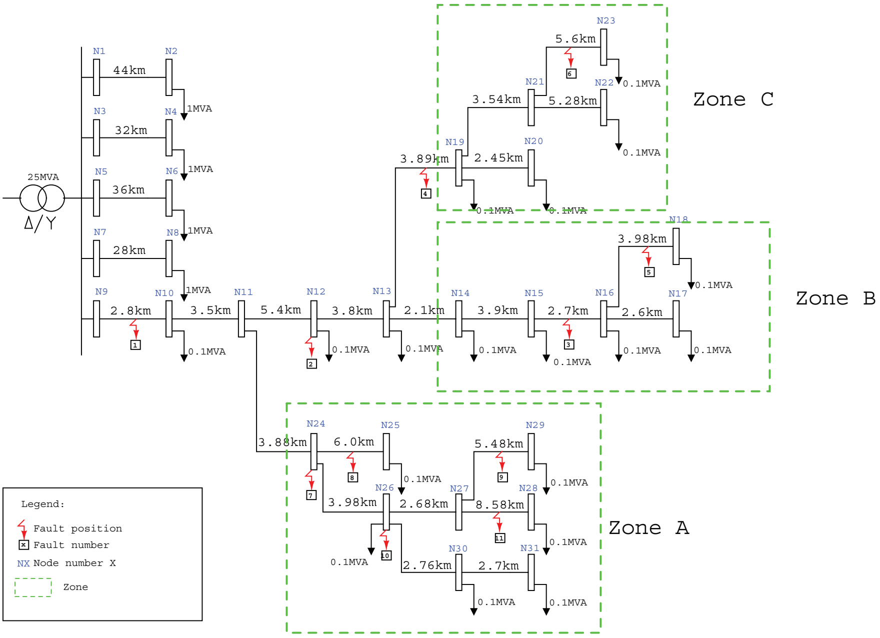

Figure 6.32. A schematic diagram of 20 kV, 227.6 km, unearthed neutral MV network.

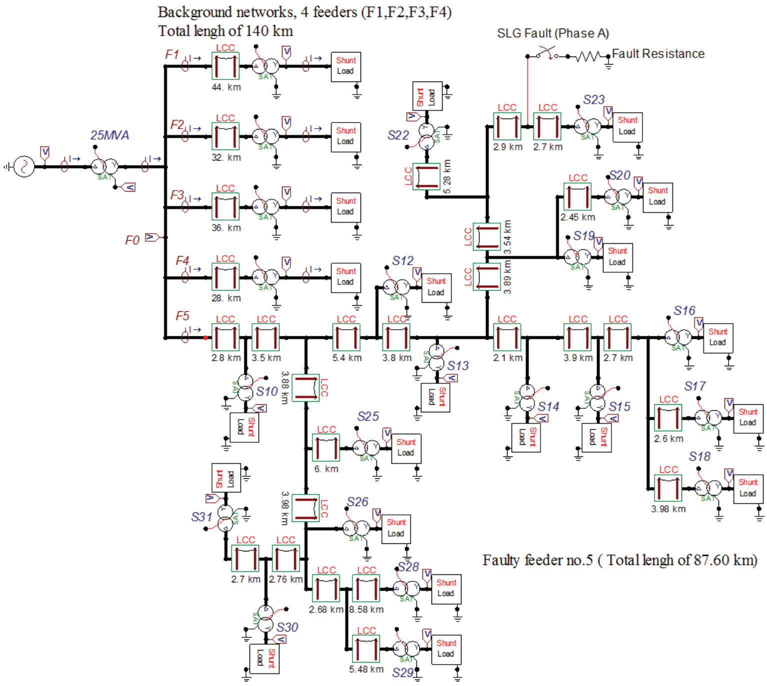

Figure 6.33. ATPdraw circuit for the simulated network model 3.

6.3.2 Result Analysis and Discussion

The results of single line to earth fault estimation with WT algorithm are shown in Tables 6.1 and 6.2. In overall, MAE of WT algorithm is 1.09 km. In Tables 6.1 and 6.2, it is shown that the fault location error is increasing when the fault is located far from the measuring point and the fault inception angle is small. Also the fault location error is higher when the fault is located far from the measuring point and has a high fault resistance. In overall, the fault distance estimation error is less than 5.2 km and 6.52 km for simulation with test angle of 90° and 45°, respectively. It is found that the test number with the longest fault distance (test number 5 (26.19 km)) calculated the highest fault location error. From our experience in analyzing the transient signal, referring to Tables 6.1 and 6.2, when the magnitude of the fault resistance is increased the transient signals become more damped and the fault location is more difficult.

Figures 6.34, 6.35 , 6.36 , 6.37 and 6.38, show results of calculated CWT FFT amplitudes of transient at MV/LV substation for fault at inception angles of 90° and 45° which are used in correct path identification algorithm. Based on the correct path identification algorithm, the highest recorded FFT amplitude will indicate which MV/LV substation should we locate in order to determine the correct fault location if there are several branches in the network. Also, based on the test results, another assumption is that if the fault distance estimation shows a large error in its calculation, the correct path algorithm can still give us a good guess about the fault position. However, this assumption cannot be true for all fault positions. For instance, in Table 6.1, the fault is located at test number 1 which is 1.4 km from measuring point and the LV substation detected is at substation S23. However, the nearest LV substation to the fault point is substation S10. Similarly, for fault located at test number 2, 3, 4, 7 and 10. Therefore, the assumption can be used only if the fault happens exactly at the section which located at the end of the feeder branches such as the faults located at test number 5, 6, 8, 9 and 11.

In this work, the zones were defined based on the location of the MV/LV substation located in the same main branches. For examples, it can be seen that MV/LV substations number S25, S26, S28, S29, S30 and S31 located in zone A, MV/LV substations number S14, S15, S16, S17 and S18 is located at zone B and MV/LV substations number S19, S20, S22 and S23 is located at zone C.

Table 6.1. Test results of single line to earth fault for 90° fault inception angle using the WT algorithm.

Test number (distance)	Test Section / Node	Candidates	Substation detected			Fault location error (km)			MAE (km)
			R_{f0}	R_{f25}	R_{f50}	R_{f0}	R_{f25}	R_{f50}	
1 (1.4km)	N9-N10	N9-N10√	S23	S23	S23	-0.07	-0.43	-1.75	0.75
2 (11.7km)	N12	N11-N13√ N24-N25 N24-N26	S20	S20	S20	0.53	0.52	-0.02	0.36
3 (22.8km)	N15-N16	N15-N16√ N19-N21	S18	S18	S18	-0.07	-0.38	-1.44	0.63
4 (17.5km)	N13-N19	N13-N14 N13-N19√ N27-N28 N27-N29 N30-N31	S20	S20	S20	0.58	-1.46	-0.84	0.96
5 (26.19km)	N16-N18	N16-N17 N16-N18√ N21-N23 N21-N22	S18	S18	S18	-2.09	-3.09	-5.11	3.43
6 (25.83km)	N21-N23	N21-N22 N21-N23√ N16-N17 N16-N18	S23	S23	S23	-0.87	-1.24	-1.64	1.25
7 (10.18km)	N24	N11-N12 N11-N25√ N11-N26√	S29	S25	S25	0.75	0.05	0.91	0.57
8 (12.53km)	N24-N25	N12-N13 N24-N25√ N24-N26	S25	S25	S25	0.64	0.58	0.25	0.49
9 (19.72km)	N27-N29	N14-N15 N19-N20 N19-N21 N27-N28 N27-N29√	S29	S29	S29	-0.6	-1.44	-2.16	1.4
10 (14.16km)	N26	N12-N13 N24-N27√ N24-N30 N24-N25	S28	S28	S28	0.52	0.37	-0.78	0.52
11 (21.72km)	N27-N28	N27-N28√ N27-N29 N16-N17 N16-N18 N19-N21	S28	S28	S28	0.34	0.18	-3.11	1.21
All simulation tests									1.05

*Note: Symbol(√) in the table indicate the correct section

Table 6.2. Test results of single line to earth fault for 45° fault inception angle

Test number (distance)	Test Section / Node	Candidates	Substation detected			Fault location error (km)			MAE
			R_{f0}	R_{f25}	R_{f50}	R_{f0}	R_{f25}	R_{f50}	(km)
1 (1.4km)	N9-N10	N9-N10√	S23	S23	S28	0.15	-1.27	-2.06	1.16
2 (11.7km)	N12	N11-N13√ N24-N25 N24-N26	S15	S15	S14	0.55	0.83	-0.23	0.54
3 (22.8km)	N15-N16	N15-N16√ N19-N21	S18	S18	S18	0.52	-0.08	-0.42	0.34
4 (17.5km)	N13-N19	N13-N14 N13-N19√ N27-N28 N27-N29 N30-N31	S20	S20	S20	-0.07	0.74	0.46	0.42
5 (26.19km)	N16-N18	N16-N17 N16-N18√ N21-N23 N21-N22	S18	S18	S18	-2	-2.26	-6.52	3.59
6 (25.83km)	N21-N23	N21-N22 N21-N23√ N16-N17 N16-N18	S23	S23	S23	-1.38	-1.9	0.03	1.1
7 (10.18km)	N24	N11-N12 N11-N25 N11-N26√	S31	S31	S31	0.96	0.45	-0.16	0.52
8 (12.53km)	N24-N25	N12-N13 N24-N25√ N24-N26	S25	S25	S25	0.68	0.92	0.11	0.57
9 (19.72km)	N27-N29	N14-N15 N19-N20 N19-N21 N27-N28 N27-N29√	S29	S29	S29	-0.67	-0.94	-3.84	1.82
10 (14.16km)	N26	N12-N13 N24-N27√ N24-N30 N24-N25	S29	S29	S29	-0.84	0.68	-2.32	1.28
11 (21.72km)	N27-N28	N27-N28√ N27-N29 N16-N17 N16-N18 N19-N21	S28	S28	S28	-0.19	-0.14	-2.44	0.92
All simulation tests									1.12

*Note: Symbol(√) in the table indicate the correct section

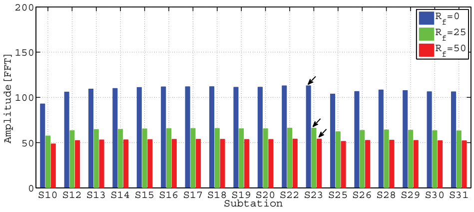

(a) 90° fault inception angle

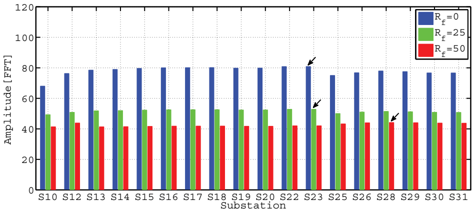

(b) 45° fault inception angle

Figure 6.34. CWT FFT amplitude of MV/LV substation for fault test number 1 with fault inception angle of 90° and 45°. The arrow indicates the substation with the highest amplitude.

From Figure 6.35, for example CWT FFT amplitude of MV/LV substations for test number 7, it can be seen that MV/LV substations number S25, S26, S28, S29, S30 and S31 estimated almost the same CWT FFT amplitude value, where substation S29 estimated the highest value. S25, S26, S28, S29, S30 and S31 is actually placed inside zone A, as shown in Figure 6.32. Therefore, if any one of these substations indicated the highest amplitude for test number 7 earth fault, we can make an assumption that the correct path should go through that zone. Similar assumption can be used for test number 8, 9, 10 and 11. The assumption also can further be used for fault located at other zone, for instant test number 3, referring to result in Figure 6.36, where it shows that CWT FFT amplitude of MV/LV substations for S15, S16, S17 and S18 have close value and fault is located at Zone B. Therefore, based from the earlier studies of the simulation results, zoning the branches gives the first indication of the correct path of fault passage in the network. However, this assumption cannot be used for exact correct path of fault location since more branches were located inside the zone. From the simulation results in Figures 6.34, 6.35, 6.36, 6.37 and 6.38, the correct path algorithm managed to identify the correct LV substation to be used as a guidance of calculating the fault distance from the measuring point towards the fault position. Figures 6.39, 6.40, 6.41, 6.42 and 6.43 show an example of schematic diagram of correct path identification for test number 2, 3, 4, 6, and 8, respectively.

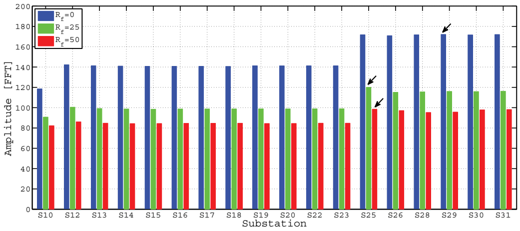

(a) Test number 7 (10.18 km)

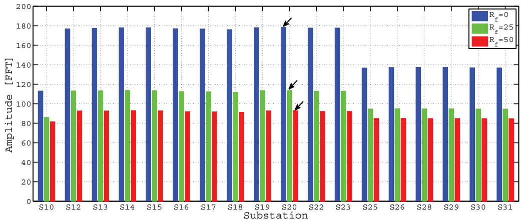

(b) Test number 2 (11.70 km)

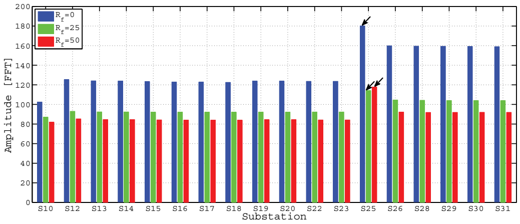

(c) Test number 8 (12.53 km)

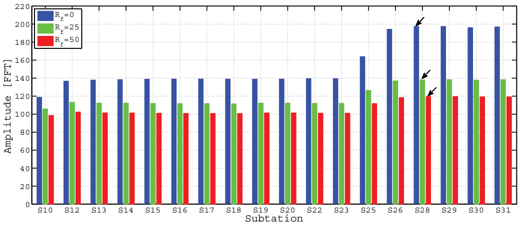

(d) Test number 10 (14.16 km)

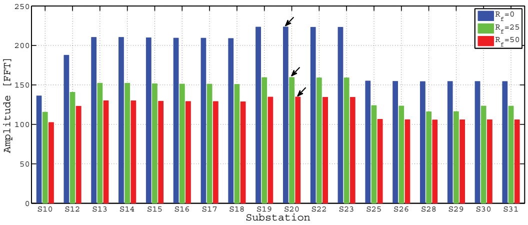

(e) Test number 4 (17.50 km)

Figure 6.35. CWT FFT amplitude of MV/LV substation for fault test number 7, 2, 8, 10 and 4 with fault inception angle of 90°. The arrow indicates the substation with the highest amplitude.

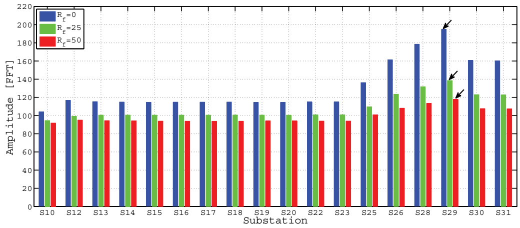

(a) Test number 9 (19.72 km)

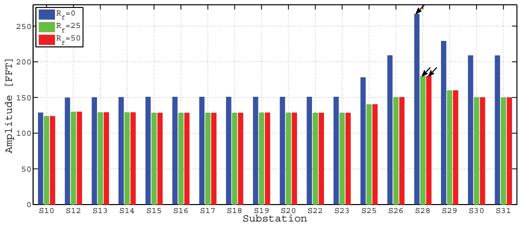

(b) Test number 11 (21.72 km)

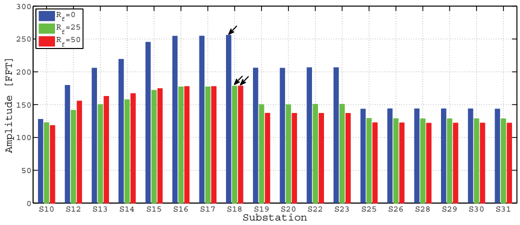

(c) Test number 3 (22.80 km)

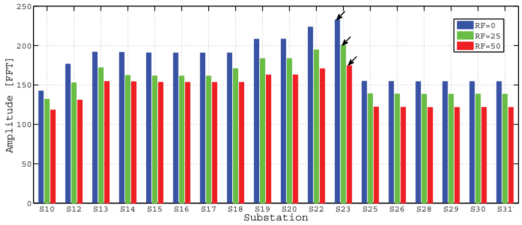

(d) Test number 6 (25.83 km)

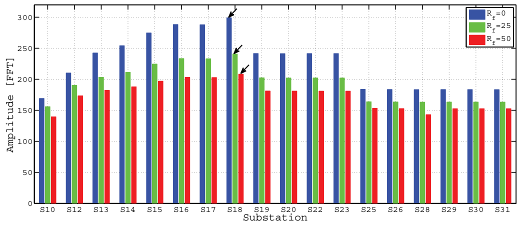

(e) Test number 5 (26.19 km)

Figure 6.36. CWT FFT amplitude of MV/LV substation for fault test number 9, 11, 3, 6 and 5 with fault inception angle of 90°. The arrow indicates the substation with the highest amplitude.

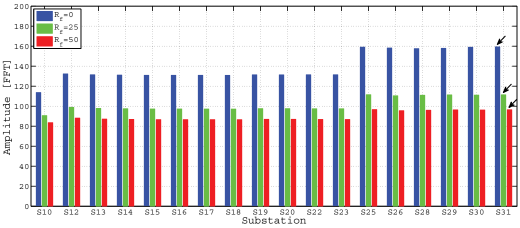

(a) Test number 7 (10.18 km)

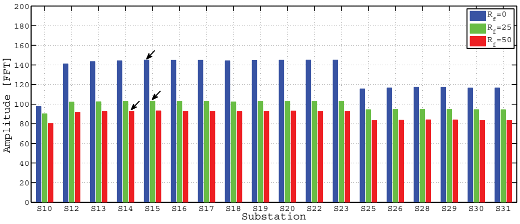

(b) Test number 2 (11.70 km)

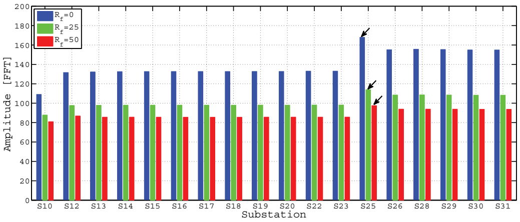

(c) Test number 8 (12.53 km)

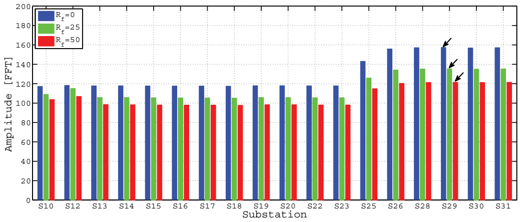

(d) Test number 10 (14.16 km)

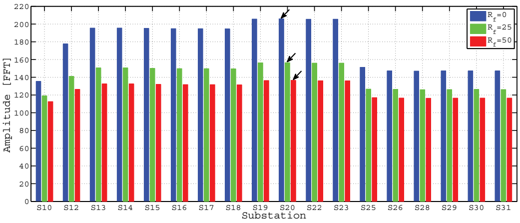

(e) Test number 4 (17.50 km)

Figure 6.37. CWT FFT amplitude of MV/LV substation for fault test number 7, 2, 8, 10 and 4 with fault inception angle of 45°. The arrow indicates the substation with the highest amplitude.

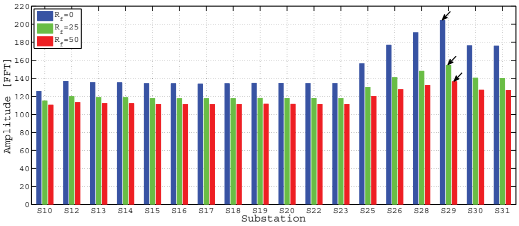

(a) Test number 9 (19.72 km)

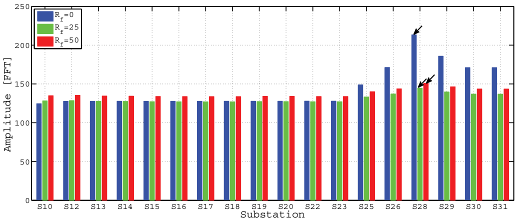

(b) Test number 11 (21.72 km)

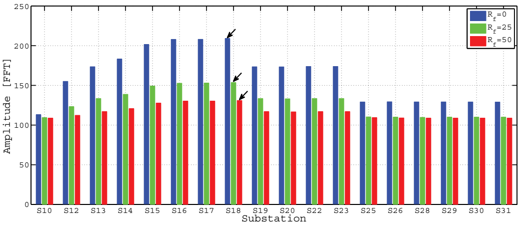

(c) Test number 3 (22.80 km)

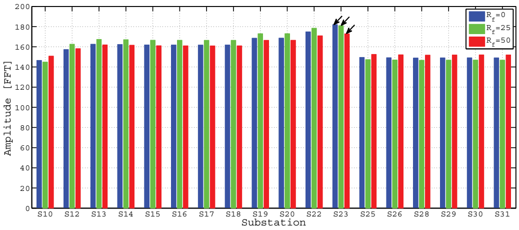

(d) Test number 6 (25.83 km)

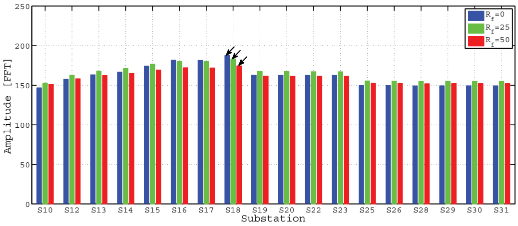

(e) Test number 5 (26.19 km)

Figure 6.38. CWT FFT amplitude of MV/LV substation for fault test number 9, 11, 3, 6 and 5 with fault inception angle of 45°. The arrow indicates the substation with the highest amplitude.

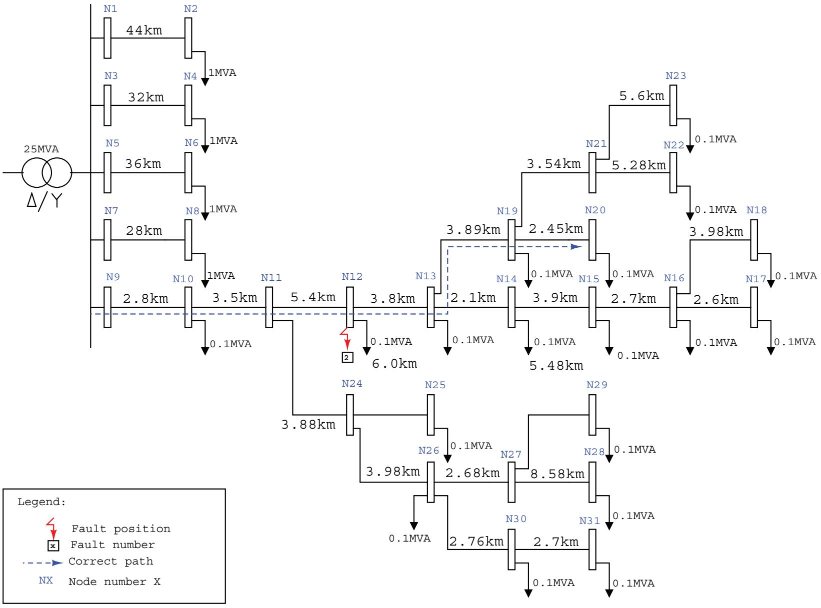

Figure 6.39. Test number 2 (11.70 km) correct path identification.

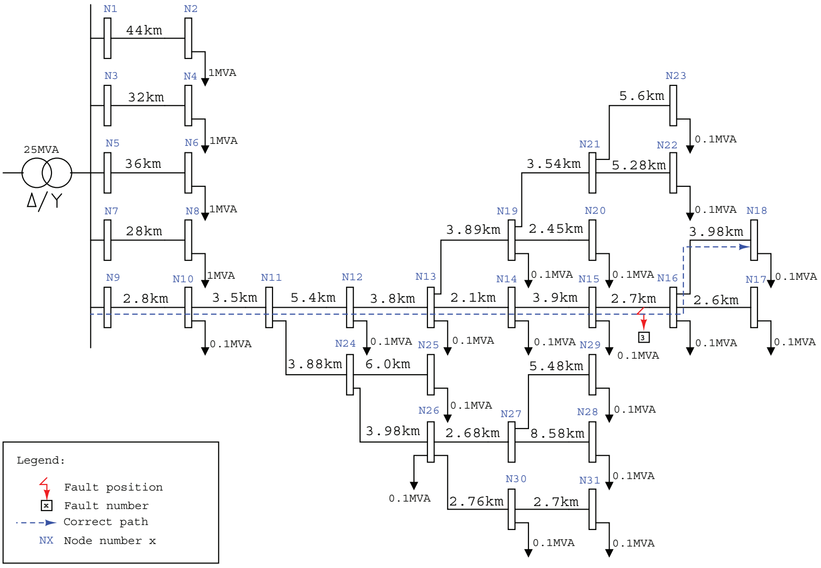

Figure 6.40. Test number 3 (22.80 km) correct path identification.

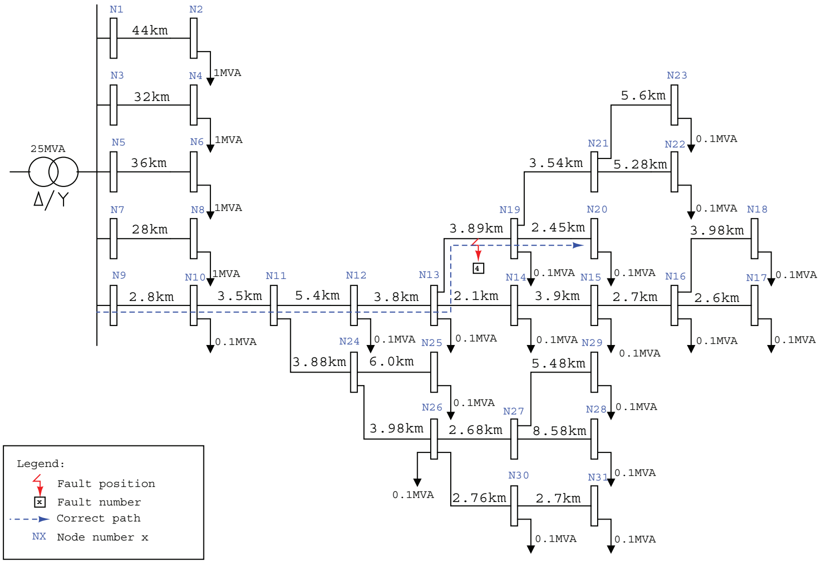

Figure 6.41. Test number 4 (17.50 km) correct path identification.

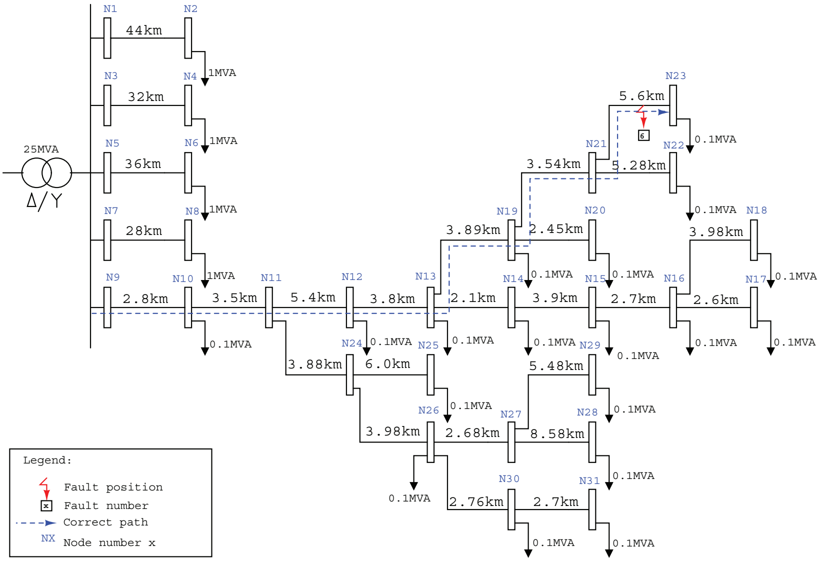

Figure 6.42. Test number 6 (25.83 km) correct path identification.

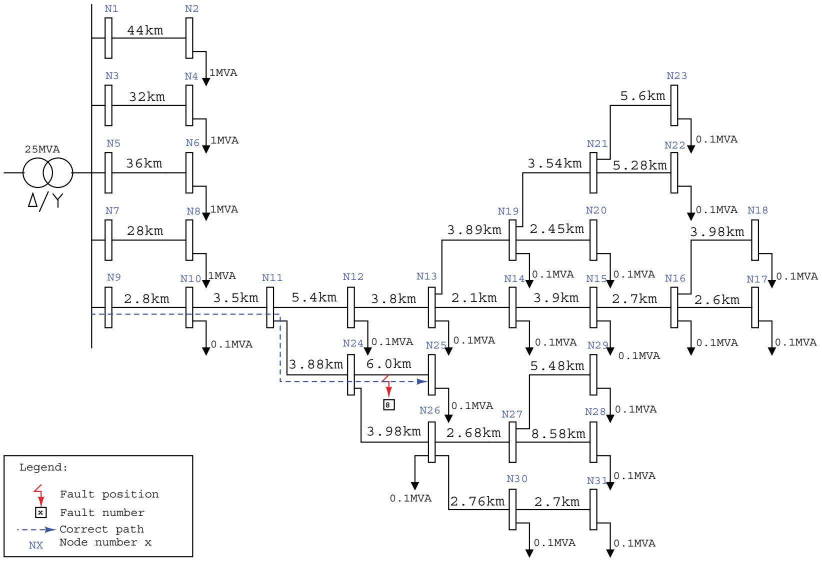

Figure 6.43. Test number 8 (12.53 km) correct path identification.

6.4 Simulated Network Model 4

In this section, we examine the performance of the methods based on multiple regression analysis (MRA), neural network (NN), GM algorithm and EM algorithm with the simulation network model 4. The description of the network model is given in a following section. Single line to earth faults were simulated in a 20 kV unearthed neutral radially operated MV distribution network. The examined algorithms used the transient voltage signal measured from the secondary side of MV/LV distribution transformer to estimate the fault distance. The aim of the simulation is to evaluate the proposed algorithms with alternative approaches as described in Chapter 5, Section 5.4.

6.4.1 Description of the simulation and the network model

A schematic diagram and ATPDraw circuit of the simulated network is illustrated in Figure 6.44 and Figure 6.45, respectively. The data of the simulation network is presented in Appendix B Table B1. The network consists of a total of 158.51 km overhead line (OH) network and 6 feeders. The length of the faulty feeder is 22.51 km. The feeder OH lines are represented with the frequency dependent JMarti line model and its ATPDraw line configuration is given in Appendix B, Figure B2.

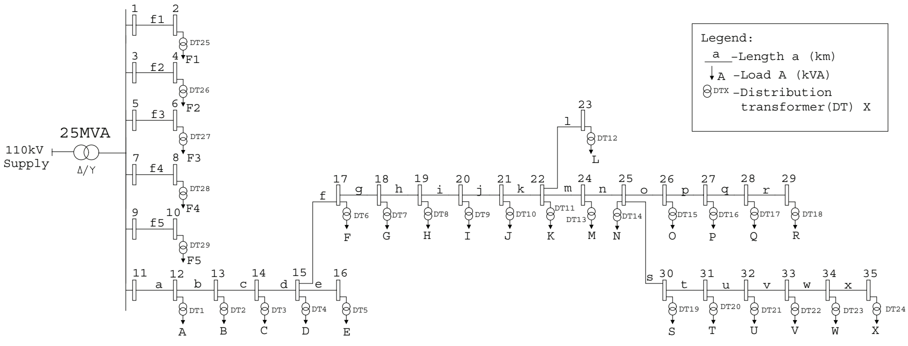

Figure 6.44. Schematic diagram of 20 kV isolated neutral MV network.

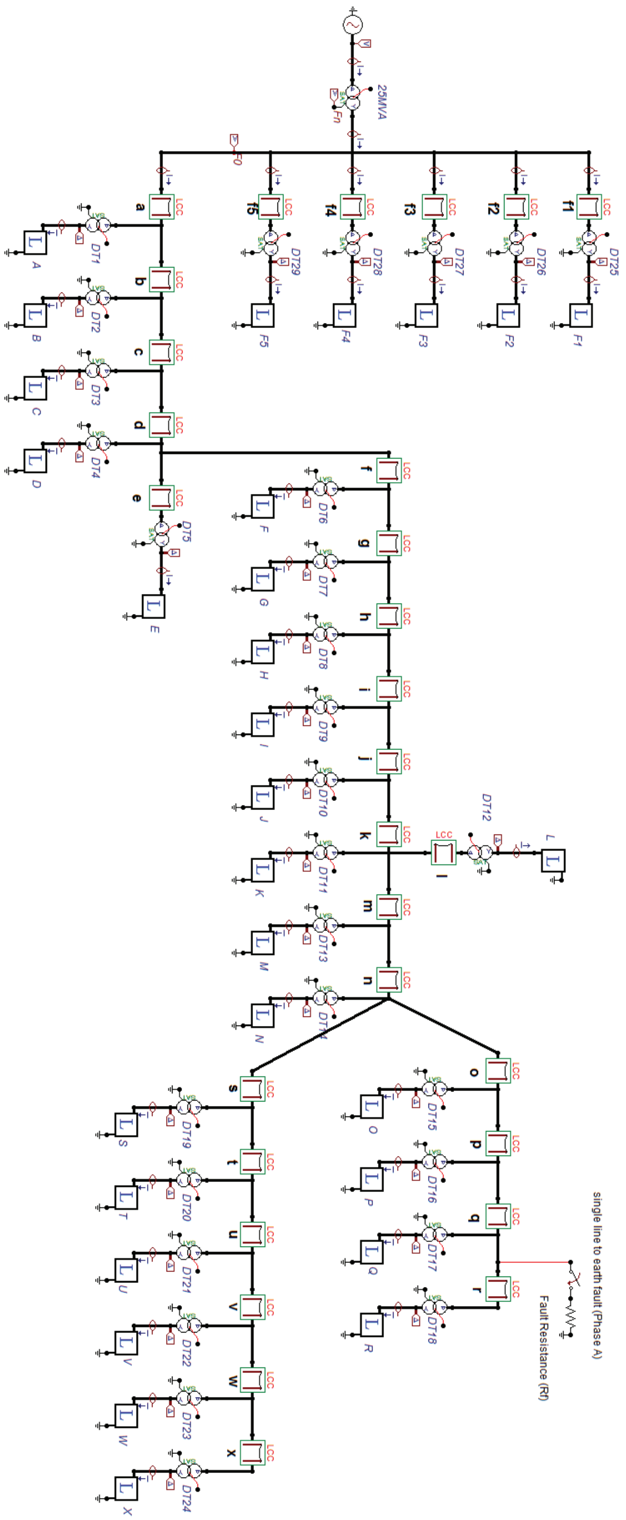

Figure 6.45. ATPdraw circuit for the simulated network model 4.

In this work, the transient signal is measured from the secondary side of MV/LV substation number 24 (DT24), as shown in Figure 6.44. In order to examine the performance of the algorithms, a large number of data sets is required. The variation of the data sets used for formula construction and testing in this work is given in Table 6.3 and Table 6.4, respectively . In Table 6.3, the network model was simulated with 5 different load conditions. For each load condition given in Table 6.3, the fault distance, fault resistance and fault inception angle were varied. Similarly in Table 6.4, the network model was simulated with load conditions as in Table 6.3 but with different fault distance.

Table 6.3. Data generation for MRA and NN formulation. Fault resistances are 0, 25 and 50 Ω. Inception angles are 90, 60 and 30 ° for load 1 and load 2. 90 and 45 ° for load 3 , 4 and 5.

Load number	1	2	3	4	5
	Number of variations				
Fault distance	13	13	2	2	2
Fault resistance	3	3	3	3	3
Inception angle	3	3	2	2	2
Total	117	117	12	12	12
Data sets	**270**				

Table 6.4. Data generation for testing the MRA and NN algorithm. Fault resistances are 0, 25 and 50 Ω. Inception angles are 90 and 45 °.

Load number	1	2	3	4	5
	Number of variations				
Fault distance	2	2	1	1	1
Fault resistance	2	2	2	2	2
Inception angle	3	3	3	3	3
Total	12	12	6	6	6
Data sets	**42**				

Using the data in Table 6.3, the formula obtained for MRA algorithm, which corresponds to Equation (5.33), is given as:

$$l = -15.4735 + 0.0052A + 1.0511S + 0.0621L \tag{6.5}$$

where dependent and independent factors are: l is fault distance, A is FFT amplitude of extracted CWT coefficient, S is scale of extracted CWT coefficient and L is total load (MVA) of the network prior to the single line to earth fault. In this work, the random error e in MRA model is neglected. In case of ANN algorithm, the formula based on Equation (5.34) constructed with 3 observed factors in this simulation can be expresses as:

$$l = ANN(A, S, L) \tag{6.6}$$

where, Equation (6.6) is a non-linear relation between l and A, S and L which cannot be expressed explicitly, therefore it has been designed as a 'knowledge base'. A detailed architecture of proposed ANN used in this section is explained in Chapter 5, Section 5.4.3. In this simulation study, the performance accuracy of MRA, NN, GM and EM algorithm has been investigated with different fault conditions as given in Table 6.4. For MRA and NN algorithms, the performance accuracy is defined by mean absolute error ($\mathrm{MAE_{MRA}}$) and ($\mathrm{MAE_{NN}}$) as expressed as in Equation (6.7) and Equation (6.8) below , while for GM and EM algorithms, the performance accuracy is defined as given in Equation (6.1) and Equation (6.3), respectively.

$$MAE_{MRA} = \frac{1}{n}\sum_{i=1}^{n}|MRA_i - l_i| = \frac{1}{n}\sum_{i=1}^{n}|\Delta MRA_i| \tag{6.7}$$

$$MAE_{NN} = \frac{1}{n}\sum_{i=1}^{n}|NN_i - l_i| = \frac{1}{n}\sum_{i=1}^{n}|\Delta NN_i| \tag{6.8}$$

where ΔMRA_i and ΔNN_i is the absolute error fault distance using MRA and NN algorithm, MRA_i and NN_i is estimated fault distance using MRA and NN algorithm, l_i is exact fault distance and n is numbers of observation of parameter error.

6.4.2 Result Analysis and Discussion

An example of the comparison of FFT amplitude of extracted CWT coefficient measured from 4 distribution transformers (DTs) is presented in Figures 6.46, 6.47 and 6.48. The results show a relationship between estimated FFT amplitude of extracted CWT coefficient and the fault distance, plotted as a linear function with a positive gradient. Clearly, the FFT amplitude of the extracted CWT coefficient is considerably increasing with an increase of fault distance. In Figures 6.46, 6.47 and 6.48, we can notice a separation of the straight line between DTs, but the separation is reduced when the fault resistance is increased and fault inception angle is decreased. In the graph, the linear functions of DT12, DT17 and DT24 have almost similar gradient, and the differences become small when high fault resistance and low inception angle were used.

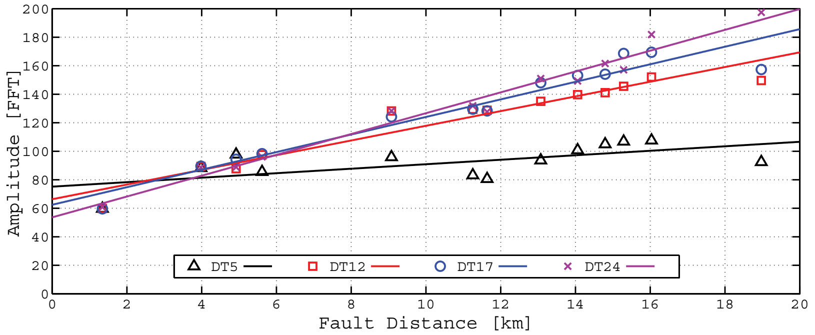

(a) R_f=0 Ω

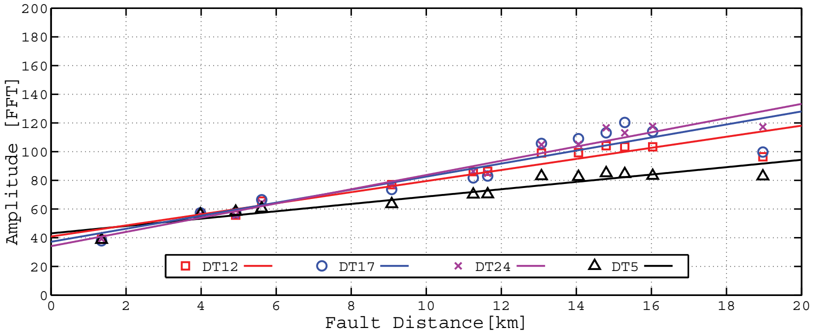

(b) R_f=25 Ω

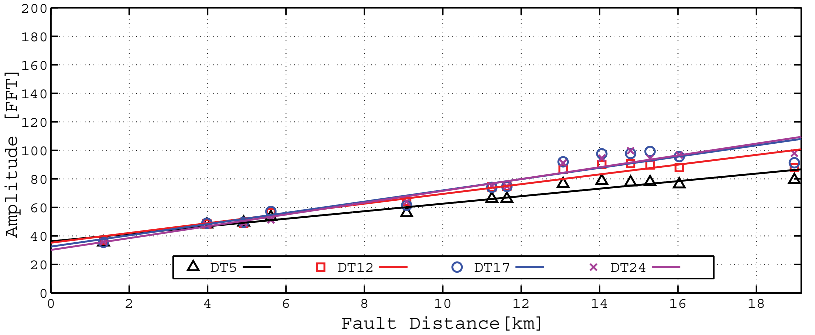

(c) R_f=50 Ω

Figure 6.46. A comparison of estimated FFT amplitudes of extracted CWT coefficient at 4 different MV/LV distribution transformers (DT). A single line to earth fault is simulated with varied fault distance and fault resistance. An inception angle of 90° is used with Load 1 condition. DT5, DT12, DT17 and DT24 represent the distribution transformer number 5, 12, 17 and 24.

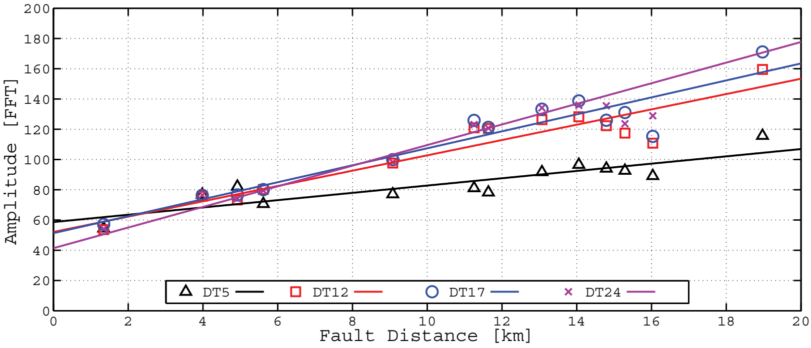

(a) R_f=0 Ω

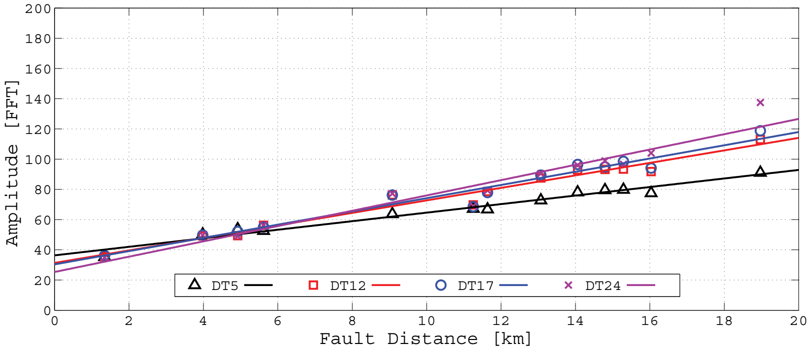

(b) R_f=25 Ω

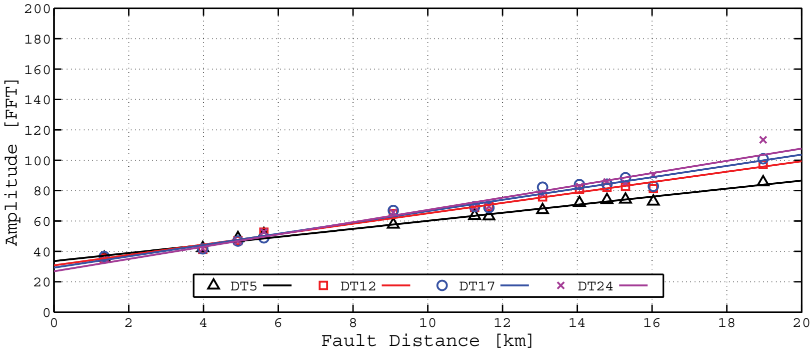

(c) R_f=50 Ω

Figure 6.47. A comparison of estimated FFT amplitudes of extracted CWT coefficient at 4 different MV/LV distribution transformers (DT). A single line to earth fault is simulated with varied fault distance and fault resistance. An inception angle of 60° is used with Load 1 condition. DT5, DT12, DT17 and DT24 represent the distribution transformer number 5, 12, 17 and 24.

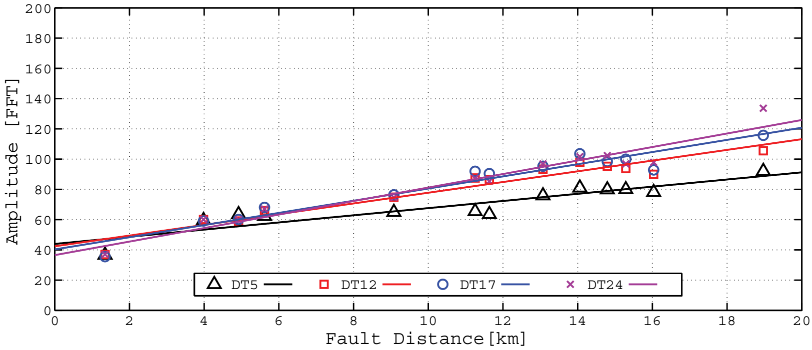

(a) R_f=0 Ω

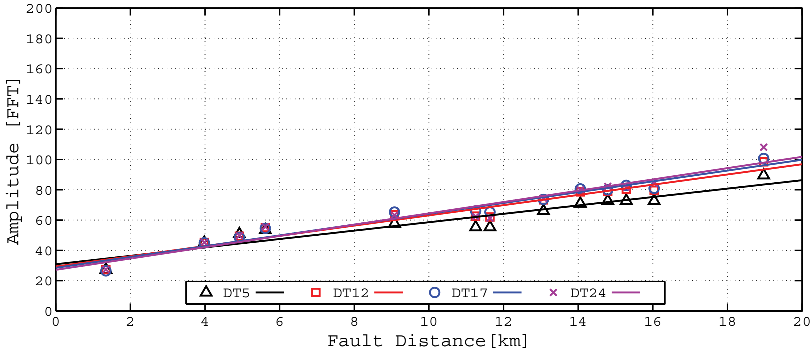

(b) R_f=25 Ω

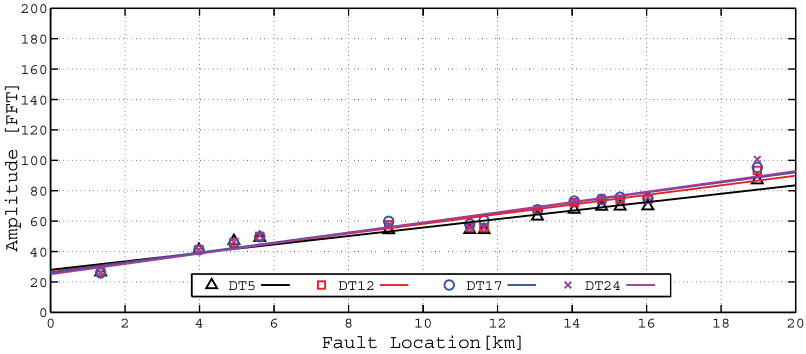

(c) R_f=50 Ω

Figure 6.48. A comparison of estimated FFT amplitudes of extracted CWT coefficient at 4 different MV/LV distribution transformers (DT). A single line to earth fault is simulated with varied fault distance and fault resistance. An inception angle of 30° is used with Load 1 condition. DT5, DT12, DT17 and DT24 represent the distribution transformer number 5, 12, 17 and 24.

Figures 6.49 and 6.50 show the results of fault location performance by using MRA and NN algorithms at fault inception angles of 90 and 45 degrees. The tabulated results can be found in Appendix C, Table C16 and C17, respectively. In comparison of calculated MAE of both algorithms, it shows that NN algorithm performed slightly better than MRA algorithm. Both algorithms have fault location error less than 1 km. It can be seen that, fault resistance and fault inception angle have a small effect on the result of the algorithms. It seems that the result of fault distance estimation from simulated earth fault at 45 degrees of fault inception angle is slightly lower than in the case of 90 degrees of fault inception angle.

Figures 6.51 and 6.52 show the results of fault location performance by using GM(GM1, GM2, GM4) algorithms at fault inception angles of 90 and 45 degrees. The tabulated results can be found in Appendix C Table C18 and C19, respectively. The results show that GM2 algorithm was a bit better than GM1 and GM4 algorithms for fault inception angle of 90 degree, with calculated MAE 0.88 km. In case of fault inception angle of 45 degree, GM1 performed slightly better than the other two GM algorithms. It is found that the results of MAE for all GM algorithms worked better at fault inception angle of 45 degrees. In case of simulated fault with inception angle of 90 degrees, the distance estimation error is highest at fault distances of 7.86 km and 13.56 km. However, in the case of fault simulated with inception angle of 45 degrees, the error of fault distance 15.59 km is the highest.

Comparison of distance estimation errors calculated using EM (EM1, EM2, EM3) algorithms with the effect of fault inception angle and fault resistance are shown in Figures 6.53 and 6.54. Calculated MAE of EM algorithms can be found in Appendix C, Table C20 and C21. From the results, with the effect of fault inception angle of 90 degrees, it shows that the MAE of EM3 algorithm is the lowest compared with the other EM algorithms. But EM2 algorithm shows a slightly better performance when fault inception angle of 45 degrees is used. EM algorithms distance estimated error is less than 2 km when simulated earth fault is not affected by the fault resistance. In overall, EM algorithms fault distance estimation error was less than 4 km.

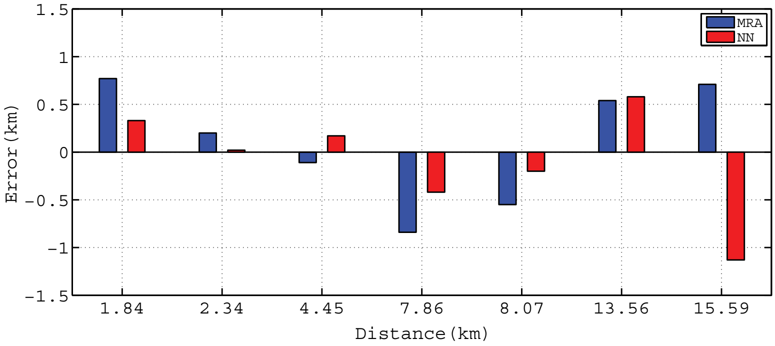

(a) R_f=0 Ω

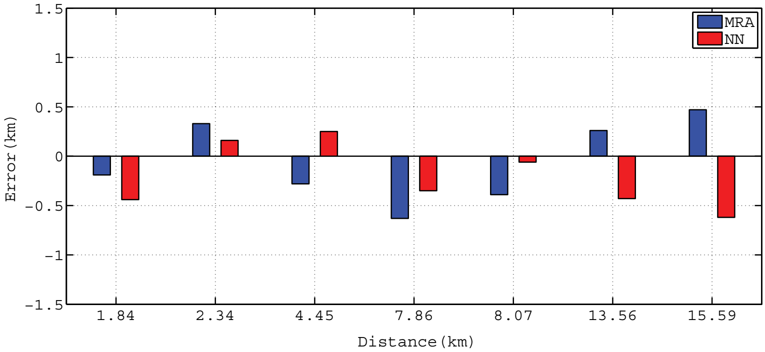

(b) R_f=25 Ω

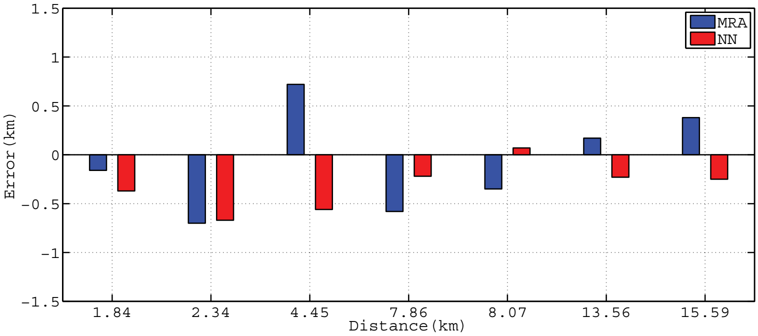

(c) R_f=50 Ω

Figure 6.49. Comparison of the distance estimate errors obtained from multiple regression (MRA) and neural network (NN) algorithm with the effect of fault resistance (R_f). Fault inception angle is 90°. MRA denotes a distance calculation error using multiple regression and NN denotes a distance calculation error using neural network algorithm.

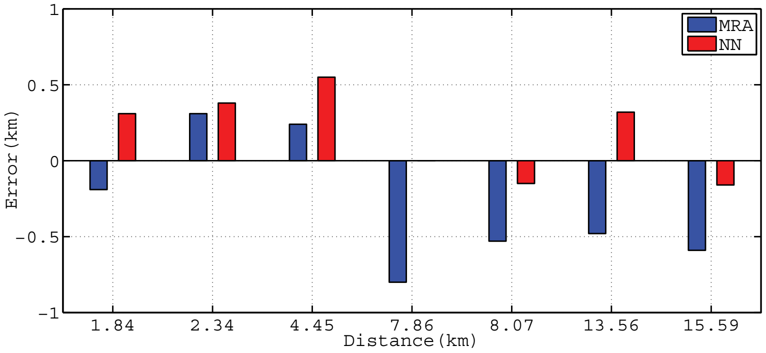

(a) R_f=0 Ω

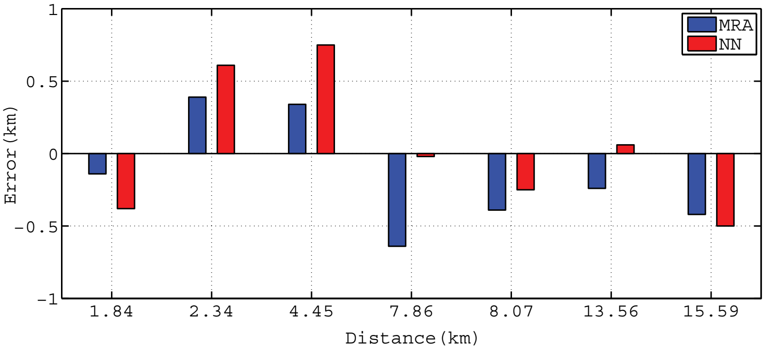

(b) R_f=25 Ω

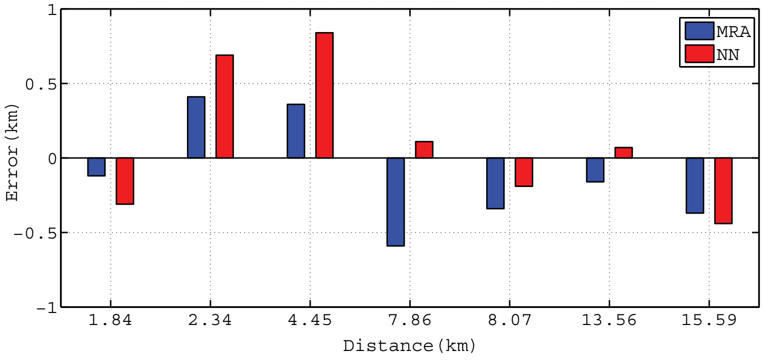

(c) R_f=50 Ω

Figure 6.50. Comparison of the distance estimate errors obtained from multiple regression (MRA) and neural network (NN) algorithm with the effect of fault resistance (R_f). Fault inception angle is 45°. MRA denotes a distance calculation error using multiple regression and NN denotes a distance calculation error using neural network algorithm.

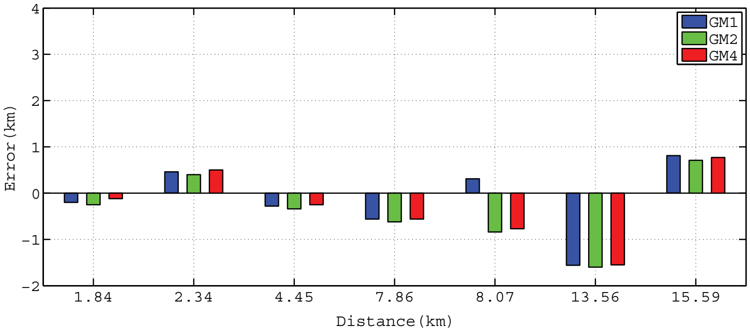

(a) R_f=0 Ω

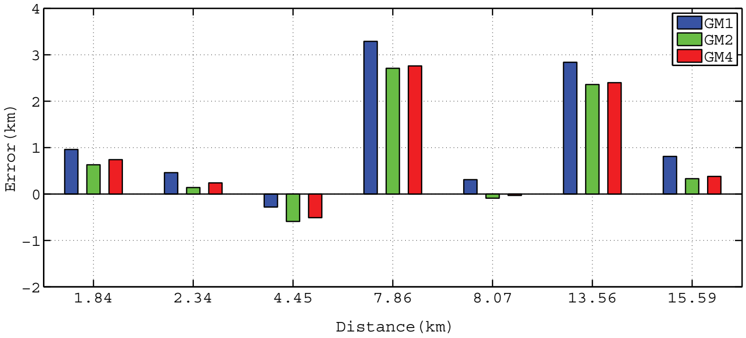

(b) R_f=25 Ω

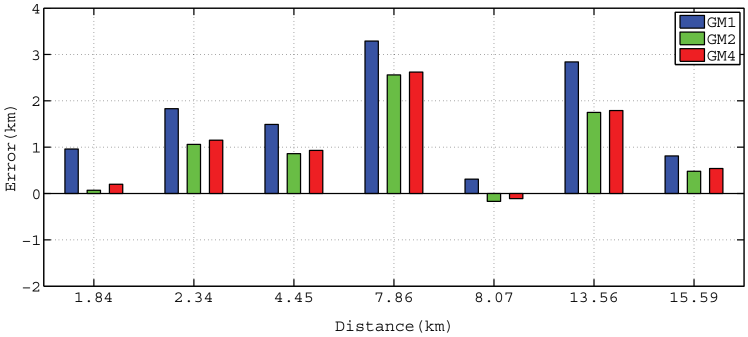

(c) R_f=50 Ω

Figure 6.51. Comparison of the distance estimate errors obtained from general model (GM1,GM2,GM4) algorithms with the effect of fault resistance (R_f). Signal measured from MV/LV substation and fault inception angle is 90°. GM1 denotes a distance calculation error using general model 1, GM2 denotes a distance calculation error using general model 2 and GM4 denotes a distance calculation error using general model 4.

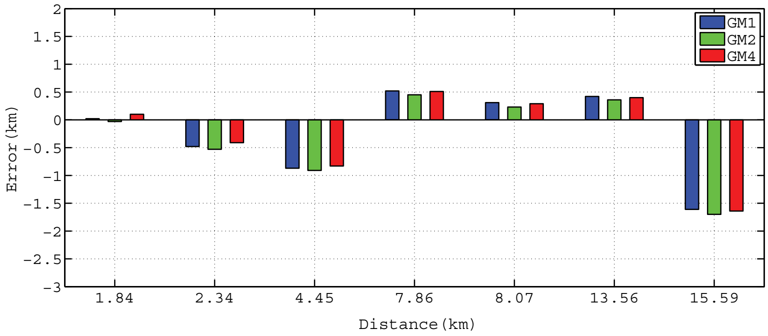

(a) R_f=0 Ω

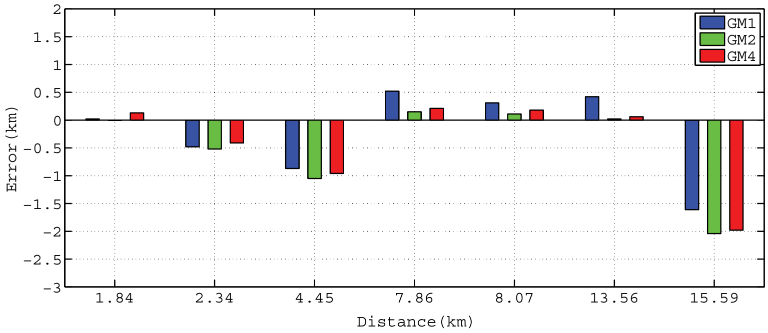

(b) R_f=25 Ω

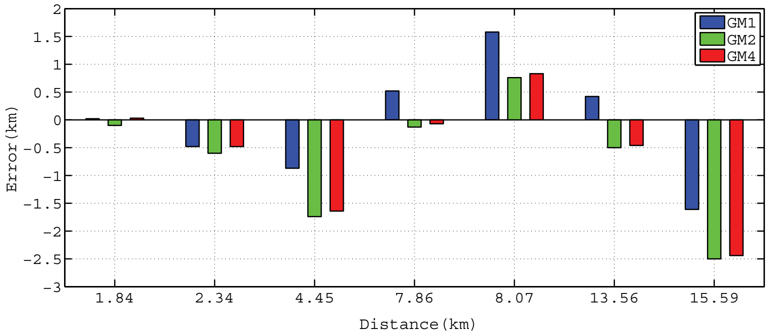

(c) R_f=50 Ω

Figure 6.52. Comparison of the distance estimate errors obtained from general model (GM1,GM2,GM4) algorithms with the effect of fault resistance (R_f). Signal measured from MV/LV substation and fault inception angle is 45°. GM1 denotes a distance calculation error using general model 1, GM2 denotes a distance calculation error using general model 2 and GM4 denotes a distance calculation error using general model 4.

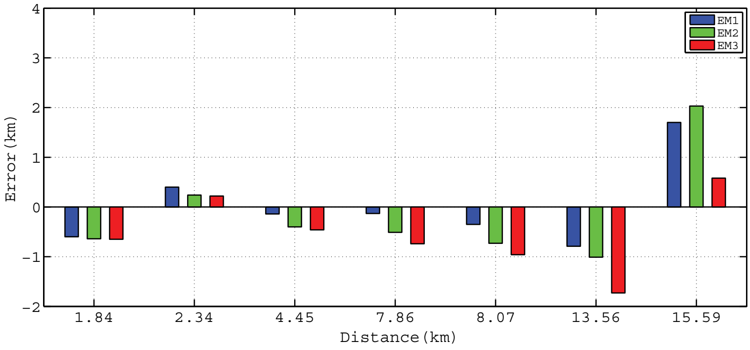

(a) R_f=0 Ω

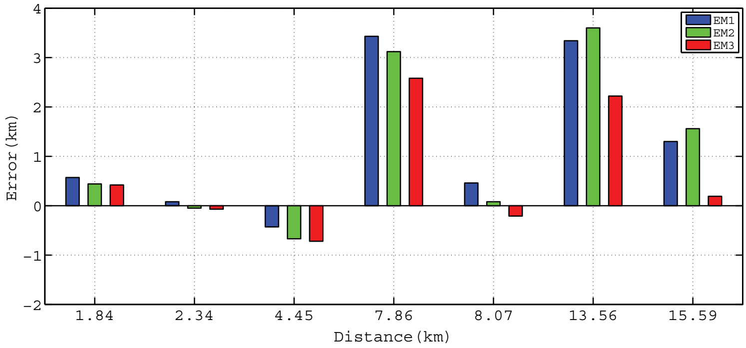

(b) R_f=25 Ω

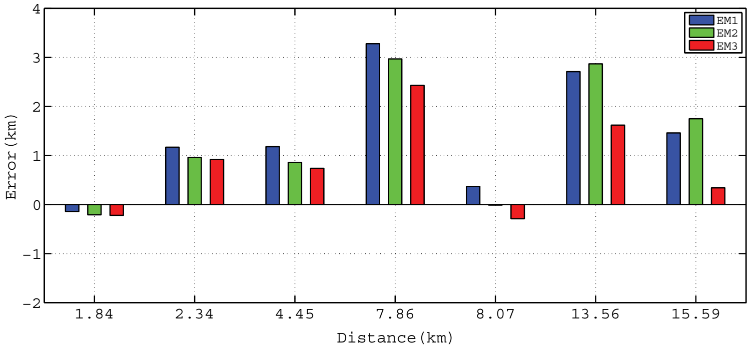

(c) R_f=50 Ω

Figure 6.53. Comparison of the distance estimate errors obtained from exact model (EM1-EM3) algorithms with the effect of fault resistance (R_f). Signal measured from MV/LV substation and fault inception angle is 90°. EM1 denotes a distance calculation error using exact model 1, EM2 denotes a distance calculation error using exact model 2 and EM3 denotes a distance calculation error using exact model 3.

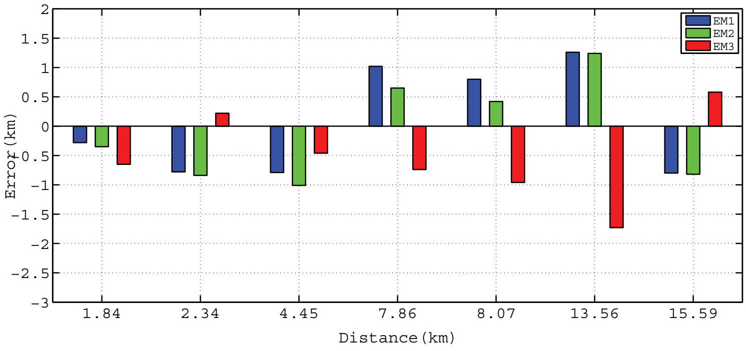

(a) R_f=0 Ω

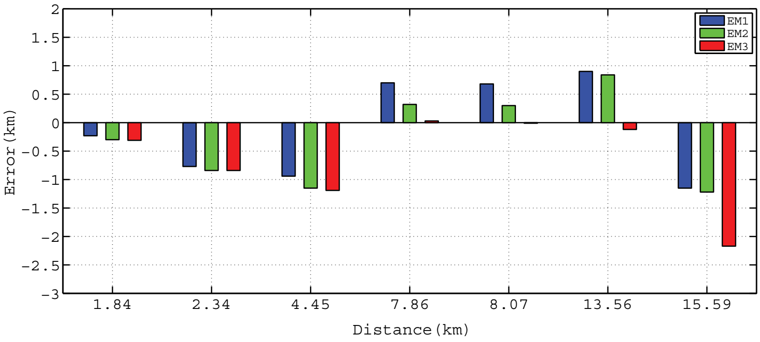

(b) R_f=25 Ω

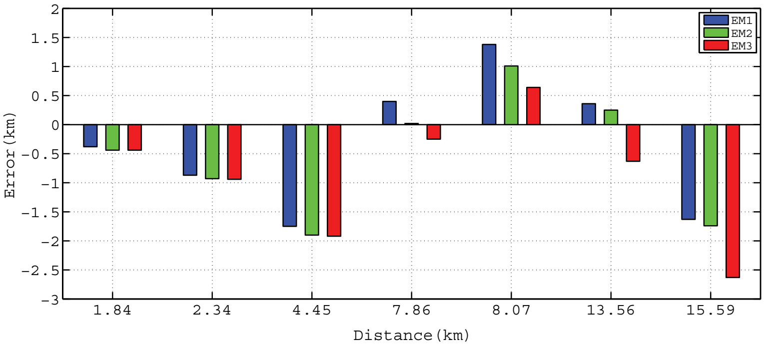

(c) R_f=50 Ω

Figure 6.54. Comparison of the distance estimate errors obtained from exact model (EM1-EM3) algorithms with the effect of fault resistance (R_f). Signal measured from MV/LV substation and fault inception angle is 45°. EM1 denotes a distance calculation error using exact model 1, EM2 denotes a distance calculation error using exact model 2 and EM3 denotes a distance calculation error using exact model 3.

In overall, the proposed algorithms are able to perform well with the use of transient signal measured from the secondary side of the MV/LV distribution transformer.

Considering the fault distance estimation results in this simulation, NN algorithm shows a better performance compared with the other algorithms. The lowest MAE calculated was 0.34 km and the highest was 1.18 km. The proposed fault location algorithms proved much more accurate in this simulation model compared with previous simulation model (model 3). We noticed that the number of branches in this simulation network model is less than in the previous simulation network model. Also, the length of the branches in simulation network model 4 is short compared with the simulation network model 3. In this section, we did not investigate the performance of WT algorithm because the transient signals that we used were measured from the secondary side of the MV/LV distribution substation transformer.

It is worth to mentioned here that, based on our experience when processing the measured transient signals, we found that it is more difficult to analyze those measured transient signals when the fault distance is far from the measuring MV/LV substation (DT24). In addition, with high resistance values and low fault inception angles, the task is more critical. This is because the damping will be increased and the transient signal is damped much faster. In the following chapter, the proposed algorithms are investigated using transient signals measured in real networks.

7. Performance Evaluation of Proposed Fault Location Algorithms Using Transients Recorded in Real Networks

Three real case studies are presented in this chapter. These consist of isolated, compensated and partially compensated neutral MV distribution networks. Two of the cases were conducted in Finnish distribution networks and the third is performed in a Czech distribution network. The recorded data is used to test selected fault location algorithms that we have proposed in Chapter 5. Due to the limitation of information of line parameters in real networks, only GM2 and CWT algorithm were tested using real recorded data.

7.1 Case study 1

In this case, an artificial single line to earth fault was carried out in a 21 kV Finnish overhead line network. The case consists of unearthed and compensated neutral MV distribution networks in Vaasan Sähkö Oy. The data was recorded with sampling frequency of 20 kHz. In this case study, CWT and GM2 algorithms were used to estimate the fault distance. The procedures used to estimate the fault distance based on the measured transient signals are explained in Chapter 5 of this dissertation. The performance accuracy of the selected algorithms was measured using MAE as given in Equation (6.1) and Equation (6.4).

7.1.1 Description of Real Network Case 1

The parameters of the networks used in this analysis are given in Table 7.1. The network diagrams of the field tests are shown in Figures 7.1, 7.2 and 7.3.

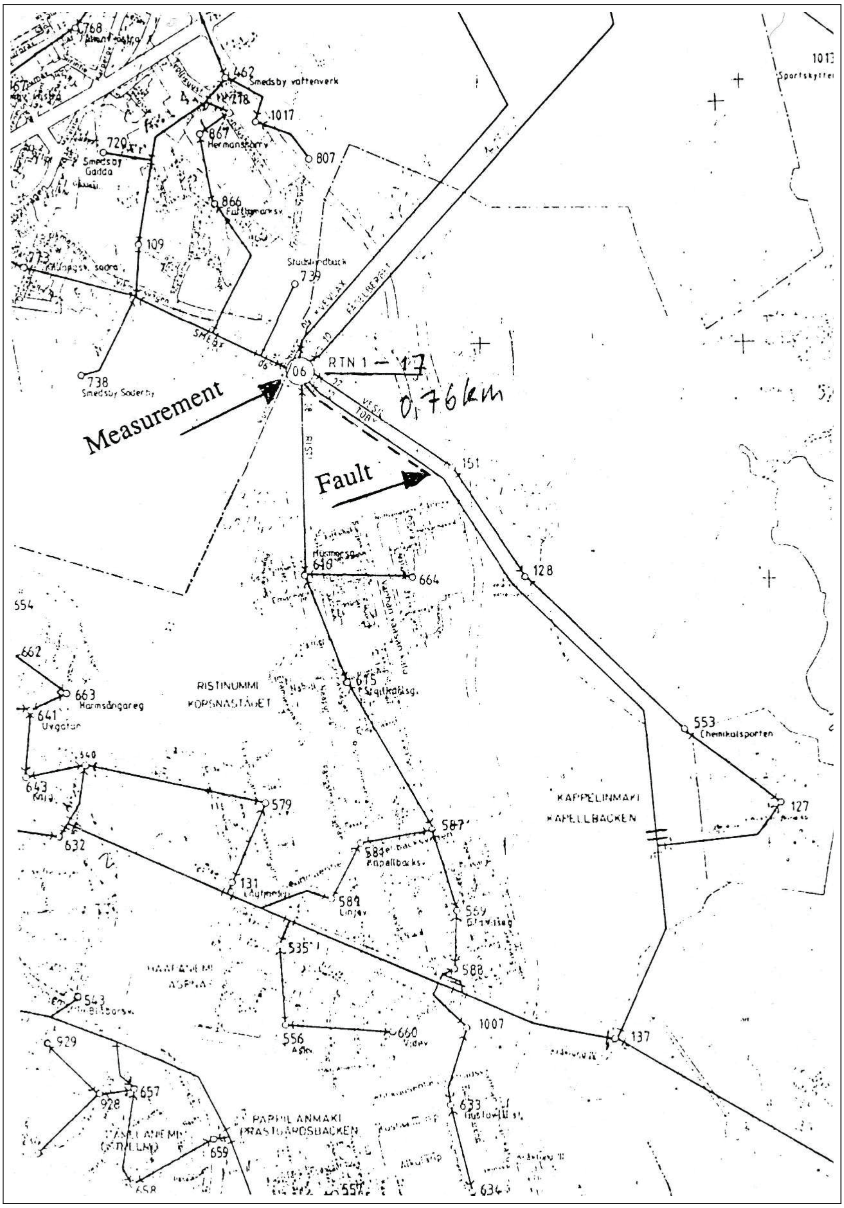

Figure 7.1. Compensated neutral network test diagram for test 1-2, 0.76 km [40].

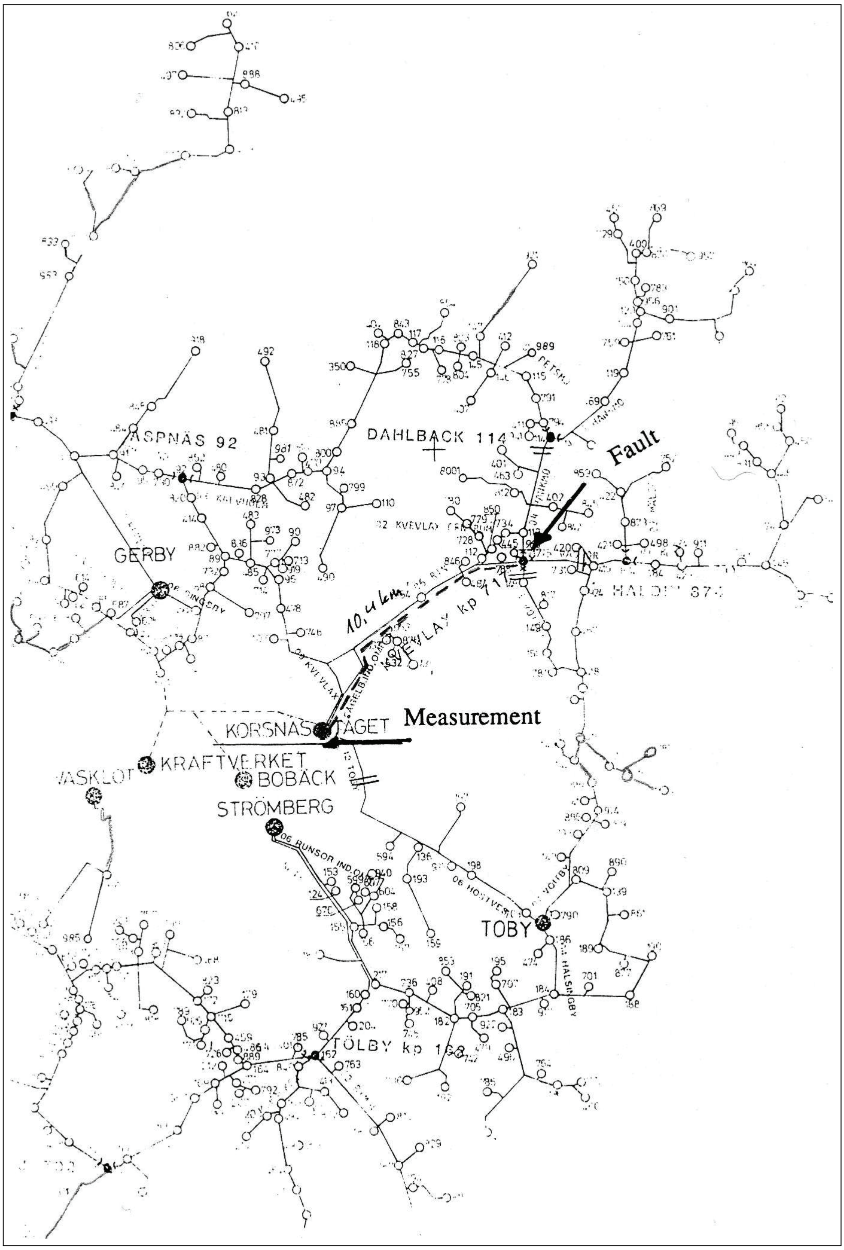

Figure 7.2. Compensated neutral network test diagram for test 3-4, 10.40 km [40].

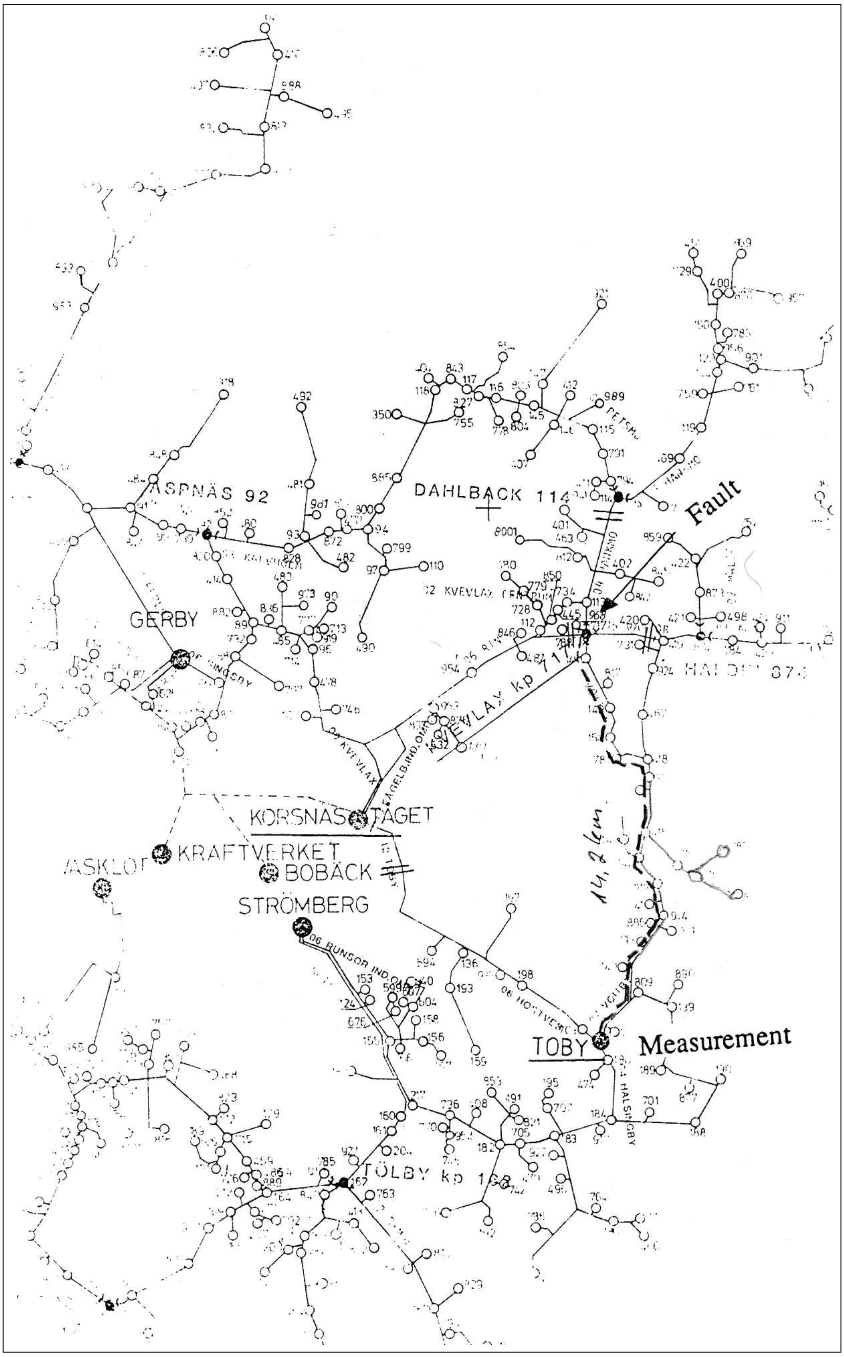

Figure 7.3. Isolated neutral network test diagram for test 5-8, 14.20 km [40].

Table 7.1. Case 1 network parameters [40].

Test number	1-2	3-4	5-8
Network	Compensated neutral	Compensated neutral	Isolated neutral
Voltage	110/21 kV	110/21 kV	110/21 kV
Transformer	25 MVA 10%	25 MVA 10%	16 MVA 10%
Arc supression	90 A	90 A	
Substation load	12 MW	12 MW	2.7 MW
$L_{lp,n}$	1 mH/km	1 mH/km	1 mH/km
L_{l0}	5 mH/km	5 mH/km	5 mH/km
C_p	10.1 μF	8.5 μF	2.1 μF
C_0	9.7 μF	8.1 μF	1.2 μF
Earth resistance	0.32 Ω	0.32 Ω	0.20 Ω
Soil resistivity	1000 Ωm	1000 Ωm	1000 Ωm

7.1.2 Result Analysis and Discussion

The recorded fault voltages and currents are shown in Figures 7.4, 7.5, 7.6 and 7.7. As an example of pre processing used in this work, one single phase to ground fault from test number 1 is presented in Figure 7.8 and the output from fault distances algorithm based on CWT is depicted in Figure 7.9. The results of estimated fault distance using CWT algorithm for test number 1, 3, 5 and 7 are depicted in Figure 7.10.

The summary of the results are given in Table 7.2. In order to compare the performance accuracy of both algorithms, we used similar information and parameters determined from the measured earth fault transient signals for both algorithms. Based on the results, CWT algorithm produced good results compared to GM2 algorithm. GM2 algorithm performed well in compensated neutral network compared to its result in isolated neutral network. The MAE calculated was 0.52 km. In case of GM2 algorithm, the MAE calculated was 3.80 km. GM2 algorithm gave good results when the fault distance is short and close to the measuring point and when the effect of fault resistance was low. Unfortunately, when fault distance is far from the measuring point, the fault distance estimation error is high. The result is of no use if the fault distance and fault resistance is to high.

Table 7.2. Calculation results using CWT and GM2 algorithm.

Test number	l	R_f	CWT	$\triangle$CWT	GM2	$\triangle$GM2
1	0.76	0	0.38	-0.38	0.10	-0.66
2	0.76	0	0.17	-0.59	0.10	-0.66
3	10.40	0	9.92	-0.48	10.00	-0.40
4	10.40	0	9.81	-0.59	9.90	-0.50
5	14.20	0	13.57	-0.63	16.70	2.50
6	14.20	0	14.77	0.57	21.20	7.00
7	14.20	50	14.12	-0.08	20.63	6.43
8	14.20	50	13.39	-0.81	26.46	12.26
MAE				**0.52**		**3.80**

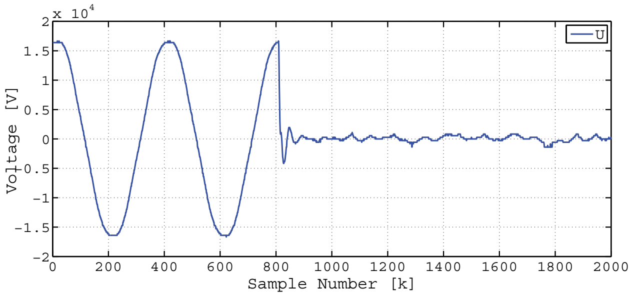

(a) Test number 1 phase voltage

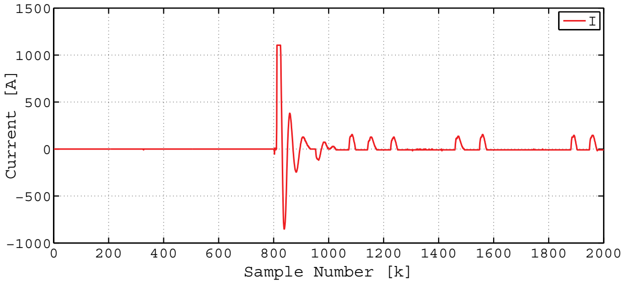

(b) Test number 1 phase current

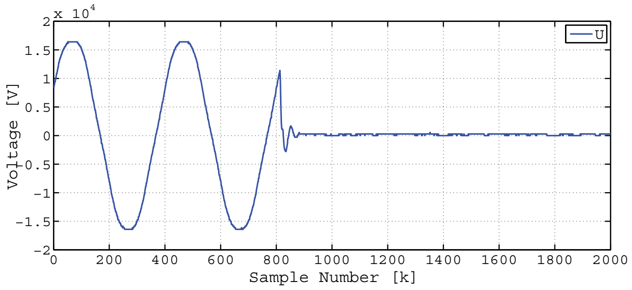

(c) Test number 2 phase voltage

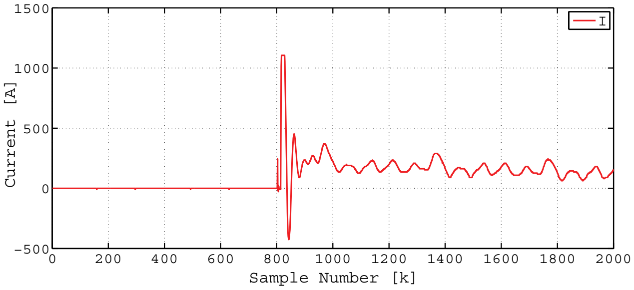

(d) Test number 2 phase current

Figure 7.4. Recorded signals of single line to earth fault at 0.46 km.

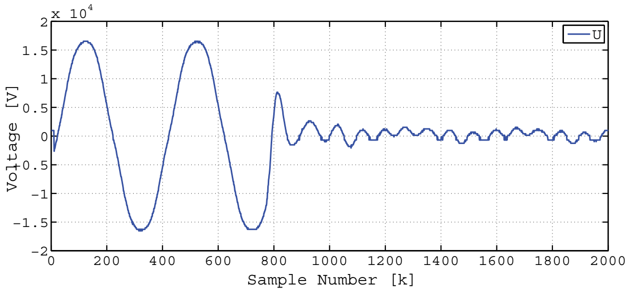

(a) Test number 3 phase voltage

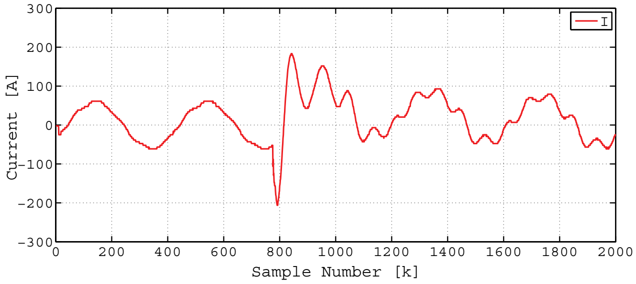

(b) test number 3 phase current

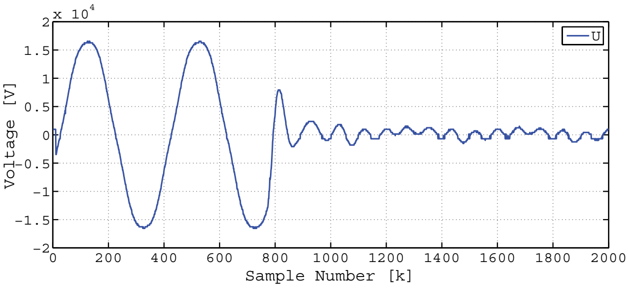

(c) Test number 4 phase voltage

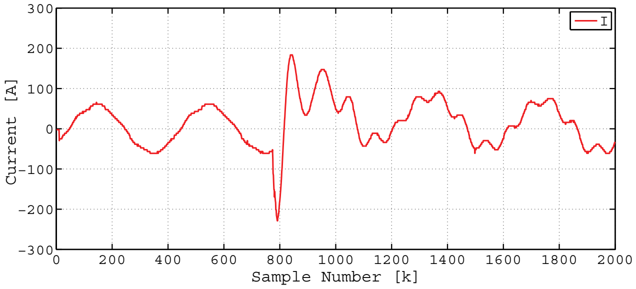

(d) Test number 4 phase current

Figure 7.5. Recorded signals of single line to earth at 10.40 km.

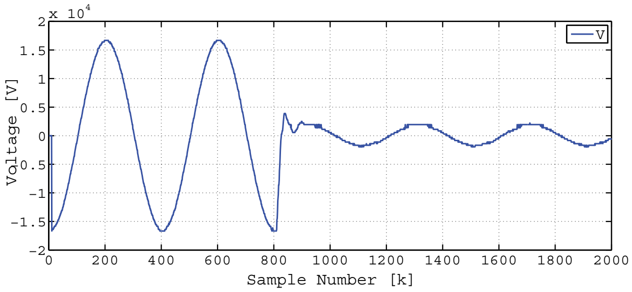

(a) Test number 5 phase voltage

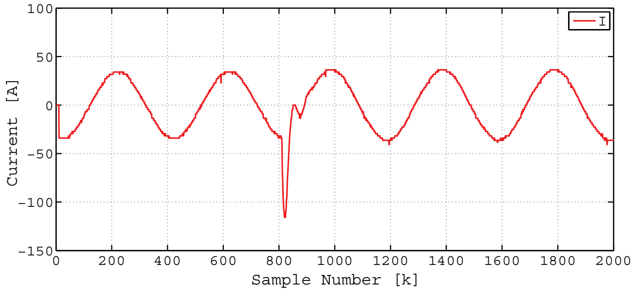

(b) Test number 5 phase current

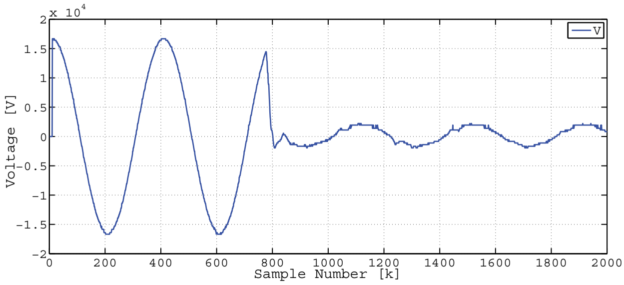

(c) Test number 6 phase voltage

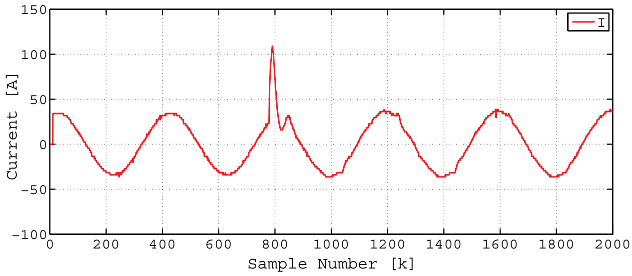

(d) Test number 6 phase current

Figure 7.6. Recorded signals of single line to earth fault at 14.20 km. Test number 5 and 6.

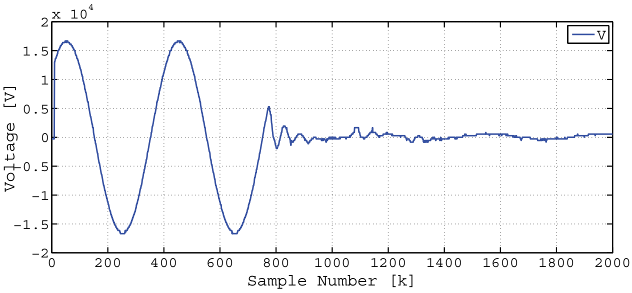

(a) Test number 7 phase voltage

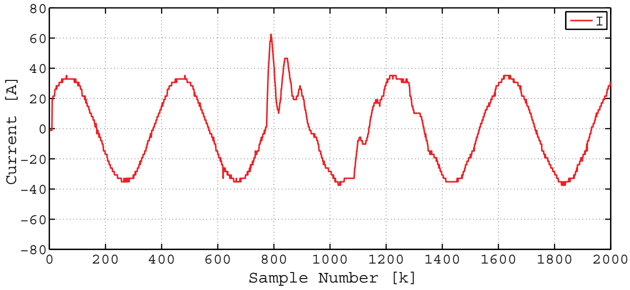

(b) Test number 7 phase current

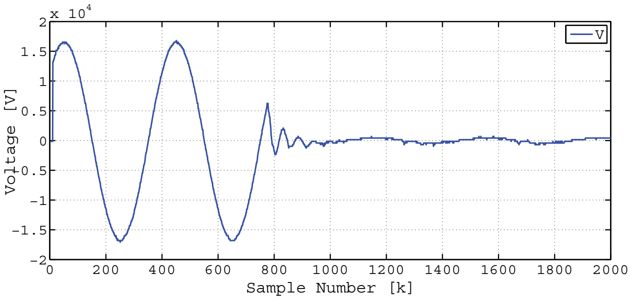

(c) Test number 8 phase voltage

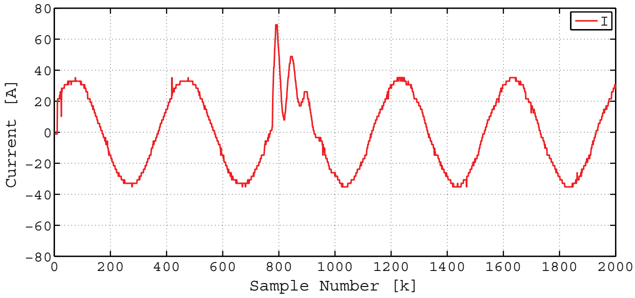

(d) Test number 8 phase current

Figure 7.7. Recorded signals of single line to earth fault at 14.20 km. Test number 7 and 8.

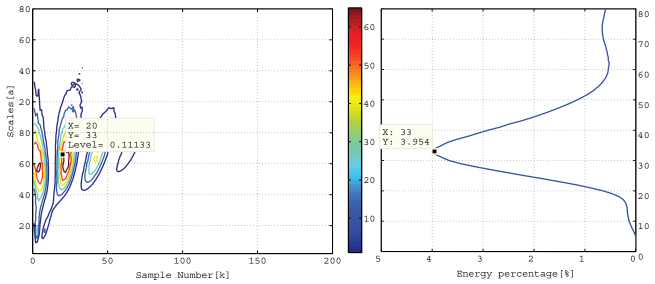

(a) Voltage CWT scalogram (left) and Scale-dependent energy percentage distribution(right)

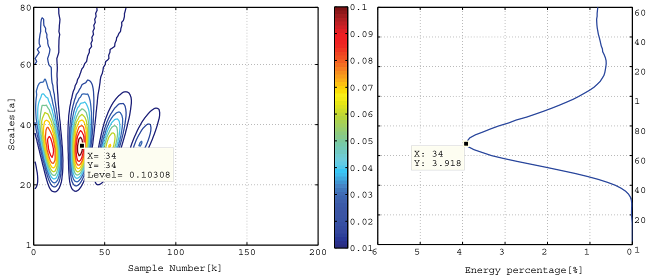

(b) Current CWT scalogram (left) and Scale-dependent energy percentage distribution(right)

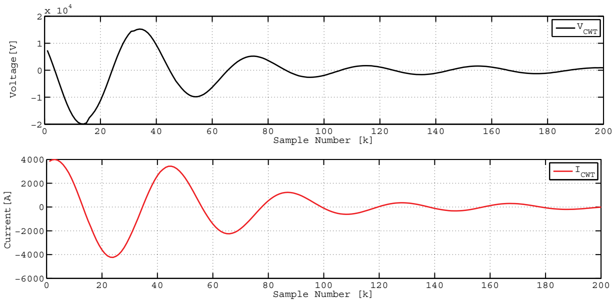

(c) Extracted CWT coefficients

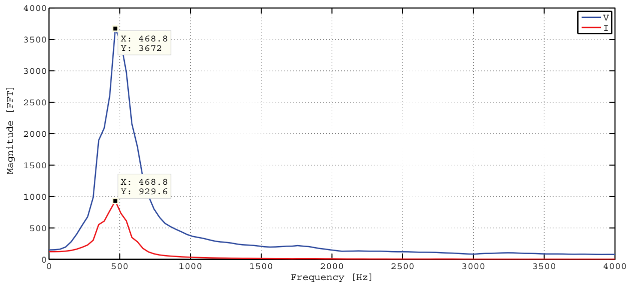

(d) Voltage and Current FFT frequency spectrum of extracted CWT

Figure 7.8. Example of output from pre-processing of test number 1 (0.76 km) transient signal using CWT analysis.

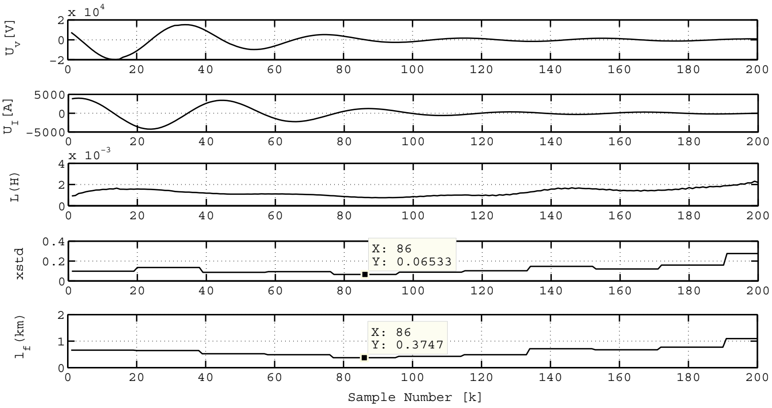

Figure 7.9. Example of output from fault distances algorithm based on CWT for test number 1.

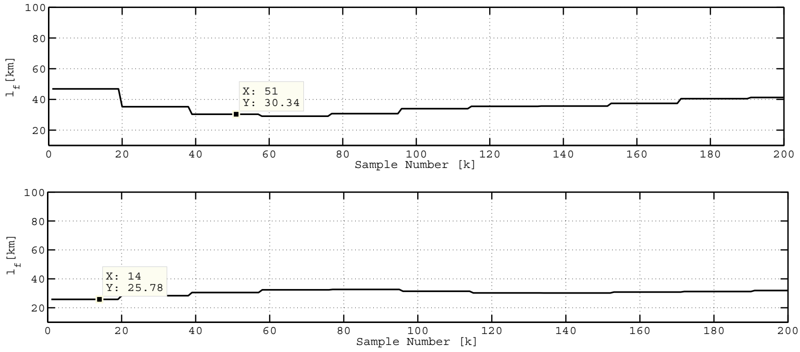

(a) Test number 1 (above) and test number 3 (below)

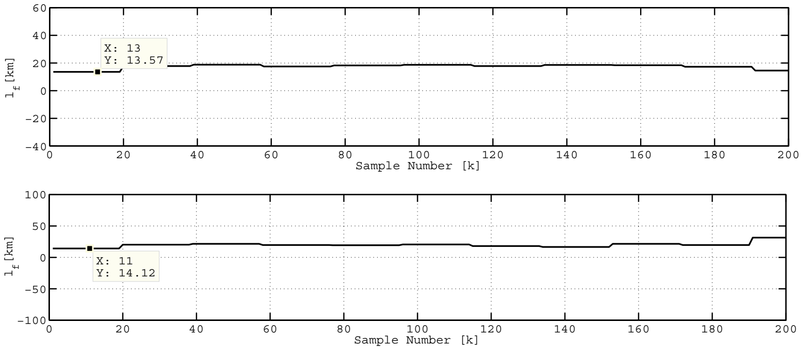

(b) Test number 5 (above) and test number 7 (below)

Figure 7.10. Results of fault distance estimation (l_f) using CWT algorithm.

7.2 Case study 2

In this section an artificial single line to earth fault was carried out in a 22 kV Finnish overhead line network. The field test was recorded in Lounais-Suomen Sähkö Oy. The network is partially compensated neutral network. The data was recorded with sampling frequency of 20 kHz. In this case study, CWT and GM2 algorithms were used to estimate the fault distance. The procedure used to estimate the fault distance was based on the measured transient signal as is explained in Chapter 5 of this dissertation. The performance accuracy of the selected algorithms were measured using MAE as given in Equation (6.1) and Equation (6.4).

7.2.1 Description of Real Network Case 2

The parameters of the network are given in Table 7.3. The network diagrams of the field test are shown in Figure 7.11.

7.2.2 Result Analysis and Discussion

The recorded fault voltages and currents are shown in Figures 7.12, 7.13, 7.14 and 7.15. Figure 7.16 and 7.17 shows an example of output from pre-processing of test number 4 transient signal using CWT analysis and Hilbert transformation. The results of estimated fault distance using CWT algorithm for test number 1, 3, 6 and 8 is depicted in Figure 7.18. The summary of the results are given in Table 7.4. By comparison of MAE for both algorithms, CWT algorithm performed slightly better compared to GM2 algorithm. There are 2 results showing unacceptable accuracy performed by GM2 algorithm where MAE increased significantly. The lowest fault estimation error was 0.1 km and the highest was 12.40 km. In this case GM2 algorithm gave good results when the fault distance is far from the measuring point. In comparison with the result of GM2 algorithm in previous case study for fault distance far from the measuring point, it seems that the algorithm has performed well in compensated neutral network compared to its result in isolated neutral network.

Table 7.3. Case 2 network parameters [40].

Test number	1-5	6-8
Network	Partially compensated	
Voltage	110/22 kV	
Transformer	25 MVA 10.6%	
Arc supression	8.5 A	
Compensation capacitor	1800 kVAr	
Substation load	5.3 MW	6.9 MW
$L_{lp,n}$	1.1 mH/km	
L_0	4.36 mH/km	
C_p	18.7 μF	21.5 μF
C_0	2.5 μF	3.6 μF
Earth resistance	0.6 Ω	
Ground resistivity	200 Ωm	

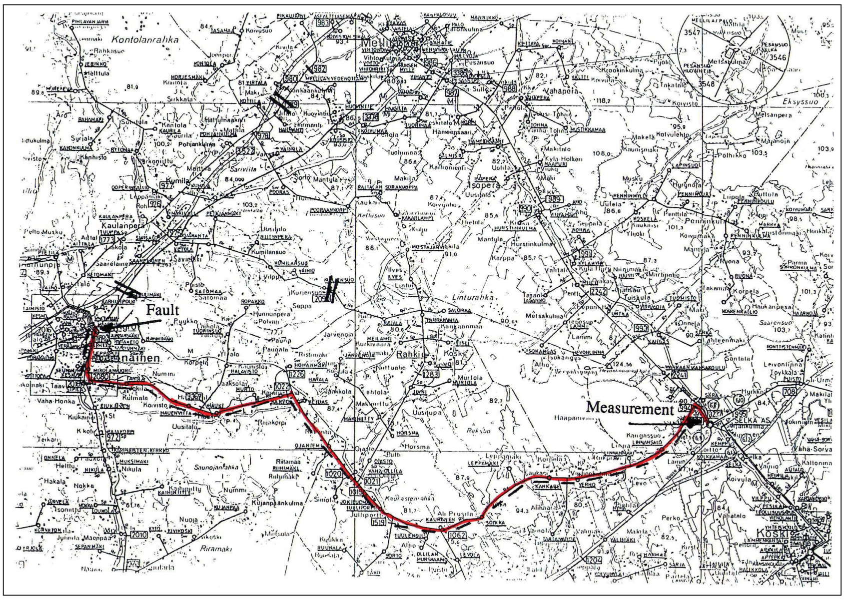

(a) Network diagram for test 1-5, 25.40 km

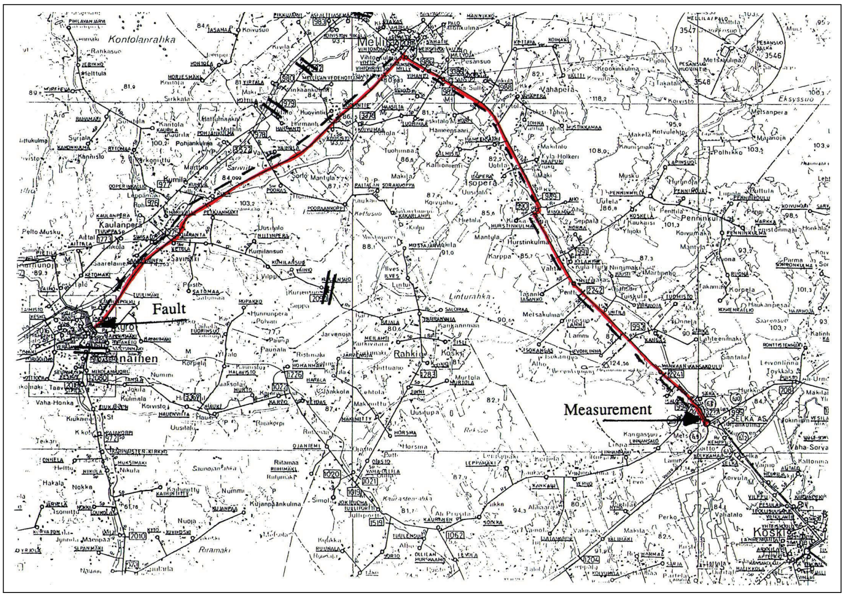

(b) Network diagram for test 6-8, 36.00 km

Figure 7.11. Lounais-Suomen Sahko OY network test diagram [40].

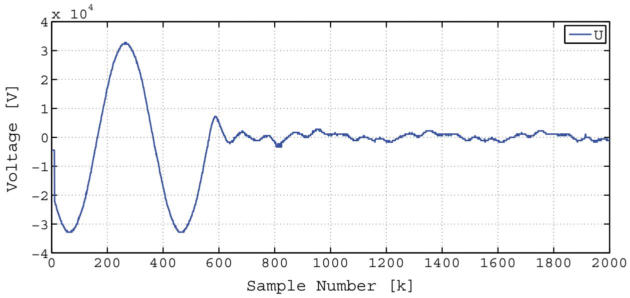

(a) Test number 1 phase voltage

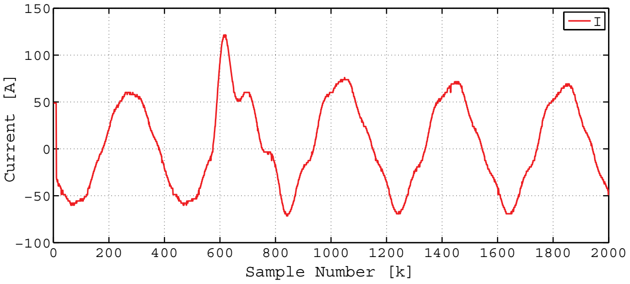

(b) Test number 1 phase current

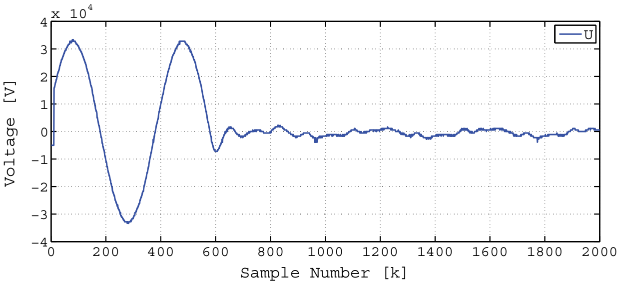

(c) Test number 2 phase voltage

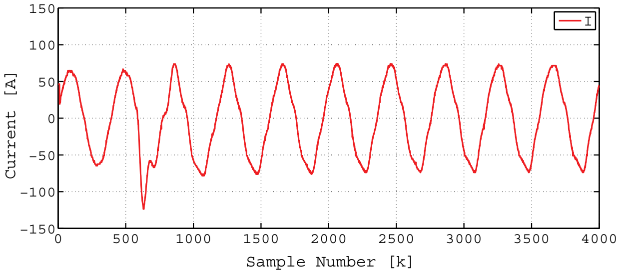

(d) Test number 2 phase current

Figure 7.12. Recorded signals of single line to earth fault at 25.40 km. Test number 1 and 2.

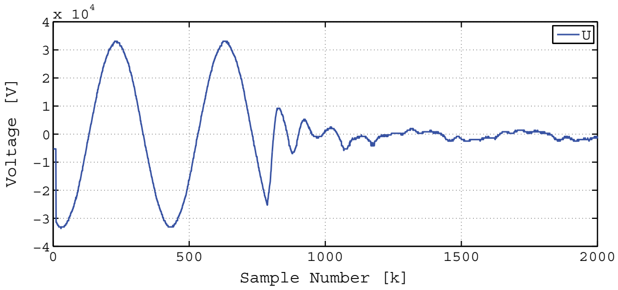

(a) Test number 3 phase voltage

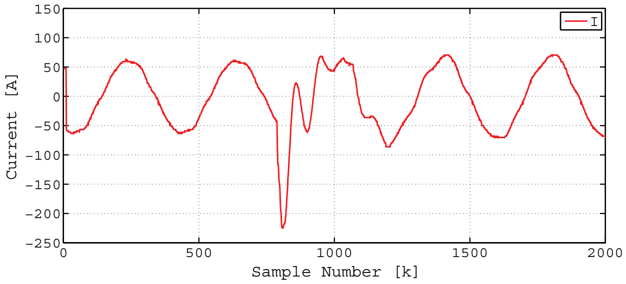

(b) Test number 3 phase current

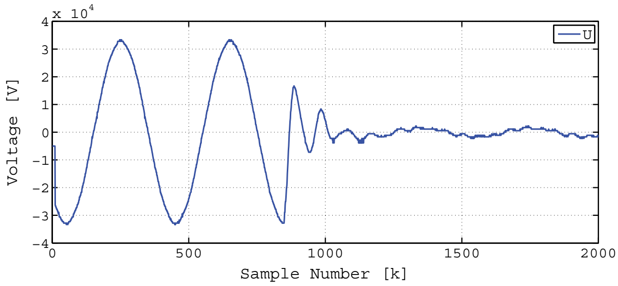

(c) Test number 4 phase voltage

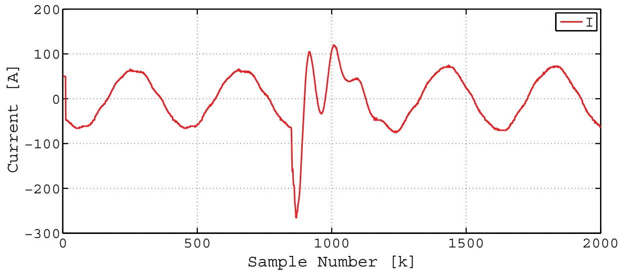

(d) Test number 4 phase current

Figure 7.13. Recorded signals of single line to earth fault at 25.40 km. Test number 3 and 4.

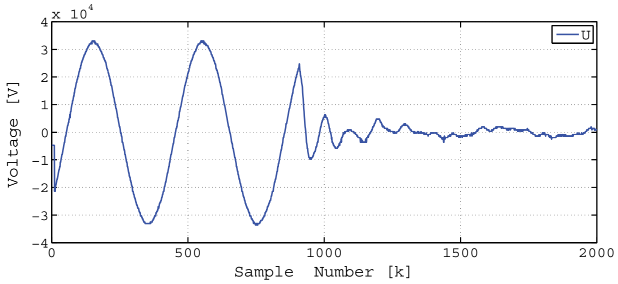

(a) Test number 5 phase voltage

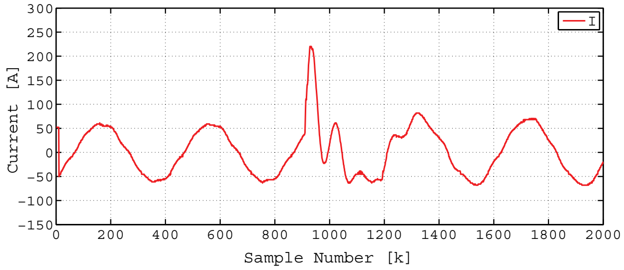

(b) test number 5 phase current

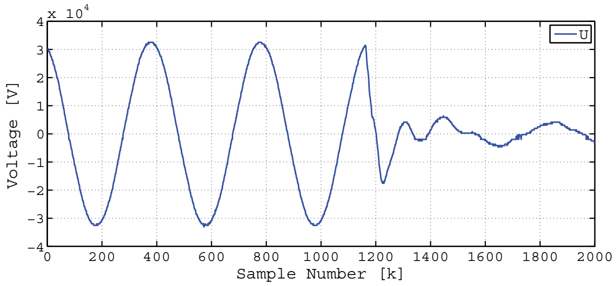

(c) Test number 6 phase voltage

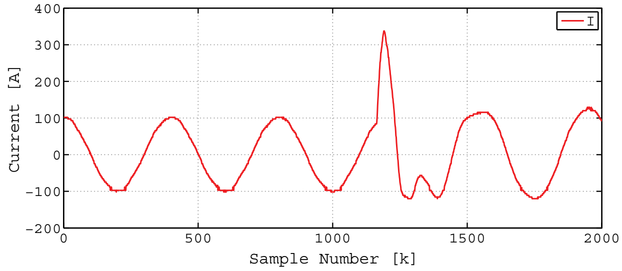

(d) Test number 6 phase current

Figure 7.14. Recorded signals of single line to earth fault at 25.40 km (test number 5) and 36.0 km (test number 6).

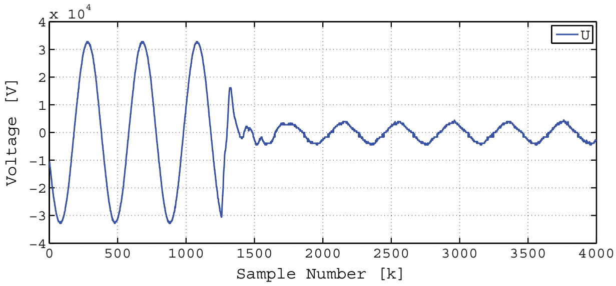

(a) Test number 7 phase voltage

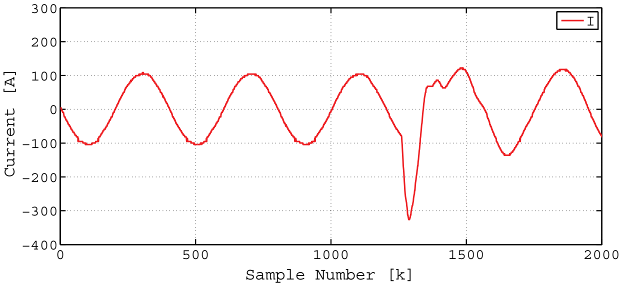

(b) Test number 7 phase current

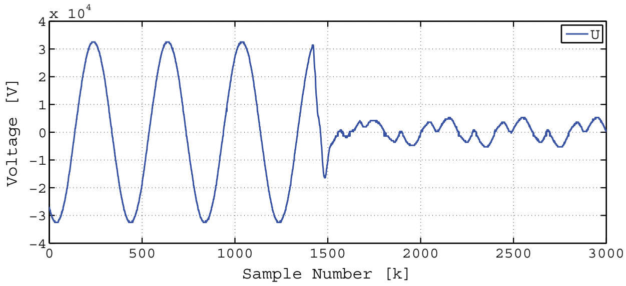

(c) Test number 8 phase voltage

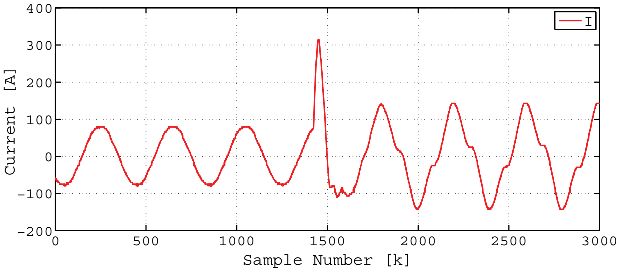

(d) Test number 8 phase current

Figure 7.15. Recorded signals of single line to earth fault at 36.0 km.

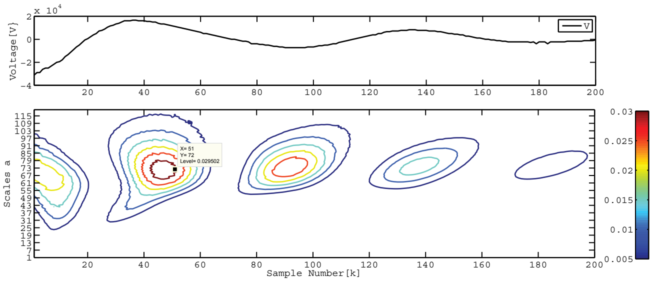

(a) Voltage CWT scalogram(below) and measured signal(above)

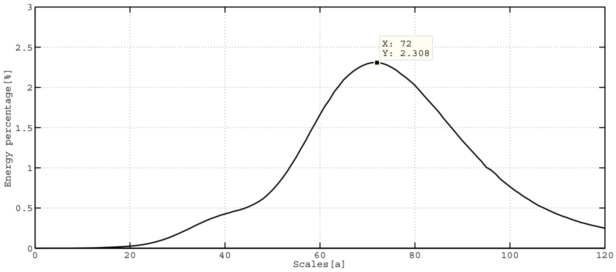

(b) Voltage scale-dependent energy percentage distribution

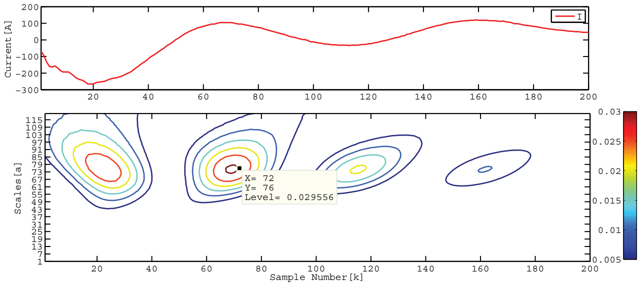

(c) Current CWT scalogram(below)and measured signal(above)

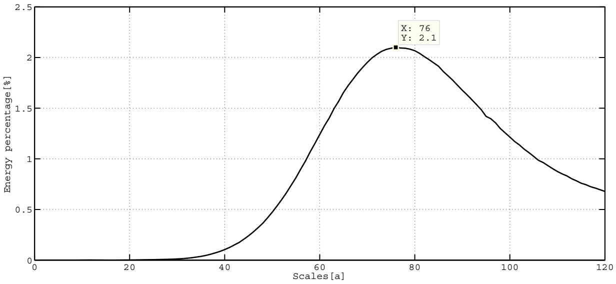

(d) Current scale-dependent energy percentage distribution

Figure 7.16. Example of CWT scalogram and energy percentage distribution of test number 4 (25.4 km) transient signal.

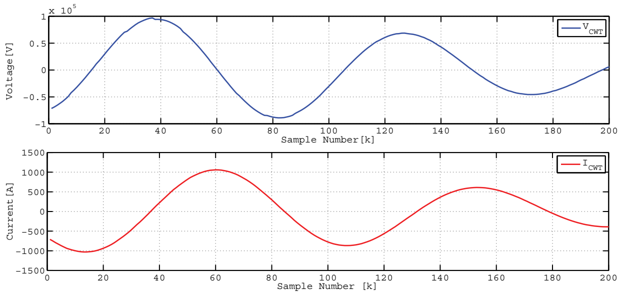

(a) Extracted CWT coefficients

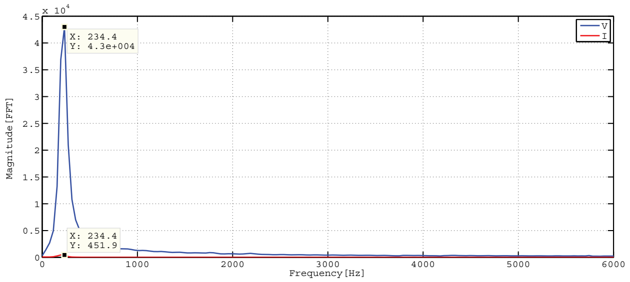

(b) FFT frequency spectrum of extracted CWT

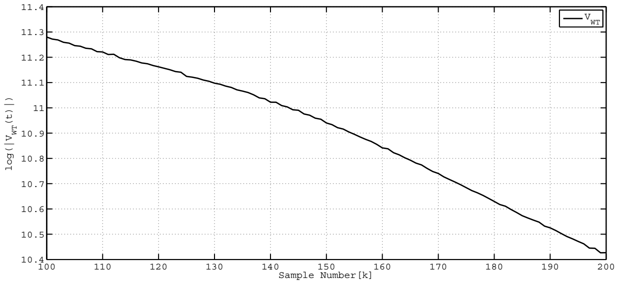

(c) Voltage linear decaying of extracted CWT coefficient

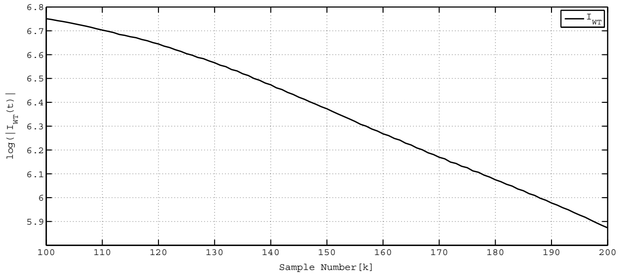

(d) Current linear decaying of extracted CWT coefficient

Figure 7.17. Example of CWT extracted coefficients, FFT frequency spectrum of ectracted coefficent and, voltage and current linear decaying of extracted CWT coefficient of test number 4 (25.4 km) transient signal.

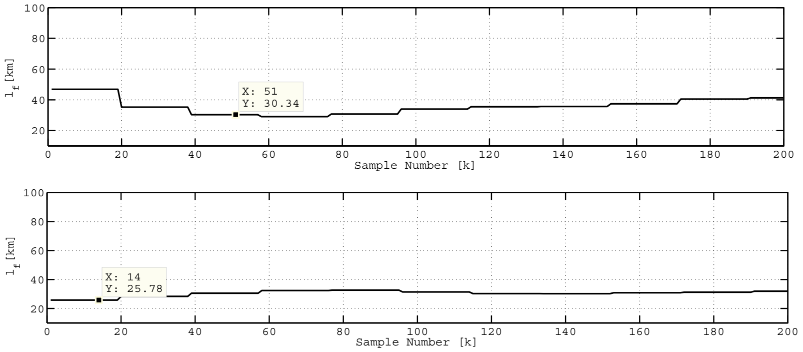

(a) Test number 1 (above) and test number 3 (below)

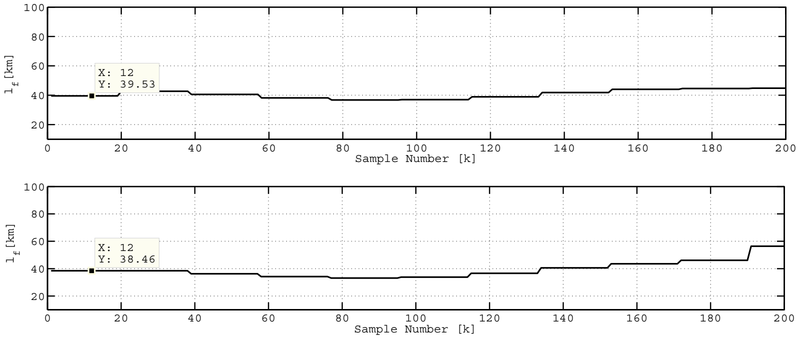

(b) Test number 6 (above) and test number 8 (below)

Figure 7.18. Fault distances calculated using CWT algorithm.

Table 7.4. Calculation results using CWT and GM2 algorithm.

Test number	l	R_f	CWT	ΔCWT	GM2	ΔGM2
1	25.4	0	30.34	4.94	25.30	-0.10
2	25.4	0	29.82	4.42	25.30	-0.10
3	25.4	0	25.78	0.38	36.70	11.30
4	25.4	0	21.02	-4.38	25.30	-0.10
5	25.4	0	24.19	-1.21	37.80	12.40
6	36.0	0	39.53	3.53	36.70	0.70
7	36.0	0	38.70	2.70	36.10	0.10
8	36.0	0	38.46	2.46	35.50	-0.50
MAE				**3.00**		**3.16**

7.3 Case study 3

In this section an artificial single line to earth fault was carried out in a 22 kV Czech compensated neutral network. The field test was recorded by David Topolanek and his team from Brno University. The data was used during his research visit in autumn 2012 at Aalto University. The measured signal was recorded from MV substation and secondary side of MV/LV distribution transformer. Due to the limitation of information, the data was tested only with CWT algorithm described in Section 5.3.

7.3.1 Description of Real Network Case 3

The experiment was conducted in a compensated neutral distribution network. Initially, there were 29 units of LV distribution transformers scattered along the faulty feeder. However only 4 of them were selected for the experiment. The network consisted of a mix of underground cables and overhead lines. The average line parameters are as follows: positive sequence inductance is 1.1459 mH per km and zero sequence inductance is 4.4551 mH per km. In this case, we assumed the negative sequence parameters to be equal to the positive ones. During the experiment, the digital recorder units were installed in four selected 22/0.4 kV LV distribution transformers and at the 110/22 kV MV substation as shown in Figure 7.19.

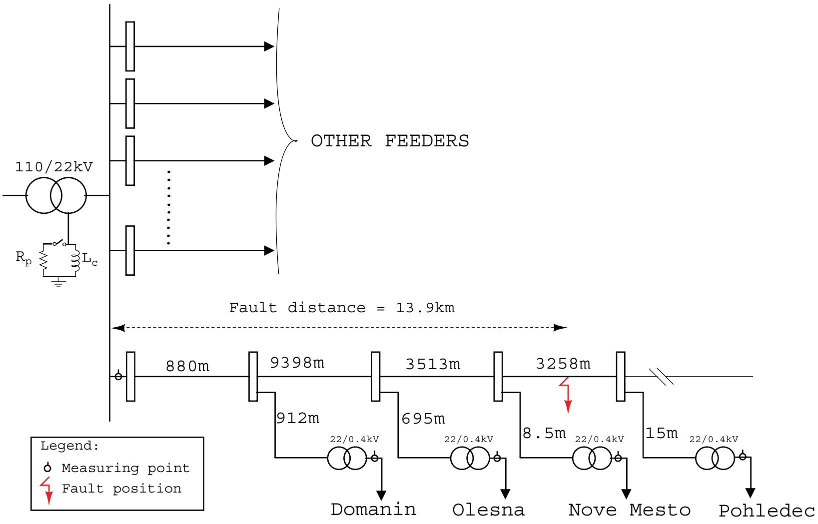

Figure 7.19. Schematic diagram of Czech distribution network.

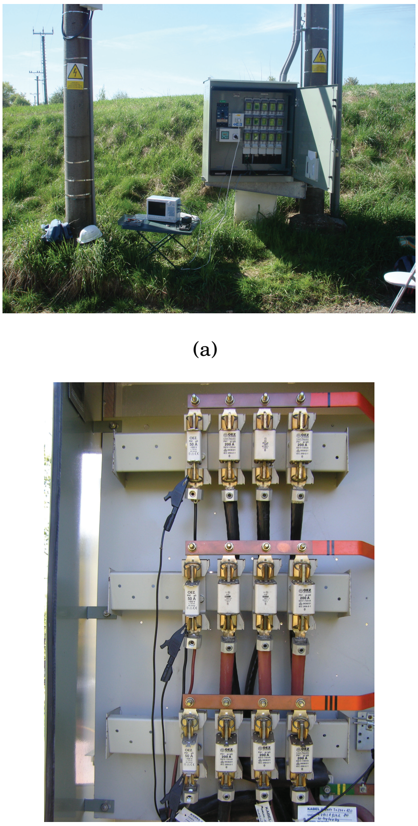

(a)

(b)

Figure 7.20. (a) Photo of one of the low voltage (LV) switch-boards and the digital oscilloscope used during the field test. (b) Connection of measuring probe at the back of the LV distribution panel

The recorder sampling rate at MV substation, and at the LV substations “Domanin”, “Olesna”, “Nove Mesto” and “Pohledec” were 50 kHz, 50 kHz, 20 kHz, 50 kHz and 28 kHz respectively. For the purpose of normalization in calculation, all the recorded data were resampled to 32 kHz. The sampling frequency used in this case study is slightly higher than the previous case sampling frequency. Unfortunately, in this work, we did not study the effect of sampling frequency on the performance of the algorithm. Perhaps, in order to see its influence to the algorithms correctness, it shall be investigate in future.

In order to verify the algorithm used in this paper, an earth fault was simulated about 13.90 km from measuring point located at MV substation as shown in Figure 7.19. Three of the LV distribution substations were located in front of the fault location, while the fourth LV distribution substation was located approximately 3 km behind the fault. During the experiment a basic metallic earth fault was conducted so that affected phase was directly connected to the grounding system of the substation.

The experiment was also performed for the three basic levels of compensation of the distribution system. The levels of compensation were full compensation state, under compensation by about 15% and over compensation by about 15%. The parameters and the states of individual experiments conducted are given in Table 7.5.

Table 7.5. Description of actual single line to earth fault experiment.

Experiment number	Type of earth fault	State of compensation	I_L (A)	I_C (A)
1	Metallic	Ideal	267	267
2	Metallic	Ideal	267	267
3	Metallic	Ideal	267	267
4	Metallic	Undercompensated	220	267
5	Metallic	Overcompensated	305	267

*Note: I_L = current at Peterson coil, I_C=capacitive current of the network

7.3.2 Result Analysis and Discussion

The recorded fault voltages and currents are shown in Figures 7.21, 7.22, 7.23, 7.24 and 7.25. The fault location accuracy is measured with mean average error (MAE) in km as in Equation (6.4). Table 7.6 shows the results of the proposed scheme tested on the real recorded data. In overall, the MAE for fault distance is 0.65 km. The fault distance for test number 1 , 3, 4 and 5 calculated using CWT algorithm is depicted in Figure 7.26. The summary of the results are given in Table 7.6.

In Table 7.6, the results show that by using the proposed algorithm we managed to identify the correct LV substation to be used as indicator for selecting a correct path towards the fault position. Based on the results, the detected LV substation is located in front of the fault position. The distance between the detected LV substation and the fault location is about 118.5 meters, which is very close. The results from test number 1 to test number 4 show that substation “Pohledec” record the second highest peak amplitude. The substation is located 3.148 km behind the fault position. In this experiment result, it seems that the first and second highest peak amplitude of the LV substations gives us an indication that the fault is located in the section between these two substations.

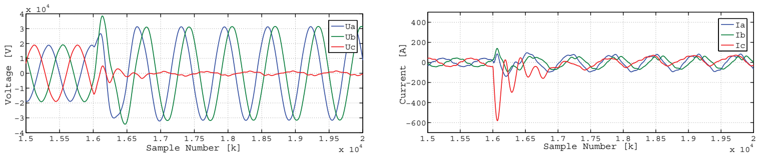

(a) MV phase voltages (b) MV phase currents

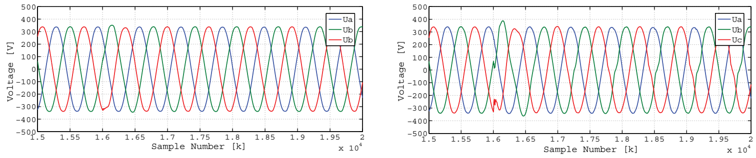

(c) LV DOM phase voltages (d) LV NOVE phase voltages

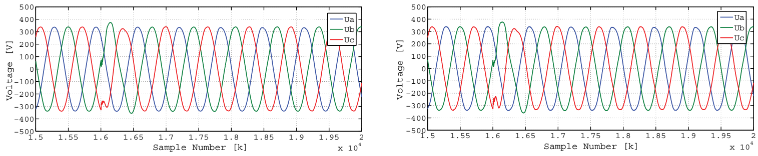

(e) LV OLE phase voltages (f) LV POH phase voltages

Figure 7.21. Recorded signals of experiments 1.

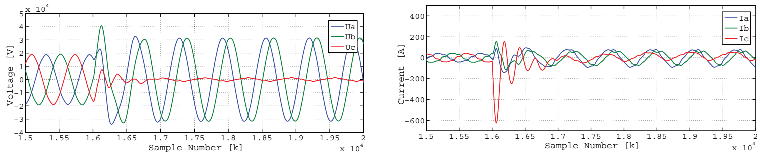

(a) MV phase voltages (b) MV phase currents

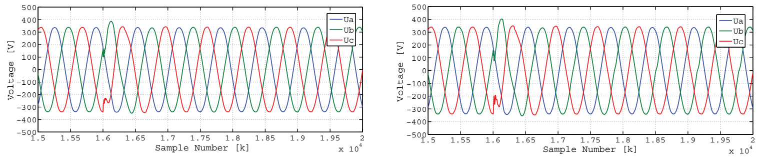

(c) LV DOM phase voltages (d) LV NOVE phase voltages

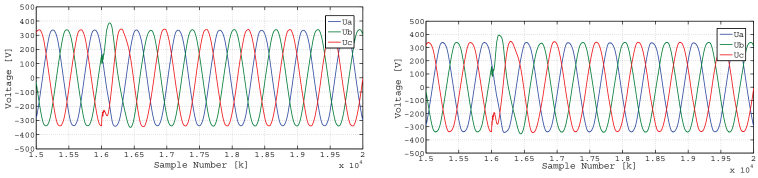

(e) LV OLE phase voltages (f) LV POH phase voltages

Figure 7.22. Recorded signals of experiments 2.

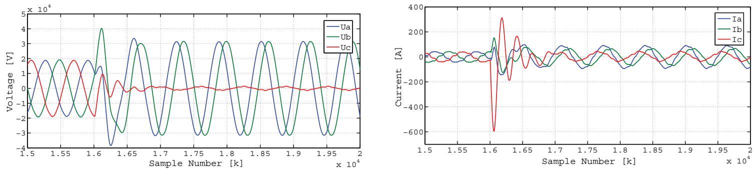

(a) MV phase voltages (b) MV phase currents

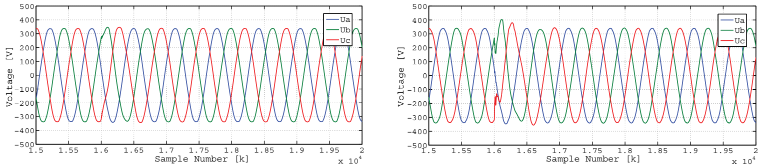

(c) LV DOM phase voltages (d) LV NOVE phase voltages

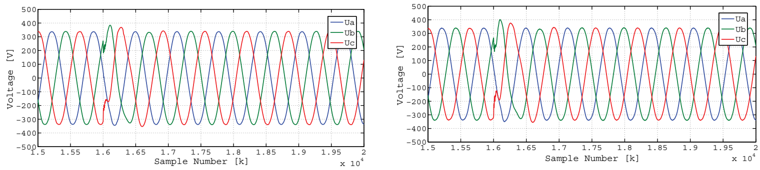

(e) LV OLE phase voltages (f) LV POH phase voltages

Figure 7.23. Recorded signals of experiments 3.

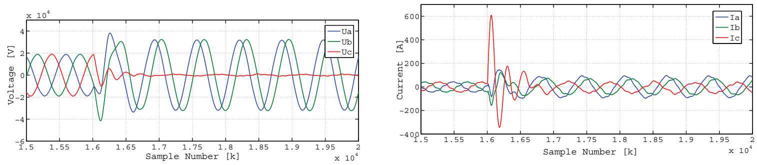

(a) MV phase voltages (b) MV phase currents

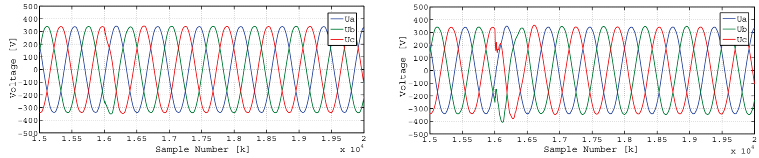

(c) LV DOM phase voltages (d) LV NOVE phase voltages

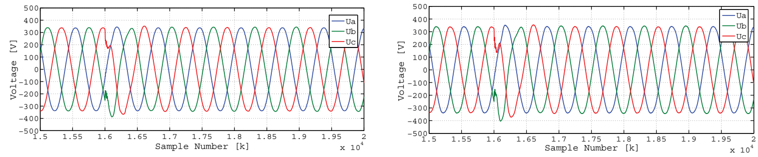

(e) LV OLE phase voltages (f) LV POH phase voltages

Figure 7.24. Recorded signals of experiments 4.

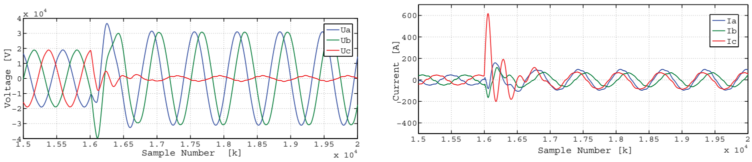

(a) MV phase voltages (b) MV phase currents

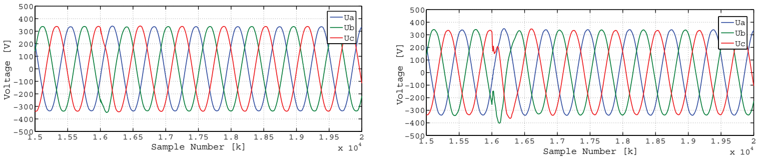

(c) LV DOM phase voltages (d) LV NOVE phase voltages

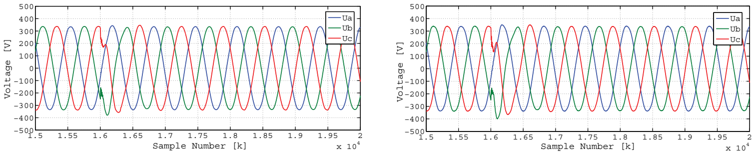

(e) LV OLE phase voltages (f) LV POH phase voltages

Figure 7.25. Recorded signals of experiments 5.

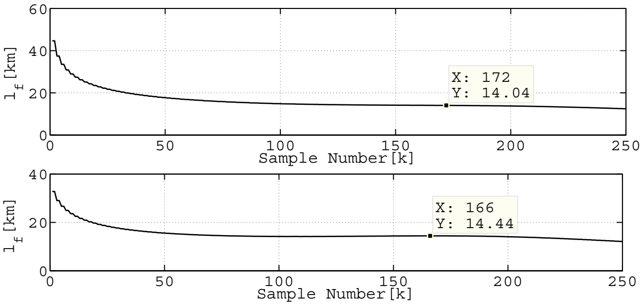

(a) Test number 1 (above) and test number 3 (below)

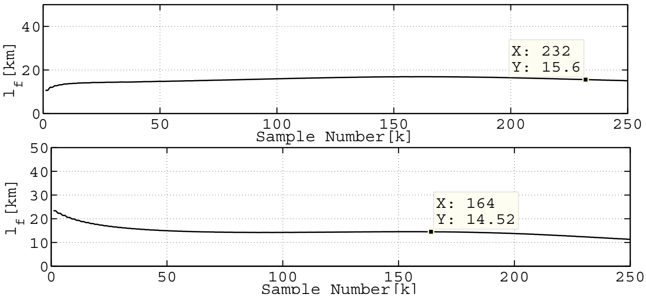

(b) Test number 4 (above) and test number 5 (below)

Figure 7.26. Fault distances calculated using CWT algorithm.

Table 7.6. Test result of single line to earth fault using recorded signal.

Test number	1	2	3	4	5	
State of Compensation	Ideal	Ideal	Ideal	Under compensated	Over compensated	MAE (km)
Fault Location (km)	14.01	14.15	14.44	15.6	14.52	
Error (km)	-0.14	-0.25	-0.54	-1.7	-0.62	0.65
Secondary substation	Amp. |FFT|	Amp. |FFT|	Amp. |FFT|	Amp. |FFT|	Amp. |FFT|	
Pohledec	1150.04	1187.78	1134.6	1106.2	1070.23	
Nove Mesto	1163.74	1195.16	1135.3	1111.4	1067.95	
Olesna	1038.6	1007.38	939.44	908.58	895.97	
Domanin	693.82	631.67	458.22	455.28	479.76	
Detected substation	Nove Mesto	Nove Mesto	Nove Mesto	Nove Mesto	Pohledec	

8. Conclusions and Future Work

This thesis presented fault location algorithms for earth faults in unearthed and compensated neutral networks using measured transient signals. The initial transients of the earth faults are important especially in unearthed and compensated neutral networks. In this work, five types of fault location algorithms based on initial transients of the earth faults have been developed. Two of the algorithms were developed using the measured transient signals from secondary side of the MV/LV distribution transformers. Five types of fault location algorithms developed in this thesis are known as general model (GM), exact model (EM), continuous wavelet transform (CWT), multiple regression analysis (MRA) and artificial neural network (ANN) algorithms.

Considering the results from the simulated network model 1, we can conclude that the damped and undamped charge transient frequency and damping factor from the simulation agreed with the result calculated by theoretical formula of the general model algorithms, with acceptable small error. Based on the fault distance result, it was shown that GM1 and GM2 algorithms have almost identical result. It shows that, in order to estimate the fault distance, by using the undamped charge transient frequency, GM2 algorithm managed to compensate the effect of fault resistance as well as the unknown resistive parameters of the circuit.

We compared the performance of EM1 and GM2 algorithms using sequence component network in simulation model 2. In overall, we conclude that EM1 algorithm has performed much better than GM2 algorithm. The main reason why EM1 algorithm performs much better than GM2 is that the EM1 circuit model has a similar structure as the simulation network, except that we purposely neglected the resistive part in EM1 model. On the other hand, GM2 circuit model is more robust and simple. Both algorithms used same signal pre processing technique to estimate the undamped charge transient frequency.

Based on the results in simulated network model 3, CWT algorithm works well in estimating fault distance using both voltage and current of the earth fault transient signals. The performance of CWT algorithm is slightly effected when the magnitude of the fault resistance is increased. In this simulation case, by using the measured transient signal from secondary side of the MV/LV distribution transformers, we able to identified the correct patch of fault location using the proposed algorithm.

MRA and NN algorithms have shown a good performance in estimating fault distance in simulated network model 4. The network is typical MV distribution network used in [144] with some modification on its data. In order for MRA and NN algorithm to perform well, we need to developed a database for having a relationship between the fault location and the information gathered from the measured transient signals. In this simulation case, the length of each feeder was almost the same (32 km, 20 km, 25 km, 40 km, 19 km and 22.511 km (faulty feeder). Based on the results, GM and EM algorithms have shown an acceptable performance with this kind of MV network. In overall, for GM and EM algorithms, estimated fault location error is less than 3.5 km. In conclusion, it was proved that using the recorded transient signal from the secondary side of the MV/LV distribution transformer it is possible to present a good result of fault distance estimation.

The feasibility of the proposed algorithms was investigated using the data from simulations and field experiments with fault resistance setting up to 50 Ω. Due to the limitation of real network, only CWT and GM2 algorithms were evaluated. In overall, CWT has shown a better performance compared with the GM2 algorithm. However, in terms of the accuracy the difference is not so much. In some cases GM2 algorithm gave better result than the CWT algorithm. Since GM2 can be implemented with only one measurement it is a good option to install a transient recorder in some small network with balanced length of its feeders, for instance in a rural area.

It is worth to mention here that, since the proposed algorithms in this thesis are based on earth fault transient signals, the limitations of the proposed algorithms are related to the earth fault resistance, sampling frequency, loads and also network configuration. The error is also caused by the inaccuracy in the identification of charge transient component by CWT and in addition by inaccuracy in the estimation of the damping attenuation through Hilbert transformation method. Whenever the magnitude of the fault resistance and the resistive load is increased, the transients become more damped, with the result that the estimation of the charge transient frequency becomes more difficult, which affects the overall computation of the fault distance.

There are several things that can be done in the future to evaluate and to improve the proposed algorithms. In this thesis we have managed to test only two algorithms using real system data. Therefore it is important in the future to evaluate the other algorithms with the real network measured data as well. The GM and EM algorithms' performance is affected by the configuration of the network. Therefore, it is important to study the correction factor required to reduce the error due to unbalanced lengths of the feeders with many branches. In this work, the simulation used only OH lines, in the future we should consider developing the simulation network with underground cables as well. The studies should consider the effect of capacitances of underground cables which normally have much higher value those of the OH line. It seems that measuring the transient frequency from the secondary side of the MV/LV distribution transformer opens new possibilities for the fault location algorithms. Therefore, instead of using only one transient signal, it is worth to study in the future the overall behavior of the voltages and currents at secondary side of the MV/LV distribution transformers during the earth faults in the MV network in order to develops new fault location and detection algorithms.

References

[1] S. Hänninen and M. Lehtonen, “Characteristics of earth faults in electrical distribution networks with high impedance earthing,” *Electric Power Systems Research*, vol. 44, no. 3, pp. 155–161, Mar 1998.

[2] K. Winter, “Null point analysis - new method for detecting high resistance earth faults,” *Elektricitetens Rationella Användning (ERA)*, vol. 61, pp. 18–20,23–24, 1988.

[3] Sähköenergialiitto ry SENER, *Keskeytystilasto 2001 (Interruption Statistics 2001)*. Helsinki: Adato Energia Oy, 2002.

[4] P. Heine, J. Pitkänen, and M. Lehtonen, “Voltage sag characteristics of covered conductor feeders,” in *38th International Universities Power Engineering Conference (UPEC2003)*. Thessaloniki Greece, Sept 2003, pp. 1–3.

[5] G. Eberl and P. Schegner, “Earth fault location based on short time low ohmic neutral earthing in cabled medium voltage networks of the DREWAG - Stadtwerke Dresden GmbH,” in *Seminar on Methods and Techniques for Earth Fault Detection, Indication and Location*. Espoo Finland, Feb 2011, pp. 135–141.

[6] P. Järventausta, “Feeder fault management in medium voltage electricity distribution networks,” Ph.D. dissertation, Tampere University of Technology, Tampere, 1995.

[7] M. Lehtonen and T. Hakola, *Neutral earthing and power system protection: earthing solutions and protective relaying in medium voltage distribution networks*. ABB Transmit Oy, 1996.

[8] O. Chaari, M. Meunier, and F. Brouaye, “Wavelets: a new tool for the resonant grounded power distribution systems relaying,” *IEEE Transactions on Power Delivery*, vol. 11, no. 3, pp. 1301–1308, July 1996.

[9] A. Nikander and P. Järventausta, “Safety aspects and novel technical solutions for earth fault management in MV electricity distribution networks,” in *IET Conference Proceedings of 3rd IEE International Conference on Reliability of Transmission and Distribution Networks (RTDN 2005)*, vol. 4. London UK, Jan 2005, pp. 207–211.

[10] J. Altonen and A. Wahlroos, “Novel algorithm for earth-fault location in compensated MV-networks,” in *22nd International Conference and Exhi-*

bition on Electricity Distribution (CIRED 2013). Stockholm Sweden, June 2013, pp. 1–4.

[11] B. Yong, C. Wei, L. Jiansheng, D. Lei, L. Qingdong, and Y. Ning, “Single phase to earth fault location method in distribution network based on signal injection principle,” in *4th International Conference on Electric Utility Deregulation and Restructuring and Power Technologies (DRPT)*. Shandong China, July 2011, pp. 204–208.

[12] K. Jia, D. Thomas, and M. Sumner, “Impedance-based earth fault location for a non-directly grounded distribution systems,” *IET Generation, Transmission Distribution*, vol. 6, no. 12, pp. 1272–1280, Dec 2012.

[13] G. Achleitner, C. Obkircher, L. Fickert, M. Sakulin, and C. Raunig, “An earth fault distance location algorithm in compensated networks with additional estimation of the fault impedance and fault current,” in *Power Quality and Supply Reliability Conference (PQ 2008)*. Parnu Estonia, Aug 2008, pp. 193–198.

[14] G. Eberl, S. Hänninen, M. Lehtonen, and P. Schegner, “Comparison of artificial neural networks and conventional algorithms in ground fault distance computation,” in *IEEE Power Engineering Society Winter Meeting*, vol. 3. Singapore, Jan 2000, pp. 1991–1996.

[15] L. V. Bogdashova and V. E. Kachesov, “Parametric on-line fault location methods for distribution MV networks,” in *IEEE Power Tech Conference*. St. Petersburg Russia, June 2005, pp. 1–7.

[16] P. Imriš, “Transient based earth fault location in 110 kV subtransmission networks,” Ph.D. dissertation, Helsinki University of Technology, 2006.

[17] A. Girgis, C. Fallon, and D. Lubkeman, “A fault location technique for rural distribution feeders,” *IEEE Transactions on Industry Applications*, vol. 29, no. 6, pp. 1170–1175, Nov 1993.

[18] R. Aggarwal, Y. Aslan, and A. Johns, “New concept in fault location for overhead distribution systems using superimposed components,” *IEE Proceedings-Generation, Transmission and Distribution*, vol. 144, no. 3, pp. 309–316, May 1997.

[19] M. Lehtonen, S. Pettissalo, and J.-H. Etula, “Calculational fault location for electrical distribution networks,” in *Third International Conference on Power System Monitoring and Control*. London UK, June 1991, pp. 38–43.

[20] P. Imriš and M. Lehtonen, “Transient based ground fault location using wavelets,” in *4th IASTED International Conference on Power and Energy Systems*. Rhodes, Greece, 28-30 June 2004, pp. 507–511.

[21] A. Borghetti, S. Corsi, C. Nucci, M. Paolone, L. Peretto, and R. Tinarelli, “On the use of continuous-wavelet transform for fault location in distribution power systems,” *International Journal of Electrical Power and Energy Systems*, vol. 28, no. 9, pp. 608 – 617, Nov 2006.

[22] F. H. Magnago and A. Abur, “A new fault location technique for radial distribution systems based on high frequency signals,” in *IEEE Power Engineering Society Summer Meeting*, vol. 1. Edmonton, Alberta, Canada, 18-22 July 1999, pp. 426–431.

[23] M. R. Adzman and M. Lehtonen, "A method for ground fault distance computation in unearthed medium voltage distribution network," *International Review on Modelling and Simulations*, vol. 5, no. 4, pp. 1765–1772, Aug 2012.

[24] A. Borghetti, M. Bosetti, C. Nucci, M. Paolone, and A. Abur, "Integrated use of time-frequency wavelet decompositions for fault location in distribution networks: Theory and experimental validation," *IEEE Transactions on Power Delivery*, vol. 25, no. 4, pp. 3139–3146, Oct 2010.

[25] M. El-Hami, L. L. Lai, D. J. Daruvala, and A. Johns, "A new travelling-wave based scheme for fault detection on overhead power distribution feeders," *IEEE Transactions on Power Delivery*, vol. 7, no. 4, pp. 1825–1833, Oct 1992.

[26] H. Hizman, P. Crossley, P. Gale, and G. Bryson, "Fault section identification and location on a distribution feeder using travelling waves," in *IEEE Power Engineering Society Summer Meeting*, vol. 3. Chicago USA, July 2002, pp. 1107–1112.

[27] S. Navaneethan, J. J. Soraghan, W. Siew, F. McPherson, and P. F. Gale, "Automatic fault location for underground low voltage distribution networks," *IEEE Transactions on Power Delivery*, vol. 16, no. 2, pp. 346–351, Apr 2001.

[28] P. Gale, "Cable-fault location by impulse-current method," *Proceedings of the Institution of Electrical Engineers*, vol. 122, no. 4, pp. 403–408, Apr 1975.

[29] A. Dan and D. Raisz, "Towards a more reliable operation of compensated networks in case of single phase to ground faults," in *14th International Conference on Harmonics and Quality of Power (ICHQP)*. Bergamo Italy, Sept 2010, pp. 1–4.

[30] Y.-Y. Hsu *et al.*, "An expert system for locating distribution system faults," *IEEE Transactions on Power Delivery*, vol. 6, no. 1, pp. 366–372, Jan 1991.

[31] P. Järventausta, P. Verho, and J. Partanen, "Using fuzzy sets to model the uncertainty in the fault location process of distribution networks," *IEEE Transactions on Power Delivery*, vol. 9, no. 2, pp. 954–960, Apr 1994.

[32] Y. D. Xue, B. Y. Xu, and Z. H. Wang, "The fault location technology using transient signals for single phase earth fault in non-solidly earthed network," in *22nd International Conference and Exhibition on Electricity Distribution (CIRED 2013)*. Stockholm Sweden, June 2013, pp. 1–4.

[33] W.-R. Chen, Q.-Q. Qian, and X.-R. Wang, "Wavelet neural network based transient fault signal detection and identification," in *Proceedings of 1997 International Conference on Information, Communications and Signal Processing (ICICS)*, vol. 3. Singapore, 9-12 Sept 1997, pp. 1377–1381.

[34] X.-H. Zhang, S.-X. Fan, H. Duan, and B.-Y. Xu, "Analysis of transient dominant frequency signal for single-phase earthed fault based on Prony algorithm," in *China International Conference on Electricity Distribution (CICED)*. Guangzhou China, 10-13 Dec 2008, pp. 1–6.

[35] S. Huang and X. G. Wang, “A fault location scheme based on spectrum characteristic of fault-generated high-frequency transient signals,” in *IEEE Power Energy Society General Meeting (PES ’09)*. Calgary Canada, July 2009, pp. 1–5.

[36] R. Willheim and M. Waters, *Neutral grounding in high-voltage transmission*, 1st ed. Elsevier Science Ltd, New York, 1956.

[37] G. Druml, A. Kugi, and O. Seifert, “A new directional transient relay for high ohmic earth faults,” in *CIRED 17th International Conference on Electricity Distribution*. Barcelona Spain, 12-15 May 2003, pp. 1–6.

[38] H. Pundt, “Untersuchung der ausgleichsvorgänge bei erdschluß in energieversorgungsnetzen,” *Energietechnik*, vol. 15, pp. 469–477, 1965.

[39] G. Herold, *Elektrische Energieversorgung III.: Drehstrommaschinen, Sternpunktbehandlung, Kurzschlußströme*, ser. Elektrische Energieversorgung. Schlembach Fachverlag, 2002.

[40] M. Lehtonen, *Transient Analysis for Ground Fault Distance Estimation in Electrical Distribution Networks*, ser. VTT Publication 115. Espoo: Espoo : Technical Research Centre of Finland, 1992.

[41] P. Schegner and G. Eberl, “Overview of methods for earth fault distance calculation,” in *Seminar on Methods and Techniques for Earth Fault Detection, Indication and Location*. Espoo Finland, Feb 2011, pp. 36–49.

[42] M. Janssen, *Lokalisatie van eenfase-aardfouten in middenspanningsnetten met niet-geaard sterpunt*, ser. TU Eindhoven. Fac. Elektrotechniek : afstudeerverslagen ; 7591. Eindhoven : Technische Universiteit Eindhoven, Aug 1998.

[43] S. Hänninen, *Single phase earth faults in high impedance grounded networks: characteristics, indication and location*, ser. VTT Publications 453. Espoo: Espoo : Technical Research Centre of Finland, 2001.

[44] S. Hänninen, M. Lehtonen, T. Hakola, and R. Rantanen, “Comparison of wavelet and differential equation algorithms in earth fault distance computation,” in *Proceedings of 13th Power Systems Computations Conference (PSCC’99)*, vol. 2. Trondheim Norway, June 1999, pp. 801–807.

[45] A. G. Phadke and J. S. Thorp, *Computer relaying for power systems*, 2nd ed. John Wiley & Sons Ltd, England, 2009.

[46] P. Schegner, “Digitaler erdschlussuniversalschutz: Konzept und erste realisierung,” Ph.D. dissertation, Saarland University, Saarbrucken, 1989.

[47] M. Lehtonen, “Method for distance estimation of single-phase-to-ground faults in electrical distribution networks with an isolated or compensated neutral,” *European Transactions on Electrical Power*, vol. 5, no. 3, pp. 193–198, May 1995.

[48] M. Igel, “Neuartige verfahren für den erdschlussdistanzschutz in isoliert und kompensiert betriebenen netzen: Signale und algorithmen im frequenzbereich,” Ph.D. dissertation, Saarland University, Saarbrucken, 1990.

[49] T. W. Stringfield, D. Marihart, and R. Stevens, “Fault location methods for overhead lines,” *IEEE Transactions of Power Apparatus and Systems*, vol. 76, no. 3, pp. 518–529, Apr 1957.

[50] P. Crossley and P. McLaren, “Distance protection based on travelling waves,” *IEEE Transactions of Power Apparatus and Systems*, vol. PAS-102, no. 9, pp. 2971–2983, Sept 1983.

[51] Z. Q. Bo, G. Weller, F. Jiang, and Q. X. Yang, “Application of GPS based fault location scheme for distribution system,” in *Proceedings of International Conference on Power System Technology (POWERCON ’98)*, vol. 1. Beijing China, Aug 1998, pp. 53–57.

[52] M. Aurangzeb, P. Crossley, and P. Gale, “Fault location using the high frequency travelling waves measured at a single location on a transmission line,” in *Seventh International Conference on Developments in Power System Protection*. Amsterdam Netherlands, Apr 2001, pp. 403–406.

[53] J. Liang, S. Elangovan, and J. Devotta, “Application of wavelet transform in travelling wave protection,” *International Journal of Electrical Power & Energy Systems*, vol. 22, no. 8, pp. 537 – 542, Nov 2000.

[54] L. V. Bewley, “Traveling waves on transmission systems,” *Transactions of the American Institute of Electrical Engineers*, vol. 50, no. 2, pp. 532–550, June 1931.

[55] A. M. Elhaffar, “Power transmission line fault location based on current traveling waves,” Ph.D. dissertation, Helsinki University of Technology, Helsinki, 2008.

[56] M. Gilany, D. Ibrahim, and E. Eldin, “Traveling-wave-based fault-location scheme for multiend-aged underground cable system,” *IEEE Transactions on Power Delivery*, vol. 22, no. 1, pp. 82–89, Jan 2007.

[57] A. Borghetti, M. Bosetti, M. Di Silvestro, C. A. Nucci, and M. Paolone, “Continuous-wavelet transform for fault location in distribution power networks: definition of mother wavelets inferred from fault originated transients,” *IEEE Transactions on Power Systems*, vol. 23, no. 2, pp. 380–388, Apr 2008.

[58] G. Krzysztof, R. Kowalik, and D. Rasolomampionona, “Regular paper traveling wave fault location in power transmission systems: An overview,” *Journal of Electrical Systems (JES)*, vol. 7, no. 3, pp. 287–296, 2011.

[59] Z. Q. Bo and A. T. Johns, “Transient based protection-a new concept in power system protection,” in *International conference on Power Systems transients (IPST97)*. Seattle USA, June 1997, pp. 401–406.

[60] S. Hänninen and M. Lehtonen, *Earth fault distance computation with fundamental frequency signals based on measurements in substation supply bay*, ser. VTT tiedotteita - Research Notes 2153. Espoo : Technical Research Centre of Finland, 2002.

[61] S. Lin, Z. He, X. Li, and Q. Qian, “Travelling wave time-frequency characteristic-based fault location method for transmission lines,” *IET Generation, Transmission and Distribution*, vol. 6, no. 8, pp. 764–772, Aug 2012.

[62] P. Gale, P. Crossley, X. Bingyin, Y. Ge, B. Cory, and J. R. G. Barker, "Fault location based on travelling waves," in *Fifth International Conference on Developments in Power System Protection*. York UK, Mar 1993, pp. 54–59.

[63] C.-H. Kim *et al.*, "A study on the fault indentification of underground cable using neural networks," in *Proceedings of International Conference on Energy Management and Power Delivery (EMPD '95)*, vol. 2. Singapore, Nov 1995, pp. 571–576.

[64] A. S. Bretas, L. Pires, M. Moreto, and R. H. Salim, "A BP neural network based technique for HIF detection and location on distribution systems with distributed generation," in *Computational Intelligence: Lecture Notes in Computer Science*, ser. 4114. Springer Berlin Heidelberg, Aug 2006, pp. 608–613.

[65] Y. Assef, P. Bastard, and M. Meunier, "Artificial neural networks for single phase fault detection in resonant grounded power distribution systems," in *Proceedings of Transmission and Distribution Conference*. Los Angeles USA, Sep 1996, pp. 566–572.

[66] A. Rafinia and J. Moshtagh, "A new approach to fault location in three-phase underground distribution system using combination of wavelet analysis with ANN and FLS," *International Journal of Electrical Power & Energy Systems*, vol. 55, pp. 261 – 274, Feb 2014.

[67] S. Ekici, S. Yildirim, and M. Poyraz, "Energy and entropy-based feature extraction for locating fault on transmission lines by using neural network and wavelet packet decomposition," *Expert Systems with Applications*, vol. 34, no. 4, pp. 2937 – 2944, May 2008.

[68] Z. Yujun and W. Xiaowei, "Research on wavelet neural network for fault location in power distribution network," in *Electrical, Information Engineering and Mechatronics 2011*, ser. Lecture Notes in Electrical Engineering, X. Wang, F. Wang, and S. Zhong, Eds. Springer London, 2012, vol. 138, pp. 1049–1057.

[69] H. Zayandehroodi, A. Mohamed, M. Farhoodnea, and M. Mohammadjafari, "An optimal radial basis function neural network for fault location in a distribution network with high penetration of DG units," *Measurement*, vol. 46, no. 9, pp. 3319 – 3327, Nov 2013.

[70] R. Mahanty and P. D. Gupta, "Application of RBF neural network to fault classification and location in transmission lines," *IEE Proceedings - Generation, Transmission and Distribution*, vol. 151, pp. 201–212, Mar 2004.

[71] H. Zayandehroodi, A. Mohamed, H. Shareef, and M. Mohammadjafari, "Performance comparison of MLP and RBF neural networks for fault location in distribution networks with DGs," in *IEEE International Conference on Power and Energy (PECon)*. Kuala Lumpur Malaysia, Nov 2010, pp. 341–345.

[72] D. Thukaram, H. P. Khincha, and H. P. Vijaynarasimha, "Artificial neural network and support vector machine approach for locating faults in radial distribution systems," *IEEE Transactions on Power Delivery*, vol. 20, no. 2, pp. 710–721, Apr 2005.

[73] R. Salat and S. Osowski, "Accurate fault location in the power transmission line using support vector machine approach," *IEEE Transactions on Power Systems*, vol. 19, no. 2, pp. 979–986, May 2004.

[74] K. Gayathri and N. Kumarappan, "Accurate fault location on EHV lines using both RBF based support vector machine and SCALCG based neural network," *Expert Systems with Applications*, vol. 37, no. 12, pp. 8822–8830, Dec 2010.

[75] R. Aggarwal, M. Joorabian, and Y. Song, "Fuzzy neural network approach to accurate transmission line fault location," *Engineering Intelligent Systems for Electrical Engineering and Communications*, vol. 5, no. 4, pp. 251–258, Dec 1997.

[76] F. Chunju, K. Li, W. Chan, Y. Weiyong, and Z. Zhaoning, "Application of wavelet fuzzy neural network in locating single line to ground fault (SLG) in distribution lines," *International Journal of Electrical Power & Energy Systems*, vol. 29, no. 6, pp. 497–503, July 2007.

[77] P. Dash, A. Pradhan, and G. Panda, "A novel fuzzy neural network based distance relaying scheme," *IEEE Transactions on Power Delivery*, vol. 15, no. 3, pp. 902–907, July 2000.

[78] S. Hänninen and M. Lehtonen, "Earth fault distance computation with artificial neural network trained by neutral voltage transients," in *IEEE Power Engineering Society Summer Meeting*, vol. 2. Vancouver Canada, July 2001, pp. 1187–1192.

[79] S. Haykin, *Neural networks: a comprehensive foundation*, 2nd ed. Prentice Hall PTR Upper Saddle River, New Jersey USA, 1999.

[80] T. ElAli, *Discrete Systems and Digital Signal Processing with MATLAB, Second Edition*, 2nd ed. Boca Raton : CRC Press, Dec 2011.

[81] H. Darwish, M. Hesham, A.-M. Taalab, and N. Mansour, "Close accord on DWT performance and real-time implementation for protection applications," *IEEE Transactions on Power Delivery*, vol. 25, no. 4, pp. 2174–2183, Oct 2010.

[82] D. Robertson, O. Camps, J. Mayer, and W. B. Gish, "Wavelets and electromagnetic power system transients," *IEEE Transactions on Power Delivery*, vol. 11, no. 2, pp. 1050–1058, Apr 1996.

[83] W. Cochran *et al.*, "What is the fast Fourier transform?" *Proceedings of the IEEE*, vol. 55, no. 10, pp. 1664–1674, Oct 1967.

[84] G. Heydt, "A new method for the calculation of subtransmission and distribution system transients based on the FFT," *IEEE Transactions on Power Delivery*, vol. 4, no. 3, pp. 1869–1875, July 1989.

[85] L. Penghui, Z. Lijie, B. Haijun, and Z. Yanhua, "Power quality monitoring of power system based on spectrum analysis," in *International Conference on E-Product E-Service and E-Entertainment (ICEEE)*. Henan China, Nov 2010, pp. 1–4.

[86] L. Mandache and K. Al-Haddad, “New high precision harmonic analysis method for power quality assessment,” in *Canadian Conference on Electrical and Computer Engineering*. Saskatoon Canada, May 2005, pp. 1958–1961.

[87] R. Melicio, V. M. F. Mendes, and J. P. S. Catalao, “Electrical grid integration and power quality studies of a variable-speed wind energy conversion system,” in *IEEE PowerTech*. Bucharest Romania, June 2009, pp. 1–6.

[88] R. Haddad and E. Strangas, “Fault detection and classification in permanent magnet synchronous machines using Fast Fourier Transform and Linear Discriminant Analysis,” in *9th IEEE International Symposium on Diagnostics for Electric Machines, Power Electronics and Drives (SDEMPED)*. Valencia Spain, Aug 2013, pp. 99–104.

[89] K. Musasa, W. Siti, and J. Jordaan, “Evaluating the contribution in the harmonic distortion level based on Digital Fault Recorder (DFR) analysis,” in *IEEE AFRICON*. Livingstone Zambia, Sept 2011, pp. 1–6.

[90] Z. Radojevic, V. Terzija, G. Preston, S. Padmanabhan, and D. Novosel, “Smart overhead lines autoreclosure algorithm based on detailed fault analysis,” *IEEE Transactions on Smart Grid*, vol. 4, no. 4, pp. 1829–1838, Dec 2013.

[91] M. S. Mamiş, M. Arkan, and C. Keleş, “Transmission lines fault location using transient signal spectrum,” *International Journal of Electrical Power & Energy Systems*, vol. 53, pp. 714 – 718, Dec 2013.

[92] M. Gilany, E. El Din, M. Abdel Aziz, and D. Ibrahim, “An accurate scheme for fault location in combined overhead line with underground power cable,” in *IEEE Power Engineering Society General Meeting*, vol. 3. San Francisco USA, June 2005, pp. 2521–2527.

[93] Hasniaty, A. Mohamed, and A. Hussain, “Automating power quality disturbance analysis using the IPQDA software tool,” in *4th Student Conference on Research and Development (SCOReD)*. Selangor Malaysia, June 2006, pp. 211–214.

[94] C. Moo, Y. Chang, and P. Mok, “A digital measurement scheme for time-varying transient harmonics,” *IEEE Transactions on Power Delivery*, vol. 10, no. 2, pp. 588–594, Apr 1995.

[95] J. Goswami and A. Chan, *Fundamentals of Wavelets: Theory, Algorithms, and Applications*, 2nd ed., ser. Wiley Series in Microwave and Optical Engineering. John Wiley & Sons , Hoboken, New Jersey, 2011.

[96] R. Rao and A. Bopardikar, *Wavelet transforms: introduction to theory and applications*, 1st ed. Reading, MA : Addison-Wesley, 1998.

[97] C. Zhao, M. He, and X. Zhao, “Analysis of transient waveform based on combined short time Fourier transform and wavelet transform,” in *International Conference on Power System Technology (PowerCon 2004)*, vol. 2. Singapore, Nov 2004, pp. 1122–1126.

[98] L. Satish, “Short-time Fourier and wavelet transforms for fault detection in power transformers during impulse tests,” *IEE Proceedings - Science, Measurement and Technology*, vol. 145, no. 2, pp. 77–84, Mar 1998.

[99] B. Xu, H. Wang, L. Sun, and F. Yang, “Detection methods of broken rotor bar fault in squirrel cage induction motor with light-load,” in *International Conference on Electrical Machines and Systems (ICEMS 2008)*. Wuhan China, Oct 2008, pp. 759–762.

[100] J.-Y. Lee, “Variable short-time Fourier transform for vibration signals with transients,” *Journal of Vibration and Control*, vol. 1, pp. 1–15, July 2013.

[101] V. Climente-Alarcon *et al.*, “Diagnosis of stator short-circuits through Wigner-Ville transient-based analysis,” in *35th Annual Conference of IEEE Industrial Electronics (IECON ’09)*. Porto Portugal, Nov 2009, pp. 1097–1102.

[102] N. Mishra and G. V. Anand, “Transient signal detection using Wigner-Ville distribution and wavelet denoising,” in *IEEE Region 10 Conference TENCON*. Hongkong, Nov 2006, pp. 1–4.

[103] G. Andria, E. D’Ambrosio, M. Savino, and A. Trotta, “Application of Wigner-Ville distribution to measurements on transient signals,” in *IEEE Instrumentation and Measurement Technology Conference (IMTC/93)*. Irvine California USA, May 1993, pp. 612–617.

[104] J. Rosero, L. Romeral, J. Ortega, and E. Rosero, “Short circuit fault detection in PMSM by means of Empirical Mode Decomposition (EMD) and Wigner Ville Distribution (WVD),” in *IEEE Twenty-Third Annual Applied Power Electronics Conference and Exposition (APEC 2008)*. Austin Texas USA, Feb 2008, pp. 98–103.

[105] J. Fonollosa and C. Nikias, “Analysis of transient signals using higher-order time-frequency distributions,” in *IEEE International Conference on Acoustics, Speech, and Signal Processing (ICASSP-92)*, vol. 5. San Francisco USA, Mar 1992, pp. 197–200.

[106] W. Liu and X. Guo, “Detection of transient power quality disturbances based EMD combined with Choi-Williams distribution,” in *IEEE International Conference on Automation and Logistics (ICAL)*. Zhengzhou China, Aug 2012, pp. 588–591.

[107] M. Prieto, A. Espinosa, J.-R. Ruiz, J. Urresty, and J. Ortega, “Feature extraction of demagnetization faults in permanent-magnet synchronous motors based on box-counting fractal dimension,” *IEEE Transactions on Industrial Electronics*, vol. 58, no. 5, pp. 1594–1605, May 2011.

[108] N. Elkalashy, M. Lehtonen, H. Darwish, M. Izzularab, and A.-M. Taalab, “DWT-based investigation of phase currents for detecting high impedance faults due to leaning trees in unearthed MV networks,” in *IEEE Power Engineering Society General Meeting*. Tampa, Florida, USA, June 2007, pp. 1–7.

[109] F. Jiang, Z. Bo, P. Chin, M. Redfern, and Z. Chen, “Power transformer protection based on transient detection using discrete wavelet transform (DWT),” in *IEEE Power Engineering Society Winter Meeting*, vol. 3. Singapore, Jan 2000, pp. 1856–1861.

[110] A. Quinquis and C. Dugal, “Using the wavelet transform for the detection of magnetic underwater transient signals,” in *Proceedings Oceans Engineering for Today’s Technology and Tomorrow’s Preservation (OCEANS ’94)*, vol. 2. Brest, France, Sep 1994, pp. 538 – 543.

[111] F. Truchetet and O. Laligant, “Wavelets in industrial applications: a review,” in *Proceedings of the SPIE*, vol. 5607. France, Nov 2004, pp. 1–14.

[112] C. H. Kim and R. Aggarwal, “Wavelet transforms in power systems. I. General introduction to the wavelet transforms,” *Power Engineering Journal*, vol. 14, no. 2, pp. 81–87, Apr 2000.

[113] C. H. Kim and R. Aggarwal, “Wavelet transforms in power systems. Part 2: Examples of application to actual power system transients,” *Power Engineering Journal*, vol. 15, no. 4, pp. 193–202, Aug 2001.

[114] S. Chen and H. Y. Zhu, “Wavelet transform for processing power quality disturbances,” *EURASIP Journal on Advances in Signal Processing*, vol. 2007, pp. 1–20, Feb 2007.

[115] L. Angrisani, P. Daponte, M. D’apuzzo, and A. Testa, “A measurement method based on the wavelet transform for power quality analysis,” *IEEE Transactions on Power Delivery*, vol. 13, no. 4, pp. 990–998, Oct 1998.

[116] M. Karimi, H. Mokhtari, and M. R. Iravani, “Wavelet based on-line disturbance detection for power quality applications,” *IEEE Transactions on Power Delivery*, vol. 15, no. 4, pp. 1212–1220, Oct 2000.

[117] S. Santoso, E. Powers, W. Grady, and P. Hofmann, “Power quality assessment via wavelet transform analysis,” *IEEE Transactions on Power Delivery*, vol. 11, no. 2, pp. 924–930, Apr 1996.

[118] R. Shariatinasab, M. Akbari, and B. Rahmani, *Application of Wavelet Analysis in Power Systems*, ser. Advances in Wavelet Theory and Their Applications in Engineering, Physics and Technology, D. Baleanu, Ed. Rijeka : InTech, Corp., 2012, vol. 2, no. 221-244.

[119] M. Mirzaei, M. Kadir, E. Moazami, and H. Hizam, “Review of fault location methods for distribution power system,” *Australian Journal of Basic & Applied Sciences*, vol. 3, no. 3, 2009.

[120] R. M. de Castro Fernández and H. N. D. Rojas, “An overview of wavelet transforms application in power systems,” in *Proceedings of the fourteenth Power Systems Computation Conference (PSCC 14)*. Seville Spain, June 2002, pp. 1–8.

[121] F. H. Magnago and A. Abur, “Fault location using wavelets,” *IEEE Transactions on Power Delivery*, vol. 13, no. 4, pp. 1475–1480, Oct 1998.

[122] Z. Wenhai, X. Xianyong, W. Ying, Z. Tianwen, Z. Hong, and W. Henggui, “Charging-transient based SLG fault location in neutral-unearthed distribution system,” in *Asia-Pacific Power and Energy Engineering Conference (APPEEC)*. Wuhan China, Mar 2011, pp. 1–4.

[123] A. R. Sedighi, M. R. Haghifam, O. P. Malik, and M. H. Ghassemian, “High impedance fault detection based on wavelet transform and statistical pattern recognition,” *IEEE Transactions on Power Delivery*, vol. 20, no. 4, pp. 2414–2421, Oct 2005.

[124] T. Lobos, P. Kostyla, J. Pospieszna, and M. Jaroszewski, "Location of faults on transmission lines using wavelet transforms," in *International Conference on High Voltage Engineering and Application (ICHVE 2008)*. Chongqing China, Nov 2008, pp. 633–636.

[125] A. Borghetti, S. Corsi, C. Nucci, M. Paolone, L. Peretto, and R. Tinarelli, "On the use of continuous-wavelet transform for fault location in distribution power networks," in *15th Power Systems Computation Conference (PSCC05)*. Liege Belgium, 22-26 Aug 2005, pp. 1–7.

[126] M. Misiti, Y. Misiti, G. Oppenheim, and J.-M. Poggi, *Wavelet toolbox for use with MATLAB*, 1st ed. Natick, Mass. : Math Works, 1997.

[127] R. Bracewell, *The Fourier Transform and Its Applications*, 3rd ed., ser. McGraw-Hill international editions. New Delhi : Tata McGraw-Hill, 2000.

[128] A. Oppenheim and R. Schafer, *Discrete-Time Signal Processing: Pearson New International Edition*, 3rd ed. Harlow : Pearson Education Limited, 2013.

[129] M. R. Adzman and M. Lehtonen, "The correlation of fault distance and transient frequency," in *Seminar on Methods and Techniques for Earth Fault Detection, Indication and Location*. Espoo Finland, Feb 2011, pp. 123–134.

[130] H. Pundt, "Untersuchungen der ausgleichsvorgänge bei erdschluß in hochspannungsnetzen mit isoliertem sternpunkt und induktiver sternpunkterdung als grundlage zur selektiven erdschlußerfassung: Beilagenband," Ph.D. dissertation, Dresden University of Technology, 1963.

[131] A. Agarwal and J. Lang, *Foundations of Analog and Digital Electronic Circuits*, 3rd ed., ser. The Morgan Kaufmann Series in Computer Architecture and Design. Amsterdam ; Boston : Elsevier : Morgan Kaufman Publishers, 2005.

[132] K. Winter and A. Ljungberg, *Jordfelslokalisering I 10-70 kV nat Vattenfall FUD - rapport U 1988/39*. Ärvkarleby: Vattenfall, 1988.

[133] T. Welfonder, "Localisation de défauts monophasés dans les réseaux de distribution à neutre compensé," Ph.D. dissertation, Grenoble Institute of Technology, 1998.

[134] A. Chuang. (2008, October) Epri smart grid R&D overview. Presentation at HP sustainability innovation workshop. EPRI. [Online]. Available: http://www.hpl.hp.com/open_innovation/workshops/microgrid%20and%20distributed%20power/HP_Chuang_102008_post.pdf

[135] P. Järventausta, S. Repo, A. Rautiainen, and J. Partanen, "Smart grid power system control in distributed generation environment," *Annual Reviews in Control*, vol. 34, no. 2, pp. 277 – 286, Dec 2010.

[136] D. Topolanek and P. Toman, "Possible ground fault location using data recorded on the secondary side of distribution transformers," in *The 12th international Scientific Conference on Electric Power Engineering (EPE12)*. Kouty nad Desnou, Czech Republic, May 2011, pp. 209–212.

[137] M. R. Adzman, D. Topolanek, M. Lehtonen, and P. Toman, "An earth fault location scheme for isolated and compensated neutral distribution systems," *International Review of Electrical Engineering*, vol. 8, no. 5, pp. 1520–1531, Sept 2013.

[138] P. Heine, "Voltage sags in power distribution networks," Ph.D. dissertation, Helsinki University of Technology , Helsinki, Nov 2005.

[139] M. R. Adzman and M. Lehtonen, "Fault location in MV unearthed distribution network using the undamped frequency of the transient signal," in *Proceedings of the 3rd International Conference on Energy, Environment, Devices, Systems, Communications, Computers (INEEE '12)*. Rovaniemi Finland, Apr 2012, pp. 165–170.

[140] S. H. Brown, "Multiple linear regression analysis: a matrix approach with MATLAB," *Alabama Journal of Mathematics*, vol. 34, pp. 1–3, 2009.

[141] J. E. Dayhoff, *Neural Network Architectures: An Introduction*. New York USA: Van Nostrand Reinhold Co., 1990.

[142] M. Danyek, P. Handl, and D. Raisz, "Comparison of simulation tools atp-emtp and matlab-simulink for time domain power system transient studies," in *EEUG Meeting*. Sopron, Hungary, Dec 2002, pp. 1–14.

[143] H. Høidalen, L. Prikler, and J. Hall, "ATPDraw-Graphical preprocessor to ATP, Windows version," in *International Conference on Power Systems Transients (IPST1999)*. Budapest Hungary, June 1999, pp. 20–24.

[144] S. Kazemi, "Reliability evaluation of smart distribution grids," Ph.D. dissertation, Aalto University, Oct 2011.

Appendices

A. Mathematical Derivations and MATLAB Scripts

A.1 Derivation of Equation for General Model 1 Damped Natural Frequencies

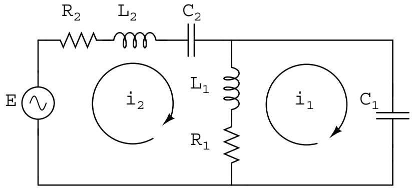

Figure A1. The equivalent circuit for ground fault transient model 1

The equations for voltages around the loops of the circuit are in Laplace-domain as follows

$$i_1(s)(R_1 + SL_1 + \frac{1}{SC_1}) - i_2(s)(R_1 + SL_1) = 0 \tag{1}$$

$$-i_1(s)(R_1 + SL_1) + i_2(s)(R_1 + R_2 + SL_1 + SL_2 + \frac{1}{SC_2}) = \frac{E}{S} \tag{2}$$

The current $i_2(s)$ can be solved by rearranging $i_1(s)$ from equation (1) and substituting it into equation (2). After the substitutions and rearranging the terms, equation (2) becomes:

$$i_2(s)Q(s) = P(s) \tag{3}$$

where,

$$P(s) = C_2E(SR_1C_1 + S^2L_1C_1 + 1) \tag{4}$$

and

$$\begin{aligned}Q(s) = S^4 L_2 C_2 L_1 C_1 + S^3 (R_2 C_2 L_1 C_1 + L_2 C_2 R_1 C_1) \\ + S^2 (R_2 C_2 R_1 C_1 + L_1 C_2 + L_1 C_1 + L_2 C_2) \\ + S (R_1 C_2 + R_2 C_2 + R_1 C_1) + 1 \end{aligned} \tag{5}$$

A.2 Derivation of Equation for General Model 2 Undamped Natural Frequencies

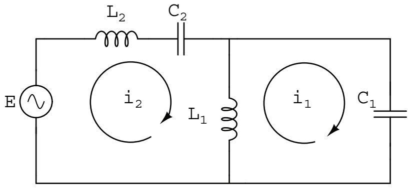

Figure A2. The equivalent circuit for ground fault transient model 2

The equations for voltages around the loops of the circuit are in Laplace-domain as follows

$$i_1(s)(SL_1 + \frac{1}{SC_1}) - i_2(s)(SL_1) = 0 \tag{1}$$

$$-i_1(s)SL_1 + i_2(s)(SL_1 + SL_2 + \frac{1}{SC_2}) = \frac{E}{S} \tag{2}$$

The current $i_2(s)$ can be solved by rearranging $i_1(s)$ from equation (1) and substituting it into equation (2). After the substitutions and rearranging the terms, equation (2) becomes,

$$i_2(s)Q(s) = P(s) \tag{3}$$

where,

$$P(s) = (S^2 L_1 C_1 + 1)EC_2 \tag{4}$$

and

$$Q(s) = S^4 L_2 C_2 L_1 C_1 + S^2 (L_1 C_2 + L_2 C_2 + L_1 C_1) + 1 \tag{5}$$

A.3 Derivation of Equation for General Model 3 Damped Natural Frequencies

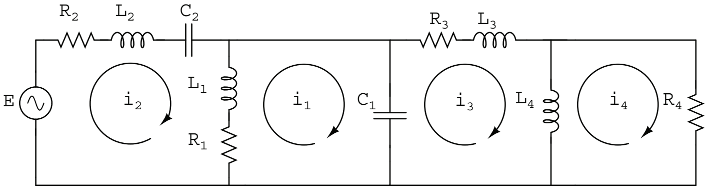

Figure A3. The equivalent circuit for ground fault transient model 3

The equations for voltages around the loops of the circuit are in Laplace-domain as follows

$$i_1(s)(R_1 + SL_1 + \frac{1}{SC_1}) - i_2(s)(R_1 + SL_1) - i_3(s)\frac{1}{SC_1} = 0 \qquad (1)$$

$$-i_1(s)(R_1 + SL_1) + i_2(s)(R_2 + SL_1 + SL_2 + \frac{1}{SC_2}) = \frac{E}{S} \qquad (2)$$

$$-i_1(s)\frac{1}{SC_1} + i_3(s)(R_3 + SL_3 + SL_4 + \frac{1}{SC_1}) - i_4(s)SL_4 = 0 \qquad (3)$$

$$-i_3(s)SL_4 + i_4(s)(R_4 + SL_4) = 0 \qquad (4)$$

From which the current $i_2(s)$ can be solved in the following steps, First Solving $i_4(s)$ from equation (4) and substituting it into equation (3). Then, solving $i_3(s)$ from equation (3) and substituting it into equation (1). Next, solving $i_1(s)$ from equation (4) and substituting it into equation (2). After the substitutions and rearranging the terms, equation (2) becomes:

$$i_2(s)Q(s) = P(s) \qquad (5)$$

where,

$$\begin{aligned} P(s) = EC_2(&S^4 L_1L_3C_1L_4 + S^3(L_1R_3C_1L_4 + L_1L_3C_1R_4 \\ &+ R_1L_3C_1L_4 + L_1L_4C_1R_4) + S^2(L_1R_3C_1R_4 + R_1L_4C_1R_4 + L_4L_1 \\ &+ R_1R_3C_1L_4 + L_3L_4 + R_1L_3C_1R_4) + S(R_3L_4 + R_1R_3C_1R_4 + L_1R_4 \\ &+ L_4R_1 + L_4R_4 + L_3R_4) + R_1R_4 + R_3R_4) \qquad (6) \end{aligned}$$

and,

$$
\begin{aligned}
Q(s) = {} & S^6(L_3L_1L_2C_2L_4C_1) + S^5(C_1L_4L_3L_1R_2C_2 + C_1L_3R_4L_1L_2C_2 \\
& + C_1L_4L_3R_1L_2C_2 + R_4L_4L_1C_1L_2C_2 + C_1L_4R_3L_1L_2C_2) + \\
& S^4(C_1L_4R_3R_1L_2C_2 + L_4L_1L_2C_2 + C_1L_4R_3L_1R_2C_2 \\
& + C_1L_4L_3R_1R_2C_2 + R_4L_4R_1C_1L_2C_2 + R_4L_4L_1C_1R_2C_2 \\
& + C_1L_3R_4L_1R_2C_2 + L_4L_3L_2C_2 + C_1R_3R_4L_1L_2C_2 \\
& + C_1L_3R_4R_1L_2C_2 + L_3L_4L_1C_2 + L_1L_3C_1L_4) + \\
& S^3(R_4L_4R_1C_1R_2C_2 + C_1L_3R_4R_1R_2C_2 + C_1R_3R_4R_1L_2C_2 \\
& + C_1L_4R_3R_1R_2C_2 + C_1R_3R_4L_1R_2C_2 + L_4R_3L_2C_2 \\
& + L_4R_4L_2C_2 + L_4L_1R_2C_2 + L_4L_3R_2C_2 + R_4L_1L_2C_2 \\
& + L_3R_4L_2C_2 + L_4R_1L_2C_2 + L_1L_3C_1R_4 + L_1L_4C_1R_4 \\
& + L_1R_3C_1L_4 + L_3R_4L_1C_2 + L_4R_4L_1C_2 + R_3L_4L_1C_2 \\
& + R_1L_3C_1L_4 + L_3L_4R_1C_2) + S^2(L_4R_4R_2C_2 + L_4R_3R_2C_2 \\
& + L_4R_1R_2C_2 + R_4L_1R_2C_2 + R_3R_4L_2C_2 + L_3R_4R_2C_2 + L_1L_4 \\
& + R_4R_1L_2C_2 + C_1R_3R_4R_1R_2C_2 + L_3R_4R_1C_2 + R_3L_4R_1C_2 \\
& + R_3R_4L_1C_2 + L_1R_3C_1R_4 + L_4R_4R_1C_2 + R_1L_3C_1R_4 \\
& + R_1L_4C_1R_4 + L_3L_4 + R_1R_3C_1L_4) + S(R_3R_4R_2C_2 + R_4R_1R_2C_2 \\
& + L_4R_4 + L_3R_4 + R_3L_4 + L_1R_4 + R_3R_4R_1C_2 + R_1R_3C_1R_4 \\
& + L_4R_1) + R_1R_4 + R_3R_4 \qquad (7)
\end{aligned}
$$

A.4 Derivation of Equation for General Model 4 Undamped Natural Frequencies

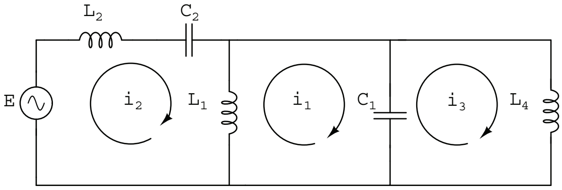

Figure A4. The equivalent circuit for ground fault transient model 4

The equations for voltages around the loops of the circuit are in Laplace-domain as follows

$$i_1(s)(SL_1 + \frac{1}{SC_1}) - i_2(s)SL_1 - i_3(s)\frac{1}{SC_1} = 0 \tag{1}$$

$$-i_1(s)SL_1 + i_2(s)(SL_1 + SL_2 + \frac{1}{SC_2}) = \frac{E}{S} \tag{2}$$

$$-i_1(s)\frac{1}{SC_1} + i_3(s)(SL_4 + \frac{1}{SC_1}) = 0 \tag{3}$$

From which the current $i_2(s)$ can be solved in the following steps, First Solving $i_3(s)$ from equation (3) and substituting it into equation (1). Next, solving $i_1(s)$ from equation (1) and substituting it into equation (2). After the substitutions and rearranging the terms, equation (2) becomes:

$$i_2(s)Q(s) = P(s) \tag{4}$$

where,

$$P(s) = (S^2 L_1 L_4 C_1 + L_1 + L_4)EC_2 \tag{5}$$

and

$$Q(s) = S^4 L_2 C_2 L_1 L_4 C_1 + S^2(L_1 C_2 L_4 + L_2 C_2 L_4 + L_2 C_2 L_1 + L_1 L_4 C_1) + L_1 + L_4 \tag{6}$$

A.5 Example of Matlab Script for MRA model

```
load X; % Independent variables
load Y1; % Dependent variable
load B1; % FFT amplitude of extracted CWT coefficient
load B2; % Scale of extracted CWT coefficient
load B3; % Total loads prior to earth fault
A=X′*X;
K=(X′*X)^-1;
B=K*X′*Y1;
Y=B(1,1)+(B(2,1)*B1)+(B(3,1)*B2)+(B(4,1)*B3)
```

B. ATPDraw OH Line Configurations and Load Variation

B.1 ATPDraw OH Line Geometrical and Electrical Configurations

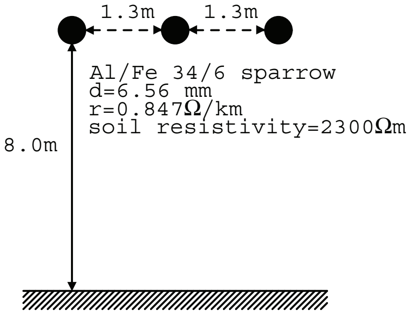

Figure B1. Simulation network model 3 ATPDraw OH configurations

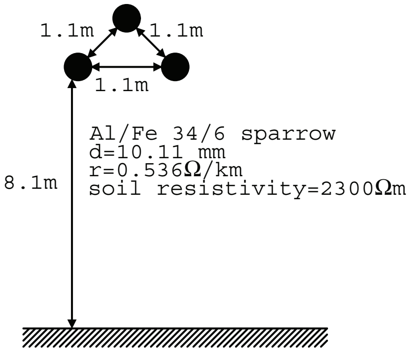

Figure B2. Simulation network model 4 ATPDraw OH configurations

B.2 Load Variation for Simulation Model 4

Table B1. Simulation model 4 data.

Section	Length	Dist.	(kVA)	(%)	Load	Load 1	Load 2	Load 3	Load 4	Load 5	Pf
	(km)	Trans. (DT)				kVA	kVA	kVA	kVA	kVA	
a	0.63	1.00	100.00	4.00	A	14.30	20.02	18.59	10.01	22.17	0.91
b	0.72	2.00	200.00	4.00	B	94.00	131.60	122.20	65.80	145.70	0.95
c	1.90	3.00	315.00	4.00	C	170.00	238.00	221.00	119.00	263.50	0.90
d	0.73	4.00	100.00	4.00	D	35.70	49.98	46.41	24.99	55.34	0.92
e	0.94	5.00	100.00	4.00	E	40.20	56.28	52.26	28.14	62.31	0.93
f	0.35	6.00	200.00	4.00	F	101.00	141.40	131.30	70.70	156.55	0.92
g	1.28	7.00	100.00	4.00	G	29.20	40.88	37.96	20.44	45.26	0.94
h	1.25	8.00	100.00	4.00	H	42.70	59.78	55.51	29.89	66.19	0.91
i	2.21	9.00	100.00	4.00	I	36.30	50.82	47.19	25.41	56.27	0.96
j	1.40	10.00	100.00	4.00	J	11.40	15.96	14.82	7.98	17.67	0.97
k	0.78	11.00	200.00	4.00	K	91.40	127.96	118.82	63.98	141.67	0.98
l	0.38	12.00	100.00	4.00	L	32.90	46.06	42.77	23.03	51.00	0.99
m	0.47	13.00	100.00	4.00	M	23.60	33.04	30.68	16.52	36.58	0.94
n	1.35	14.00	200.00	4.00	N	118.00	165.20	153.40	82.60	182.90	0.95
o	0.50	15.00	100.00	4.00	O	63.60	89.04	82.68	44.52	98.58	0.98
p	0.49	16.00	315.00	4.00	P	154.00	215.60	200.20	107.80	238.70	0.99
q	0.74	17.00	100.00	4.00	Q	2.43	3.40	3.16	1.70	3.77	0.91
r	0.50	18.00	500.00	4.00	R	256.00	358.40	332.80	179.20	396.80	0.93
s	0.72	19.00	200.00	4.00	S	117.00	163.80	152.10	81.90	181.35	0.94
t	1.00	20.00	315.00	4.00	T	167.00	233.80	217.10	116.90	258.85	0.95
u	0.80	21.00	100.00	4.00	U	45.20	63.28	58.76	31.64	70.06	0.96
v	0.44	22.00	100.00	4.00	V	25.90	36.26	33.67	18.13	40.15	0.97
w	0.71	23.00	100.00	4.00	W	49.40	69.16	64.22	34.58	76.57	0.98
x	2.23	24.00	100.00	4.00	X	21.10	29.54	27.43	14.77	32.71	0.92
f1	32.00	25.00	2000.00	6.00	F1	1000.00	1000.00	1000.00	1000.00	1000.00	0.90
f2	20.00	26.00	2000.00	6.00	F2	1000.00	1000.00	1000.00	1000.00	1000.00	0.90
f3	25.00	27.00	2000.00	6.00	F3	1600.00	1600.00	1600.00	1600.00	1600.00	0.90
f4	40.00	28.00	2000.00	6.00	F4	1200.00	1200.00	1200.00	1200.00	1200.00	0.90
f5	19.00	29.00	2000.00	6.00	F5	1100.00	1100.00	1100.00	1100.00	1100.00	0.90

C. Tables of Simulation Results

C.1 Tabulated Results of Simulated Network Model 1

Table C1. Comparison of simulation test result to the theory of earth fault transient. f_{dc} , f_{nc} and ζ_c are calculated using the GM1 equations. f_{dm} , f_{nm} and ζ_m are estimated transient parameters from the simulated earth fault transient waveforms.

l (km)	f_d (Hz)			ζ			f_n (Hz)		
	f_{dm}	f_{dc}	Δf_d	ζ_m	ζ_c	$\Delta\zeta$	f_{nm}	f_{nc}	Δf_n
2	1132.81	1164.22	-31.41	0.0038	0.0039	-0.0001	1132.86	1164.27	-31.41
4	976.56	985.82	-9.25	0.0093	0.0095	-0.0002	976.71	985.96	-9.26
6	859.38	862.41	-3.04	0.0165	0.0166	0.0000	859.61	862.66	-3.05
8	781.25	773.77	7.48	0.0224	0.0233	-0.0009	781.56	774.10	7.46
10	703.13	706.95	-3.83	0.0297	0.0292	0.0005	703.51	707.35	-3.83
12	664.06	654.51	9.55	0.0345	0.0341	0.0005	664.51	654.97	9.54
14	625.00	612.04	12.96	0.0389	0.0383	0.0006	625.49	612.55	12.94
16	585.94	576.77	9.17	0.0407	0.0421	-0.0014	586.47	577.33	9.14
18	546.88	546.90	-0.03	0.0445	0.0455	-0.0009	547.47	547.51	-0.04
20	507.81	521.19	-13.38	0.0491	0.0486	0.0006	508.48	521.85	-13.37
MAE			**10.01**			**0.0006**			**10.00**

Notes: l = Actual fault distance (km), f_d = Damped transient frequency (Hz), f_{dm} = Estimated damped transient frequency (Hz), f_{dc} = Calculated damped transient frequency (Hz), Δf_d = Error of damped transient frequency (Hz), ζ = Damping factor, ζ_m = Estimated damping factor, ζ_c = Calculated damping factor, $\Delta\zeta$ = Error of damping factor, f_n = Undamped transient frequency (Hz), f_{nm} = Estimated undamped transient frequency (Hz), f_{nc} = Calculated undamped transient frequency (Hz), Δf_n = Error of undamped transient frequency (Hz), MAE = Mean average error.

Table C2. Comparison of the distance estimates obtained using GM algorithms for the simulated single line to earth faults with varies fault distance.

l (km)	$\mathrm{GM1}_{fdm}$	$\Delta\mathrm{GM1}_{fdm}$	$\mathrm{GM1}_{fnm}$	$\Delta\mathrm{GM1}_{fnm}$	GM2	ΔGM2
2	2.30	0.30	2.30	0.30	2.30	0.30
4	4.13	0.13	4.13	0.13	4.13	0.13
6	6.06	0.06	6.06	0.06	6.06	0.06
8	7.81	-0.19	7.81	-0.19	7.81	-0.19
10	10.13	0.13	10.13	0.13	10.13	0.13
12	11.60	-0.40	11.60	-0.40	11.60	-0.40
14	13.35	-0.65	13.35	-0.65	13.35	-0.65
16	15.45	-0.55	15.45	-0.55	15.45	-0.55
18	18.00	0.00	18.00	0.00	18.00	0.00
20	21.16	1.16	21.16	1.16	21.16	1.16
MAE (km)		**0.36**		**0.36**		**0.36**

Notes: l = Actual fault distance (km), $\mathrm{GM1}_{fdm}$ = Estimated fault distance using general model 1 and damped transient frequency (km), $\Delta\mathrm{GM1}_{fdm}$ = Error of estimated fault distance using general model 1 and damped transient frequency (km), $\mathrm{GM1}_{fnm}$ = Estimated fault distance using General model 1 and undamped transient frequency (km), $\Delta\mathrm{GM1}_{fnm}$ = Error of estimated fault distance using general model 1 and undamped transient frequency (km), $\mathrm{GM2}_{fnm}$ = Estimated fault distance using General model 2 and undamped transient frequency (km), ΔGM2 = Error of estimated fault distance using general model 2 and undamped transient frequency (km), MAE = Mean average error.

Table C3. Comparison of simulation test result to the theory of earth fault transient with the effect of fault resistance. f_{dc} , f_{nc} and ζ_c are calculated using GM1 equations. f_{dm} , f_{nm} and ζ_m are estimated transient parameters from the simulated earth fault transient waveforms.

l (km)	R_f (Ω)	f_d (Hz)			ζ			f_n (Hz)		
		f_{dm}	f_{dc}	Δf_d	ζ_m	ζ_c	$\Delta\zeta$	f_{nm}	f_{nc}	Δf_n
2	0	1132.81	1164.22	-31.41	0.01	0.01	0.00	1132.86	1164.27	-31.41
	25	1132.81	1164.53	-31.71	0.0536	0.0538	-0.0002	1134.44	1166.22	-31.77
	50	1132.81	1165.30	-32.49	0.0980	0.0987	-0.0007	1138.29	1171.02	-32.73
	100	1093.75	1168.32	-74.57	0.1650	0.1905	-0.0254	1108.95	1190.11	-81.16
4	0	976.56	985.82	-9.25	0.0171	0.0174	-0.0003	976.71	985.96	-9.26
	25	976.56	984.95	-8.38	0.0594	0.0605	-0.0011	978.29	986.75	-8.46
	50	976.56	983.10	-6.53	0.1013	0.1037	-0.0024	981.61	988.42	-6.81
	100	937.50	976.11	-38.61	0.1594	0.1912	-0.0318	949.64	994.45	-44.81
10	0	703.13	706.95	-3.83	0.0333	0.0334	-0.0001	703.51	707.35	-3.83
	25	703.13	705.87	-2.75	0.0663	0.0668	-0.0005	704.67	707.45	-2.78
	50	703.13	704.08	-0.95	0.0995	0.1001	-0.0006	706.63	707.63	-1.00
	100	664.06	698.26	-34.20	0.1387	0.1669	-0.0282	670.55	708.20	-37.65
16	0	585.94	576.77	9.17	0.0428	0.0441	-0.0013	586.47	577.33	9.14
	25	585.94	575.88	10.05	0.0693	0.0717	-0.0023	587.35	577.37	9.98
	50	546.88	574.57	-27.69	0.1024	0.0992	0.0032	549.76	577.42	-27.65
	100	546.88	570.64	-23.77	0.1403	0.1543	-0.0140	552.34	577.56	-25.22
MAE				**21.59**			**0.01**			**22.73**

Notes: l = Actual fault distance (km), f_d = Damped transient frequency (Hz), f_{dm} = Estimated damped transient frequency (Hz), f_{dc} = Calculated damped transient frequency (Hz), Δf_d = Error of damped transient frequency (Hz), ζ = Damping factor, ζ_m = Estimated damping factor, ζ_c = Calculated damping factor, $\Delta\zeta$ = Error of damping factor, f_n = Undamped transient frequency (Hz), f_{nm} = Estimated undamped transient frequency (Hz), f_{nc} = Calculated undamped transient frequency (Hz), Δf_n = Error of undamped transient frequency (Hz), R_f = Fault resistance (Ω), MAE = Mean average error.

Table C4. Comparison of the distance estimates obtained of the GM algorithm methods with effect of fault resistance.

l (km)	R_f (Ω)	GM1$_{fdm}$	ΔGM1$_{fdm}$	GM1$_{fnm}$	ΔGM1$_{fnm}$	GM2	ΔGM2
2	0	2.30	0.30	2.30	0.30	2.30	0.30
	25	2.30	0.30	2.29	0.29	2.29	0.29
	50	2.30	0.30	2.25	0.25	2.25	0.25
	100	2.70	0.70	2.55	0.55	2.55	0.55
4	0	4.13	0.13	4.13	0.13	4.13	0.13
	25	4.13	0.13	4.11	0.11	4.10	0.10
	50	4.13	0.13	4.06	0.06	4.06	0.06
	100	4.70	0.70	4.52	0.52	4.52	0.52
10	0	10.13	0.13	10.13	0.13	10.13	0.13
	25	10.13	0.13	10.09	0.09	10.09	0.09
	50	10.13	0.13	10.02	0.02	10.02	0.02
	100	11.60	1.60	11.36	1.36	11.36	1.36
16	0	15.45	-0.55	15.45	-0.55	15.45	-0.55
	25	15.45	-0.55	15.39	-0.61	15.39	-0.61
	50	18.00	2.00	17.84	1.84	17.84	1.84
	100	18.00	1.65	17.65	1.65	17.65	1.65
MAE (km)			**0.59**		**0.53**		**0.53**

Notes: l = Actual fault distance (km), GM1$_{fdm}$ = Estimated fault distance using general model 1 and damped transient frequency (km), ΔGM1$_{fdm}$ = Error of estimated fault distance using general model 1 and damped transient frequency (km), GM1$_{fnm}$ = Estimated fault distance using General model 1 and undamped transient frequency (km), ΔGM1$_{fnm}$ = Error of estimated fault distance using general model 1 and undamped transient frequency (km), GM2 = Estimated fault distance using General model 2 and undamped transient frequency (km), ΔGM2 = Error of estimated fault distance using general model 2 and undamped transient frequency (km), R_f = Fault resistance (Ω), MAE = Mean average error.

Table C5. Comparison of simulation test result to the theory of ground fault transient with effect of fault inception angle. f_{dc} , f_{nc} and ζ_c are calculated using the GM1 equations. f_{dm} , f_{nm} and ζ_m are estimated transient parameters from the simulated earth fault transient waveform.

l (km)	R_f (Ω)	f_d (Hz)			ζ			f_n (Hz)		
		f_{dm}	f_{dc}	Δf_d	ζ_m	ζ_c	$\Delta\zeta$	f_{nm}	f_{nc}	Δf_n
4	90	976.56	985.82	-9.25	0.0171	0.0174	-0.0003	976.71	985.96	-9.26
	45	976.56	985.82	-9.25	0.0171	0.0174	-0.0003	976.71	985.96	-9.26
	0	976.56	985.82	-9.25	0.0172	0.0174	-0.0002	976.71	985.96	-9.26
16	90	585.94	576.77	9.17	0.0428	0.0441	-0.0013	586.47	577.33	9.14
	45	585.94	576.77	9.17	0.0429	0.0441	-0.0012	586.48	577.33	9.14
	0	585.94	576.77	9.17	0.0431	0.0441	-0.0010	586.48	577.33	9.15
MAE				**9.21**			**0.0007**			**9.20**

Notes: l = Actual fault distance (km),f_d = Damped transient frequency (Hz), f_{dm} = Estimated damped transient frequency (Hz), f_{dc} = Calculated damped transient frequency (Hz), Δf_d = Error of damped transient frequency (Hz), ζ = Damping factor, ζ_m = Estimated damping factor, ζ_c = Calculated damping factor, $\Delta\zeta$ = Error of damping factor, f_n = Undamped transient frequency (Hz), f_{nm} = Estimated undamped transient frequency (Hz), f_{nc} = Calculated undamped transient frequency (Hz), Δf_n = Error of undamped transient frequency (Hz), R_f = Fault resistance (Ω), MAE = Mean average error.

Table C6. Comparison of the distance estimates obtained of the GM algorithm methods with the effect of fault inception angle.

l (km)	Angle (°)	GM1$_{fdm}$	ΔGM1$_{fdm}$	GM1$_{fdm}$	ΔGM1$_{fnm}$
4	90	4.13	0.13	4.13	0.13
	45	4.13	0.13	4.13	0.13
	0	4.13	0.13	4.13	0.13
16	90	15.45	-0.55	15.45	-0.55
	45	15.45	-0.55	15.45	-0.55
	0	15.45	-0.55	15.45	-0.55
MAE (km)			**0.34**		**0.34**

Notes: l = Actual fault distance (km), GM1$_{fdm}$ = Estimated fault distance using general model 1 and damped transient frequency (km), ΔGM1$_{fdm}$ = Error of estimated fault distance using general model 1 and damped transient frequency (km), GM1$_{fnm}$ = Estimated fault distance using General model 1 and undamped transient frequency (km), ΔGM1$_{fnm}$ = Error of estimated fault distance using general model 1 and undamped transient frequency (km), MAE = Mean average error.

Table C7. Comparison of simulation test result to the theory of ground fault transient with the effect of composite loads. f_{dc} , f_{nc} and ζ_c are calculated using the general model 3 equations. f_{dm} , f_{nm} and ζ_m are estimated transient parameters from the simulated earth fault transient waveforms.

l (km)	Load (MVA)	R_f (Ω)	f_d (Hz)			ζ			f_n (Hz)		
			f_{dm}	f_{dc}	$\Delta\ f_d$	ζ_m	ζ_c	$\Delta\zeta$	f_{nm}	f_{nc}	$\Delta\ f_n$
4	5.0	0	1015.63	1020.08	-4.46	0.0380	0.0388	-0.0009	1016.36	1020.85	-4.49
		25	1015.63	1016.61	-0.99	0.0828	0.0853	-0.0025	1019.12	1020.33	-1.20
		50	976.56	1011.57	-35.00	0.1311	0.1318	-0.0007	985.06	1020.47	-35.41
		100	976.56	996.34	-19.78	0.2093	0.2256	-0.0163	998.68	1022.71	-24.03
	12.5	0	1015.63	1030.09	-14.46	0.0284	0.0288	-0.0004	1016.04	1030.52	-14.48
		25	1015.63	1027.84	-12.22	0.0743	0.0754	-0.0011	1018.44	1030.77	-12.34
		50	1015.63	1024.01	-8.39	0.1194	0.1221	-0.0027	1022.94	1031.73	-8.79
		100	976.56	1011.21	-34.64	0.1839	0.2163	-0.0324	993.51	1035.72	-42.21
10	5.0	0	703.13	714.78	-11.65	0.0438	0.0435	0.0003	703.80	715.45	-11.65
		25	703.13	713.07	-9.95	0.0779	0.0777	0.0002	705.27	715.23	-9.96
		50	703.13	710.56	-7.44	0.1106	0.1119	-0.0012	707.47	715.05	-7.58
		100	664.06	703.08	-39.01	0.1592	0.1803	-0.0210	672.64	714.79	-42.14
	12.5	0	703.13	719.16	-16.03	0.0403	0.0399	0.0005	703.70	719.73	-16.03
		25	703.13	717.74	-14.61	0.0748	0.0741	0.0007	705.10	719.72	-14.61
		50	703.13	715.51	-12.38	0.1097	0.1084	0.0013	707.39	719.75	-12.36
		100	664.06	708.58	-44.52	0.1773	0.1770	0.0003	674.75	719.95	-45.20
16	5.0	0	585.94	579.92	6.02	0.0492	0.0505	-0.0013	586.65	580.66	5.99
		25	585.94	578.76	7.18	0.0761	0.0784	-0.0022	587.64	580.55	7.10
		50	585.94	577.15	8.78	0.1027	0.1062	-0.0035	589.05	580.44	8.61
		100	546.88	572.57	-25.70	0.1454	0.1620	-0.0166	552.75	580.24	-27.49
	12.5	0	585.94	582.53	3.41	0.0477	0.0488	-0.0011	586.61	583.22	3.39
		25	585.94	581.48	4.46	0.0749	0.0767	-0.0018	587.59	583.20	4.39
		50	585.94	579.99	5.95	0.1017	0.1047	-0.0030	588.99	583.19	5.80
		100	546.88	575.63	-28.75	0.1722	0.1607	0.0115	555.17	583.20	-28.04
MAE					**15.66**			**0.0052**			**16.39**

Notes: l = Actual fault distance (km), f_d = Damped transient frequency (Hz), f_{dm} = Estimated damped transient frequency (Hz), f_{dc} = Calculated damped transient frequency (Hz), $\Delta\ f_d$ = Error of damped transient frequency (Hz), ζ = Damping factor, ζ_m = Estimated damping factor, ζ_c = Calculated damping factor, $\Delta\zeta$ = Error of damping factor, f_n = Undamped transient frequency (Hz), f_{nm} = Estimated undamped transient frequency (Hz), f_{nc} = Calculated undamped transient frequency (Hz), $\Delta\ f_n$ = Error of undamped transient frequency (Hz), R_f = Fault resistance (Ω), MAE = Mean average error.

Table C8. Comparison of the distance estimates obtained of the GM algorithm methods with effect of composite loads.

l (km)	MVA	R_f (Ω)	GM1	ΔGM1	GM2	ΔGM2	GM3	ΔGM3	GM4	ΔGM4
4	5.0	0	3.60	-0.40	3.60	-0.40	4.05	0.05	3.63	-0.37
		25	3.57	-0.43	3.57	-0.43	4.02	0.02	3.59	-0.41
		50	4.01	0.01	4.01	0.01	4.44	0.44	4.04	0.04
		100	3.83	-0.17	3.83	-0.17	4.27	0.27	3.85	-0.15
	12.5	0	3.61	-0.39	3.61	-0.39	4.17	0.17	3.63	-0.37
		25	3.58	-0.42	3.57	-0.43	4.14	0.14	3.60	-0.40
		50	3.52	-0.48	3.52	-0.48	4.09	0.09	3.55	-0.45
		100	3.90	-0.10	3.90	-0.10	4.45	0.45	3.92	-0.08
10	5.0	0	10.12	0.12	10.12	0.12	10.39	0.39	10.14	0.14
		25	10.07	0.07	10.07	0.07	10.34	0.34	10.09	0.09
		50	10.00	0.00	9.99	-0.01	10.26	0.26	10.02	0.02
		100	11.27	1.27	11.27	1.27	11.52	1.52	11.29	1.29
	12.5	0	10.13	0.13	10.12	0.12	10.53	0.53	10.17	0.17
		25	10.08	0.08	10.08	0.08	10.48	0.48	10.12	0.12
		50	10.00	0.00	10.00	0.00	10.41	0.41	10.05	0.05
		100	11.19	1.19	11.19	1.19	11.59	1.59	11.24	1.24
16	5.0	0	15.44	-0.56	15.44	-0.56	15.64	-0.36	15.45	-0.55
		25	15.38	-0.62	15.38	-0.62	15.59	-0.41	15.39	-0.61
		50	15.30	-0.70	15.29	-0.71	15.50	-0.50	15.31	-0.69
		100	17.63	1.63	17.62	1.62	17.82	1.82	17.64	1.64
	12.5	0	15.44	-0.56	15.44	-0.56	15.80	-0.20	15.46	-0.54
		25	15.38	-0.62	15.38	-0.62	15.74	-0.26	15.40	-0.60
		50	15.30	-0.70	15.30	-0.70	15.66	-0.34	15.32	-0.68
		100	17.46	1.46	17.45	1.45	17.80	1.80	17.47	1.47
MAE (km)				**0.51**		**0.51**		**0.54**		**0.51**

Notes: l = Actual fault distance (km), GM1 = Estimated fault distance using General model 1 and undamped transient frequency (km), ΔGM1 = Error of estimated fault distance using general model 1 and undamped transient frequency (km), GM2 = Estimated fault distance using General model 2 and undamped transient frequency (km), ΔGM2 = Error of estimated fault distance using general model 2 and undamped transient frequency, GM3 = Estimated fault distance using General model 3 and undamped transient frequency (km), ΔGM3 = Error of estimated fault distance using general model 3 and undamped transient frequency (km), GM4 = Estimated fault distance using General model 4 and undamped transient frequency (km), ΔGM4 = Error of estimated fault distance using general model 4 and undamped transient frequency (km), MAE = Mean average error.

C.2 Tabulated Results of Simulated Network Model 2

Table C9. Comparison of the distance estimates obtained between EX1 and GM2 algorithm. f_{dm} , f_{nm} and ζ are estimated transient parameters from the simulated earth fault transient waveform.

l	f_{dm}	ζ	f_{nm}	EM1	$\triangle$EM1	GM2	$\triangle$GM2
2	1250.00	0.015	1250.13	2.23	0.23	2.88	0.88
4	1083.33	0.020	1083.56	3.91	-0.09	4.21	0.21
6	955.88	0.025	956.19	5.69	-0.31	5.70	-0.30
8	855.26	0.029	855.63	7.61	-0.39	7.37	-0.63
10	773.81	0.034	774.26	9.68	-0.32	9.20	-0.80
12	706.52	0.036	706.99	11.90	-0.10	11.22	-0.78
14	650.00	0.041	650.55	14.25	0.25	13.42	-0.59
16	625.00	0.043	625.58	15.48	-0.52	14.58	-1.42
18	580.36	0.047	580.99	18.03	0.03	17.04	-0.96
20	560.34	0.048	560.99	19.35	-0.65	18.34	-1.66
MAE					**0.29**		**0.82**

Notes:

l = Actual fault distance (km), f_{dm} = Estimated damped transient frequency (Hz), ζ = Damping factor, f_{nm} = Estimated undamped transient frequency (Hz), EM1 = Estimated fault distance using exact model 1 (km) , $\triangle$EM1 = Error of estimated fault distance using exact model 1 (km), GM2 = Estimated fault distance using General model 2, $\triangle$GM2 = Error of estimated fault distance using general model 2 (km), MAE = Mean average error.

Table C10. Comparison of the distance estimates obtained between EM1 and GM2 algorithm with the effect of fault resistance. f_{dm} , f_{nm} and ζ are estimated transient parameters from the simulated earth fault transient waveform.

l	Rf	f_{dm}	ζ	f_{nm}	EM1	ΔEM1	GM2	ΔGM2
4	10	1083.33	0.0370	1084.08	3.90	-0.10	4.21	0.21
	30	1083.33	0.0705	1086.04	3.88	-0.12	4.19	0.19
	50	1083.33	0.1041	1089.26	3.84	-0.16	4.16	0.16
	100	1015.63	0.1978	1036.09	4.51	0.51	4.71	0.71
					MAE	**0.22**		**0.32**
10	10	773.81	0.0456	774.61	9.67	-0.33	9.20	-0.80
	30	773.81	0.0707	775.75	9.64	-0.36	9.17	-0.83
	50	773.81	0.0955	777.36	9.59	-0.41	9.12	-0.88
	100	738.64	0.1634	748.69	10.46	0.46	9.91	-0.09
					MAE	**0.39**		**0.65**
16	10	625.00	0.0529	625.88	15.46	-0.54	14.56	-1.44
	30	625.00	0.0737	626.70	15.42	-0.58	14.52	-1.48
	50	601.85	0.0980	604.76	16.61	0.61	15.66	-0.34
	100	601.85	0.1498	608.72	16.38	0.38	15.45	-0.55
					MAE	**0.53**		**0.95**
Overall MAE (km)						**0.38**		**0.64**

Notes: l = Actual fault distance (km), f_{dm} = Estimated damped transient frequency (Hz), ζ = Damping factor, f_{nm} = Estimated undamped transient frequency (Hz), EM1 = Estimated fault distance using exact model 1 (km) , ΔEM1 = Error of estimated fault distance using exact model 1 (km), GM2 = Estimated fault distance using General model 2, ΔGM2 = Error of estimated fault distance using general model 2 (km), MAE = Mean average error.

Table C11. Comparison of the distance estimates obtained between EM1 and GM2 algorithm with the effect of fault inception angle. f_{dm} , f_{nm} and ζ are estimated transient parameters from the simulated earth fault transient waveform.

l	Angle (°)	f_{dm}	ζ	f_{nm}	EM1	ΔEM1	GM2	ΔGM2
4	90.00	1083.33	0.020	1083.56	3.91	-0.09	4.21	0.21
	45.00	1083.33	0.020	1083.56	3.91	-0.09	4.21	0.21
	0.00	1083.33	0.020	1083.56	3.91	-0.09	4.21	0.21
16	90.00	625.00	0.042	625.56	15.48	-0.52	14.58	-1.42
	45.00	625.00	0.042	625.56	15.48	-0.52	14.58	-1.42
	0.00	601.85	0.043	602.42	16.74	0.74	15.79	-0.21
MAE (km)						**0.34**		**0.61**

Notes: l = Actual fault distance (km), f_{dm} = Estimated damped transient frequency (Hz), ζ = Damping factor, f_{nm} = Estimated undamped transient frequency (Hz), EM1 = Estimated fault distance using exact model 1 (km) , ΔEM1 = Error of estimated fault distance using exact model 1 (km), GM2 = Estimated fault distance using General model 2, ΔGM2 = Error of estimated fault distance using general model 2 (km), MAE = Mean average error.

Table C12. Comparison of the distance estimates obtained between EM1 and GM2 algorithm with the effect of resistive loads. The loads are located at the end of each feeders. f_{dm} , f_{nm} and ζ are estimated transient parameters from the simulated earth fault transient waveform.

l	Load	Rf	f_{dm}	ζ	f_{nm}	EM1	ΔEM1	GM2	ΔGM2
2.00	400 kW	30	1250.00	0.095	1255.70	2.19	0.19	2.85	0.85
		50	1250.00	0.136	1261.80	2.14	0.14	2.81	0.81
		100	1160.71	0.219	1189.53	2.78	0.78	3.31	1.31
	800 kW	30	1250.00	0.120	1259.16	2.16	0.16	2.83	0.83
		50	1250.00	0.173	1269.23	2.07	0.07	2.76	0.76
		100	1160.71	0.223	1190.72	2.77	0.77	3.30	1.30
	2 MW	30	1354.17	0.107	1362.05	1.35	-0.65	2.23	0.23
		50	1250.00	0.158	1265.94	2.10	0.10	2.78	0.78
		100	1250.00	0.206	1277.52	2.01	0.01	2.71	0.71
						MAE	**0.32**		**0.84**
10.00	400 kW	30	773.81	0.084	776.58	9.62	-0.38	9.14	-0.86
		50	738.64	0.114	743.46	10.63	0.63	10.06	0.06
		100	738.64	0.177	750.51	10.40	0.40	9.86	-0.14
	800 kW	30	773.81	0.096	777.42	9.59	-0.41	9.12	-0.88
		50	738.64	0.127	744.67	10.59	0.59	10.03	0.03
		100	738.64	0.189	752.16	10.35	0.35	9.81	-0.19
	2 MW	30	773.81	0.118	779.24	9.54	-0.46	9.08	-0.92
		50	773.81	0.143	781.88	9.46	-0.54	9.01	-0.99
		100	738.64	0.204	754.52	10.28	0.28	9.74	-0.26
						MAE	**0.45**		**0.48**
18.00	400 kW	30	580.36	0.091	582.79	17.92	-0.08	16.93	-1.07
		50	580.36	0.111	584.00	17.84	-0.16	16.86	-1.14
		100	560.34	0.167	568.29	18.85	0.85	17.85	-0.15
	800 kW	30	580.36	0.104	583.55	17.87	-0.13	16.89	-1.11
		50	580.36	0.125	584.91	17.78	-0.22	16.80	-1.20
		100	560.34	0.180	569.62	18.77	0.77	17.76	-0.24
	2 MW	30	580.36	0.138	585.94	17.72	-0.28	16.74	-1.26
		50	580.36	0.158	587.78	17.61	-0.39	16.63	-1.37
		100	560.34	0.215	573.81	18.49	0.49	17.49	-0.51
						MAE (km)	**0.37**		**0.89**
Overall MAE (km)							**0.38**		**0.74**

Notes: l = Actual fault distance (km), f_{dm} = Estimated damped transient frequency (Hz), ζ = Damping factor, f_{nm} = Estimated undamped transient frequency (Hz), EM1 = Estimated fault distance using exact model 1 (km) , ΔEM1 = Error of estimated fault distance using exact model 1 (km), GM2 = Estimated fault distance using General model 2, ΔGM2 = Error of estimated fault distance using general model 2 (km), MAE = Mean average error.

Table C13. Comparison of the distance estimates obtained between EM1 and GM2 algorithm with the effect of inductive loads. The loads are located at the end of each feeders. f_{dm} , f_{nm} and ζ are estimated transient parameters from the simulated earth fault transient waveform.

l	Load	Rf	f_{dm}	ζ	f_{nm}	EM1	ΔEM1	GM2	ΔGM2
2.00	400 kVAr	30	1250.00	0.069	1253.03	2.21	0.21	2.86	0.86
		50	1250.00	0.106	1257.02	2.18	0.18	2.84	0.84
		100	1250.00	0.210	1278.56	2.00	0.00	2.70	0.70
	800 kVAr	30	1250.00	0.070	1253.05	2.21	0.21	2.86	0.86
		50	1250.00	0.106	1257.07	2.18	0.18	2.84	0.84
		100	1250.00	0.174	1269.44	2.07	0.07	2.76	0.76
	2 MVAr	30	1250.00	0.070	1253.10	2.21	0.21	2.86	0.86
		50	1250.00	0.107	1257.21	2.17	0.17	2.84	0.84
		100	1250.00	0.176	1269.87	2.07	0.07	2.76	0.76
						MAE	**0.14**		**0.81**
10.00	400 kVAr	30	773.81	0.071	775.77	9.64	-0.36	9.17	-0.83
		50	738.64	0.101	742.41	10.66	0.66	10.09	0.09
		100	738.64	0.147	746.74	10.52	0.52	9.96	-0.04
	800 kVAr	30	773.81	0.071	775.74	9.64	-0.36	9.17	-0.83
		50	738.64	0.100	742.37	10.66	0.66	10.09	0.09
		100	738.64	0.165	748.85	10.46	0.46	9.90	-0.10
	2 MVAr	30	773.81	0.071	775.74	9.64	-0.36	9.17	-0.83
		50	773.81	0.096	777.37	9.59	-0.41	9.12	-0.88
		100	738.64	0.165	748.95	10.45	0.45	9.90	-0.10
						MAE	**0.47**		**0.42**
18.00	400 kVAr	30	580.36	0.089	582.67	17.92	-0.08	16.94	-1.06
		50	580.36	0.096	583.02	17.90	-0.10	16.92	-1.08
		100	580.36	0.143	586.41	17.69	-0.31	16.71	-1.29
	800 kVAr	30	580.36	0.076	582.03	17.96	-0.04	16.98	-1.02
		50	580.36	0.096	583.02	17.90	-0.10	16.92	-1.08
		100	580.36	0.143	586.41	17.69	-0.31	16.71	-1.29
	2 MVAr	30	580.36	0.076	582.03	17.96	-0.04	16.98	-1.02
		50	580.36	0.095	583.02	17.90	-0.10	16.92	-1.08
		100	580.36	0.144	586.43	17.69	-0.31	16.71	-1.29
						MAE	**0.15**		**1.14**
Overall MAE (km)							**0.26**		**0.79**

Notes: l = Actual fault distance (km), f_{dm} = Estimated damped transient frequency (Hz), ζ = Damping factor, f_{nm} = Estimated undamped transient frequency (Hz), EM1 = Estimated fault distance using exact model 1 (km) , ΔEM1 = Error of estimated fault distance using exact model 1 (km), GM2 = Estimated fault distance using General model 2, ΔGM2 = Error of estimated fault distance using general model 2 (km), MAE = Mean average error.

Table C14. Comparison of the distance estimates obtained between EM1 and GM2 algorithm with the effect of loads of 0.9 power factor. The loads are located at the end of each feeders. f_{dm} , f_{nm} and ζ are estimated transient parameters from the simulated earth fault transient waveform.

l	PF	(MVA)	Rf	f_{dm}	ζ	f_{nm}	EM1	ΔEM1	GM2	ΔGM2
2.00	0.90	400	30.00	1250.00	0.096	1255.86	2.19	0.19	2.85	0.85
			50.00	1250.00	0.140	1262.46	2.13	0.13	2.80	0.80
			100.00	1160.71	0.261	1202.36	2.66	0.66	3.21	1.21
		800	30.00	1250.00	0.120	1259.03	2.16	0.16	2.83	0.83
			50.00	1250.00	0.164	1267.13	2.09	0.09	2.77	0.77
			100.00	1160.71	0.294	1214.23	2.55	0.55	3.13	1.13
							MAE	**0.30**		**0.93**
18.00	0.90	400	30.00	580.36	0.090	582.72	17.92	-0.08	16.94	-1.06
			50.00	580.36	0.110	583.90	17.85	-0.15	16.86	-1.14
			100.00	560.34	0.165	568.15	18.86	0.86	17.86	-0.14
		800	30.00	580.36	0.101	583.37	17.88	-0.12	16.90	-1.10
			50.00	580.36	0.122	584.70	17.80	-0.20	16.82	-1.18
			100.00	560.34	0.177	569.32	18.79	0.79	17.78	-0.22
							MAE	**0.37**		**0.81**
Overall MAE (km)								**0.33**		**0.87**

Table C15. Comparison of the distance estimates obtained between EM1 and GM2 algorithm with the effect of loads of 0.5 power factor. The loads are located at the end of each feeders. f_{dm} , f_{nm} and ζ are estimated transient parameters from the simulated earth fault transient waveform

l	PF	(MVA)	Rf	f_{dm}	ζ	f_{nm}	EM1	ΔEM1	GM2	ΔGM2
2.00	0.50	400	30.00	1250.00	0.084	1254.40	2.20	0.20	2.86	0.86
			50.00	1250.00	0.122	1259.47	2.16	0.16	2.82	0.82
			100.00	1250.00	0.202	1276.18	2.02	0.02	2.72	0.72
		800	30.00	1250.00	0.098	1256.05	2.18	0.18	2.85	0.85
			50.00	1250.00	0.135	1261.63	2.14	0.14	2.81	0.81
			100.00	1250.00	0.203	1276.46	2.01	0.01	2.72	0.72
							MAE	**0.12**		**0.79**
18.00	0.50	400	30.00	580.36	0.081	582.28	17.95	-0.05	16.96	-1.04
			50.00	580.36	0.101	583.34	17.88	-0.12	16.90	-1.10
			100.00	560.34	0.156	567.25	18.92	0.92	17.92	-0.08
		800	30.00	580.36	0.087	582.59	17.93	-0.07	16.94	-1.06
			50.00	580.36	0.107	583.73	17.86	-0.14	16.87	-1.13
			100.00	560.34	0.162	567.85	18.88	0.88	17.88	-0.12
							MAE	**0.37**		**0.75**
Overall MAE (km)								**0.24**		**0.77**

Notes: l = Actual fault distance (km), f_{dm} = Estimated damped transient frequency (Hz), ζ = Damping factor, f_{nm} = Estimated undamped transient frequency (Hz), EM1 = Estimated fault distance using exact model 1 (km) , ΔEM1 = Error of estimated fault distance using exact model 1 (km), GM2 = Estimated fault distance using General model 2, ΔGM2 = Error of estimated fault distance using general model 2 (km), MAE = Mean average error.

C.3 Tabulated Results of Simulated Network Model 4

Table C16. Comparison of the distance estimates obtained from multiple regression (MRA) and neural network (NN) algorithm with the effect of fault resistance (R_f). Fault inception angle is 90°.

l	Load (MVA)	$R_f (\Omega)$	MRA	ΔMRA	NN	ΔNN
1.84	7.55	0	1.07	0.77	1.51	0.33
		25	2.03	-0.19	2.28	-0.44
		50	2.01	-0.16	2.22	-0.37
2.34	6.93	0	2.14	0.2	2.32	0.02
		25	2.02	0.33	2.18	0.16
		50	3.04	-0.7	3.02	-0.67
4.45	6.97	0	4.34	-0.11	4.28	0.17
		25	4.17	-0.28	4.2	0.25
		50	5.17	0.72	5.01	-0.56
7.86	6.93	0	8.71	-0.84	8.28	-0.42
		25	8.5	-0.63	8.22	-0.35
		50	8.46	-0.58	8.08	-0.22
8.07	7.55	0	8.63	-0.55	8.28	-0.2
		25	8.47	-0.39	8.14	-0.06
		50	8.43	-0.35	8.01	0.07
13.56	5.51	0	14.1	0.54	12.99	0.58
		25	13.83	0.26	14	-0.43
		50	13.74	0.17	13.8	-0.23
15.59	7.78	0	16.31	0.71	16.72	-1.13
		25	16.07	0.47	16.22	-0.62
		50	15.97	0.38	15.84	-0.25
MAE (km)				**0.44**		**0.36**

Notes: l = Actual fault distance (km), MRA = Estimated fault distance using multiple regression algorithm (km), ΔMRA = Error of estimated fault distance using multiple regression algorithm(km), NN = Estimated fault distance using neural network algorithm (km), ΔNN = Error of estimated fault distance using neural network algorithm (km), MAE = Mean average error (km).

Table C17. Comparison of the distance estimates obtained from multiple regression (MRA) and neural network (NN) algorithm with the effect of fault resistance (R_f). Fault inception angle is 45°.

l	Load (MVA)	$R_f(\Omega)$	MRA	ΔMRA	NN	ΔNN
1.84	7.55	0	2.04	-0.19	1.53	0.31
		25	1.98	-0.14	2.23	-0.38
		50	1.96	-0.12	2.16	-0.31
2.34	6.93	0	2.04	0.31	1.97	0.38
		25	1.95	0.39	1.73	0.61
		50	1.93	0.41	1.66	0.69
4.45	6.97	0	4.21	0.24	3.9	0.55
		25	4.12	0.34	3.71	0.75
		50	4.09	0.36	3.61	0.84
7.86	6.93	0	8.66	-0.8	7.86	0
		25	8.5	-0.64	7.89	-0.02
		50	8.45	-0.59	7.76	0.11
8.07	7.55	0	8.6	-0.53	8.23	-0.15
		25	8.47	-0.39	8.33	-0.25
		50	8.42	-0.34	8.27	-0.19
13.56	5.51	0	14.04	-0.48	13.25	0.32
		25	13.81	-0.24	13.51	0.06
		50	13.73	-0.16	13.5	0.07
15.59	7.78	0	16.19	-0.59	15.75	-0.16
		25	16.02	-0.42	16.09	-0.5
		50	15.96	-0.37	16.03	-0.44
MAE (km)				**0.38**		**0.34**

Notes: *l* = Actual fault distance (km), MRA = Estimated fault distance using multiple regression algorithm (km), ΔMRA = Error of estimated fault distance using multiple regression algorithm(km), NN = Estimated fault distance using neural network algorithm (km), ΔNN = Error of estimated fault distance using neural network algorithm (km), MAE = Mean average error (km).

Table C18. Comparison of the distance estimates obtained from general model (GM1,GM2,GM4) algorithms with the effect of fault resistance (R_f). Signal measured from MV/LV side and fault inception angle is 90°.

l	Load (MVA)	$R_f(\Omega)$	GM1	△GM1	GM2	△GM2	GM4	△GM4
1.84	7.55	0.00	1.64	-0.20	1.59	-0.25	1.65	-0.12
		25.00	2.80	0.96	2.47	0.63	2.52	0.74
		50.00	2.80	0.96	1.91	0.07	1.97	0.20
2.34	6.93	0.00	2.80	0.46	2.74	0.40	2.79	0.50
		25.00	2.80	0.46	2.48	0.14	2.53	0.24
		50.00	4.17	1.83	3.40	1.06	3.45	1.15
4.45	6.97	0.00	4.17	-0.28	4.12	-0.34	4.15	-0.25
		25.00	4.17	-0.28	3.86	-0.59	3.90	-0.51
		50.00	5.94	1.49	5.31	0.86	5.34	0.93
7.86	6.93	0.00	7.30	-0.56	7.24	-0.62	7.27	-0.56
		25.00	11.15	3.29	10.57	2.71	10.59	2.76
		50.00	11.15	3.29	10.42	2.56	10.45	2.62
8.07	7.55	0.00	8.38	0.31	7.23	-0.84	7.26	-0.77
		25.00	8.38	0.31	7.98	-0.09	8.01	-0.03
		50.00	8.38	0.31	7.90	-0.17	7.93	-0.11
13.56	5.51	0.00	12.01	-1.56	11.96	-1.60	11.99	-1.55
		25.00	16.40	2.84	15.92	2.36	15.95	2.40
		50.00	16.40	2.84	15.31	1.75	15.34	1.79
15.59	7.78	0.00	16.40	0.81	16.30	0.71	16.33	0.77
		25.00	16.40	0.81	15.92	0.33	15.94	0.38
		50.00	16.40	0.81	16.07	0.48	16.09	0.54
MAE				**1.17**		**0.88**		**0.90**

Notes: l = Actual fault distance (km), GM1 = Estimated fault distance using general model 1 (km), △GM1 = Error of estimated fault distance using general model 1 (km), GM2 = Estimated fault distance using general model 2 (km), △GM2 = Error of estimated fault distance using general model 2 (km), GM4 = Estimated fault distance using general model 4 (km), △GM4 = Error of estimated fault distance using general model 4 (km), MAE = Mean average error (km).

Table C19. Comparison of the distance estimates obtained from general model (GM1, GM2,GM4) algorithms with the effect of fault resistance (R_f). Signal measured from MV/LV side and fault inception angle is 45°.

l	Load (MVA)	$R_f(\Omega)$	GM1	ΔGM1	GM2	ΔGM2	GM4	ΔGM4
1.84	7.55	0.00	1.86	0.02	1.81	-0.03	1.87	0.10
		25.00	1.86	0.02	1.84	0.00	1.90	0.13
		50.00	1.86	0.02	1.74	-0.10	1.80	0.03
2.34	6.93	0.00	1.86	-0.48	1.81	-0.53	1.87	-0.41
		25.00	1.86	-0.48	1.82	-0.52	1.87	-0.41
		50.00	1.86	-0.48	1.74	-0.60	1.80	-0.48
4.45	6.97	0.00	3.59	-0.87	3.54	-0.91	3.58	-0.83
		25.00	3.59	-0.87	3.40	-1.05	3.44	-0.96
		50.00	3.59	-0.87	2.71	-1.74	2.76	-1.64
7.86	6.93	0.00	8.38	0.52	8.31	0.45	8.34	0.51
		25.00	8.38	0.52	8.01	0.15	8.04	0.21
		50.00	8.38	0.52	7.73	-0.13	7.76	-0.07
8.07	7.55	0.00	8.38	0.31	8.30	0.23	8.33	0.29
		25.00	8.38	0.31	8.18	0.11	8.21	0.18
		50.00	9.65	1.58	8.83	0.76	8.86	0.83
13.56	5.51	0.00	13.98	0.42	13.92	0.36	13.94	0.40
		25.00	13.98	0.42	13.58	0.02	13.60	0.06
		50.00	13.98	0.42	13.06	-0.50	13.08	-0.46
15.59	7.78	0.00	13.98	-1.61	13.89	-1.70	13.92	-1.64
		25.00	13.98	-1.61	13.55	-2.04	13.58	-1.98
		50.00	13.98	-1.61	13.09	-2.50	13.12	-2.44
MAE (km)				**0.66**		**0.69**		**0.67**

Notes: l = Actual fault distance (km), GM1 = Estimated fault distance using general model 1 (km), ΔGM1 = Error of estimated fault distance using general model 1 (km), GM2 = Estimated fault distance using general model 2 (km), ΔGM2 = Error of estimated fault distance using general model 2 (km), GM4 = Estimated fault distance using general model 4 (km), ΔGM4 = Error of estimated fault distance using general model 4 (km), MAE = Mean average error (km).

Table C20. Comparison of the distance estimates obtained from exact model (EM1-GM3) algorithms with the effect of fault resistance (R_f). Signal measured from MV/LV side and fault inception angle is 90°.

l	Load (MVA)	$R_f(\Delta)$	EM1	ΔEM1	EM2	ΔEM2	EM3	ΔEM3
1.84	7.55	0.00	1.24	-0.60	1.20	-0.64	1.19	-0.65
		25.00	2.41	0.57	2.28	0.44	2.26	0.42
		50.00	1.70	-0.14	1.63	-0.21	1.62	-0.22
2.34	6.93	0.00	2.74	0.40	2.58	0.24	2.56	0.22
		25.00	2.42	0.08	2.29	-0.05	2.27	-0.07
		50.00	3.51	1.17	3.30	0.96	3.26	0.92
4.45	6.97	0.00	4.31	-0.14	4.05	-0.40	3.99	-0.46
		25.00	4.02	-0.43	3.78	-0.67	3.73	-0.72
		50.00	5.63	1.18	5.31	0.86	5.19	0.74
7.86	6.93	0.00	7.73	-0.13	7.35	-0.51	7.12	-0.74
		25.00	11.29	3.43	10.98	3.12	10.44	2.58
		50.00	11.14	3.28	10.83	2.97	10.29	2.43
8.07	7.55	0.00	7.72	-0.35	7.34	-0.73	7.11	-0.96
		25.00	8.53	0.46	8.15	0.08	7.86	-0.21
		50.00	8.44	0.37	8.06	-0.01	7.78	-0.29
13.56	5.51	0.00	12.77	-0.79	12.55	-1.01	11.83	-1.73
		25.00	16.90	3.34	17.16	3.60	15.78	2.22
		50.00	16.27	2.71	16.43	2.87	15.18	1.62
15.59	7.78	0.00	17.29	1.70	17.62	2.03	16.17	0.58
		25.00	16.89	1.30	17.15	1.56	15.78	0.19
		50.00	17.05	1.46	17.34	1.75	15.93	0.34
MAE (km)				**1.14**		**1.18**		**0.87**

Notes: l = Actual fault distance (km), EM1 = Estimated fault distance using exact model 1 (km), ΔEM1 = Error of estimated fault distance using exact model 1 (km), EM2 = Estimated fault distance using exact model 2 (km), ΔEM2 = Error of estimated fault distance using Exact model 2 (km), EM3 = Estimated fault distance using exact model 3 (km), ΔGM3 = Error of estimated fault distance using exact model 3 (km), MAE = Mean average error (km).

Table C21. Comparison of the distance estimates obtained from exact model (EM1-GM3) algorithms with the effect of fault resistance (R_f). Signal measured from MV/LV side and fault inception angle is 45°.

l	Load (MVA)	$R_f(\Omega)$	EM1	ΔEM1	EM2	ΔEM2	EM3	ΔEM3
1.84	7.55	0.00	1.56	-0.28	1.49	-0.35	1.49	-0.35
		25.00	1.61	-0.23	1.54	-0.30	1.53	-0.31
		50.00	1.46	-0.38	1.40	-0.44	1.40	-0.44
2.34	6.93	0.00	1.56	-0.78	1.50	-0.84	1.49	-0.85
		25.00	1.57	-0.77	1.50	-0.84	1.50	-0.84
		50.00	1.47	-0.87	1.41	-0.93	1.40	-0.94
4.45	6.97	0.00	3.66	-0.79	3.44	-1.01	3.40	-1.05
		25.00	3.51	-0.94	3.30	-1.15	3.26	-1.19
		50.00	2.70	-1.75	2.55	-1.90	2.53	-1.92
7.86	6.93	0.00	8.88	1.02	8.51	0.65	8.19	0.33
		25.00	8.56	0.70	8.18	0.32	7.89	0.03
		50.00	8.26	0.40	7.88	0.02	7.61	-0.25
8.07	7.55	0.00	8.87	0.80	8.49	0.42	8.18	0.11
		25.00	8.75	0.68	8.37	0.30	8.06	-0.01
		50.00	9.45	1.38	9.08	1.01	8.71	0.64
13.56	5.51	0.00	14.82	1.26	14.80	1.24	13.79	0.23
		25.00	14.46	0.90	14.40	0.84	13.44	-0.12
		50.00	13.92	0.36	13.81	0.25	12.93	-0.63
15.59	7.78	0.00	14.79	-0.80	14.77	-0.82	13.76	-1.83
		25.00	14.44	-1.15	14.37	-1.22	13.42	-2.17
		50.00	13.96	-1.63	13.85	-1.74	12.96	-2.63
MAE (km)				**0.85**		**0.79**		**0.80**

Notes: l = Actual fault distance (km), EM1 = Estimated fault distance using exact model 1 (km), ΔEM1 = Error of estimated fault distance using exact model 1 (km), EM2 = Estimated fault distance using exact model 2 (km), ΔEM2 = Error of estimated fault distance using Exact model 2 (km), EM3 = Estimated fault distance using exact model 3 (km), ΔGM3 = Error of estimated fault distance using exact model 3 (km), MAE = Mean average error (km).

Aalto-DD 189/2014

This dissertation focuses on single phase to earth faults in medium voltage (MV) distribution feeders. Single phase to earth fault is the most common fault type in power distribution networks. In Finland and in most of countries in Europe the MV networks are operated with neutral isolated or resonant earthed systems. The way the neutral is connected is important since it will affect the type of protection system needed and power system component selection. In isolated neutral networks earth fault currents are relatively small compared with earthed systems. The initial transients of earth faults are important for fault location especially in unearthed and compensated neutral network. The electromagnetic transient provide the available information for estimating fault location. This dissertation proposes fault location algorithms based on earth fault transient signals measured at secondary side of MV and LV distribution transformers in order to locate a single line to earth fault in unearthed and compensated neutral MV distribution networks.

9 789526 059730

ISBN 978-952-60-5973-0 (printed)
ISBN 978-952-60-5974-7 (pdf)
ISSN-L 1799-4934
ISSN 1799-4934 (printed)
ISSN 1799-4942 (pdf)

Aalto University
School of Electrical Engineering
Department of Electrical Engineering and Automation
www.aalto.fi

BUSINESS +
ECONOMY

ART +
DESIGN +
ARCHITECTURE

SCIENCE +
TECHNOLOGY

CROSSOVER

DOCTORAL
DISSERTATIONS